Modeling of Self-Assembled Quantum Dot Lasers

Yiling Xiong

A Thesis

In the Department

of

Electrical and Computer Engineering

Presented in Partial Fulfillment of the Requirements

For the Degree of

Doctor of Philosophy (Electrical and Computer Engineering) at

Concordia University

Montréal, Québec, Canada

August 2019

© Yiling Xiong, 2019

CONCORDIA UNIVERSITY

SCHOOL OF GRADUATE STUDIES

This is to certify that the thesis prepared

By: Yiling Xiong

Entitled: Modeling of Self-Assembled Quantum Dot Lasers

and submitted in partial fulfillment of the requirements for the degree of

Doctor Of Philosophy (Electrical and Computer Engineering)

complies with the regulations of the University and meets the accepted standards with respect to originality and quality.

Signed by the final examining committee:

_____ Chair
Dr. Anjali Awasthi

_____ External Examiner
Dr. Jose Azana

_____ External to Program
Dr. Zhibin Ye

_____ Examiner
Dr. Ahmed A. Kishk

_____ Examiner
Dr. Jiaren Liu

_____ Thesis Supervisor
Dr. John Xiupu Zhang

Approved by _____
Dr. Rastko Selmic, Graduate Program Director

October 21, 2019

Dr. Amir Asif, Dean
Gina Cody School of Engineering & Computer Science

ABSTRACT

Modeling of Self-Assembled Quantum Dot Lasers

Yiling Xiong, Ph.D.
Concordia University, 2019

The study of active region structure for semiconductor lasers began in the 1960s. Most recently, quantum dot (QD) based lasers have attracted increasing attention. Modeling is crucial for the design of semiconductor QD-based lasers. Many attempts have been made to the macroscopic and, particularly, the microscopic modeling of III-V semiconductor QD as well as its applications during these decades. However, these proposed approaches use a very similar but outdated way to calculate the elastic strain field, referred to as one-step model, without rigorous consideration of the influence of the growth interruption in double-capping procedure, as the latter is currently used in epitaxial self-assembly for the control over the size of QDs. This thesis aims to contribute to the design improvements of QD-based laser applications through more accurate modeling.

In this thesis, we have focused on improving the modeling accuracy by elaborately analyzing the elastic strain and quantum confinement potential. By applying this accurate modeling methodology, not only the general semiconductor QD-based lasers but also the structures with an interlayer/sublayer or tightly coupled QD ensemble can be numerically modeled, giving rise to the possibility for predicting the behavior and even structural design of lasers, paving the way to potentially novel applications. The following work has been done in this thesis.

Firstly, we propose an accurate method of modeling a single QD, including a thorough so-called two-step elastic strain analysis, by considering the influence of growth interruption. A series of settings in terms of the three-dimensional (3D) geometry of QD and surrounding matrix are considered. The 3D confinement potential profile is found significantly different compared with

the counterpart using the conventional one-step model. The electronic band structure is then calculated by using the strain-dependent eight-band $\boldsymbol{k \cdot p}$ method. The simulation results by using the two-step model are found in better agreement than one-step model in comparison with measurements. Moreover, the impact of the quaternary compositions of barrier material is, for the first time, systematically studied.

Secondly, the two-step model is further extended to three- and multi-step analysis to model the structures with additional GaP ultrathin layer above or beneath the QDs. It is found that, instead of preventing the As/P exchange, the main impact of GaP interlayer/sublayers is enhancing the quantum confinement and thereby blue-shifting the emission peak. Based on the ability to efficiently shifting the spectrum, a new vertically chirped multi-layer structure is proposed. By simultaneously optimizing the interlayer/sublayer thickness and double-capping settings, a total gain spectral bandwidth of 245.7 nm (i.e. 30% increase) is predicted, and peak wavelength is shortened to 1510 nm (i.e. 70 nm blueshift, in comparison to the case without interlayer/sublayer).

Thirdly, laterally and vertically coupled QDs are modeled to investigate a variety of coupling effects in the active region of lasers. In particular, multi-step strain analysis is applied to the modeling of closely stacked QDs to reproduce a more realistic unidirectional compressive strain accumulation, evidenced by the morphological observation of cross-section images obtained from measurements. A “quasi continuum band” formed by the mixing of bonding and antibonding states is found, giving rise to the possibility of emission at excited state (ES) instead of the ground state (GS). Using this feature, a new laser structure allowing two-state lasing under continuous wave (CW) electrical pumping is proposed for the first time and characterized through the simulation of spectral linewidth and relative intensity noise (RIN). The new structure exhibits lower (i.e. −130 versus −110 dBc/Hz) integrated RIN compared with the conventional counterpart under relatively high CW current injection.

Overall, this thesis sheds light on new device physics and provide guidelines to realize QD-based lasers with new features, and would be interesting to the scientific community.

Acknowledgements

I would like to express my sincere thanks to my supervisor Prof. John Xiupu Zhang, for his advice, guidance, and financial help for me to finish this thesis.

I am grateful to my wife, Xi Chen, and my daughter, Yuexi Cécile Xiong, for bringing the sunshine into my life.

I would like to thank my parents for their love, understanding, and support.

Table of Contents

List of Figures

List of Tables

List of Acronyms

0D	Zero-dimensional
1D	One-dimensional
2D	Two-dimensional
3D	Three-dimensional
AFM	Atomic force microscopy
BC	Boundary condition
BES	Bright exciton splitting
CBE	Chemical beam epitaxy
cPDE	Coefficient-form partial differential equation
CCL	Coherent comb laser
CB	Conduction band
CBE	Conduction band edge
CPE	Confinement potential energy
CW	Continuous-wave
CM	Continuum mechanical
CLT	Critical layer thickness
X-STM	Cross-sectional scanning tunneling microscopy
DOF	Degree of freedom
DOS	Density of state
DBR	Distributed Bragg reflector
DFB	Distributed feedback laser
DE	Droplet epitaxy
EEL	Edge-emitting laser
EME	Eigenmode expansion
EM	Electromagnetic
EP	Empirical pseudopotential
ES	Excited state
FP	Fabry-pérot

FBG	Fiber Bragg grating
FSS	Fine structure splitting
FEM	Finite element method
FDTD	Finite-difference time-domain
FCL	First capping layer
FL	Flat lens
FvdM	Frank-van der Merwe
FSR	Free spectral range
FWHM	Full width at half magnitude
GUI	Graphical user interface
GS	Ground state
GSSS	Ground state spectrum-splitting
GVD	Group-velocity dispersion
HH	Heavy-hole
HAADF	High angle annular dark field
HB	Homogeneous broadening
IHB	Inhomogeneous broadening
IE	Isotropy-elasticity
KPFM	Kelvin probe force microscopy
LiDAR	Light detection and ranging
LED	Light emitting diode
LH	Light-hole
LEF	Linewidth enhancement factor
LPE	Liquid-phase epitaxy
LO	Local oscillator
LT	Low temperature
MOCVD	Metal-organic chemical vapor deposition
MLL	Mode-locked laser
MBE	Molecular beam epitaxy
ML	Monolayers
ODE	Ordinary differential equation

PDE	Partial differential equation
PL	Photoluminescence
PIC	Photonic integrated circuits
PZT	Piezoelectric
PDF	Probability density function
BPM	Propagation method
Qdashe	Quantum dashe
QD	Quantum dot
QIP	Quantum information processing
QW	Quantum well
RAM	Random access memory
RE	Rate equation
RAS	Reflectance anisotropy spectroscopy
RHEED	Reflection high-energy electron diffraction
RIN	Relative intensity noise
RT	Room temperature
SPM	Scanning probe microscopy
STEM	Scanning transmission electron microscopy
STS	Scanning tunneling spectroscopy
SCL	Second capping layer
SA	Self-assembled
SCP	Self-consistent pseudopotential
SPM	Self-phase modulation
SOA	Semiconductor optical amplifier
SCH	Separate confinement heterostructure
SFL	Single-frequency laser
SO	Split-off
SLN	Stacking-layer number
SK	Stranski-Krastanov
TCAD	Technology computer aided design
TB	Tight-binding

TDTW	Time-domain travelling-wave
TEM	Transmission electron microscopy
TE	Transverse electric
TM	Transverse magnetic
TP	Truncated pyramid
VB	Valence band
VBE	Valence band edge
VFF	Valence force field
VW	Volmer-Weber
WDM	Wavelength-division-multiplexing
WL	Wetting layer

When you have confidence, you can have a lot of fun.
And when you have fun, you can do amazing things.
Joe Namath

Chapter 1 Introduction

1.1 Introduction

Demand for higher performance active optical elements always exists in modern society, such as semiconductor diode lasers, light emitting diodes (LEDs), and semiconductor optical amplifiers (SOAs), etc. In particular, since playing a vital role in broadband optical telecommunication applications, higher performance, compact, and low-cost laser sources generating light across the visible, near-infrared and THz spectral ranges are in strong demand, driving the innovations of semiconductor laser technologies to meet the requirement of increasing data traffic. The semiconductor based device of light amplification by the stimulated emission of radiation (i.e. LASER operation) in gain medium was first demonstrated in 1960s. The lasing was realized by the onset of population inversion in the depletion region, resulting in the radiative recombination of electron-hole pairs injected across a pn-junction [1]. Since then, advanced structures have been proposed, e.g. one composed of two different direct-gap III-V compound materials (i.e. heterostructures [2]), in particular, another comprising two such heterostructures back-to-back to form a "wide-gap−narrow-gap−wide-gap" sandwich (i.e. double heterostructures [3]), which greatly improved diode lasers' performances (e.g. high injection efficiency, low lasing threshold, and loose temperature restriction). The improvement was achieved by the enhanced localized photons and carriers thereby maximizing the interaction between them. Crucially, the use of double heterostructure leads to a breakthrough in semiconductor diode lasers from only an academic interest towards actual industrial and commercial applications e.g. gas and biomolecule sensors, medical instruments and therapeutics, LiDAR components for self-driving vehicles, interconnects for telecom applications, even photonic integrated circuits (PIC) for the on-chip realization, etc.

In recent years, driven by the need of structural evolution of active medium, various crystal growth techniques has also been developed, such as molecular beam epitaxy (MBE), metal-organic

chemical vapor deposition (MOCVD), liquid-phase epitaxy (LPE), chemical beam epitaxy (CBE) etc. [4] These refined growth techniques allowed better control over the fabrications of more complex and featured double heterostructures, such as superlattices, quantum wells (QWs) [5], nanowires, quantum dashes (Qdashes), and quantum dots (QDs). It should be clear that, since then, the key advantages (e.g. more engineerable electronic properties of gain region, reduced threshold current densities and temperature sensitivities of devices) came about from the reduced dimensionality (i.e. approaching to de Broglie wavelength of the carrier), quantum confinement, and density of state (DOS). The underlying physics is discussed in Chapter 2. For instance, first proposed in 1982 by Arakawa and Sakaki [6] and first implemented in lasers in 1994 by Kirstaedter *et al.* [7], it have been proven that for laser applications, QD lasers with delta-function-like DOS can offer superior properties to the common QW lasers in terms of high temperature insensitivity of threshold current [6], low threshold current density [8], high spectral purity, enhanced differential gain, and chirp-free characteristics [9]. The flexible and engineerable inhomogeneous broadening of gain introduced by the distribution of QD size is another interesting feature, depending on the specific applications in which the QDs are utilized [10]. Thus, although currently showing good performance for QW as the gain medium, QD is considered more promising in the advanced optoelectronics domain for better performance and economic viability. Since the Stranski−Krastanov (SK) growth mode was used to fabricate self-assembled QDs [7], these III-V (or II-VI) semiconductor "artificial atoms" have attracted a lot of attention in the community; naturally, computational modeling of the nanostructure has become more than a research subject in academies and laboratories, but also aroused the intensive industrial interest due to its predictive character in structural designs (i.e. the surrounding material chosen, the size and shape of QDs, the dot layer number, the distance between the stacked layers, etc.) and further optimizations. Notably, the strain introduced by self-assembly causes a tetragonal distortion of the unit cell, thus results in a significant modification to the electronic structure of nanostructures. Therefore, except for bringing two significant advantages (e.g. a wider choice of compound materials enabling to cover

a wider range of lasing wavelengths and more tunability of electronic properties of the structure [11]), the use of strained layers also bring about the complexity and challenge of numerical simulation: More than ever before, it requires a comprehensive knowledge to deal with the modeling for predicting the electronic properties and optical spectra.

1.1.1 QD lasers in optical communications

Material systems: Since the first InGaAs/GaAs QD laser was demonstrated in 1994 [7], great effort has been devoted to the QDs grown on GaAs substrate (i.e. GaAs-based QDs), which has successfully brought the self-assembled InAs/GaAs QD lasers commercialized in two decades [12]. Nevertheless, since the GaAs-based QD lasers usually emit in the O-band (1260–1360 nm) telecommunication window, there has been a growing interest in another key type, the InAs/InP QD lasers, which is more promising for the applications working in the C-band (1530–1565 nm) to reach long-haul optical communications. However, it is still a challengeable work to make the epitaxially grown InAs/InP QD as a perfect material system, due to relatively smaller lattice mismatch (3.1%) compared with InAs/GaAs (6.7%), resulting in a larger QD size distribution and thereby a reduced peak gain, from typically 100 cm^{-1} in ideal QD system to about 20 cm^{-1} [11, 13]. Moreover, the smaller lattice often leads to the formation of unexpected bigger dots, or elongated dashes, resulting in their emitting peak at a wavelength longer than ~1.6 μm easily at room temperature (RT) [14]. Other systems, such as II-VI and nitride-based QDs, are not discussed in this thesis.

In terms of the material of the barrier layers, there are two main material systems used in the structures of InAs QDs grown on InP substrate: InAs/InGaAlAs/InP and InAs/InGaAsP/InP. These quaternary alloys are grown either on (100) or (311)B InP substrates, which require a match between the lattice parameter of barrier layers to substrates by simply adjusting the relative ratio of Ga and Al (or Ga and As), to prevent formation of defects or dislocations thus degradation of device performances. Roughly speaking, compared to the common (100) oriented InP under the

same growth conditions, the growth on the high index (311)B InP substrate allows the formation of InAs QDs with smaller size, higher areal density, and higher uniformity [15]; in contrast, the growth on (100) InP substrate often results in undesirable elongated dots along the $(1\bar{1}0)$ direction and a low areal density (on the order of 10^9~10^{10} cm^{-2}) [16, 17], as shown in the atomic force microscopy (AFM) images in Fig. 1.1. However, persistent effort has been devoted to improve the InAs/InP (100) system rather than relying on InAs/InP (311)B due to the incompatibility of latter one with the standard laser fabrication process. Hereinafter, the improvement of the InAs/InGaAsP/InP (100) QDs is the main focus of this thesis.

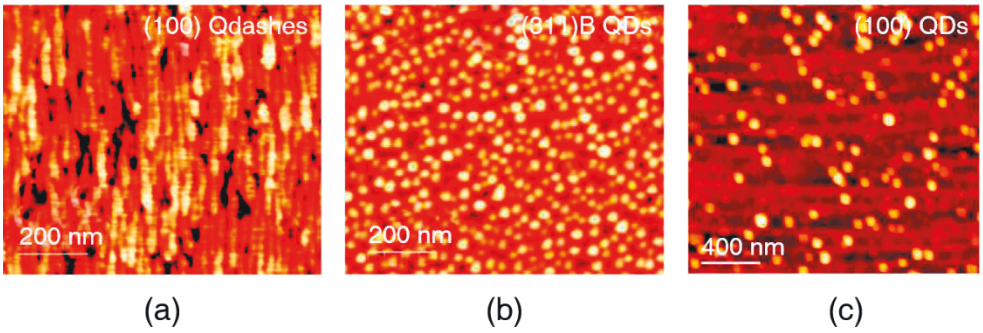

Fig. 1.1 AFM image of InAs/InP (a) Qdashes on (100) orientation substrate [18], (b) QDs on (311)B substrate [18], and (c) QDs on (100) substrate [19].

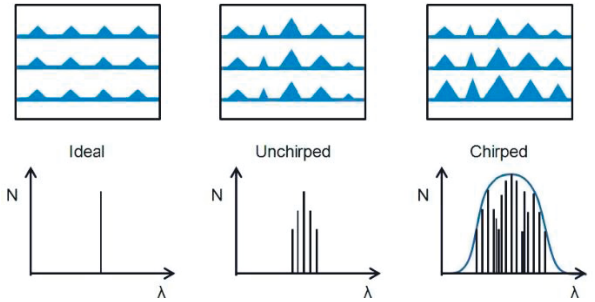

Fig. 1.2 Schematic representation of ideal (totally identical size), unchirped (identical from layer to layer) and chirped (intentionally non−identical from layer to layer) quantum dot layers, with their corresponding DOS, considering only the lowest-energy state [20].

Applications: There are two types of QD lasers, i.e. the single-frequency lasers (SFLs) operating in continuous-wave (CW), and ultrashort pulse lasers based on the mode-locking mechanism, driving the QD lasers evolving towards two opposite extremes: For the SFL, only the central mode

survives in the cavity, and all other side-longitudinal-modes are suppressed, while the ultrashort pulse laser aims to incorporate as many as possible modes in the active medium. There are different approaches to realize single-wavelength lasing in the SFLs, determined by the specified requirement of the application. The most straightforward solution is reducing the inhomogeneous broadening, thereby narrowing the spectral range of gain as much as possible, and the gain peak is tuned at the wavelength of resonator mode by effective control of either the average size of QDs or the composition of surrounding material. Therefore, this type of SFL benefits from the atom-like DOS (e.g. low temperature-sensitivity, high spectral purity and differential gain) of ideal QD scenario (i.e. an ensemble of totally identical QDs, as illustrated in Fig. 1.2), at the expense of achievable tunability of lasing wavelength. A typical and extreme application realized by using this approach is the single-photon source [21, 22], a key building block of quantum communication and quantum information processing (QIP). Since being in very high demand for the indistinguishability of emitted photons, the performance of the QD single-photon sources is not only susceptible to the uniformity of QD size, even to the in-plane symmetry of QD geometry, as the latter is the source of fine-structure splitting (FSS). Another category of SFL called broadly-tunable laser does not require a reduced inhomogeneous broadening. In contrast, in order to take advantage of achievable tuning range, intentionally increasing the level of inhomogeneous broadening thus resulting in wider gain bandwidth is quite essential. With such wide achievable spectral range in gain medium, the wavelength tunability can be demonstrated through employing an external cavity (e.g. diffraction grating or FBG) [23] or embedding an internal grating into the laser (i.e. DFB or DBR lasers) [24]. An example of communication applications is the tunable local oscillator (LO) used in the coherent detections [25]. Fig. 1.3 summarizes the progress of tunability ranges in InAs/GaAs QD SFLs at RT in the two decades.

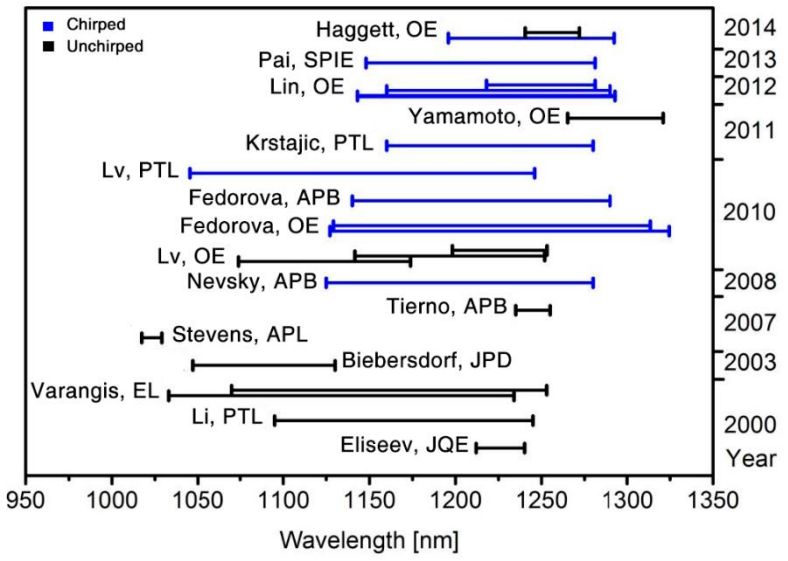

Fig. 1.3 Chronological progress in RT tunability ranges in CW tunable InAs/GaAs QD lasers with chirped (blue) and unchirped (black) QD layers [20].

Essentially, although the second type of SFLs and ultrashort pulse lasers have very different key performance indications (i.e. tuning range and linewidth for the SFLs, emission bandwidth and pulse width for the ultrashort pulse lasers), in terms of the active media, they have the same prerequisite (i.e. a very broad bandwidth of gain), which is opposite to the first type of SFLs. The ultrashort pulse laser is also referred to as the mode-locked laser (MLL) or coherent comb laser (CCL). InAs/InP MLLs as compact and low-cost transmitters are of great interest for high-speed and long-range fiber optic communication systems, e.g. dense wavelength-division-multiplexing (WDM) technology [26]. In MLLs, the mode-locking is achieved by a superposition of multiple longitudinal modes with fixed relative phase, resulting in a periodic train of optical pulses. The more modes with synchronized phases are incorporated in the cavity, the shorter width the pulses have [27]. Thanks to the inherent inhomogeneous nature and ultra-broad gain profile, QD MLL exhibits an improved ability to generate a high repetition rate and short duration pulses [28, 29]. Fig. 1.4 summarizes the progress of key performances in InAs/InP QD and Qdash MLLs at RT.

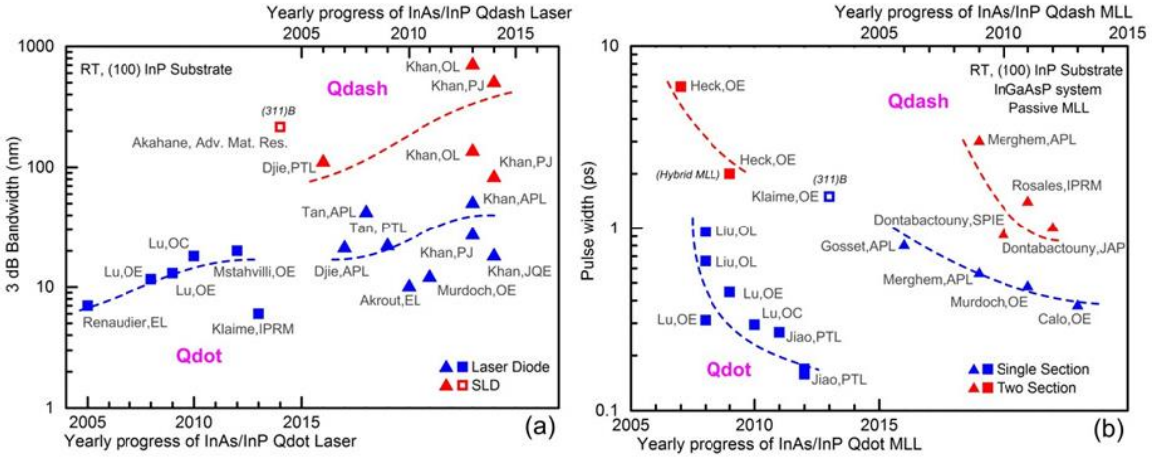

Fig. 1.4 Chronological progress in (a) achieving ultrabroad emission bandwidth, and (b) reduction in pulse width of InAs/InP QD (squares) and Qdash (triangles) MLLs at RT [30].

The passive mode-locking was commonly thought to only occur in a two-section structure (i.e. with a gain section and a saturable absorber). Recently, on the contrary, the mode-locking has also been found in single-section Qdash- and QD-based Fabry-Perot (FP) lasers under CW bias without a separated reverse-biased absorber [31, 32]. This single-section structure allows significantly reduced bulky size, complexity, and simplified fabrication process as well. However, the underlying physics of self-pulsing and self-generated mode-locking in the single-section QD lasers has not been fully understood yet. On the other hand, increasing inhomogeneous broadening implicates a deviation from the ideal QD scenario (see Fig. 1.2), and thus, to some extent, leads to an increase in transparency and threshold current and a reduction of the modal and differential gain [33, 34]. High modal and differential gain are expected to overcome the optical loss. Otherwise broadband gain is still impeded by the loss. This suggests that there is a tradeoff between the threshold current, the modal gain level and the gain spectral bandwidth, which is more complicated situation compared with the first type of SFL in terms of the structural design, and thus the in-depth study and computational modeling are more essential. Especially for long-haul optical communication applications, this tradeoff is even more crucial in InAs/InP material system with smaller lattice mismatch. Besides, a Gaussian-shaped intrinsic inhomogeneous broadening

brought by natural dot-size dispersion is not a perfect solution; by contrast, a flattop-shaped gain spectral profile can be engineered by careful design to great advantage in MMLs and broadly-tunable SFLs. Last but not the least, emitting peak at a wavelength longer than ~1.63 μm at RT is another obstacle to broaden the net modal gain bandwidth, as the majority of energy at longer wavelength is easily dissipated in long-haul transmission due to the high optical loss.

1.1.2 State of the art in QD lasers

Many innovations based on the growth process of QDs have been proposed for different purposes. In the following, they are briefly introduced.

One direction of development is to take advantage of the quantum confinement effects of QD (i.e. the first type of SFL) fully, that is, to reduce the inhomogeneous broadening as much as possible. The most immediate way would be by reducing the size dispersion. The double-capping procedure method, based on the SK growth mode and discontinuous capping management, is the most popular to reduce the size dispersion and the overgrowth of self-assembled QDs during the past decade [35-40]: As illustrated in Fig. 1.5, the dots are partially capped with a thin barrier layer, referred to the first capping layer (FCL), then they are followed by a short growth interruption (i.e. exposure under AsH_3 + PH_3), and finally they are capped with the second capping layer (SCL). The dot height corresponds exactly to the thickness of FCL in given thickness range (i.e. below 3.5 nm, reported by Ulloa *et al*. [37]). Thus, except for enhancing the modal gain aforementioned, the double-capping method allows very accurate control of the QD height, which can be applied to tune the emitting wavelength of laser sources. The disadvantage of this technique is that we cannot take care the symmetric properties of QDs when dealing with the InAs/InP material system, and the resulting elongated QDs lead to larger FSS that is not ideal enough for making single-photon sources. Most recently, Müller *et al.* demonstrated that InAs/InP QDs grown by droplet epitaxy (DE) could be an advantageous alternative and could exhibit very low FSS [21]: Consisting of the formation of indium (In) nanosized droplets on the substrate and then the crystallization of

these droplets to transform to InAs QDs by MOVPE, the DE technique was not restricted by the lattice mismatch conditions, thus strain-free and highly symmetric InAs/InP QDs are allowed.

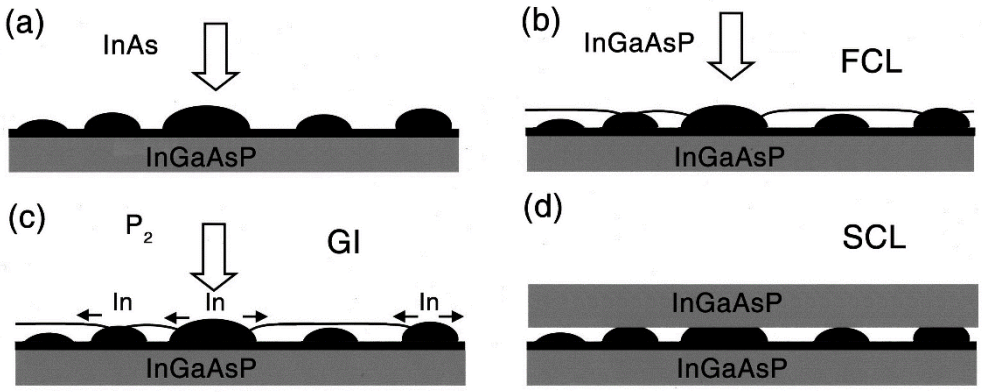

Fig. 1.5 Schematic illustration of double-capping procedure [41].

The other direction to improve the performance of QD lasers, in contrast, is to engineer further broadening of the gain not only within a dot layer but also from layer to layer. Based on this idea, the non-identical or chirped multi-layer structure has been proposed, mainly used to create high performance broadly-tunable SFLs, MLLs, and LEDs [42-45]. The chirped layers can be achieved, e.g. by manipulation of the InAs QD deposition or by variation of the barrier composition [28, 46-48]; however, both approaches were not perfect: The former led to undesirable high variations on areal density and radiative efficiency from layer to layer [49, 50], and the latter required sophisticated control over mismatch conditions and intermixing between QDs and surrounding materials. Therefore, the double-capping technique is the best candidate to deal with the tradeoff in chirped layers, so that broadband and high power can be concurrently achieved: By varying the thickness of FCL in each active layer, on the one hand, very broad coverage of spectral distribution is realized. By limiting the dot size dispersion in each active layer, on the other hand, a maximum modal gain is reached. Last but not the least, the spectral contributions of different active layers are almost identical, i.e. an almost flattop gain spectrum is allowed via using chirped multi-layer structure.

Inserting an ultra-thin GaAs or GaP interlayer/sublayer between QDs and upper/lower barrier layers, which has been proven a more effective way to shift the gain and photoluminescence (PL) spectrum of InP-based QD to C-band, improves the blue-shifting range of laser sources [51-53]. A smaller amount of GaP was required to obtain the same wavelength blue shift compared to GaAs [52]. In addition, the use of interlayer/sublayer allows better control over stacked QDs areal density, overgrowth, and size dispersion brought by the strain accumulation between the dot layers. Combining the double-capping procedure and employing a GaP interlayer/sublayer, Poole *et al.* were able to stack 1 to 10 dot layers without any change in PL peak wavelength or PL linewidth [35]. However, the present theoretical study on the exact influence of interlayers/sublayers is not sufficient and complete, and no physic model of InAs/InP QD lasers engineered by interlayers/sublayers has been applied to predict the emitting wavelength successfully. For instance, in order to explain the phenomenon of PL blue-shifting caused by the interlayer/sublayers in the most previous work [35, 51, 52, 54], the wavelength blue-shifting has been attributed to the stronger Ga–P or Ga–As bond introduced by ultra-thin GaP or GaAs interlayer/sublayers, thereby resulting in a weaker As/P exchange between InAs QD layers and InGaAsP barrier layers. This weaker As/P exchange leads to a smaller average QD size, compared to no GaP/GaAs interlayer/sublayer used, as illustrated in Fig. 1.6 (a)−(b). Intuitively, the explanation sounds plausible; however, it may contradict the measurement results in [35]: If the smaller dots and shorter PL peak wavelength are related to stronger molecular bond, then the blue-shifting of RT PL spectrum in [35] is supposed to be prevented by double-capping process, which forces the InAs QD heights to be identical, no matter if a GaP/GaAs interlayer/sublayer is used or not, as shown in Fig. 1.6 (c)−(d). In short, good knowledge about the exact influence of interlayer/sublayer along with an associated model is still in demand for developing novel structures.

Last but not the least, QDs are generally implemented to practical devices in the form of vertical multilayer stack to increase the small modal gain of a single layer heterostructure, in which there is a poor spatial overlap between gain medium and optical modes. Thus, the inter-dot distance

[55-61], the QD size lateral and vertical homogeneity [62-64], the multi-stacking alignment [65, 66], and stacking-layer number (SLN) are the main parameters [67, 68], and a variety of customized QD stacks have been proposed for various purposes, e.g., increase of absorber or gain medium volume [69], generation of quantum entanglement [70], quantum information processing [71], tuning of the transverse magnetic (TM)/transverse electric (TE) polarization ratio [72, 73], arising from the tuning of aforementioned structural parameters, particularly the spacer thickness which simultaneously affects the morphology and various coupling mechanisms.

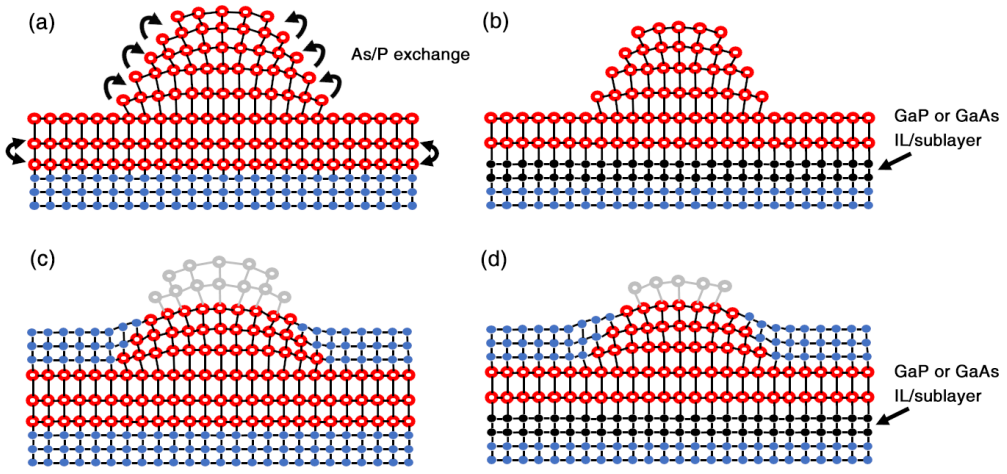

Fig. 1.6 Schematic illustration of (a) inflation of uncapped QD size due to As/P exchange, (b) being stopped by additional ultra-thin interlayer/sublayer due to stronger covalent bonds, and (c)−(d) difference in QD height being even out after double-capping procedure.

1.1.3 Overview of modeling

Due to the complexity and the nonlinear nature of the underlying physics, the computational modeling of QD laser dynamics is important but also difficult. In distinction to other laser structures, semiconductor QD lasers are characterized by some unique features (e.g. quantum confinement, engineerable strain, and inhomogeneous broadening) that have to be reflected in realistic computer models. In order to analyze the optical and electronic properties of the various subsystems, the modeling of self-assembled QD devices consists of two categories or stages:

microscopic and macroscopic approaches, as summarized in Fig. 1.7. On the one hand, the main objective of the microscopic modeling is simulating the semiconductor QD gain structure of lasers, i.e. constructing a single QD (with various shapes, dimensions, compositions, etc.) embedded in various surrounding materials, or stacking several QD layers to include the coupling effects, and taking into account the elastic strain distribution and the effects of piezoelectric (PZT) potential in and around the dots, then calculating the electronic band structure (e.g. see [74-77] for InAs/InP system, [78-84] for InAs/GaAs system, [83, 85] for InP/GaInP system, and [79, 86] for an universal system). As a fundamental and the core part of the microscopic modeling, the calculation of electronic bands was implemented by utilization of various semi-empirical approaches, e.g. the tight-binding theory [76, 87-90], the pseudopotential theory [75, 91, 92], and the $\boldsymbol{k} \cdot \boldsymbol{p}$ formalism [74, 77-79, 81-84]. Details are discussed in Chapter 2.

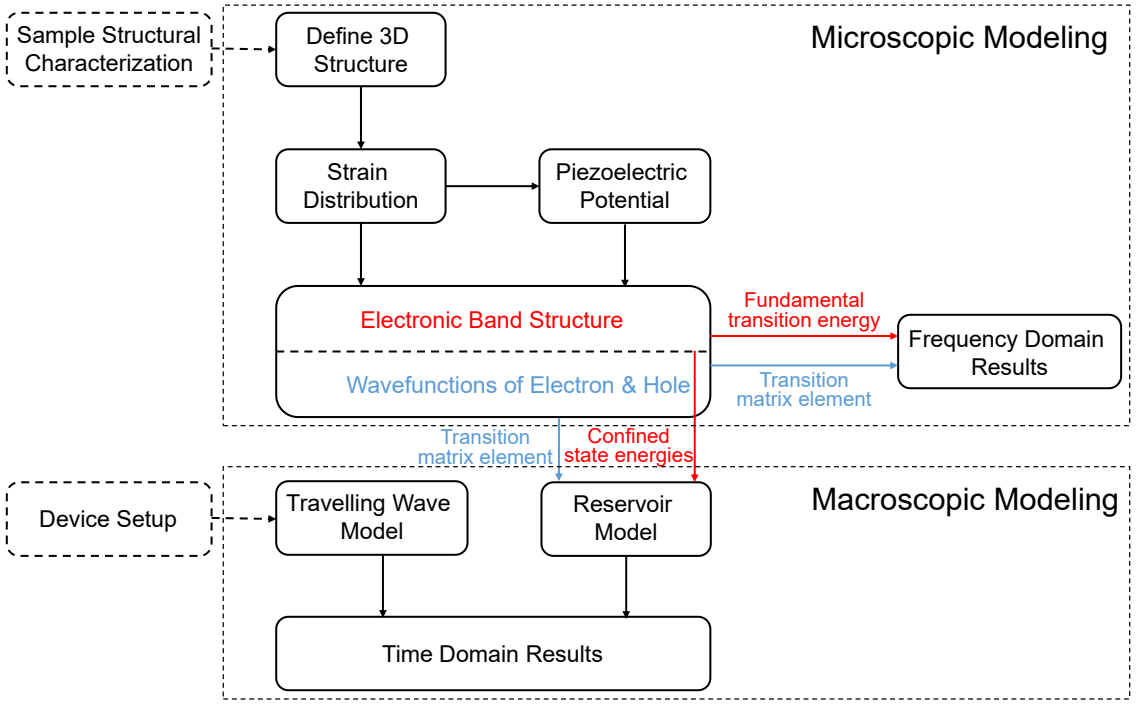

Fig. 1.7 Overview of the commonly applied approaches for describing the gain medium with semiconductor QDs (i.e. microscopic modeling) and the optical field dynamics in the scale of diode laser (i.e. macroscopic modeling).

On the other hand, aiming to describe the emitted photon or optical field dynamics in diode

laser models and taking into account the geometrical and physical setup of entire devices, the macroscopic modeling based on the semiclassical framework has concentrated on analyzing the scattering process of particles (i.e. electron and hole), particularly statistics of spontaneously and excitedly emitted photons in each energy state, e.g. ground state (GS) and excited state (ES) using rate equations (see [93, 94] for InAs/InP system, [95, 96] for InAs/GaAs system), or describing the exact electromagnetic (EM) wave using travelling-wave equation propagating in the cavity (see [97] for InAs/InP system, [98-101] for InAs/GaAs system). The approach chosen depended on the specified demand for modeling goals and the required computing resources. For instance, time-domain travelling-wave (TDTW) method offers a flexible and expandable tool appropriate to deal with the coupled dynamics of intra-cavity optical fields and active gain material, therefore particularly suitable for the diode lasers composed of complex structured cavities (e.g. DFB lasers), or simple ones (i.e. FP lasers) but characterized by the nonlinear properties consisting of carrier dynamics (e.g. spectral hole burning and four-wave mixing), spatial effects (e.g. spatial hole burning and self-focusing), and thermally induced changes of gain medium.

In a nutshell, microscopic modeling was applied to calculate the state-resolved interband transition energies (i.e. in frequency or wavelength domain), thus some experimental results irrelevant to time (e.g. PL peak wavelength) can be compared with the model; macroscopic modeling enables giving dynamics (i.e. in time domain), e.g. amplitude modulation response of free-running QD lasers (without TDTW) [102], or even spatio-temporal predictions, e.g. optical pulse width of MMLs (with TDTW) [97]. It should be clear that the microscopic and macroscopic models do not have to be combined and can be applied independently, determined by the specified targets and computing resources; however, in some cases, the microscopically analytical treatment is a prerequisite for the macroscopic study when experimental data of electronic band structure or transition energy are unavailable. Recently, Kayhani *et al.* have demonstrated a modeling method combining the microscopic and reservoir approaches to investigate the relationship between the QD size and modulation bandwidth of InAs/InP QD lasers [103].

1.1.4 Structural characterization

Structural characterization is a necessary step after the growth process. The quality of growth itself can be evaluated by structural characterization, which is determined by the control over the strain. In addition, key properties of epitaxially self-assembled QDs (e.g. size, shape and composition) can also be obtained as the input parameters used in the microscopic modeling. Thus, the techniques of structural characterization are fundamentally important for further studying/modeling their electronic/optical properties even on the atomic level, and thereby improving their performance. In what follows, we highlight widely used techniques and explore the morphological effects due to the strain.

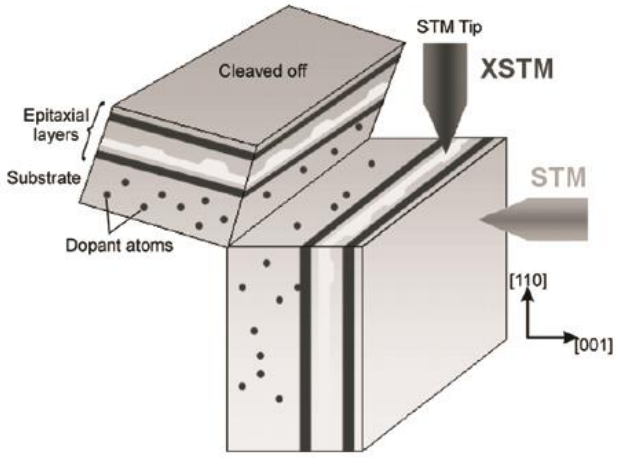

Fig. 1.8 Schematic illustration of STM and X-STM techniques.

Direct imaging methods: The aforementioned AFM plan-view measurements, based on the scanning probe microscopy (SPM), are only performed on uncapped QD samples (e.g. see Fig. 1.1). It is currently a well-established technique in surface science to diagnose the morphology of fabricated QDs' surface on the atomic scale. The main advantage of the AFM is, compared with the cross-sectional scanning tunneling microscopy (X-STM) as will be introduced later, it is a nondestructive method allowing a high resolution (~0.1 nm) in the growth direction. In addition, the AFM can help the fabrication of high-quality QD arrays by the use of tip-introduced nano-

oxidation and DE techniques [104]. However, the disadvantage should also be addressed that, as said, it can only measure the upper-most uncapped dot layer, which may not reflect the actual morphology of encapsulated QDs due to the different strain environment, thus misleading the further modeling.

In order to probe the structure of the internal QDs as well as the barrier layers between neighboring dot-layers (i.e. spacers), the X-STM has been proposed to perform on surfaces prepared by *in-situ* cleavage, as shown in Fig. 1.8. It can provide the actual size, shape and composition of encapsulated QDs (e.g. see Refs. [105, 106]), in particular, the accumulated strain distribution in vertically stacked QDs (e.g. see Refs. [107, 108]), as their findings are illustrated in Fig. 1.9. Furthermore, the X-STM, along with another version of STM (i.e. scanning tunneling spectroscopy: STS), enables direct visualization of probability density (i.e. $|\psi(\boldsymbol{r})|^2$) thanks to its spectroscopic ability [109, 110]. The so-called wavefunction mapping techniques investigate the spatial standing-wave pattern in InAs QDs associated with the lowest energy states close to the conduction band edge, as shown in Fig. 1.10. However, the major limitation in using STM comes from that the sample must be electronically conductive, which means plating or spurting is often required for the measurements of semiconductor nanostructures.

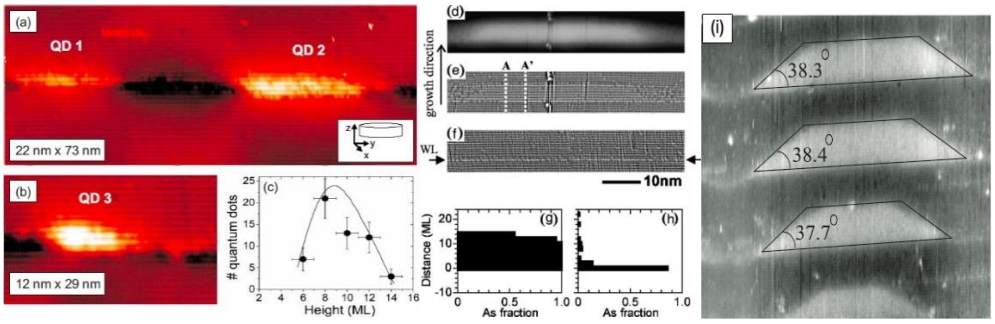

Fig. 1.9 (a)−(c) X-STM characterization of InAs/InP (100) QDs gives an average QD height of ~2.4 nm and a diameter of ~35 nm [105]. (d)−(h) X-STM images of InAs/InP (100) QD and wetting layer (WL) obtained at a bias voltage of −1.5 V, giving a critical layer thickness (CLT) of ~2 monolayers (ML) and an almost homogeneous compositional distribution in QDs [106]. (i) X-STM image of InAs/InP (100) QDs from a tenfold dot structure obtained at a bias voltage of −2.4 V, implicating by bottom-top nonidentical sizes the significant influence of accumulated strain on morphology [108].

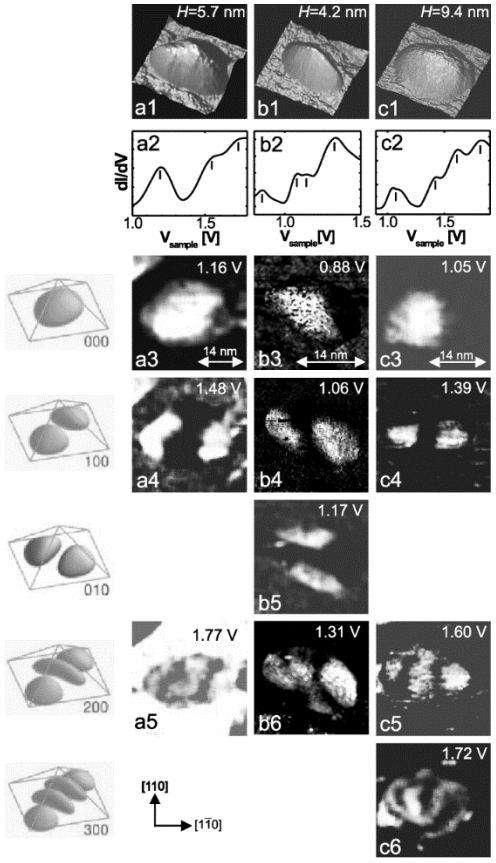

Fig. 1.10 STS data of three different InAs/GaAs (100) QDs with various heights and spatial distributions of probability density associated with the lowest energy states close to the conduction band edge [110].

A promising alternative is the transmission electron microscopy (TEM), operating on similar basic principles to those of an optic microscope, where electrons are used instead of light. In scanning TEM (i.e. STEM), a highly coherent beam of electrons is focused on a probe and is scanned point by point across a thin sample prepared to thickness (d < 200 nm) so that electrons can transmit through it to form an image. The main strength of STEM is, without a cleavage as X-STM requires which may change the strain distribution formed during QD growth, STEM can provide the information about fully buried QDs with original displacement fields (except those exposed QDs due to the segment). Therefore, the high-resolution STEM (e.g. high angle annular dark field: HAADF) imaging techniques have been proven to be powerful tools for the quantitative strain mapping, one of examples is shown in Fig. 1.11. Another unique feature of STEM is the

ability of visualization of 3D properties by electron tomography, as shown in Fig. 1.12.

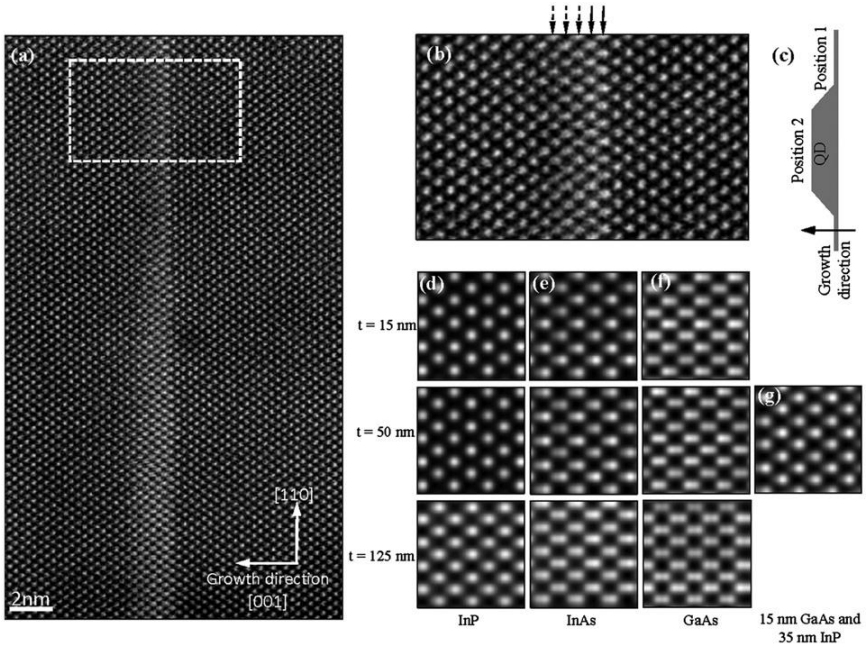

Fig. 1.11 HAADF STEM cross-sectional image of part of a single InAs/InP (100) QD overgrown with 1.7 ML of GaAs interlayer prior to be fully overgrown with InP [111].

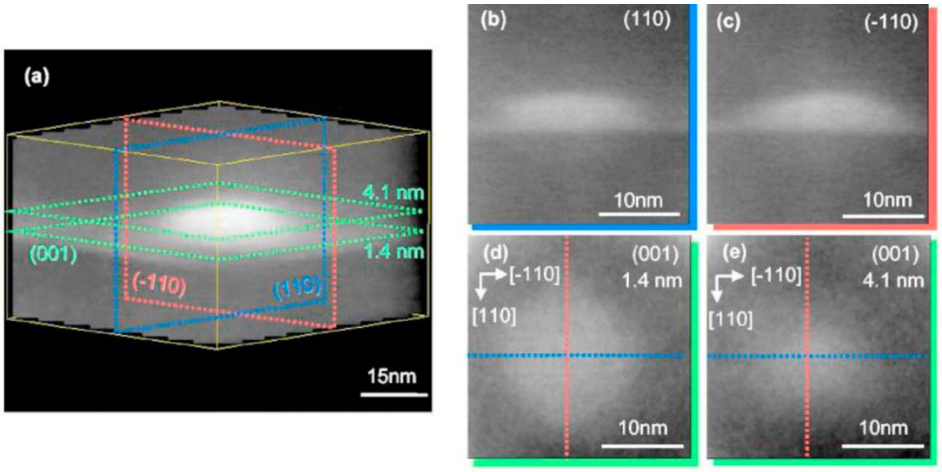

Fig. 1.12 Reconstructed 3D tomography image of a buried InAs/GaAs QD and its respective 2D cross-section images. The specimen was prepared as a nanopillar, so that rotating imaging was enabled [112].

Diffraction methods: As an end, three diffraction methods are briefly introduced here [113]. Reflection high-energy electron diffraction (**RHEED**) is a highly surface-sensitive ultra-high vacuum technique. Due to its ability of *in-situ* monitoring of QD formation, RHEED is widely

used for monitoring of the MBE growth. Reflectance anisotropy spectroscopy (**RAS**) enables the monitoring of asymmetrically dielectric properties of the surface. At last, **X-ray diffraction** provides a useful tool for the measurement of alloy composition in InGaAs WL.

1.2 Overview of Thesis

1.2.1 Motivation

In this thesis, the research focuses on developing a framework consisting of both microscopic and macroscopic models. Thus a theoretical description of the spatio-temporal dynamics in a given structure can be obtained. Existing modeling approaches are revised and extended to account for the challenging requirements imposed by the improved gain and cavity designs. Special attention is paid with regard to quantum-confined gain structures. Thus, the theory of semiconductor QD lasers is able to be continuously revised and sequentially adapted to the novel techniques and growth procedures, such as double-capping procedure and the use of interlayer/sublayer, which have been described in the previous sections. It is important to clear up at this point is the fact that strain distribution is calculated under the assumption that dot is already formed in most previous work [74-76, 78-80, 114], referred to as *one-step* modeling method hereinafter. In this one-step model, the upper and lower barrier layers and the QD together with the wetting layer (WL) are treated as a single body. This conventional strain analysis method *might* be valid for the continuous-capping growth scenario. However, it does not consider the widely used double-capping growth procedure to date, which may degrade the accuracy of modeling. To overcome the limitations and problems in the one-step model, a preliminary *two-step* modeling method was proposed by Kuo *et al.* for InAs/GaAs, rather than InAs/InP self-assembled QD system [115]. Unfortunately, the details of the two-step model are not given carefully, and the model is difficult to be followed and applied directly to this study. Besides, the actual impact of double-capping procedure on the strain profile and thereby on the quantum confinement has never been clarified deliberately based on the epitaxial growth process.

Furthermore, on the basis of the microscopic model with revised strain analysis, we aim to optimize the aforementioned laser applications (i.e. tunable SFLs and MLLs) mainly for 1.55 μm optical communications by developing the active structures with chirped and unchirped QD layers. In regards to the macroscopic model, we concentrate on obtaining a quantitative understanding of the interaction between the nonlinearity of gain medium and the intracavity light field dynamics in the defined FP edge-emitting laser (EEL) structures. The simulations of key performance indications, e.g. relative intensity noise (RIN) and phase noise, are also desirable.

1.2.2 Original contributions

This thesis contributes to the advancement of knowledge in the field of QD optoelectronics, including:

1) Proposition and application of an improved two-step elastic strain analysis based on the realistic growth process including an interruption, to the modeling of a three-dimensional self-assembled QD with the arbitrary variations of shape, size, and compositions in both dot and the surrounding matrix.
2) Modeling and simulation of the ultra-thin GaP interlayer/sublayer based on extending the two-step strain analysis to multi-step analysis, so that the physics of emitted wavelength blueshift in InAs/InGaAsP/InP QDs is straightforwardly revealed without additionally complicated theory, e.g. As/P exchange process.
3) Application of modeled interlayer/sublayer to the design of a vertically chirped multi-layer structure allowing the significant broadening of gain spectrum through the joint action of well-designed variation in the QD height and interlayer/sublayer thickness.
4) Modeling and simulation of the laterally and, in particular, vertically coupled QDs to carefully isolate and identify each coupling mechanism and its influence through the variation of inter-dot distance, dot size homogeneity and alignment, etc., based on the realistic growth process for the first time.

5) Application of modeled closely stacked QD active layers to an FP EEL allowing for the first time the spectrally two-state lasing under CW electrical pumping at RT, which is not possible in the counterpart with comparatively large spacer.
6) Characterization of the two-state laser through the simulation of spectral linewidth and RIN.

1.2.3 Thesis outline

This thesis starts with the introduction, as given in Chapter 1. The remaining major content consists of four chapters, which are arranged in order of the modeling process, i.e. "microscopic → macroscopic," and "theory → application," outlined as follows:

In Chapter 2, the fundamentals of microscopic modeling approaches are reviewed. This chapter starts with the important Bloch's theorem in semiconductor, and several approximations are applied to make the computational cost acceptable. The advantages of QDs are illustrated through the introduction of the density of states. As the focus of this thesis, the influences of elastic strain distribution, as well as the resulting piezoelectricity on the electronic band structure, are related to the SK growth mode. Detailed strain-dependent Hamiltonian based on the eight-band $\boldsymbol{k} \cdot \boldsymbol{p}$ method is presented. COMSOL Multiphysics and its operation are also introduced.

In Chapter 3, the fundamentals of macroscopic modeling approaches are reviewed. The important properties of the characterization of quantum confined devices such as the optical gain and the spontaneous emission spectrum are introduced.

Chapter 4 starts with the comparison of an improved two-step model and one-step model with a conventional strain analysis. Based on the new strain model, the aforementioned modeling approaches are sequentially applied first to a 3D self-assembled QD with variations of shape and size to investigate the influences on optical properties, then to a QD ensemble to include the lateral and vertical coupling effects.

In Chapter 5, three potential applications of our modeling method are proposed to ameliorate a QD-based FP EEL in terms of emission peak (for 1.55 μm application), gain spectral bandwidth

(for tunable SFLs and MLLs), and spectrally dual lasing possibility (for a variety of high-performance applications).

In Chapter 6, the thesis is concluded, and recommendations for future work are also given.

Chapter 2 Modeling of Semiconductor Nanostructures

2.1 Introduction

A semiconductor low-dimensional structure exhibits very interesting features tightly associated with its unique confinement of electrons. Before discussing the 3D confined QD structure, it is always a good idea to first understand the association between realistic geometry and resulting electronic properties. In Sec. 2.2, starting with common bulk crystal, we briefly summarize the Bloch's theorem i.e. a method can greatly simplify the task of obtaining the electron energy states and the wavefunctions in various confinements. On the basis of this important theorem, a commonly used method for the electronic band calculation i.e. eight-band $\boldsymbol{k \cdot p}$ model is introduced in Sec. 2.4. Before that, we have to introduce in Sec. 2.3 another important task of microscopic modeling, i.e. the analysis of strain distribution and piezoelectricity as well, which is closely related to crystal growth mode (e.g. SK mode). In the last two sections of this chapter, we briefly introduce the numerical method and commercial software i.e. COMSOL Finite Element Method (FEM) tool used in this work, then we move gradually towards the optoelectronic properties in a scale of device.

2.2 Quantum Confinement

2.2.1 Bloch's theorem in a bulk crystal

The complications and difficulties of applying Schrödinger equation to the modeling of quantum phenomena follow from the fact that any realistic solid, even with the nanoscale sizes, may have a considerable number of particles (e.g. ~10^{23} atoms/cm^3). Solving such a cumbersome equation could be an impossible mission as it requires huge computing resource. Fortunately, we can greatly simplify this apparently formidable task by additionally taking into account the spatial symmetry (periodicity) of crystals through Bloch's theorem: The common wavefunctions in a periodic

structure has the form

$$\psi(\boldsymbol{r}) = e^{i\boldsymbol{k}\cdot\boldsymbol{r}_i} u_k(\boldsymbol{r}), \tag{2.1}$$

where $u_k(\boldsymbol{r})$ is the oscillatory part of wavefunction repeated throughout the structure with the same periodicity of the atomic potential $V(\boldsymbol{r})$, as illustrated in Fig. 2.1. At any lattice site $\boldsymbol{r}_i$, the amplitude of $\psi(\boldsymbol{r})$ is determined by a slowly varying plane wave $e^{i\boldsymbol{k}\cdot\boldsymbol{r}_i}$, which is characterized by a Bloch wavevector of the state $\boldsymbol{k}$. Thus, based on the description that a single particle is modulated by a periodic potential field, it is unnecessary to consider each of the many unit cells throughout the bulk crystal; instead, the properties of electron states in bulk crystal can be calculated for one single unit cell, leading to reduce the computing resource significantly.

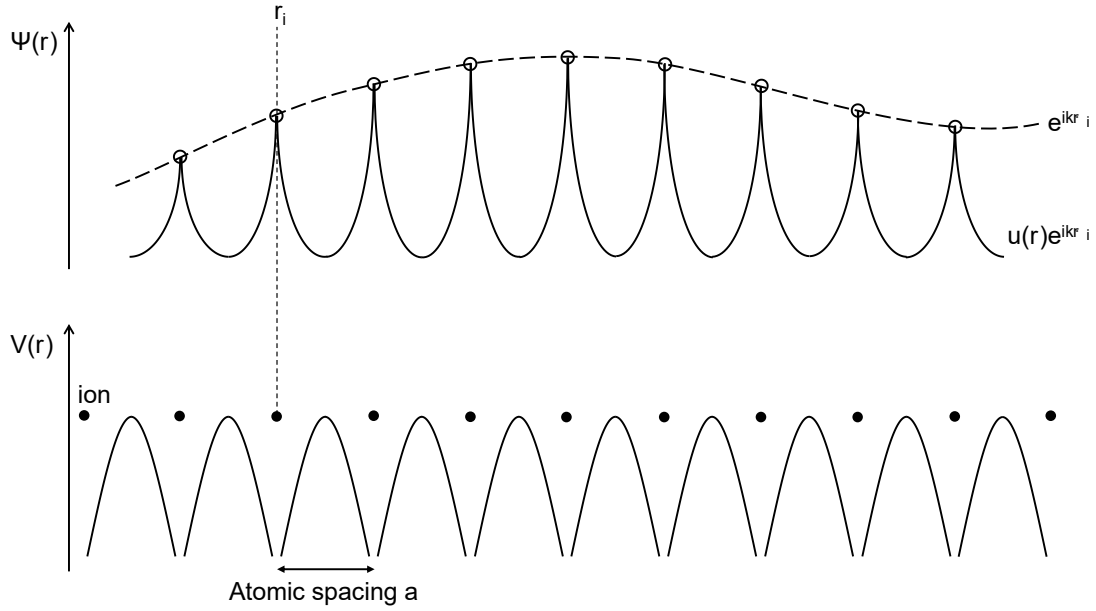

Fig. 2.1 Schematic illustration of Bloch's theorem for a wavefunction in a crystal.

It is not trivial to understand the Bloch's theorem since based on that, more approximations have been made to simplify the computation further, and different single-particle band structure models have been developed relying on the different treatments of potential $V(\boldsymbol{r})$:

Pseudopotential method: There is one called pseudopotential method assuming that valence electrons on the outer atomic orbitals are very loosely bound; thus, the interaction between valence electrons and ion cores is weak. In order to account for this weak interaction, a perturbation of the

constant potential for the electron in a free space (i.e. nearly-free electron approximation) is used, represented by a linear superposition of *all* the effects arising from the atomic potentials

$$V(\boldsymbol{r}) = \sum_{j,\alpha} v_j\left(\left|\boldsymbol{r} - \boldsymbol{R}_{j,\alpha}\right|\right), \tag{2.2}$$

where the index j runs over all atoms in the unit cell and v_i are the atomic potentials centered at the atomic sites $\boldsymbol{R}_j$ of atom type α. There are two ways to realize the pseudopotential method: empirical (EP) and self-consistent (SCP) method (i.e. *ab initio*). EP extremely relies upon the fitting parameters extracted from experimental data because there is no analytical tool to select the actual pseudopotential for a given material [116]. Thus, unpredictable inaccuracy in EP may arise from the measurements [4, 117]. On the other hand, SCP based on the parameter-free approach and a repetitive iteration process, which usually gives good accuracy, however, at the cost of commonly unaffordable computational complexity.

The $\boldsymbol{k}\cdot\boldsymbol{p}$ method: Also based on nearly-free electron approximation, another called $\boldsymbol{k}\cdot\boldsymbol{p}$ method does not modify the $V(\boldsymbol{r})$ as the pseudopotential method does; instead, the small perturbation of periodic potential (defined by given material) is equivalent to a modified electron mass m^* (i.e. effective mass approximation). In such a case, the Schrödinger equation with the Hamiltonian H_0 is

$$H_0\psi(\boldsymbol{r}) = \left(\frac{\boldsymbol{p}^2}{2m_0} + V(\boldsymbol{r})\right)\psi(\boldsymbol{r}) = \frac{\boldsymbol{p}^2}{2m^*}\psi(\boldsymbol{r}) = E\psi(\boldsymbol{r}), \tag{2.3}$$

where $\boldsymbol{p}$ ($\equiv -i\hbar\nabla$) is the momentum operator. By substitution of the Bloch wavefunction into equation and considering the small momentum perturbation $\hbar\boldsymbol{k}$, we can modify Eq. (2.3) to

$$\left(\frac{\boldsymbol{p}^2}{2m^*} + \frac{\hbar^2\boldsymbol{k}^2}{2m^*} + \frac{\hbar\boldsymbol{k}\cdot\boldsymbol{p}}{m^*}\right)u_{nk}(\boldsymbol{r}) = E_{nk}u_{nk}(\boldsymbol{r}), \tag{2.4}$$

or

$$Hu_{nk}(\boldsymbol{r}) = \left(H_0 + \frac{\hbar\boldsymbol{k}\cdot\boldsymbol{p}}{m^*}\right)u_{nk}(\boldsymbol{r}) = \left(E_{nk} - \frac{\hbar^2\boldsymbol{k}^2}{2m^*}\right)u_{nk}(\boldsymbol{r}). \tag{2.5}$$

For electrons near the band edge (i.e. $\boldsymbol{k} = 0$) or some other critical points in the Brillouin zone, the second term in the brackets with $\boldsymbol{k}\cdot\boldsymbol{p}$ operator can be considered as a perturbation to original H_0,

and the E–$\boldsymbol{k}$ relationship in the vicinity of these points of given material can be obtained. Apparently, compared to EP, empirical $\boldsymbol{k}\cdot\boldsymbol{p}$ method relies on a minimal set of fitting parameters (e.g. effective mass of an electron). The simplest $\boldsymbol{k}\cdot\boldsymbol{p}$ method relies single-band $\boldsymbol{k}\cdot\boldsymbol{p}$ method has first been developed assuming bands to be completely decoupled: The electron and heavy or light hole are treated with two independent Schrödinger equations, which is considered leading to significant error in prediction due to the exclusion of interactions between bands. The more advanced multi-band $\boldsymbol{k}\cdot\boldsymbol{p}$ method is free of this weakness due to the inclusion of several most relevant bands, as well as their mixing effects. More details about multi-band approach are given in Sec. 2.4.

Tight-binding method: Apart from the nearly-free electron approximation, Slater *et al.* have developed another so-called tight-binding (TB) method in 1954 based on the assumption that the electrons are tightly bound to atoms [118]. In this case, since the valence electronic states are perturbed by the presence of adjacent atoms and there is more than one atom per unit cell, the Bloch wavefunction is given by the directional "orbitals" resulting from the linear combinations of these atomic functions, presented in the form of

$$\Psi_k(\boldsymbol{r}) = \sum_{\boldsymbol{R}_i}\sum_{\alpha}\sum_{j} C_{\alpha,j}(\boldsymbol{k})\left|\alpha, j, \boldsymbol{r}-\boldsymbol{r}_j-\boldsymbol{R}_i\right\rangle e^{i\boldsymbol{k}\cdot\boldsymbol{R}_i}, \tag{2.6}$$

where the sum over $\boldsymbol{R}_i$ runs over all unit cells, α indicates the type of atomic functions (e.g. s, p_x, p_y, and p_z types of outermost valence electrons in III-V semiconductor) , and $\boldsymbol{r}_j$ is the spatial position of atom j in unit cell $\boldsymbol{R}_i$. The coefficient $C_{\alpha,j}$ or the Hamiltonian matrix elements between the atomic orbital states are treated as disposable constants, determined by fitting the measured bandgaps and/or effective mass in the bulk material [119].

2.2.2 Quantum confined structures

We now study the Bloch's theorem in the quantum confined structures. We start with a thin double-heterostructure made up of a narrow-gap material (i.e. active layer) sandwiched by a wide-gap

material (i.e. barrier layer). Considering the electrons in the simplest 1D square potential well, we find that the wavefunction is localized in, say z-direction to form a standing wave. Apart from the strain at the moment, this localization is brought about by the potential depth given by the conduction band offset ΔE_c. In this case, the effective mass theory and envelope function approach applies very well. Similar to Eq. (2.3), we have

$$\left(\frac{\boldsymbol{p}^2}{2m_0} + V(\boldsymbol{r}) + V'(\boldsymbol{r})\right)\psi(\boldsymbol{r}) = \left(\frac{\boldsymbol{p}^2}{2m^*} + V'(\boldsymbol{r})\right)\psi(\boldsymbol{r}) = E\psi(\boldsymbol{r}), \tag{2.7}$$

where $V'(\boldsymbol{r})$ is the approximated rectangular potential well, and $V(\boldsymbol{r})$ is the periodic atomic potential. The standing wave is formed by a linear combination of plane waves

$$\psi(\boldsymbol{r}) = \sum_{\boldsymbol{k}_j} A(k_j)e^{i\boldsymbol{k}_j\cdot\boldsymbol{r}_i}u(\boldsymbol{r}) = F(\boldsymbol{r}_i)u(\boldsymbol{r}), \tag{2.8}$$

where $F(\boldsymbol{r}_i)$ is an envelope function that describes the localization of the states as a Fourier sum of plane waves, as illustrated in Fig. 2.2. Here $u(\boldsymbol{r})$ resulting from the atomic potential is assumed not $\boldsymbol{k}$-dependent, which is the case for s- and p-like functions at the band edge.

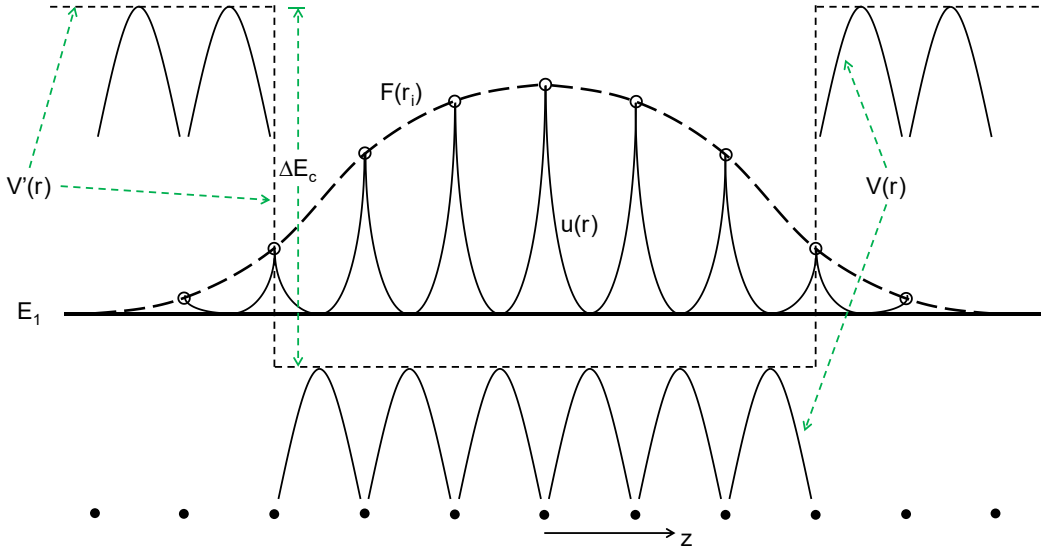

Fig. 2.2 Schematic illustration of the wavefunction consisting of an atomic part $u(r)$ and a standing wave envelope function $F(r_i)$, localized in an approximated rectangular potential well (dashed line) formed by a thin double heterostructure.

2.2.3 Why QDs?

From Eq. (2.5), the energy E (i.e. eigenvalue) of single-particle in a 3D bulk crystal is related to the wavevector $\boldsymbol{k}$ through the effective mass m^*

$$E = E_c + \frac{\hbar^2 \boldsymbol{k}^2}{2m^*} = E_c + \frac{\hbar^2}{2m^*}\left(k_x^2 + k_y^2 + k_z^2\right), \tag{2.9}$$

where E_c is the conduction band edge, and the total number of allowed $\boldsymbol{k}$ is huge, equaling to the atom number in bulk, which is determined by Born−von Kármán boundary conditions (BCs). In this case, the E–$\boldsymbol{k}$ relationship is a continuous spherical-parabolic function in the vicinity of Γ-point, and the states are regarded as a continuum. Therefore, the 3D DOS $N_3(E)$ can be derived by the expression of $\boldsymbol{k}$, reading

$$N_3(E) = \frac{1}{2\pi^2}\left(\frac{2m^*}{\hbar^2}\right)^{3/2}\sqrt{E - E_c}. \tag{2.10}$$

However, the BCs are changed when the dimensions are limited in one or more directions, leading to the changes of E and $\boldsymbol{k}$. For instance, in a 2D quantum well (i.e. the system becomes confined along the z-axis), the discreet energy levels are determined by the width of well, given by

$$E_n = E_c + \frac{\hbar^2}{2m^*}\left(k_x^2 + k_y^2\right) = E_c + \frac{\hbar^2 n^2 \pi^2}{2m^* L_z^2}, \tag{2.11}$$

where n is an integer, L_z is the width of well. The wavevector $k_n = n\pi/L_z$ irrelevant to the term $(E - E_c)^{1/2}$. Thus the 2D DOS $N_2(E)$ is

$$N_2(E) = \frac{m^*}{\pi\hbar^2 L_z}\theta(E - E_n), \tag{2.12}$$

where $\theta(E)$ is the Heaviside step function.

Similarly, when the dimensionality of the system is further reduced along the y-axis (i.e. a nanowire), we have

$$E_{n_y,n_z} = E_c + \frac{\hbar^2}{2m^*}(k_x^2) = E_c + \frac{\hbar^2\pi^2}{2m^*}\left(\frac{n_y}{L_y} + \frac{n_z}{L_z}\right)^2, \tag{2.13}$$

and the 1D DOS $N_1(E)$ is

$$N_1(E) = \frac{1}{2\pi L_y L_z}\sqrt{\frac{2m^*}{\hbar^2}}\sum_{n_y,n_z}\frac{1}{\sqrt{E - E_{n_y} - E_{n_z}}}. \tag{2.14}$$

For the 0D system (i.e. a QD), we have

$$E_{n_x,n_y,n_z} = E_c + \frac{\hbar^2\pi^2}{2m^*}\left(\frac{n_x}{L_x} + \frac{n_y}{L_y} + \frac{n_z}{L_z}\right)^2, \tag{2.15}$$

and the 0D DOS $N_0(E)$ is

$$N_0(E) = \frac{1}{L_x L_y L_z}\sum_{n_x,n_y,n_z}\delta\left(E - E_{n_x} - E_{n_y} - E_{n_z}\right). \tag{2.16}$$

The different quantum confined structures and their DOS are summarized in Fig. 2.3.

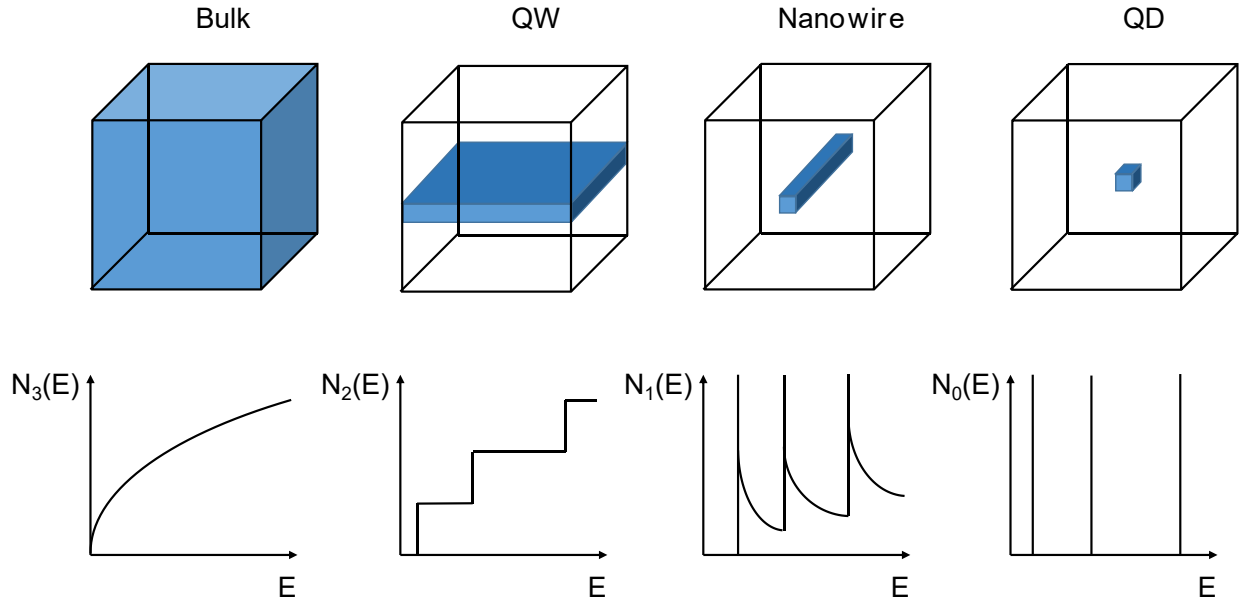

Fig. 2.3 Schematic illustration of the density of states as a function of energy for bulk (3D), QW (2D), nanowire (1D), and QD (0D) structures.

With knowledge of the DOS, the carrier density in any given structure can be calculated for a known Fermi level position E_F, i.e. the number of electrons at any energy E is given by the product of the number of states $N(E)$ and their occupation probability $\rho(E)$, reading

$$n(E) = N(E)\rho(E), \tag{2.17}$$

where $\rho(E)$ in thermal equilibrium at temperature T is given by

$$\rho(E) = \frac{1}{1 + \exp\left(\frac{E - E_F}{k_B T}\right)}, \tag{2.18}$$

where k_B is Boltzmann constant.

Apparently, it is easy to understand from Fig. 2.3 and Eq. (2.17) that the distribution of electrons localized in a QD should follow the state distribution, i.e. a series of delta functions. This (ideally) narrow distribution of electron at these discrete states should lead to aforementioned advantages (Sec. 1.1) in two aspects: on the one hand, the confined state levels are engineerable by tuning the size of QD and the depth of potential (i.e. band offset), and these states are identifiable by envelope function approximation (i.e. s-like orbital for GS, p-like orbital for ES, etc.); on the other hand, characteristics developments such as drastic increase in gain and differential gain, decrease in threshold current density and insensitivity of temperature can be obtained due to the delta-function-like DOS.

2.3 Strain in QDs

2.3.1 QD fabrications

It should be clear up that the theories we have discussed in Sec. 2.2 are important but preliminary for modeling nanostructures. Next, we discuss the elastic strain effects that can significantly affect the energy band structure as well as the QD size dispersion in the real world, thereby introducing the final numerical framework for microscopic modeling.

Since the conditions of strain in the QDs and the surrounding matrix are closely related to the techniques used in QD fabrications, in what follows, we briefly introduce them in this subsection.

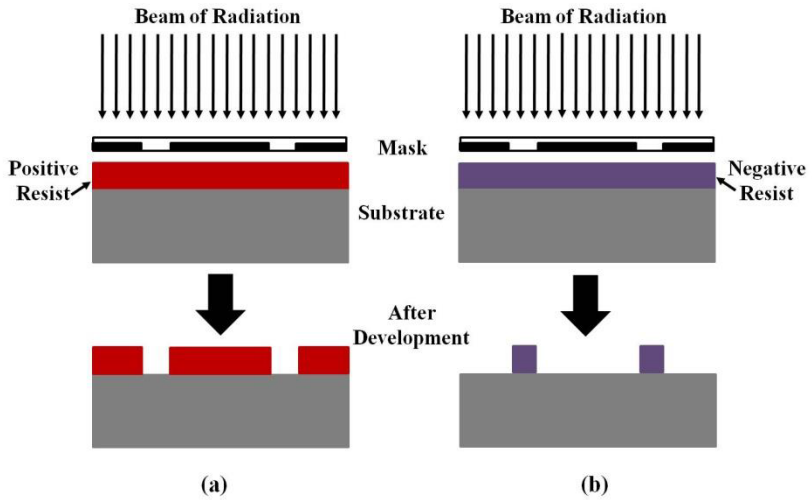

Fig. 2.4 Schematic illustrations of (a) positive and (b) negative resist exposure.

Lithographic techniques: Early attempts to produce QDs with a satisfactory quality of emission were straightforward top-down approaches, based on a combination of lithography techniques and chemical etching of QWs (e.g. see Ref. [120]). They include photolithography, E-beam lithography, X-ray lithography and ion beam lithography. Exposure defines the minimal achievable size. Positive or negative resist exposure can be selected depending on the type of nanostructures, as illustrated in Fig. 2.4.

However, the main problem with these techniques was the introduction of surface states due to the defects formed on the interface, which lead to an increase in threshold current density. In addition, low areal density and poor control over uniformity of QD size were the other two nonnegligible limitations of lithography for QD fabrications.

Epitaxial self-assembly: More promising bottom-up approaches were then proposed, i.e. directly producing QDs during the epitaxial growth process (typically grown by MBE or MOVPE) by using the self-organization phenomena on the crystal surface (e.g. see Refs. [121-123]). Tremendous self-assembled techniques have been proposed, which significantly improves the QD fabrications, mainly because they allowed manufacturing of QD layers with higher areal density and defect-free characteristics. Thus we focus on the self-assembled QDs in this thesis.

There are three main epitaxial growth modes, viz. Frank-van der Merwe (FvdM) based on

lattice-matched epitaxy, Volmer-Weber (VW) growth modes and Stranski-Krastanov (SK) growth mode based on lattice-mismatched epitaxy, as shown in Fig. 2.5, determined by the balance of the surface energies of the deposited layer (i.e. γ_A), the substrate (i.e. γ_B), and the interface energy (i.e. γ^*) formed between the two. In lattice-matched systems, if $\gamma_A + \gamma^* < \gamma_B$, the balance of energies favors increasing the area of deposited layer over leaving an exposed substrate surface and the growth proceeds in a layer-by-layer fashion (i.e. FvdM); otherwise if $\gamma_A + \gamma^* > \gamma_B$ (e.g. with very large lattice-mismatch), the interface and surface area of epitaxial layer are minimized and the growth proceeds in an island-style (i.e. VW), one example of which is the droplet epitaxy (DE) that we have discussed in Sec. 1.1.2. The balance in strained lattice-mismatched system can be tuned by adjusting the epitaxial thickness thereby the interface energy γ^*; more specifically, γ^* is small for the thin deposit and the initial growth is layer-by-layer, while the interface energy γ^* is gradually accumulated with the thicker deposit arising from the lattice mismatch. Therefore the growth converts to island-style. Subsequently, the overall growth is a layer-plus-island fashion. The previously formed layer is called wetting layer (WL), acting as a QW and connecting all QDs in one layer. On the other hand, the thickness of deposit at which conversion of growth mode starts to occur is called critical layer thickness (CLT) [4]. Notably, this layer-plus-island structure by using SK mode indeed results in a deviation from the predicted DOS in Eq. (2.16), yielding a linear combination of QW and QD in one layer. Thus, a more realistic representation of the DOS of SK QD system consisting of a WL and multiple dots is shown in Fig. 2.6, including the inhomogeneous broadening arising from the QD size dispersion. More detailed discussions are given in Sec. 2.6.3.

Colloidal self-assembly: Different from the above mentioned two groups of QDs which are grown on and are fixed onto a substrate, self-assembled colloidal QDs are typically synthesized via a wet chemical process, such as microemulsion (e.g. see Ref. [123]), hot solution decomposition (e.g. Ref. [124]), and the sol-gel (e.g. Ref. [122]) process. Although colloidal QDs are with simply and economically solution-based approaches, compared with the other two groups of QDs, which are fully encapsulated within a matrix, the former suffers from surface effects due to their exposure to

open air [125]. Therefore, sufficient control of electronic properties has not been achieved untill now, limiting their applications. A typical application of colloidal QDs is the QD LEDs, as shown in Fig. 2.7. Other applications include light downconversion, solar cells, and bioimaging. Since colloidal QDs are beyond the scope of this thesis, the self-assembled QDs (or more simply, QDs) hereinafter refer to the epitaxial ones.

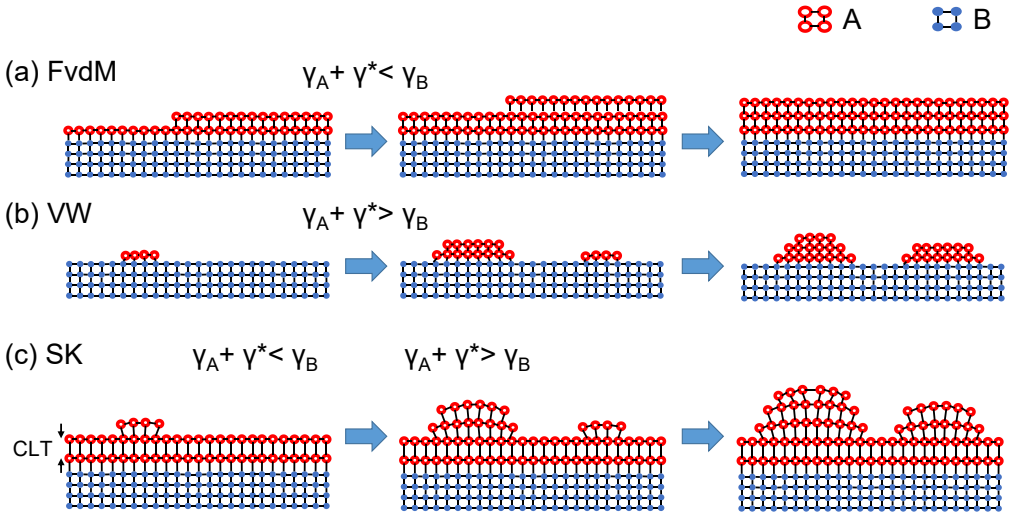

Fig. 2.5 Schematic illustrations of (a) Frank-van der Merwe (FvdM), (b) Volmer-Weber (VW), and (c) Stranski-Krastanov (SK) growth modes, determined by the balance of the surface energies of the deposited layer (i.e. γ_A), the substrate (i.e. γ_B), and the interface energy (i.e. γ^*) formed between the two layers.

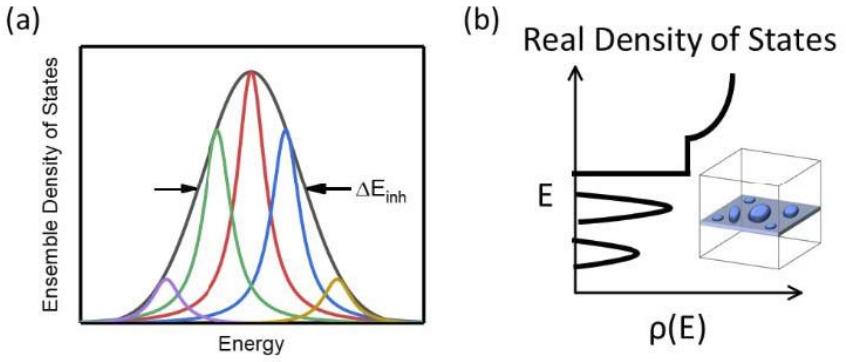

Fig. 2.6 Schematic illustration of (a) inhomogeneous broadening for an ensemble of QDs, and (b) more realistic DOS of an SK QD system consisting of multiple dots, including inhomogeneous broadening and WL, modified from [126].

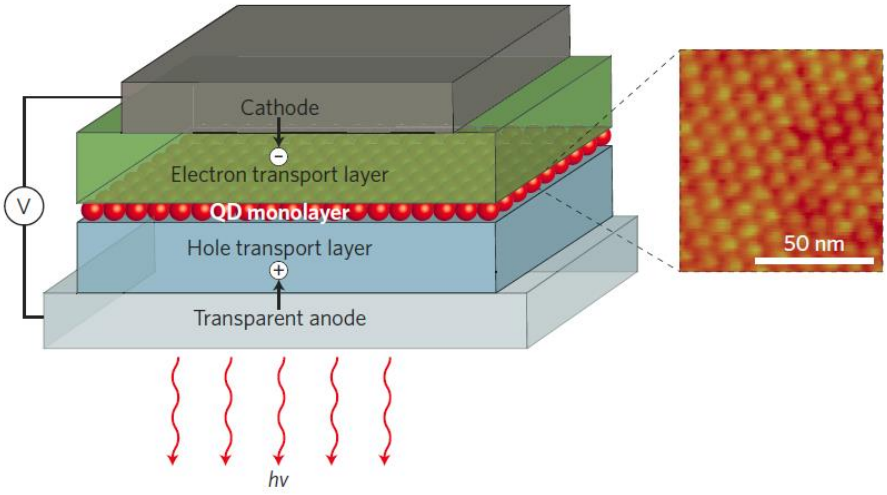

Fig. 2.7 Schematic illustration of a typical type-II QD-LED structure [127].

2.3.2 Strain effects

The wide use of SK growth mode in the production of self-assembled QDs allows excellent characteristics such as defect-free and high areal density. The defect-free requires the in-plane lattice-mismatch between deposit and substrate being below certain value so that the elasticity is not lost, while the high density, on the other hand, requires the in-plane lattice-mismatch being relatively high. Therefore, numerical analysis of elastic strain along with the corresponding effects is in demand for nanostructure design: When two semiconductor materials with different lattice constant grow on top of each other, the thin deposited layer tends to adjust its in-plane lattice constant in the vicinity of interface to maintain the system continuous (micro change of lattice also occurs on the substrate side). This adjustment of lattice constant results in crystal deformation, i.e. displacement or strain in epitaxial layer, and this displacement or strain significantly affect the quantum confinement through modifying the band edges.

To calculate the strain-induced displacement in a 3D QD system, there are two commonly used methods [128]: Valence force field (VFF) and continuum mechanical (CM) elasticity method. Another so-called isotropy-elasticity (IE) method based on the approximation of homogeneous elasticity oversimplify the problem and underestimates both electron and hole energies [129], thus,

being opted out of our discussion.

VFF: As an atomistic approach, VFF is in line with the pseudopotential and tight-binding methods (see Sec. 2.2.1). It describes the elastic energy of the atomic bond through investigating the changes of the nearest-neighbor bonds (e.g. six bonds in III-V zincblende structure) in terms of length and spatial orientation. This microscopic method allows a very precise description of lattice deformation in a short-range when the location of each atom in the system is given [130].

CM: In contrast to VFF, there is nothing microscopic involved in the CM method. Based on the harmonic approximation, CM artificially discretizes a continuous domain into a mesh of elements and nodes [78, 81, 84, 114, 131]. The behavior of these elements is predicted by calculating the total elastic energy. In other words, the total elastic energy derived from the energy conservation is minimized in order to obtain the distribution of the displacement in the structure, given by

$$U_{\text{strain}} = \frac{1}{2}\sum \boldsymbol{\sigma}\boldsymbol{\epsilon}, \tag{2.19}$$

where $\boldsymbol{\sigma}$ and $\boldsymbol{\epsilon}$ are the stress and strain tensors, respectively. The strain tensors are related to the displacement of nodes $\boldsymbol{u}$, $\boldsymbol{v}$, and $\boldsymbol{w}$ between the elements in the Cartesian coordinates system, given by

$$\boldsymbol{\epsilon} = \begin{pmatrix} \epsilon_{xx} \\ \epsilon_{yy} \\ \epsilon_{zz} \\ \epsilon_{xy} \\ \epsilon_{yz} \\ \epsilon_{xz} \end{pmatrix} = \begin{bmatrix} \partial \boldsymbol{u}/\partial x \\ \partial \boldsymbol{v}/\partial y \\ \partial \boldsymbol{w}/\partial z \\ (\partial \boldsymbol{u}/\partial y + \partial \boldsymbol{v}/\partial x)/2 \\ (\partial \boldsymbol{v}/\partial z + \partial \boldsymbol{w}/\partial y)/2 \\ (\partial \boldsymbol{w}/\partial x + \partial \boldsymbol{u}/\partial z)/2 \end{bmatrix}. \tag{2.20}$$

The stress tensors can be derived from the stress-strain relation, which is in line with the Hooke's law, given by

$$\boldsymbol{\sigma} = \boldsymbol{C}(\boldsymbol{\epsilon} - \boldsymbol{\epsilon_0}) + \boldsymbol{\sigma_0} \tag{2.21}$$

and

$$\epsilon_0 = \frac{a_d - a_s}{a_d}, \boldsymbol{\epsilon_0} = (\epsilon_0 \quad \epsilon_0 \quad \epsilon_0 \quad 0 \quad 0 \quad 0)^{\mathrm{T}} \tag{2.22}$$

where ϵ_0 denotes the initial strain arising from the lattice-mismatch, determined by a_d and a_s which are the intrinsic lattice constants of the deposit and substrate, respectively. $\boldsymbol{C}$ is the elasticity matrix or stiffness matrix. For an anisotropic cubic crystal,

$$\boldsymbol{C} = \begin{pmatrix} C_{11} & C_{12} & C_{12} & 0 & 0 & 0 \\ C_{12} & C_{11} & C_{12} & 0 & 0 & 0 \\ C_{12} & C_{12} & C_{11} & 0 & 0 & 0 \\ 0 & 0 & 0 & C_{44} & 0 & 0 \\ 0 & 0 & 0 & 0 & C_{44} & 0 \\ 0 & 0 & 0 & 0 & 0 & C_{44} \end{pmatrix}, \tag{2.23}$$

where C_{11}, C_{12}, and C_{44} are elasticity moduli. Thus, the strain energy U_{strain} can be given in the form only related to strain tensors and elasticity moduli. Then, following Eq. (2.19), the strain-induced displacement field can be obtained by minimizing the total strain energy throughout the system.

Due to the ability of precise description of atomic displacement in the system, the VFF approach can give a satisfactory result in terms of validity; however, it is not suitable for the large structure due to its computationally intensive [75, 76, 80]. In particular, our accurate strain analysis process consists of several steps, making VFF even more difficult to carry out. In such case, CM is a good compromise between validity and efficiency. In addition, it is more in line with the $\boldsymbol{k \cdot p}$ method, as the latter is neither an atomic approach.

Next, the modification effects on the confinement due to the strain in and around QD is briefly introduced. Starting with the Bir−Pikus theory [132], the direct effect of strain is the change of volume, given by

$$\frac{\Delta V}{V} = \epsilon_{xx} + \epsilon_{yy} + \epsilon_{zz} = \epsilon_h, \tag{2.24}$$

where ϵ_h is also known as the hydrostatic strain, which is linearly related to the change in energy for both conduction band edge (CBE) and valence band edges (VBEs) at Γ-point, where interests us the most:

$$\Delta E_{\text{c}} = a_{\text{c}} \epsilon_h \tag{2.25}$$

and $$\Delta E_{\mathrm{v}} = -a_{\mathrm{v}}\epsilon_h, \tag{2.26}$$

where a_{c} and a_{v} are the empirical deformation potential constants for CBE and VBEs, respectively. Eqs. (2.25) and (2.26) reflect the fact that the bandgap ($\Delta E_g = \Delta E_{\mathrm{c}} + \Delta E_{\mathrm{v}}$) increases for a compressive hydrostatic strain ($\epsilon_h < 0$) due to the nature of the atomic bonding in III-V material. More specifically, the CBE shifts upwards in energy while the VBEs shift downwards, with most of the change being in the CBE [133].

On the other hand, Eq. (2.26) is insufficient to describe the total effect of strain on VBEs. Two additional potential constants, i.e. b and d are necessary to describe the splitting of degenerate VBEs arising from the increase of biaxial strain ϵ_b and shear strain tensors: In the absence of strain and spin interaction, the three uppermost VBEs are degenerate; while in the presence of spin-orbit interaction, the six-fold degenerate bands of Γ_{15} symmetry split into four-fold degenerate bands of Γ_8 symmetry and doubly degenerate split-off (SO) band of Γ_7 symmetry. The increase of ϵ_b further results in a deviation from the four-fold degeneracy, which splits into doubly heavy-hole (HH) plus doubly light-hole (LH) valence bands. The splitting is linearly related to ϵ_b, given by

$$\Delta E_{HH-LH} = 2|b\epsilon_b|, \tag{2.27}$$

where

$$\epsilon_b = \epsilon_{zz} - \frac{\epsilon_{xx} + \epsilon_{yy}}{2}. \tag{2.28}$$

For the growth of pseudomorphic layer along the (100) direction, shear strain terms are less important. Thus, the strain-induced modifications in the conduction band and valence bands can be predicted, as shown in Fig. 2.8(b) and (c). Consequently, since CB-HH and CB-LH transitions produce different polarizations in gain spectra, TE polarized gain spectrum is observed favored in compressively strained QDs due to the larger HH hole population, by contrast, TM polarization dominates in tensilely strained QDs arising from more LH hole being populated [134]. Note the above-mentioned relationship between the modifications in energy and strain tensors is simplified for a clear illustration. The full strain Hamiltonian will be discussed in Sec. 2.4.3.

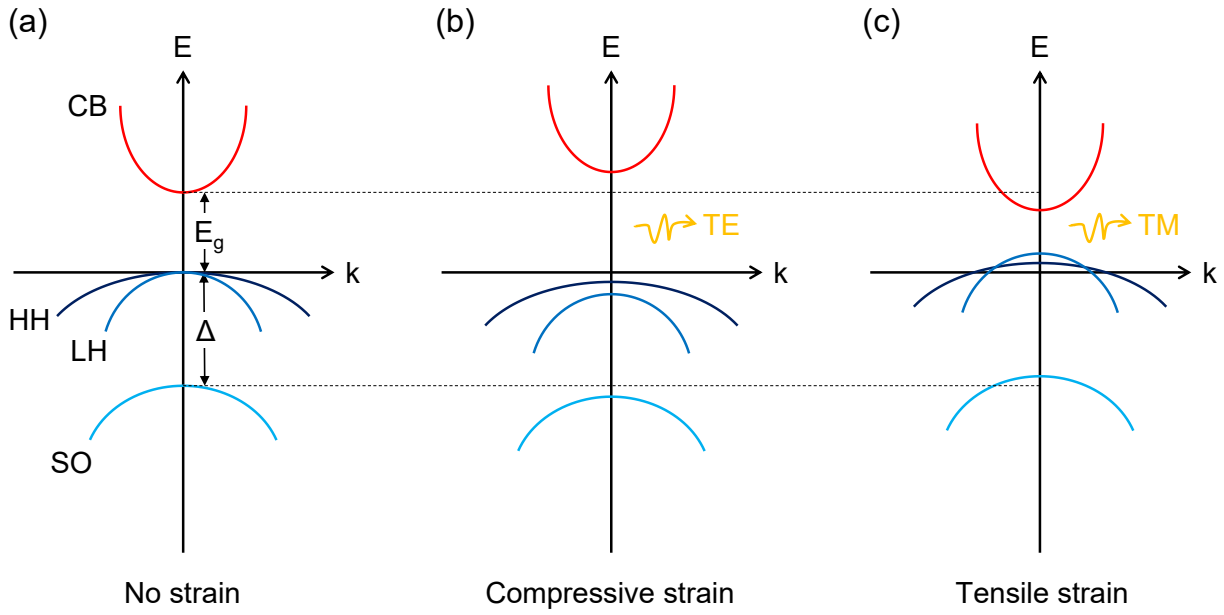

Fig. 2.8 Schematic illustration of different types of strain effect on a typical III-V semiconductor band in the vicinity of Γ-point, corresponding to different polarized gain spectra.

2.3.3 Piezoelectricity

Piezoelectric (PZT) effect is a strain-induced net charge distribution or electric polarization, due to the missing of symmetry in severely strained nanostructure like QD. At first, only a linear PZT component was included when modelling quantum wells [135] and QDs [77, 78, 136]. Later, Bester *et al.* have pointed out that the second-order term is supposed to be included since, in terms of the magnitude, the linear and quadratic components are comparable [137], then more and more researchers have included the quadratic components [131, 138]. The magnitude of the PZT effects is generally on the order of a few meV [137], which may not have significant effect on the energy; however, the quadrupole-like potential reduces the symmetry of a structural C_{4v} or $C_{\infty v}$ quantum dot to C_{2v}, leading to a degradation in symmetry of quantum confinement profile, which is regarded as one source of splitting effect into energy states for particles with different spin orientations [139]. Thus, it is necessary to include the PZT in the modeling. The equations used in this study are listed in the following.

The linear polarization component $\boldsymbol{P_1}$ arising from the calculated strain field can be represented as

$$\boldsymbol{P_1} = \begin{pmatrix} P_x \\ P_y \\ P_z \end{pmatrix} = \begin{pmatrix} 2e_{14} & 0 & 0 \\ 0 & 2e_{14} & 0 \\ 0 & 0 & 2e_{14} \end{pmatrix} \begin{pmatrix} \epsilon_{yz} \\ \epsilon_{xz} \\ \epsilon_{xy} \end{pmatrix}, \tag{2.29}$$

and the quadratic polarization component $\boldsymbol{P_2}$ is given by

$$\boldsymbol{P_2} = 2B_{114} \begin{pmatrix} \epsilon_{xx}\epsilon_{yz} \\ \epsilon_{yy}\epsilon_{xz} \\ \epsilon_{zz}\epsilon_{xy} \end{pmatrix} + 2B_{124} \begin{bmatrix} \epsilon_{yz}(\epsilon_{yy} + \epsilon_{zz}) \\ \epsilon_{xz}(\epsilon_{xx} + \epsilon_{zz}) \\ \epsilon_{xy}(\epsilon_{xx} + \epsilon_{yy}) \end{bmatrix} + 4B_{156} \begin{pmatrix} \epsilon_{xz}\epsilon_{xy} \\ \epsilon_{yz}\epsilon_{xy} \\ \epsilon_{yz}\epsilon_{xz} \end{pmatrix}, \tag{2.30}$$

where e_{14}, B_{114}, B_{124}, and B_{156} are the linear and quadratic PZT coefficients, respectively. The PZT charge density introduced by the total polarization can be derived as

$$\rho_p(\boldsymbol{r}) = -\nabla \cdot (\boldsymbol{P_1} + \boldsymbol{P_2}). \tag{2.31}$$

Then the PZT potential $V_p(\boldsymbol{r})$ is obtained by solving Poisson's equation:

$$\rho_p(\boldsymbol{r}) = \varepsilon_0 \nabla \cdot \Big(\varepsilon_s(\boldsymbol{r}) \nabla V_p(\boldsymbol{r})\Big), \tag{2.32}$$

where ε_0 and $\varepsilon_s(\boldsymbol{r})$ are vacuum permittivity and relative static dielectric tensor, respectively.

2.4 Strain-Dependent Electronic Band Structure

2.4.1 Multi-band effective mass model

In order to extend the aforementioned single-band $\boldsymbol{k} \cdot \boldsymbol{p}$ model in Sec. 2.2.1 to include the coupling between the bands, the first step is to choose the basis set based on the nature of bands near the band edges. When considering the type of involved band, we can extend the concept of bonding and antibonding orbitals introduced for molecules to the crystal: The isolated atom has *s* orbital where the electron has lower energy, and *p* orbital where the electron has higher energy; if atoms are brought together and the distance between them is getting smaller, orbitals of each atom overlap with those of its nearest neighbors, resulting in the bonding and antibonding orbitals being broadened into bands, and the energy relationship between *s*- and *p*-orbitals also being changed by the band intermixing. Since the atomic orbitals are not destroyable nor generable, the total number

of bonding and antibonding orbitals is always equal to the number of involved atoms.

A similar case can be approximated for most solids where there are roughly 10^{28} atoms/m^3: the bonding orbitals occupied by electrons form the valence bands (VBs), and the antibonding orbitals which are empty form the conduction bands (CBs), as illustrated in Fig. 2.9. The electrons in each band retain its *s*- or *p*-type character. If only the s^2 and p^6 electrons in the outer-most atomic shells are included, eight atomic orbitals, i.e. two orbitals of *s*-symmetry (CB) and six orbitals of *p*-symmetry (VB) for the two atoms in the unit cell, are introduced into the Hamiltonian, forming the initial eight-band $\boldsymbol{k}\cdot\boldsymbol{p}$ model.

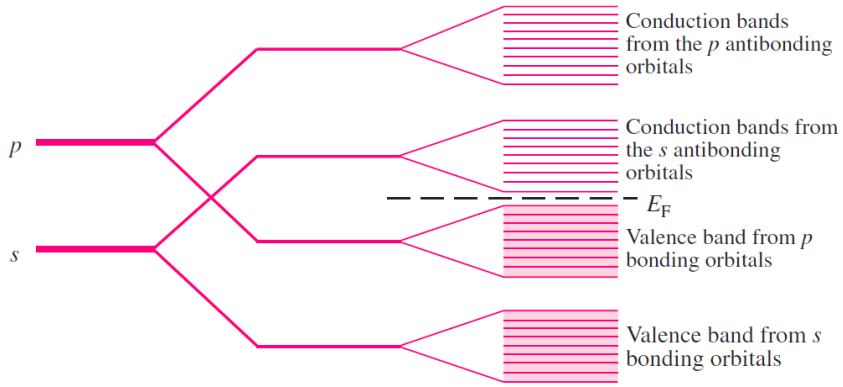

Fig. 2.9 Evolution of the atomic *s*- and *p*-orbitals into VBs and CBs in a semiconductor. E_F is the Fermi energy [4].

2.4.2 Unstrained eight-band $\boldsymbol{k}\cdot\boldsymbol{p}$ Hamiltonian

Let us first consider the zinc-blende bulk scenario without any spin-orbit or strain effects. In the absence of electron spin and spin-orbit interaction, the aforementioned eight bands can be regrouped into a two-fold degenerate $|S\rangle$ for the CB and three two-fold degenerate $|X\rangle$, $|Y\rangle$, $|Z\rangle$ for the VBs. Thus the Hamiltonian in such basis set can be written as a 4×4 matrix, given by

$$H_k = \begin{pmatrix} E_c + A_c\boldsymbol{k}^2 & Bk_yk_z + iP_0k_x & Bk_xk_z + iP_0k_y & Bk_xk_y + iP_0k_z \\ Bk_yk_z - iP_0k_x & E_v^{av} + L'k_x^2 + M(k_y^2 + k_z^2) & N'k_xk_y & N'k_xk_z \\ Bk_xk_z - iP_0k_y & N'k_xk_y & E_v^{av} + L'k_y^2 + M(k_x^2 + k_z^2) & N'k_yk_z \\ Bk_xk_y - iP_0k_z & N'k_xk_z & N'k_yk_z & E_v^{av} + L'k_z^2 + M(k_x^2 + k_y^2) \end{pmatrix} \tag{2.33}$$

where E_c is the unstrained CBE and E_v^{av} is the unstrained average VBE, P_0 is the Kane matrix element defined as

$$P_0 = -\frac{i\hbar}{m_0}\langle S|p_x|X\rangle. \tag{2.34}$$

The above mentioned three parameters come from the direct interaction between *s* and *p* wavefunctions; on the other hand, *L'*, *M*, and *N'* are defined as

$$\begin{aligned} L' &= -\frac{\hbar^2}{2m_0}(1 + \gamma_1 + 4\gamma_2), \\ M &= -\frac{\hbar^2}{2m_0}(1 + \gamma_1 - 2\gamma_2), \\ N' &= -\frac{\hbar^2}{2m_0}(6\gamma_3), \end{aligned} \tag{2.35}$$

where γ_i (i = 1, 2, 3) are modified Luttinger parameters, calculated by the ordinary Luttinger parameters γ_i^L, defined as [140]

$$\gamma_1 = \gamma_1^L - \frac{E_p}{3E_g + \Delta}, \gamma_2 = \gamma_2^L - \frac{1}{2}\frac{E_p}{3E_g + \Delta}, \gamma_3 = \gamma_3^L - \frac{1}{2}\frac{E_p}{3E_g + \Delta}, \tag{2.36}$$

where E_p is band parameter, usually determined experimentally in practice, related to P_0 by

$$E_p = \frac{2m_0P_0^2}{\hbar^2}. \tag{2.37}$$

A_c is obtained from the renormalization of single-band effective mass and can be simply approximated to $A_c = \hbar^2/2m^*$ to keep $A_c > 0$ (otherwise the electron acts as a hole) [141], and B arises from the inversion asymmetry which is usually negligible (B = 0) [142]. The above mentioned parameters A_c, B, *L'*, *M*, and *N'* come from the second-order interactions due to the perturbation of remote bands [143].

Based on the previous discussion, an additional term H_{so} representing the spin-orbit interaction is introduced into Eq. (2.5), giving Kane's model [144]

$$\left[H_0 + \frac{\hbar \boldsymbol{k}\cdot\boldsymbol{p}}{m^*} + \frac{\hbar}{4m_0^2c^2}(\nabla V \times \boldsymbol{p})\cdot\boldsymbol{\sigma}\right]u_{nk}(\boldsymbol{r}) = \left(E_{nk} - \frac{\hbar^2\boldsymbol{k}^2}{2m^*}\right)u_{nk}(\boldsymbol{r}), \tag{2.38}$$

where $\boldsymbol{\sigma}$ are the Pauli spin matrices

$$\sigma_x = \begin{pmatrix} 1 & 0 \\ 0 & 1 \end{pmatrix}, \sigma_y = \begin{pmatrix} 0 & -i \\ i & 0 \end{pmatrix}, \sigma_z = \begin{pmatrix} 1 & 0 \\ 0 & -1 \end{pmatrix}, \tag{2.39}$$

operating on the spins up and down

$$\uparrow = \begin{pmatrix} 1 \\ 0 \end{pmatrix}, \downarrow = \begin{pmatrix} 0 \\ 1 \end{pmatrix}. \tag{2.40}$$

With the introduction of spin-orbit interaction, the additional degree of freedom due to the spin should be included. Thus, the new basis set is extended in the order of $|S\downarrow\rangle$, $|S\uparrow\rangle$, $|Y\downarrow\rangle$, $|X\downarrow\rangle$, $|X\uparrow\rangle$, $|Y\uparrow\rangle$, $|Z\downarrow\rangle$, and $|Z\uparrow\rangle$, compatible with the CB, HH, LH, and SO bands with spins up and down, respectively. For the schematic of band structure in the vicinity of Γ-point one can refer to Fig. 2.8(a). As shown in the figure, the spin-orbit interaction splits the six-fold degenerate bands of Γ_{15} symmetry split into four-fold degenerate bands of Γ_8 symmetry with total angular momentum $J = 3/2$ and doubly degenerate split-off (SO) band of Γ_7 symmetry with $J = 1/2$.

Thus, the 4×4 Hamiltonian in Eq. (2.33) is expanded into an 8×8 matrix which is the final form of unstrained eight-band $\boldsymbol{k}\cdot\boldsymbol{p}$ Hamiltonian H_k, given by [82]

$$H_k = \begin{pmatrix} A & 0 & V^\dagger & 0 & \sqrt{3}V & -\sqrt{2}U & -U & \sqrt{2}V^\dagger \\ 0 & A & -\sqrt{2}U & -\sqrt{3}V^\dagger & 0 & -V & \sqrt{2}V & U \\ V & -\sqrt{2}U & -P+Q & -S^\dagger & R & 0 & \sqrt{3/2}\,S & -\sqrt{2}Q \\ 0 & -\sqrt{3}V & -S & -P-Q & 0 & R & -\sqrt{2}R & \sqrt{1/2}\,S \\ \sqrt{3}V^\dagger & 0 & R^\dagger & 0 & -P-Q & S^\dagger & \sqrt{1/2}\,S^\dagger & \sqrt{2}R^\dagger \\ -\sqrt{2}U & -V^\dagger & 0 & R^\dagger & S & -P+Q & \sqrt{2}Q & \sqrt{3/2}\,S^\dagger \\ -U & \sqrt{2}V^\dagger & \sqrt{3/2}\,S^\dagger & -\sqrt{2}R^\dagger & \sqrt{1/2}\,S & \sqrt{2}Q & -P-\Delta & 0 \\ \sqrt{2}V & U & -\sqrt{2}Q & \sqrt{1/2}\,S^\dagger & \sqrt{2}R & \sqrt{3/2}\,S & 0 & -P-\Delta \end{pmatrix} \tag{2.41}$$

$$
\begin{aligned}
A &= E_{\mathrm{c}} - \frac{\hbar^2}{2m^*}\left(\partial_x^2 + \partial_y^2 + \partial_z^2\right), \\
P &= -E_{\mathrm{v}}^{\mathrm{av}} - \frac{\hbar^2}{2m_0}\gamma_1\left(\partial_x^2 + \partial_y^2 + \partial_z^2\right), \\
Q &= -\frac{\hbar^2}{2m_0}\gamma_2\left(\partial_x^2 + \partial_y^2 - 2\partial_z^2\right), \\
R &= \sqrt{3}\frac{\hbar^2}{2m_0}\left[\gamma_2\left(\partial_x^2 - \partial_y^2\right) - 2i\gamma_3\partial_x\partial_y\right], \\
S &= -\sqrt{3}\gamma_3\partial_z\left(\partial_x - i\partial_y\right), \\
U &= \frac{-i}{3}P_0\partial_z, \\
V &= \frac{-i}{\sqrt{6}}P_0\left(\partial_x - i\partial_y\right).
\end{aligned}
\tag{2.42}
$$

where

and Δ parameterizes the spin-orbit splitting between bands of irreducible Γ_8 and Γ_7 symmetry, whose value is generally determined experimentally in practice, given by

$$
\Delta = \frac{i3\hbar}{4m_0^2c^2}\langle X|\nabla V \times \boldsymbol{p}|Z\rangle = \frac{i3\hbar}{4m_0^2c^2}\langle X\left|\frac{\partial V}{\partial x}p_z - \frac{\partial V}{\partial z}p_x\right|Z\rangle. \tag{2.43}
$$

2.4.3 Strain Hamiltonian

The full 8×8 strained Hamiltonian is denoted by H_s, compatible with H_k and defined as

$$
H_s = \begin{pmatrix}
a_{\mathrm{c}}\epsilon_h & 0 & -v^\dagger & 0 & -\sqrt{3}v & \sqrt{2}u & u & -\sqrt{2}v^\dagger \\
0 & a_{\mathrm{c}}\epsilon_h & \sqrt{2}u & \sqrt{3}v^\dagger & 0 & v & -\sqrt{2}v & -u \\
-v & \sqrt{2}u & -p+q & -s^\dagger & r & 0 & \sqrt{3/2}s & -\sqrt{2}q \\
0 & \sqrt{3}v & -s & -p-q & 0 & r & -\sqrt{2}r & \sqrt{1/2}s \\
-\sqrt{3}v^\dagger & 0 & r^\dagger & 0 & -p-q & s^\dagger & \sqrt{1/2}s^\dagger & \sqrt{2}r^\dagger \\
\sqrt{2}u & v^\dagger & 0 & r^\dagger & s & -p+q & \sqrt{2}q & \sqrt{3/2}s^\dagger \\
u & -\sqrt{2}v^\dagger & \sqrt{3/2}s^\dagger & -\sqrt{2}r^\dagger & \sqrt{1/2}s & \sqrt{2}q & -p & 0 \\
-\sqrt{2}v & -u & -\sqrt{2}q & \sqrt{1/2}s^\dagger & \sqrt{2}r & \sqrt{3/2}s & 0 & -p
\end{pmatrix}
\tag{2.44}
$$

where

$$
\begin{aligned}
p &= a_{\mathrm{v}}\epsilon_h, \\
q &= b\epsilon_b, \\
r &= \frac{\sqrt{3}}{2}b\left(\epsilon_{xx}-\epsilon_{yy}\right)-id\epsilon_{xy}, \\
s &= -d\left(\epsilon_{xz}-i\epsilon_{yz}\right), \\
u &= \frac{-i}{\sqrt{3}}P_0\left(\epsilon_{xz}\partial_x+\epsilon_{yz}\partial_y+\epsilon_{zz}\partial_z\right), \\
v &= \frac{-i}{\sqrt{6}}P_0\left[\left(\epsilon_{xx}-i\epsilon_{xy}\right)\partial_x+\left(\epsilon_{xy}-i\epsilon_{yy}\right)\partial_y+\left(\epsilon_{xz}-i\epsilon_{yz}\right)\partial_z\right].
\end{aligned}
\tag{2.45}
$$

The expressions of ϵ_h and ϵ_b are given in Eqs. (2.24) and (2.28), respectively. The $\boldsymbol{V_P}$ represents the additional PZT effect induced by strain fields, given by

$$
\boldsymbol{V_P}=\begin{pmatrix}
-V_p(\boldsymbol{r}) & 0 & 0 & 0 & 0 & 0 & 0 & 0 \\
0 & -V_p(\boldsymbol{r}) & 0 & 0 & 0 & 0 & 0 & 0 \\
0 & 0 & V_p(\boldsymbol{r}) & 0 & 0 & 0 & 0 & 0 \\
0 & 0 & 0 & V_p(\boldsymbol{r}) & 0 & 0 & 0 & 0 \\
0 & 0 & 0 & 0 & V_p(\boldsymbol{r}) & 0 & 0 & 0 \\
0 & 0 & 0 & 0 & 0 & V_p(\boldsymbol{r}) & 0 & 0 \\
0 & 0 & 0 & 0 & 0 & 0 & V_p(\boldsymbol{r}) & 0 \\
0 & 0 & 0 & 0 & 0 & 0 & 0 & V_p(\boldsymbol{r})
\end{pmatrix}
\tag{2.46}
$$

where $V_p(\boldsymbol{r})$ is the PZT potential derived by Eq. (2.32). Note the signs for conduction band and valence band are opposite since the electrons and holes flux in these two bands are with opposite electric charges. By combining Eqs. (2.41), (2.44), and (2.46), the complete strain-dependent eight-band Hamiltonian *H* is formed, given by

$$
H = H_k + H_s + \boldsymbol{V_P}. \tag{2.47}
$$

2.5 Numerical Framework for Microscopic Modeling

2.5.1 Finite element method

The eigenvalue problem for the Schrödinger equation based on the multi-band Hamiltonian has been analyzed in the last section, suggesting that the problem essentially becomes solving a group of coupled second-order partial differential equations (PDEs) in 3D space. There have been a lot

of different methods proposed to numerically solve PDEs; one of them is the finite element method (FEM). It is surprising that, compared with the widely use of FEM in fields such as fluid dynamics, structural engineering, electromagnetics, etc., it has attracted less attention in solving multi-band Schrödinger equations. Actually, FEM is quite suitable for the simulation of nanostructures based on the advantages as follows:

1) FEM allows a very accurate representation of complex and arbitrary geometries.
2) BCs at material interfaces are fulfilled automatically, and no additional treatment is needed.
3) FEM allows a flexible meshing strategy, i.e. a coarse mesh applying to the less important regions (e.g. spacer and lower barrier) and a refined mesh for high precision applying to the regions of interest (e.g. QD and matrix around interfaces).
4) FEM allows a sparse equation system resulting from the real-space FEM discretization, which requires less computing resources.
5) Convergence of solution can be obtained more easily due to the use of higher-order interpolation polynomials, and the polynomial order in FEM is adjustable.

There exist a vast variety of FEM programs used in technology computer aided designs (TCAD) and scientific researches. In addition to open source FEM projects (e.g. NEMO5 [145], and NanoFEM [146]), there are also a number of commercial software (e.g. ABAQUS, ANSYS, and COMSOL Multiphysics [147]) providing all-in-one features ranging from importing or manually building geometry to post-processing and eye-catching visualization. Although they may specialize in different fields, the general FEM process in basic steps can be summarized as follows:

1) FEM discretizes the continuous domain into elements on the basis of shape functions (e.g. triangles and tetrahedrons) and nodes connecting the adjacent elements.
2) Targeted quantity at an arbitrary point on an element's edges is interpolated by using interpolation polynomials (e.g. Lagrange polynomials). For higher-order polynomials, additional nodes are required.
3) Characteristic function of each element is formulated.

4) Elements are assembled so that the targeted quantity becomes interpolated over the entire structure.
5) Solution is, therefore, approached by minimizing the characteristic function over the entire structure.

2.5.2 COMSOL Multiphysics FEM tool

Compared with some other software (e.g. ANSYS), COMSOL Multiphysics provides a more friendly graphical user interface (GUI), resulting in much reduced learning cost. In this work, we use COMSOL in our microscopic modeling [147].

In addition to the aforementioned advantages, COMSOL has specific features, e.g. it provides a quite number of predefined and time-tested modules which hide most of the mathematically complex details, so that many standard problems can be directly solved; these modules can be easily coupled into one model and work together to solve a complex problem which simultaneously consists of more than one physics (i.e. multiphysics). Last but not the least, COMSOL allows solving the time-dependent or stationary problems in one step or arbitrary multi-step fashion, as the output solution of any step can be transferred to the next step as initial input. Note the above mentioned two flexibility features are extremely significant for our modeling, which consists of three coupled modules (corresponding to three main steps of entire study) and a multi-step strain analysis (corresponding to multi substeps in strain field calculation).

Finally, additional practical and nontrivial concerns (not only for COMSOL) that come from the hardware limitation are recorded here for reference purposes. For a given model, the RAM usage is determined by the number of bases and the so-called degree of freedom (DOF), which is linearly dependent on the number of nodes (i.e. mesh refinement). On the other hand, from last subsection we know that the mesh quality along with polynomial order number is closely related to the number of nodes thus related to DOF. Apparently, a trade-off between the mesh quality and RAM usage must be made. Otherwise, the memory overload would result in an assignment of the

calculation into virtual memory on the hard drive, leading to an intolerably long solving time. Our attempt is to fully use all RAM so that both minimum and average element quality are acceptable (e.g. rule of thumb: not lower than 0.2 and 0.7, respectively), simultaneously without any exceeding of RAM capacity. For instance, all calculations in this work were performed on a dual-processors workstation with two hexa-core 3.4 GHz XEON CPUs and 128 GB RAM by using COMSOL Multiphysics 5.4. For solving the 8×8 Hamiltonian problem, the total number DOF was kept below 1.3 M to avoid the peak RAM usage exceeding 128 GB. Due to this limitation, only the regions of interests (i.e. QD and FCL) were meshed by using "free tetrahedral" mode, and for the rest regions which are insignificant, the "swept" meshing mode was adopted. In addition to the number of DOF, the solving time is also related to (but not linearly dependent on) the desired number of eigenvalues and the solver algorithm in terms of matrix symmetry, as for the latter, the Hamiltonian must be fixed to "Hermitian symmetric" to avoid the occurrence of spurious complex or imaginary eigenvalues.

2.5.3 Microscopic modeling procedures using COMSOL

For the microscopic modeling procedures, one can refer to Fig. 1.7. In what follows, details of the building of the microscopic model, in particular, the strain analysis, will be given in the order of calculations in manual book fashion for reference purposes. Note the following descriptions of operations are based on starting with a blank model instead of using the model wizard, even though the latter is handy, we want to fully control and customize our model.

Globally define parameters: The first step is to assign the values to parameters which will be used in each step of calculations, such as dimensions of model (e.g. FCL thickness), material parameters (e.g. intrinsic lattice constants), and some expressions (e.g. initial strain tensors), for the convenience in the following steps. When dealing with the parameters of lattice-matched quaternary alloy $In_{1-x}Ga_xAs_yP_{1-y}$ used in barrier layers, we referred to Vegard's law [148]. The gallium and arsenic mole fraction x and y are correlated as

$$x = \frac{0.1894y}{0.4184 - 0.013y}. \tag{2.48}$$

The linear interpolation formulas along with parameters are listed in details latter, as shown in Table 4.1.

Build geometry: Next, there are two ways to build model geometry in COMSOL, by using the built-in drawing tools in COMSOL (as we did) or by importing relative more complicated geometry from a commercial CAD package. In this work, two types of QD geometry were studied. In particular, a systematic study focusing on a single truncated pyramid (TP) type InAs QD is presented, as depicted in Fig. 2.10(a). In order to simulate the realistic growth process, an FCL is isolated from the capping layer by inserting a work plane. The thickness of the FCL is set identical to QD height (*h*), which is varied to investigate the impact of QD height change. To include the fluctuation of base size, a diameter (*D*) range of 30 to 40 nm is considered for estimating the margin of error of QD base diameter. The top diameter and base angle are denoted by l_{top} and θ, respectively. The outer boundaries in *x*- and *y*-axes are 24 nm from the center of QD base, which is far enough due to the fact that the dot density of roughly 4×10^{10} cm^{-2} for most practical QD devices. The thickness of WL, the lower barrier and the complete capping layer (FCL plus SCL) are 1.64 nm, 20 nm and 10 nm, respectively. Simultaneously, the same configuration as above, is applied to a flat lens (FL) type QD, as shown in Fig. 2.10(b), to reveal the impact of QD shape.

After building the geometry, material properties can be added to the geometry by either entering the data directly (as we did) or using the database available in COMSOL. The material assignment is also shown in Fig. 2.10. In this step, some variables can also be defined by clicking on the definition node, such as ϵ_h and ϵ_b in entire geometry, and expressions of the strained band edges in each region with different materials.

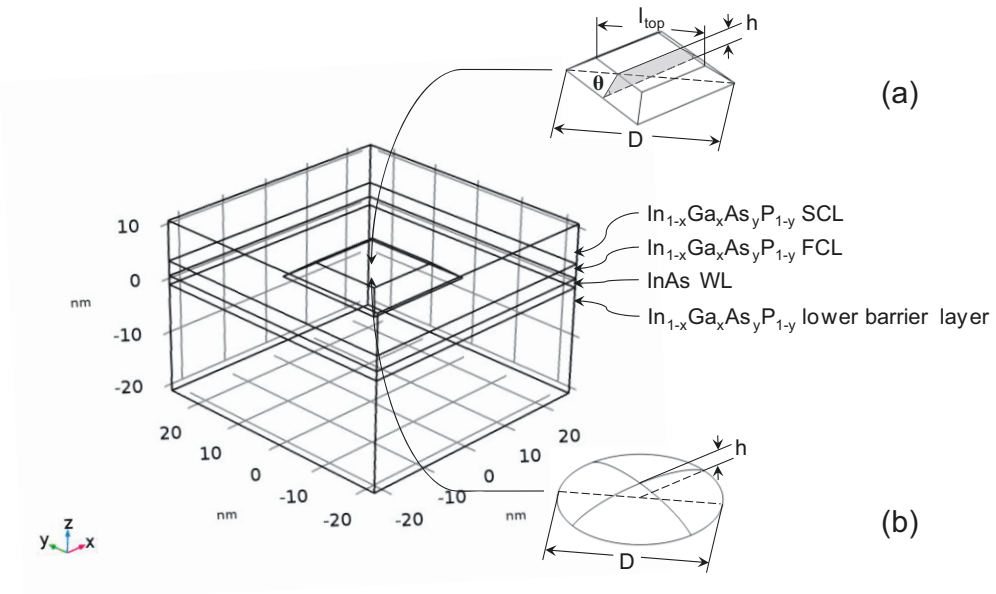

Fig. 2.10 Schematics and geometries of (a) buried TP InAs QD and (b) FL QD; *h* and *D* are the dot height and diameter of dot base, respectively.

Add physics: After building model geometry and adding material, the physics under study can be added in the order of calculations. For the strain analysis, the predefined solid structural mechanics module is used twice, dividing the entire strain field calculation into two substeps, to account for the double-capping procedure: Only the lower barrier, the QD and WL are included in the first substep; then the excluded capping layer in first substep joins back to the calculations, introducing an extra strain component in the second substep. The calculated strain tensors of the first substep are input to the second substep as new initial strain. This can be done by the configuration of study come in later. More details about the so-called two-step strain analysis will be given in Sec. 4.2.2. Then the boundary condition (BC) for each interface should be set by configuring the prescribed displacement: For each substep, the outermost interfaces of model, except the bottom and top boundaries, are constrained (i.e. prescribed displacement is fixed to zero) along *x*- and *y*-axes, and the bottom is constrained in all three dimensions. The topmost and all internal interfaces are left free (i.e. no constraint).

After strain field, the calculation for piezoelectric potential is added by switching the predefined module to coefficient-form PDE (cPDE) module which can fit into the numerical

analysis for almost any physics. Actually, COMSOL also provides predefined piezoelectricity module. The reason for the use of cPDE in this work is that the built-in module does not include the quadratic polarization component, which is very important as discussed in Sec. 2.3.3. For fully customizing our model, Eqs. (2.29)−(2.32) are modified to fit into the form of default cPDE for the stationary study, given by

$$e_a \frac{\partial^2 \boldsymbol{V_p}}{\partial t^2} + d_a \frac{\partial \boldsymbol{V_p}}{\partial t} + \nabla \cdot \left(-c\nabla \boldsymbol{V_p} - \boldsymbol{\alpha} \cdot \boldsymbol{V_p} + \boldsymbol{\gamma}\right) + \boldsymbol{\beta} \cdot \nabla \boldsymbol{V_p} + \mathrm{a}\boldsymbol{V_p} = f, \tag{2.49}$$

where the coefficients are listed in Table 2.1, if the relative permittivity for each material is assumed isotropic. For the calculation of piezoelectric potential, Dirichlet BC (i.e. variable $\boldsymbol{V_p} = 0$) is set to all the outermost interfaces of the model, as the internal interfaces are left *natural* with no additional treatment (i.e. Neumann BC).

Table 2.1 Coefficients for PDE in piezoelectric potential calculation.

e_a	0
d_a	-1
c	$-\varepsilon_s\varepsilon_0$
α	$(0 \quad 0 \quad 0)^{\mathrm{T}}$
γ	$\begin{pmatrix} 2e_{14}\epsilon_{yz} + 2B_{114}\epsilon_{xx}\epsilon_{yz} + 2B_{124}\epsilon_{yz}\epsilon_{yy} + 2B_{124}\epsilon_{yz}\epsilon_{zz} + 4B_{156}\epsilon_{xz}\epsilon_{xy} \\ 2e_{14}\epsilon_{xz} + 2B_{114}\epsilon_{yy}\epsilon_{xz} + 2B_{124}\epsilon_{xz}\epsilon_{xx} + 2B_{124}\epsilon_{xz}\epsilon_{zz} + 4B_{156}\epsilon_{yz}\epsilon_{xy} \\ 2e_{14}\epsilon_{xy} + 2B_{114}\epsilon_{zz}\epsilon_{xy} + 2B_{124}\epsilon_{xy}\epsilon_{xx} + 2B_{124}\epsilon_{xy}\epsilon_{yy} + 4B_{156}\epsilon_{yz}\epsilon_{xz} \end{pmatrix}$
β	$(0 \quad 0 \quad 0)^{\mathrm{T}}$
a	0
f	1

Finally, the calculation for electronic band energy is added, also realized by using cPDE module. In order to match the cPDE to the 8×8 matrix in Eq. (2.47), all the parameters (e.g. A, P, etc.) are converted into the form of symmetric matrix, e.g.,

$$\begin{aligned} R &= \sqrt{3}\frac{\hbar^2}{2m_0}\left[\gamma_2\left(\partial_x^2 - \partial_y^2\right) - 2i\gamma_3\partial_x\partial_y\right] \\ &= \nabla \cdot \left[-\sqrt{3}\frac{\hbar^2}{2m_0}\begin{pmatrix} -\gamma_2 & i\gamma_3 & 0 \\ i\gamma_3 & \gamma_2 & 0 \\ 0 & 0 & 0 \end{pmatrix}\nabla \boldsymbol{u}(\boldsymbol{r})\right], \end{aligned} \tag{2.50}$$

where $$\boldsymbol{u}(\boldsymbol{r}) = (u_1 \quad u_2 \quad u_3 \quad u_4 \quad u_5 \quad u_6 \quad u_7 \quad u_8)^{\mathrm{T}}, \tag{2.51}$$

then the strain-dependent eight-band $\boldsymbol{k} \cdot \boldsymbol{p}$ Hamiltonian formed by Eqs. (2.41), (2.44), and (2.46) is divided into terms with second-, first-, and zero-order partial derivatives. These terms are extracted in comparison to the corresponding coefficients of cPDE. Dirichlet BC is set to the outermost interfaces of the model, the same as the case of piezoelectricity calculation, representing that the envelope function of wavefunction is forced to vanish at these boundaries; in contrast, the envelope function is continuous across an internal interface. The complete model is summarized in Table 2.2.

Table 2.2 Summary of multiphysics model.

Calculation	Physics module	Study	Dependent variables
Strain field (first substep)	Structural mechanics (solid)	Stationary	u_1, v_1, w_1
Strain field (second substep)	Structural mechanics (solid)	Stationary	u_2, v_2, w_2
Piezoelectric potential	Coefficient-form PDE	Stationary	V_p
Electronic band	Coefficient-form PDE	Eigenvalue	ψ_1–ψ_8

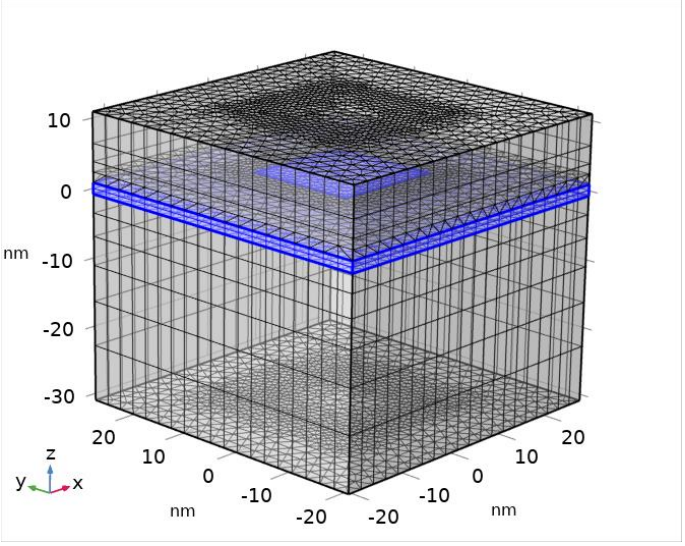

Fig. 2.11 Mesh created by using a hybrid meshing strategy. QD and WL are highlighted in blue for visualization.

Meshing: The hybrid meshing strategy due to the hardware limitation has been discussed in the last subsection, as shown in Fig. 2.11. The unevenly "swept" meshing mode results in relatively

higher density of nodes in the vicinity of internal interfaces, where there is interestingly drastic change in terms of strain distribution.

Set solver: Except for the first substep of strain field calculation, the inputs of each following step are obtained from the stored solutions of the previous step of calculations. Particularly, the searching ranges for eigenvalues of electron and hole bands are quite separated; the entire calculation is usually required to perform twice to get solution for CB and VBs, respectively: For the electron band, eigenvalues are searched for around 0.8 eV and the search method around shift is set to larger real part; for the hole band, eigenvalues are searched for around 0.4 eV, and the search method around shift is set to smaller real part. The values of 0.8 and 0.4 are obtained from the evaluation of strained CBE and VBEs, which are available once piezoelectric potential calculation is done. Typically, at least 30 eigenvalues are desired for both electron and hole bands.

2.6 Optoelectronic Properties of Nanostructures

In Sec. 2.2−2.5 the main efforts are devoted to the investigation of single-particle states. The correlation between the geometry of nanostructures (i.e. 3D confinement) and single-particle states has been explicitly illustrated by the DOS and strain effects. In this section, the major effect of geometry on the optoelectronic properties will be discussed, as well as the coupling effect in ensemble of QDs. Based on these discussions, we move towards the macroscopic modeling, which will be discussed in the next chapter.

2.6.1 Coulomb interaction

Let us first recall some fundamental concepts of semiconductors. In a picture at low temperature (LT, i.e. $k_{\mathrm{B}}T \ll E_g$), the VB is fully populated and the CB is empty. An electron in VB can be promoted to CB after gaining enough excitation energy ($> E_g$) by using the thermal, optical, or electrical pump, artificially leaving a hole in VB. This process is called the generation of an electron-hole pair. Once in CB the electron becomes a free electron (the hole in VB is also free),

they can move independently and conduct the current. Thus, for this type of electron-hole pair, the lifetime is very short. However, in another picture, the electron absorbs energy a little bit lower than the direct bandgap energy, creating a bound electron-hole pair that can be together seen as a single quasi-particle with long lifetime. In this so-called exciton (X), the electron and hole are bound, resulting from the direct Coulomb interaction. Thus, the electron cannot move independently from "that" hole. The energy difference between the absorbed and the bandgap is called binding energy $\Delta(X^0)$, which can be approximated if correlation/exchange effects are neglected, by employing Poisson's equation [149]:

$$\Delta(X^0) = -q_i \int d\boldsymbol{r} \left|\boldsymbol{\psi}_0^i\right|^2 \boldsymbol{V}_0^j, \tag{2.52}$$

where

$$q_j \left|\boldsymbol{\psi}_0^j\right|^2 = \varepsilon_0 \nabla \cdot \left(\varepsilon_s \nabla \boldsymbol{V}_0^j\right). \tag{2.53}$$

The index j denotes either the electron or the hole, and V_0^j is an additional Coulombic potential resulting from the probability density $\left|\boldsymbol{\psi}_0^j\right|^2$. We can easily understand the process in another way: For a bound electron-hole pair, the negatively charged electron (or hole) is localized by an additional potential (V_0^j), which arises from the occurrence of the positively (or negatively) charged hole (or electron) due to the attractive in between. The exciton is rarely obtained in bulk materials; by contrast, it is commonly seen in QDs at LT, as the 3D quantum confinement limits the carrier's movement, thereby increases the overlap integral of probability density between the electron and hole. Consequently, $\Delta(X^0)$ is affected by the geometry of QD: In the system of a typical InAs/InP QD as shown in Fig. 2.10 (i.e. $h \ll D$), the Coulomb interaction is interpreted to a perturbation of the spatial confinement potential, and the binding energy in general increases with the decrease in QD height. The photon energy generated from the interband transition between confined states is

$$\hbar\omega_0 = E_{e0} - E_{h0} - \Delta(X^0), \tag{2.54}$$

where E_{e0} and E_{h0} are the GS energy levels for the electron and hole.

Besides the aforementioned neutrally charged excitons (X^0), there are more complex such as

trions ($X^{\pm}$), biexcitons (XX), even charged biexcitons ($XX^{\pm}$), which leads to further splitting of the few-particle states, however, are beyond the scope of this thesis. Charge neutrality is assumed in all states.

2.6.2 Light-matter interaction

Eq. (2.54) in the last subsection gives the emission wavelength for fundamental interband transition. In this subsection, the optical strength of interband transition is discussed, which is characterized by the absorption coefficient for photons and determined by the coupling between photons and electrons.

The light-matter interaction or photon-electron coupling can be described by using a simple two-level system: The *time-dependent* wavefunction of a particle ψ_{nm} involved in a transition between the states *m* and *n* is written as a linear combination of the two states, i.e., $\psi_{nm}(\boldsymbol{r},t) = a\psi_m(\boldsymbol{r},t) + b\psi_n(\boldsymbol{r},t)$, where $a^2 + b^2 = 1$. Assuming the system starts in state *n* (i.e. $a = 0$, $b = 1$) at a lower energy level. In the presence of a perturbing optical field, the system is neither purely in the state *m* nor *n* but starting to oscillate with the angular frequency ω of optical field, as the probability density $|\psi_{nm}(\boldsymbol{r},t)|^2$ consists of an oscillating component. The oscillating component implies a *probability* of absorption of a single photon with energy $\hbar\omega_{nm} = E_m - E_n$; this probability is also time-dependent which peaks if $\omega = \omega_{nm}$ (and polarization related to strain type is matched), and once the absorption occurs, this system is excited to the state *m* (i.e. $a = 1$, $b = 0$) at higher energy level. The periodic change in probability is called Rabi oscillation, and the absorption of photon is a *statistical* process [150].

The oscillating component is interpreted to a *time-dependent* Hamiltonian $H_{nm}(t)$, derived by adding a perturbation term $e\boldsymbol{A_0}$ to Eq. (2.3):

$$H_{nm} = -\frac{e}{m_0}A_0(\boldsymbol{r},t)\boldsymbol{e}\cdot\boldsymbol{p}, \tag{2.55}$$

where *e* is the electron charge, A_0 is the magnitude of vector potential resulting from the perturbing optical field, directed along the unit vector $\boldsymbol{e}$ (i.e. polarization of incident light):

$$E(\boldsymbol{r},t) = -\frac{\partial \boldsymbol{A_0}}{\partial t}. \tag{2.56}$$

We assume that the electric field is presented as

$$\boldsymbol{E} = \boldsymbol{e}\sqrt{\frac{2\hbar\omega}{\eta\varepsilon_0\Omega}}\left(e^{i\omega t} + e^{-i\omega t}\right), \tag{2.57}$$

where η is the refractive index and Ω is the volume of the system. Now, it can be seen from Eqs. (2.55)−(2.57) that the absorption in the system is characterized by

$$|H_{nm}|^2 = \left[\frac{eA_0(\boldsymbol{r})}{2m_0}\right]^2 |M|^2 = \frac{e^2\hbar}{2\omega\eta\varepsilon_0 m_0^2\Omega}|M|^2, \tag{2.58}$$

where M is defined for convenience as a momentum matrix element

$$M = \langle m|\boldsymbol{e}\cdot\boldsymbol{p}|n\rangle = \int \psi_m^\dagger \boldsymbol{e}\cdot\boldsymbol{p}\psi_n d\boldsymbol{r}. \tag{2.59}$$

On the other hand, the interband transition rate W is given by using the *Fermi's Golden Rule* and substituting Eq. (2.58) [11]:

$$\begin{aligned} W &= \frac{2\pi}{\hbar}|\langle m|H_{nm}|n\rangle|^2\delta(\hbar\omega_{nm} - \hbar\omega) \\ &= \frac{\pi e^2}{\omega\eta\varepsilon_0 m_0^2\Omega}|M|^2\delta(\hbar\omega_{nm} - \hbar\omega), \end{aligned} \tag{2.60}$$

and since the absorption coefficient $\alpha(\hbar\omega)$ is defined by the number of photons absorbed per unit distance, finally derived as

$$\alpha(\hbar\omega) = \frac{\pi e^2}{c\omega\eta\varepsilon_0 m_0^2\Omega}|M|^2\delta(\hbar\omega_{nm} - \hbar\omega), \tag{2.61}$$

The delta function in Eq. (2.61) is determined by the DOS of the final state in QD, which can commonly be implemented by substitution of a Lorentzian lineshape (see Sec. 2.6.4 and Eq. (2.73)). Next, the analytical expression of M is studied. By substituting Eq. (2.8) into Eq. (2.59), $|M|^2$ can be described by the envelope functions $F(\boldsymbol{r})$ and the periodic component of Bloch function $u(\boldsymbol{r})$, written as

$$|M|^2 = |\langle F_m|F_n\rangle\langle u_m|\boldsymbol{e}\cdot\boldsymbol{p}|u_n\rangle + \langle u_m|u_n\rangle\langle F_m|\boldsymbol{e}\cdot\boldsymbol{p}|F_n\rangle|^2. \tag{2.62}$$

For an interband transition, the second term in the bracket vanishes due to the orthogonality of

basis functions u_m and u_n thereby $\langle u_m|u_n\rangle = 0$; while for an intraband transition, $\langle u_m|\boldsymbol{e}\cdot\boldsymbol{p}|u_n\rangle = 0$ thus the first term in the bracket disappears. As only the interband transition is our focus, *M* can be written in terms of the envelope function overlap integral to give

$$|M|^2 = |\langle F_m|F_n\rangle\langle u_m|\boldsymbol{e}\cdot\boldsymbol{p}|u_n\rangle|^2 = |I_{mn}|^2|M_{mn}|^2, \tag{2.63}$$

where

$$I_{mn} = \sum_i F_m^{\dagger}(\boldsymbol{r_i})F_n(\boldsymbol{r_i}), \tag{2.64}$$

which is closely related to the geometry of nanostructures. In addition, this overlap integral term provides an insight accounting for the selection rule, i.e. interband transitions are only possible between states belonging to the same irreducible symmetry group (e.g. *s*–*s*, *p*–*p*, etc.)

Lastly, a commonly used alternative way to calculate the absorption is given as

$$\alpha(\hbar\omega) = \frac{\omega\pi}{c\eta\varepsilon_0\Omega}|d_{mn}|^2\delta(\hbar\omega_{nm} - \hbar\omega), \tag{2.65}$$

where

$$|d_{mn}|^2 = \frac{e^2|M|^2}{\omega^2 m_0^2} \tag{2.66}$$

that is known as the dipole matrix element.

2.6.3 Coupling in QD ensemble

After investigating the carrier-carrier and photon-carrier coupling in last two subsections, important optoelectronic properties in *one* QD or an ensemble of *ideal* QDs can be determined in terms of interband transitions, such as the emission wavelength and transition rate, among which the latter can be experimentally described as absorption coefficient. As in fact that QDs with various shapes and sizes are not isolated but connected via the WL, which also affect the emission, in the following two subsections, the inter-dot coupling will be discussed to demonstrate a more macroscopic view.

It has been described in Sec. 2.4.1 that if a number of atoms are packed into a small space, the overlaps of orbitals among atoms introduce the splitting between bonding and antibonding orbitals. As the QDs are analogue atoms, this concept of orbital coupling can be applied to the coupling of electronic states in the ensemble of semiconductor QDs, particularly for those with distances in

between are very small. We obtain the basic conditions for electronic coupling by considering a composite system $A \cup B$ with Hamiltonian $H_{A\cup B}$, given by

$$H_{A\cup B} = H_K + V_{A\cup B}, \tag{2.67}$$

and the original single-particle eigenstates $\left|u_i^A\right\rangle$ and $\left|u_j^B\right\rangle$ of decoupled systems A and B are continued to $\left|u_k^{A\cup B}\right\rangle$, e.g. $|u_1^A\rangle$ becomes $|u_1^{A\cup B}\rangle$ and $|u_1^B\rangle$ turns out to be $|u_2^{A\cup B}\rangle$ in the composite system $A \cup B$, which are non-orthogonal basis set.

By inserting $|c_i\rangle = \sum_j \alpha_j \left|u_j^{A\cup B}\right\rangle$ into

$$H_{A\cup B}|c_i\rangle = E_i^{A\cup B}|c_i\rangle \tag{2.68}$$

to give

$$\begin{pmatrix} H_{11} & H_{12} & \cdots & H_{1n} \\ H_{21} & \ddots & & \\ \vdots & & & \\ H_{n1} & \cdots & & H_{nn} \end{pmatrix} \begin{pmatrix} \alpha_1 \\ \alpha_2 \\ \vdots \\ \alpha_n \end{pmatrix} = E_i^{A\cup B} \begin{pmatrix} \Gamma_{11} & \Gamma_{12} & \cdots & \Gamma_{1n} \\ \Gamma_{21} & \ddots & & \\ \vdots & & & \\ \Gamma_{n1} & \cdots & & \Gamma_{nn} \end{pmatrix} \begin{pmatrix} \alpha_1 \\ \alpha_2 \\ \vdots \\ \alpha_n \end{pmatrix} \tag{2.69}$$

with

$$H_{ij} = \left\langle u_i^{A\cup B}\middle|H_{A\cup B}\middle|u_j^{A\cup B}\right\rangle, \Gamma_{ij} = \left\langle u_i^{A\cup B}\middle|u_j^{A\cup B}\right\rangle. \tag{2.70}$$

Apply this process to a simple QD-pair system and solve Eq. (2.69) by the diagonalization of $\mathbf{\Gamma}^{-1}\mathbf{H}$ to give

$$E_\pm^{A\cup B} \approx \frac{E_1^A + E_1^B}{2} \pm \frac{1}{2}\sqrt{(E_1^A - E_1^B)^2 + 4|H_{12}|^2} \tag{2.71}$$

which are the bonding (E_-) and antibonding (E_+) eigenstate energies, if $\mathbf{\Gamma} \approx 1$ is applied. The coupling strength is then characterized by the energy separation between E_- and E_+, determined by the terms in the radical sign. We may see that, even if the single QD energies $E_1^A = E_1^B$, as long as the envelope function overlap term $H_{12} = \langle u_1^{A\cup B}|H_{A\cup B}|u_2^{A\cup B}\rangle \neq 0$, then E_- and E_+ are not degenerate: There exists electronic coupling.

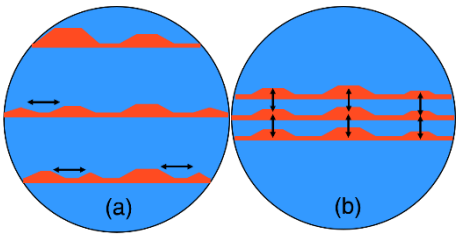

Fig. 2.12 Schematic illustration of (a) lateral and (b) vertical inter-dot coupling in a QD ensemble associated with the geometry configurations of the entire gain region.

Although the dimensional reduction of the active region (i.e. QDs) results in many benefits which have been discussed, one fact we have to remember is that it also leads to a reduced effective interaction of the photons, therefore the implementation to realistic applications requires a partial compensation by either increasing the areal density of QD or the stacking enough number of QD layers. Consequently, coupling in such QD ensemble can be divided into two categories in terms of directions: As illustrated in Fig. 2.12(a), if the areal density of dots in a single layer is large, the lateral coupling dominates; if the QDs are tightly stacked, i.e. the spacer thickness is very small, the vertical coupling is dominant, as shown in Fig. 2.12(b). The latter is comparatively more complicated which consists of several different coupling mechanisms, i.e., except for the resonant electronic coupling, the strain coupling and nonresonant quantum tunneling associated with much more factors (e.g., the spacer thickness, the QD size homogeneity, the stacking alignment, and the SLN) can also affect the optoelectronic properties of the system.

2.6.4 Broadened linewidth

It has been mentioned in Sec. 2.3.1 and illustrated in Fig. 2.6(b) that the realistic DOS in QD shows a deviation from the delta-function-like counterpart of ideal QD, as predicted by Eq. (2.16). This deviation results from a broadened linewidth in frequency domain during the optical transitions, which consists of two principal contributions, i.e. homogeneous broadening (HB) and inhomogeneous broadening (IHB), as shown in Fig. 2.6(a). Next, we analyze these two effects one by one.

As explained in the last subsection, both absorption and emission of photon are statistical processes, implying an inherent uncertainty which we should deal with, when the small particle is our object of study. This uncertainty can account for the fact that absorption can occur when the incident light is even not precisely resonant with the energy separation between two well-defined states, *m* and *n*. For the off-resonance in terms of the angular frequency relative to $E_m - E_n$, we can define this uncertainty as

$$\delta E = \hbar|\omega_{nm} - \omega| \approx \frac{2\pi\hbar c}{\delta\lambda} = \frac{\hbar}{\tau}, \tag{2.72}$$

where the τ is known as the dephasing time [11]. Thus, this uncertainty in the frequency domain transforms the ideal delta lineshape with a linewidth of zero in Eqs. (2.16), (2.60), (2.61), and (2.65) to a Lorentzian lineshape with linewidth of $2\delta E$ (e.g. $2\delta E = 10$ meV), given as

$$L(\hbar\omega_{nm}, \hbar\omega) = \frac{1}{\pi}\frac{\delta E}{|\hbar\omega_{nm} - \hbar\omega|^2 + \delta E^2} = \frac{1}{\pi}\frac{\hbar\Gamma}{|\hbar\omega_{nm} - \hbar\omega|^2 + (\hbar\Gamma)^2}, \tag{2.73}$$

where $\Gamma = 1/\tau$ is defined as the dephasing rate, which is more commonly used. Note this HB is basically independent of the geometry of nanostructures, therefore in frequency domain it homogeneously broadens every spectral line, as its name says.

The IHB, on the other hand, is easier to understand. The process of self-assembly results in a distribution of dot sizes that are dependent upon the growth conditions, and this size dispersion leads to a distribution of energies among a large number of dots in an ensemble [11], as each dot has well-defined energy states. The IHB is often represented by a normalized Gaussian function as

$$G(\hbar\omega_i) = \frac{1}{A}\exp\left(-4\ln 2 \times \frac{|\hbar\omega_i - \hbar\omega_0|^2}{\Delta E^2}\right), \tag{2.74}$$

where ω_0 is the corresponding angular frequency of the peak of the distribution and ΔE is the FWHM linewidth of IHB, as the latter is commonly measured of 30~70 meV, much larger than the counterpart of HB. The distribution is divided into *N* (e.g. *N* = 51) subgroups on the basis of QD size and the index *i* is the subgroup number from 1 to *N*. *A* is a normalization constant that

$\sum_{i=1}^{N} G(\hbar\omega_i) = 1$. Within the *i*th subgroup, QDs are assumed to have identical transition energy $\hbar\omega_i$, and the lineshape is dominated by Lorentzian HB in Eq. (2.73). Therefore, the *absorption spectrum* of the ensemble is made up of a series of homogeneously broadened spectra, centered on ω_i of each size subgroup of QDs, as illustrated in Fig. 2.13.

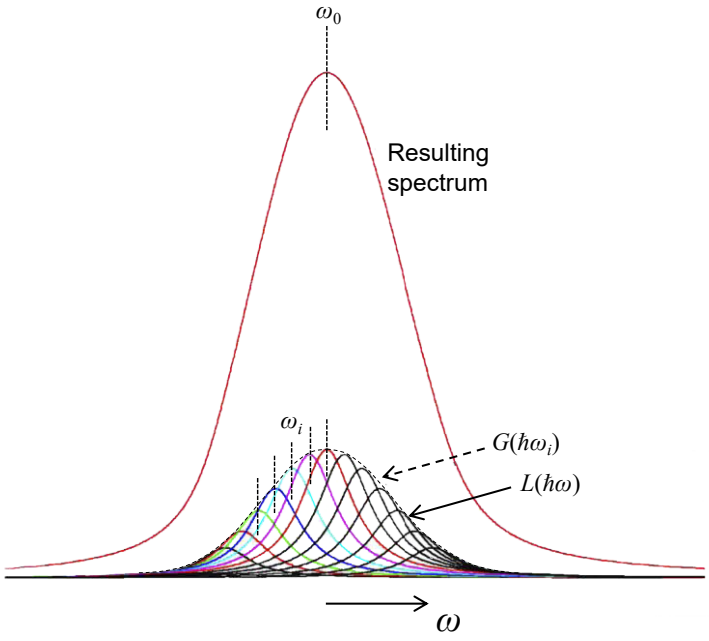

Fig. 2.13 Absorption spectrum made up of HB and IHB contributions, as the latter is characterized by the distribution of QD sizes.

2.7 Conclusions

In this chapter, we have discussed the fundamental but important Bloch's theorem and perturbation theory. Based on those, the expressions of DOS in low-dimensional systems have been derived, particularly in the QDs. In addition to the DOS, the strain field and piezoelectric potential associated with growth process are playing vital roles in the modifications of confinement potentials in semiconductor-based quantum-confined nanostructures. A strain-dependent eight-band $\boldsymbol{k} \cdot \boldsymbol{p}$ method based on effective mass and envelope function approximations has been presented to include all these effects, which is commonly used for the calculation of single-particle

electronic band structure and numerically implemented by COMSOL Multiphysics. The interactions of electron-hole and photon-electron associated with the geometry have also been addressed, providing the alternative possibilities of engineering of interband transitions and optoelectronic properties. In addition to the few-particle interactions, more macroscopic inter-dot coupling effects in the ensemble of QDs have been discussed, paving the way for the macroscopic modeling in next chapter. A more detailed workflow of the microscopic modeling in addition to Fig. 1.7 is outlined in Fig. 2.14.

Fig. 2.14 A more detailed workflow diagram that shows the numerical framework for microscopic modeling of the QD active region.

Chapter 3 Modeling of QD-Based Laser Diodes

3.1 Introduction

In this chapter, we concentrate on the description of the light field dynamics in laser cavities. A typical structure of FP EEL with QD nanostructures embedded inside is considered in Sec. 3.2, as the important modal gain properties and spontaneous emission spectra (Sec. 3.3) are not only related to the gain medium introduced in last chapter, but also related to the waveguide. In order to obtain the spatio-temporal laser dynamics during the intracavity propagation, we then have to calculate the dynamics of the spectrally-resolved carrier densities and the induced polarizations (Sec. 3.4), coupling with the optical wave described by using a time-domain travelling-wave (TDTW) model in Sec. 3.5. The numerical framework is summarized in Sec. 3.6.

3.2 Diode Laser Structures

In this section, the consideration of QDs as gain medium is based on the realistic modeling of a diode laser. An example of forward biased ridge waveguide FP EEL is illustrated in Fig. 3.1(a), and the dielectric deposited alongside the ridge is not shown. The core (i.e. active region) consists of three-fold stacked QD layers, as shown in inset, embedded in the barrier layer (commonly using quaternary alloy lattice-matched to InP, see Sec. 2.5.3) so that the band offsets and the emission wavelength can be tuned by the variation of composition. The entire core is then sandwiched by the upper and lower cladding layers (i.e. InP) with reduced effective index to form a slab waveguide (and also a double heterostructure), limiting the diffusion of carriers. The ridge, on the other hand, produces a lateral variation of carrier density and effective index along x-axis, which localizes the optical mode to the region beneath the stripe, in turn further increasing the effective index of this region due to the nonlinearity of material. This two-dimensional confinements consequently produces a good guidance of light along y-axis, forming a ridge waveguide.

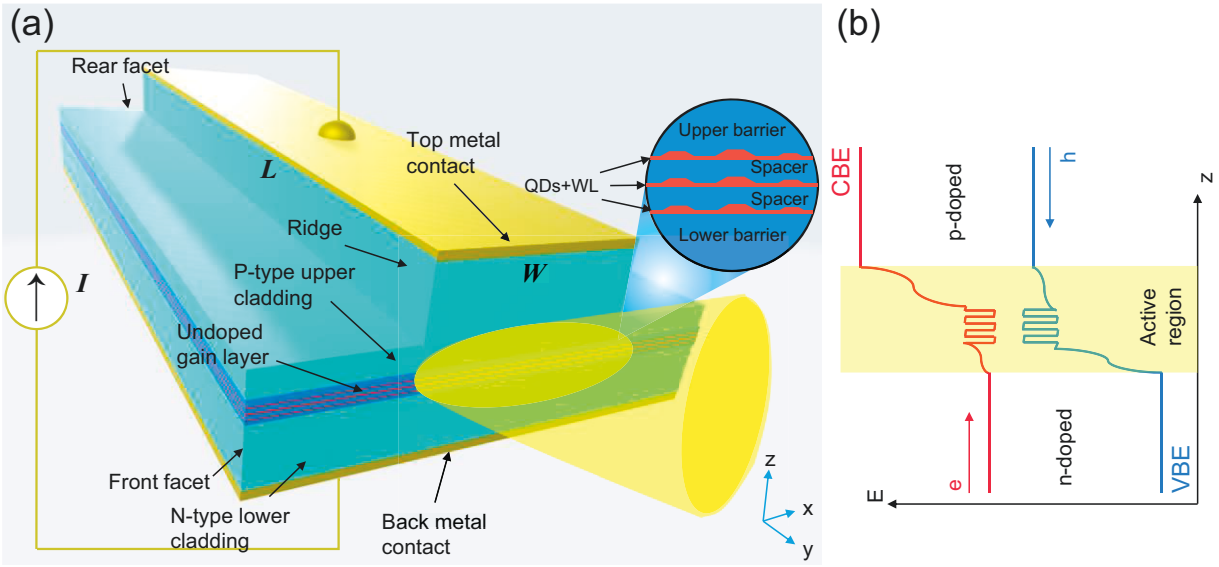

Fig. 3.1 Schematic illustration of (a) a typical ridge waveguide FP EEL under forward bias with the active region consisting of three-fold stacked QD layers (zoom-in in the inset), and (b) the corresponding energy band diagram.

A schematic of the energy band diagram of the EEL under forward bias is illustrated in Fig. 3.1(b). The structure is made up of an outer double heterostructure that forms the slab waveguide of typically 150~200 nm thick (i.e. *p*-cladding−core−*n*-cladding) and an inner double heterostructure that forms the ultrathin potential wells for electrons and holes of depths ΔE_c and ΔE_v, respectively (Sec. 2.2.2). Under forward bias, the doped cladding layers inject electrons and holes into the barrier region, which serves as a reservoir from which carriers are captured into the QDs.

3.3 Optical Gain and Spontaneous Emission

The expression of absorption derived in Eqs. (2.61) and (2.65) can be regarded as the loss of photons by upward transition of electrons between two states of an atom, when the lower state n is full of electrons and the upper state m is empty (i.e. $\rho_n = 1$ and $\rho_m = 0$), which is in general not the case and, of course, not sufficiently accurate to describe the laser action. There are other two principle downward transitions of electrons which can generate photons, i.e. stimulated

emission and spontaneous emission, as illustrated in Fig. 3.2. The basis of laser action is the coherent amplification of light by stimulated emission, made possible when the condition called *population inversion* is satisfied, resulting from the coexistence of absorption (i.e. loss) rate determined by $\rho_n(1-\rho_m)$ and emission (i.e. gain) rate determined by $\rho_m(1-\rho_n)$. Therefore, the degree of inversion (i.e. net gain) can be evaluated by $(\rho_m - \rho_n)$. The detailed discussion about the calculation in a multi-level system of the occupation probability using coupled rate equations will be given in the next section. Moreover, for the interband transition between the CB and VB, ρ_n can be replaced by $(1-\rho_n^h)$ thus the evaluation is simplified as $(2\rho^{e,h}-1)$ in the excitonic system which assumes the same dynamics of electrons and holes, i.e. $\rho_m^e = \rho_n^h = \rho^{e,h}$ (Sec. 2.6.1).

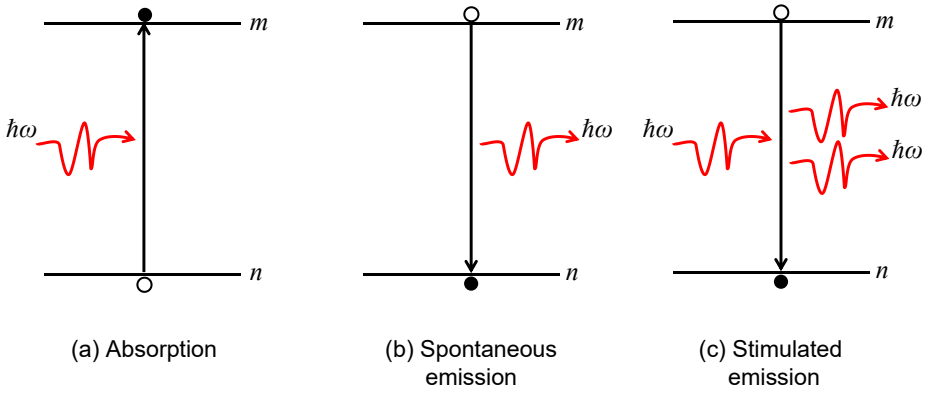

Fig. 3.2 Schematic illustration of photon absorption and generation through upward and downward transitions of one electron in a two-level system.

It is important for us to keep in mind that the optical gain of interest in a waveguide is not the *material gain* (i.e. the hypothetical gain that would be experienced by a mode that is wholly confined to the gain medium such as QDs) but the *modal gain*, as the latter is associated with the aforementioned waveguide structure instead of the volume of material Ω in Eq. (2.61) [11]. More specifically, the most relevant parameters of the modal field used in modeling are the effective index η in gain medium, the group index η_g in the dielectric waveguide, and the fraction of energy coupled to the gain medium, which is defined by field confinement factor Γ_{xy}, given by

$$\Gamma_{xy} = \frac{\iint_{A_{\text{active}}} |E(x,y)|^2 \mathrm{d}x\mathrm{d}y}{\iint_{-\infty}^{+\infty} |E(x,y)|^2 \mathrm{d}x\mathrm{d}y} = \frac{H_{\text{QD}} N_{\text{l}}}{w_{\text{mode}}}, \tag{3.1}$$

where A_{active} denotes the transversal active area, E is the optical field, H_{QD} is the FCL thickness, N_{l} is the SLN, and w_{mode} is the effective mode width, which can be evaluated by

$$w_{\text{mode}} = \frac{\int_{-\infty}^{+\infty} |E(z)|^2 \mathrm{d}z}{\left|E_{\text{peak}}\right|^2}. \tag{3.2}$$

where $\left|E_{\text{peak}}\right|^2$ is the peak energy of the mode, as shown in Fig. 3.3.

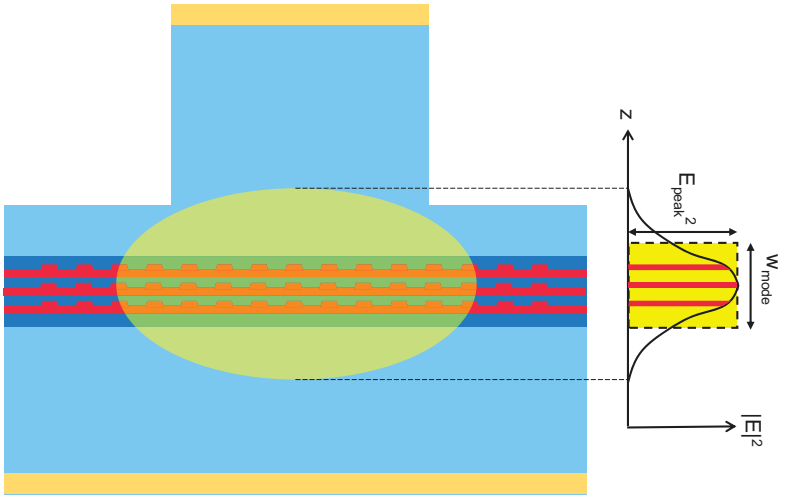

Fig. 3.3 Schematic illustration of the overlap of the transverse mode profile with potential wells resulting from three-fold stacked QD layers (highlighted in red). The mode profile is equivalent to an effective mode area (highlighted in yellow), introducing the definition of the effective mode width w_{mode}.

The total confinement factor is then given by

$$\Gamma = \frac{\eta_{\text{g}}}{\eta} \Gamma_{xy}. \tag{3.3}$$

Since in slab waveguides the ratio of refractive indices $\eta_{\text{g}}/\eta \approx 1$ whereas Γ_{xy}~0.01, therefore $\Gamma \approx \Gamma_{xy}$ is usually used in the modeling. Consequently, by combining Eqs. (2.61) [or (2.65)], (2.73), (2.74), (3.1) and by converting the material gain, the final form of expression of the modal gain for QD-based device is given by

$$g(\hbar\omega) = \frac{\pi e^2 N_{\mathrm{D}} N_{\mathrm{l}}}{c\omega\eta\varepsilon_0 m_0^2 w_{\mathrm{mode}}} \sum_{i=1}^{N} \sum_{m} G_i D_m |M_m|^2 \left(2\rho_{im}^{e,h} - 1\right) L(\hbar\omega_{im}, \hbar\omega)$$
$$= \frac{\Gamma_{xy} \pi e^2 N_{\mathrm{D}}}{c\omega\eta\varepsilon_0 m_0^2 H_{\mathrm{QD}}} \sum_{i=1}^{N} \sum_{m} G_i D_m |M_m|^2 \left(2\rho_{im}^{e,h} - 1\right) L(\hbar\omega_{im}, \hbar\omega) \tag{3.4}$$

or

$$g(\hbar\omega) = \frac{\Gamma_{xy} \omega \pi N_{\mathrm{D}}}{c\eta\varepsilon_0 H_{\mathrm{QD}}} \sum_{i=1}^{N} \sum_{m} G_i D_m |d_m|^2 \left(2\rho_{im}^{e,h} - 1\right) L(\hbar\omega_{im}, \hbar\omega), \tag{3.5}$$

where the index m here is for the QD confined state involved in the transition (e.g. GS and ES) with degeneracy D_m, and N_{D} is the areal density of QDs in a dot layer. The choice of equation depends on the type of matrix element used in the macroscopic modeling. From Eqs. (3.4) and (3.5) we can see that the modal gain cannot be increased by simply stacking a number of QD layers as large as possible, instead, only achieved by *coupling as many layers into the mode as possible*.

By contrast, the spontaneous emission in an excitonic system is only determined by $\rho^{e,h}$ instead of $(2\rho^{e,h} - 1)$ in terms of the occupation probability, as it only requires the occurrence of electron-hole pairs. In addition, the spontaneous emission is associated with the polarization of photons instead of the effective mode. Assuming the TE-polarized spontaneous emission is dominant in III-V QDs (Sec. 2.3.2), consistently with Eq. (3.5), the spontaneous emission spectrum (i.e. PL spectrum) is directly written here as

$$I_{\mathrm{PL}}(\hbar\omega) = \frac{\omega}{c\eta} \sum_{i=1}^{N} \sum_{m} \frac{G_i D_m \rho_{im}^{e,h}}{\pi} \frac{1}{\tau_{sp,TE}^{im}} L(\hbar\omega_{im}, \hbar\omega), \tag{3.6}$$

where

$$\frac{1}{\tau_{\mathrm{sp,TE}}^{im}} = \frac{1}{2} \frac{8\pi |d_m|^2 \eta^2 (\hbar\omega_{im})^2}{3\varepsilon_0 (hc)^2 \hbar} \tag{3.7}$$

is the TE-polarized spontaneous emission rate for a single spin, derived using the Einstein approach [151]. The spontaneous emission spectrum is useful for model validation by comparing with the PL measurement data. In addition, it can be seen that in equilibrium, the rates of stimulated emission and absorption are related to the rate of spontaneous emission. Therefore it is possible to obtain the gain spectrum from the spontaneous emission spectrum, which is referred to as Henry method [152].

3.4 Rate Equations Approach

Based on the discussion about the balance between gain and loss in the last section, this consideration can be extended into a multi-level system, and the occupation probability of each level can be calculated by employing the phenomenological rate equation (RE) approach. In the conventional multi-reservoir model [150], a set of nonlinear first-order differential equations for the average carrier density and for the average photon density in the active region are coupled with each other. Except for the gain of active medium, on the one hand, the captured carriers from other reservoirs are also treated as gain; on the other hand, instead of carrier lifetime, the escaped and relaxed carriers to other levels, together with the consumed ones in various recombination processes, account for the loss. Based on these general principles of RE approach, a number of variants have been developed to include additional effects or increase the accuracy of model, particularly for the active region with nanostructures. For instance, at first, the capture and escape of carriers existed only between two adjacent confined states (i.e. cascade model) [95, 96], and then direct relaxation paths between nonadjacent subbands were added to account for some phenomena [93, 153, 154]. The competitive emission from both GS and ES [155], the interaction of the inhomogeneously broadened gain medium with many lasing longitudinal modes [96], and different time scales of the separated electron and hole dynamics [156-159] were also included in the current RE variants. In addition, the expression of the photon density was substituted with the optical field represented by two counter-propagating waves, so that the total field was obtained by a standing wave with amplitude $(E^+ + E^-)$ and the net stimulated transition rate was proportional to $(E^+ + E^-)^2$. It is appropriate to couple this approach with the time-domain modeling of the propagating electro-optic field when longitudinal distribution dynamics of carriers and photons in waveguide become significant, which is discussed in detail in next section.

A more complex version of the lastly mentioned RE approach is used in this thesis, as a full description of dipole polarization is included to relate the refractive index change to the optical gain variation [100]. Start with the complex optical susceptibility

$$\chi(\hbar\omega) = \frac{1}{\eta^2\varepsilon_0}\frac{p_{im}(\hbar\omega)}{E(\hbar\omega)}. \tag{3.8}$$

which is related to the microscopic polarization $p_{im}(\hbar\omega)$ contributed from each QD subgroup via the amplitude of the optical field $E(\hbar\omega)$. Based on the definition

$$\frac{d}{dt}E(t) = \Gamma_{xy}\frac{cg_{\text{mod}}}{2\eta}E(t) + j\frac{\omega\Delta\eta}{\eta}E(t), \tag{3.9}$$

we can obtain the relationship between the modal gain [Eq. (3.5)], the carrier-induced refractive index $\Delta\eta$, the susceptibility and the polarization:

$$g(\hbar\omega) = -\frac{\omega\eta}{c}\text{Im}\{\chi(\hbar\omega)\} = -\frac{\omega}{\varepsilon_0\eta c}\frac{\text{Im}\{p_{im}(\hbar\omega)\}}{E(\hbar\omega)} \tag{3.10}$$

and

$$\Delta\eta(\hbar\omega) = \frac{\eta}{2}\text{Re}\{\chi(\hbar\omega)\} = \frac{1}{2\varepsilon_0\eta}\frac{\text{Re}\{p_{im}(\hbar\omega)\}}{E(\hbar\omega)}. \tag{3.11}$$

According to Eq. (3.5), the refractive index change related to the real part of complex susceptibility in QD is then represented as

$$\Delta\eta(\hbar\omega) = \frac{\Gamma_{xy}\pi N_{\text{D}}}{2\varepsilon_0\eta H_{\text{QD}}}\sum_{i=1}^{N}\sum_{m} G_i D_m |d_m|^2\left(2\rho_{im}^{e,h} - 1\right)\frac{1}{\pi}\frac{\hbar\omega - \hbar\omega_{im}}{|\hbar\omega_{im} - \hbar\omega|^2 + (\hbar\Gamma)^2}. \tag{3.12}$$

The microscopic polarization contributed from each QD subgroup can be written as

$$p_{im}^{\pm}(\hbar\omega) = \left[2\varepsilon_0\eta\Delta\eta_{im}(\hbar\omega) - \frac{\varepsilon_0\eta c}{\omega}g_{im}(\hbar\omega)\right]E^{\pm}(\hbar\omega), \tag{3.13}$$

and in time domain [100]

$$p_{im}^{\pm}(z,t) = \frac{j\omega_0\Gamma_{xy}N_{\text{D}}}{2\eta c\hbar H_{\text{QD}}}\sum_{i=1}^{N}\sum_{m} G_i D_m |d_m|^2\left(2\rho_{im}^{e,h} - 1\right) I_{im}^{\pm}(z,t), \tag{3.14}$$

where

$$I_{im}^{\pm}(z,t) = \int_{-\infty}^{t} e^{j(\omega_{im}-\omega_0)(t-\tau)}e^{-\Gamma(t-\tau)}E^{\pm}(z,t)d\tau \tag{3.15}$$

representing the convolution between the *complex* Lorentzian function and the optical field. Finally, the macroscopic polarization is given by

$$P^{\pm}(z,t) = \sum_{i=1}^{N}\sum_{m} p_{im}^{\pm}(z,t). \tag{3.16}$$

Now we consider a 4-level excitonic model (no GS quenching has been experimentally

observed in InAs/InP QDs [160]) consisting of two confined states GS and ES in InAs QDs and two states at higher energies represent the lowest edges of continuum band in the InAs WL and InGaAsP separate confinement heterostructure (SCH). Both GS and ES are assumed to simultaneously exhibit stimulated and spontaneous emissions (i.e. two-state lasing). Polarizations are also included to account for the frequency detuning induced by carrier dynamics. Only cascade relaxation paths are considered, as illustrated in Fig. 3.4.

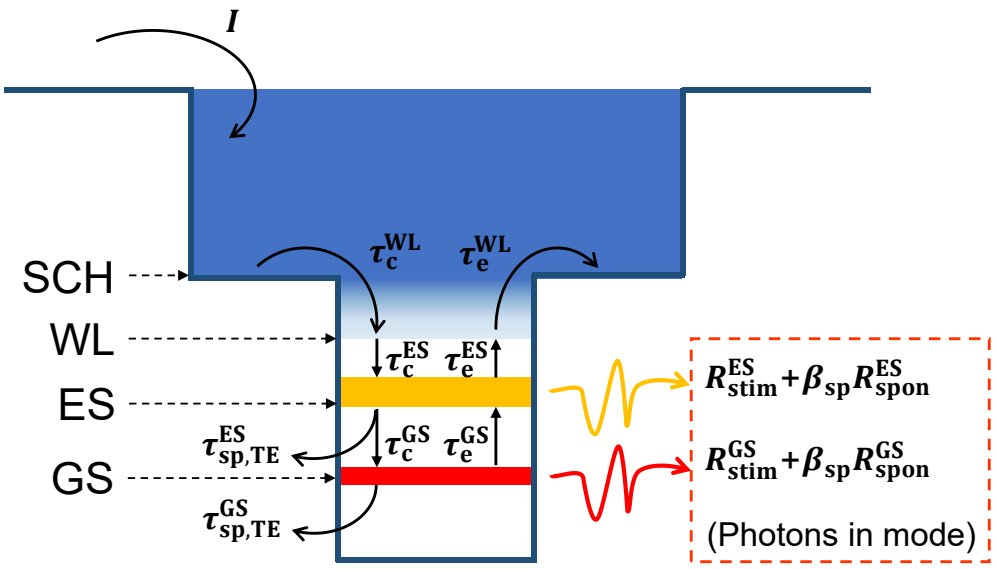

Fig. 3.4 Schematic of carrier dynamics in a 4-level excitonic model of the active region of a typical QD laser.

The whole set of RE of such model following the Pauli Exclusion Principle is given by [161]

SCH:
$$\frac{dN_{SCH}^{e,h}}{dt} = \frac{J}{e}\Delta z W - \frac{N_{SCH}^{e,h}}{\tau_c^{WL}} + \frac{N_{WL}^{e,h}}{\tau_e^{WL}} \tag{3.17}$$

WL:
$$\frac{dN_{WL}^{e,h}}{dt} = \frac{N_{SCH}^{e,h}}{\tau_c^{WL}} - \frac{N_{WL}^{e,h}}{\tau_e^{WL}} - \sum_{i=1}^{N}\frac{G_i}{\tau_c^{ES}}N_{WL}^{e,h}\left(1-\rho_{iES}^{e,h}\right) + \sum_{i=1}^{N}\frac{N_{iES}^{e,h}}{\tau_e^{iES}} \tag{3.18}$$

ES:
$$\begin{aligned}\frac{dN_{iES}^{e,h}}{dt} = {} & \frac{G_i}{\tau_c^{ES}}N_{WL}^{e,h}\left(1-\rho_{iES}^{e,h}\right) - \frac{N_{iES}^{e,h}}{\tau_e^{iES}} - \frac{N_{iES}^{e,h}}{\tau_c^{GS}}\left(1-\rho_{iGS}^{e,h}\right) + \frac{N_{iGS}^{e,h}}{\tau_e^{iGS}}\left(1-\rho_{iES}^{e,h}\right) \\ & - \frac{N_{iES}^{e,h}}{\tau_{sp,TE}^{iES}} - \frac{j\Delta z}{\hbar\omega_{iES}}\left[\left(E^{+}{p_{iES}^{+}}^{*} - E^{+*}p_{iES}^{+}\right) + \left(E^{-}{p_{iES}^{-}}^{*} - E^{-*}p_{iES}^{-}\right)\right]\end{aligned} \tag{3.19}$$

$$\text{GS:}\quad \frac{dN_{i\text{GS}}^{e,h}}{dt} = \frac{N_{i\text{ES}}^{e,h}}{\tau_{\text{c}}^{\text{GS}}}\left(1-\rho_{i\text{GS}}^{e,h}\right) - \frac{N_{i\text{GS}}^{e,h}}{\tau_{\text{e}}^{i\text{GS}}}\left(1-\rho_{i\text{ES}}^{e,h}\right) - \frac{N_{i\text{GS}}^{e,h}}{\tau_{\text{sp,TE}}^{i\text{GS}}} - \frac{j\Delta z}{\hbar\omega_{i\text{GS}}}\left[\left(E^{+}p_{i\text{GS}}^{+\,*} - E^{+\,*}p_{i\text{GS}}^{+}\right) + \left(E^{-}p_{i\text{GS}}^{-\,*} - E^{-\,*}p_{i\text{GS}}^{-}\right)\right] \tag{3.20}$$

where $\tau_{\text{sp,TE}}^{im}$ have been given by Eq. (3.7), ω_0 is the reference frequency chosen between the GS and ES transitions which usually has the highest occupation probability: $\omega_0 = (\omega_{i\text{GS}} + \omega_{i\text{ES}})/2$ for $i = (N+1)/2$, and the total number of carriers per square meters $N_{im}^{e,h}(z,t)$ is associated with their occupation probabilities as

$$N_{im}^{e,h}(z,t) = N_{\text{I}}N_{\text{D}}G_iD_m\rho_{im}^{e,h}(z,t)W\Delta z. \tag{3.21}$$

The relationship between carrier capture time (e.g. state $m \rightarrow n$) and escape time (state $n \rightarrow m$) in quasi-equilibrium is given by

$$\frac{\tau_{n\rightarrow m}}{\tau_{m\rightarrow n}} = \frac{D_n}{D_m}\exp\left(\frac{\hbar\omega_m - \hbar\omega_n}{k_{\text{B}}T}\right). \tag{3.22}$$

where the effective DOS in the 3D SCH and 2D WL can be calculated as

$$D_{\text{SCH}} = 2\left(2\frac{\pi m_{\text{SCH}}^{*}k_{\text{B}}T}{h^2}\right)^{\frac{3}{2}}, D_{\text{WL}} = \frac{m_{\text{WL}}^{*}k_{\text{B}}T}{\pi\hbar^2}, \tag{3.23}$$

which are derived from Eqs. (2.10) and (2.12), respectively. Note the last terms including $E^{\pm}$ and $p_{im}^{\pm}$ in Eqs. (3.19) and (3.20) describe all the effects (i.e. gain and detuning) introduced by light-matter interaction in each subgroup.

3.5 Time-Domain Modeling of Propagating Field

There are a variety of approaches and photonic CAD tools available to model the propagating field in passive optical components, e.g., OptiBPM based on beam propagation method (BPM) [162], and FIMMPROP based on eigenmode expansion (EME) [163]. These approaches are based on the frequency-domain modeling algorithm and suitable for the simulation of medium (e.g. optical fibers and couplers) whose refractive index is basically constant, i.e. high nonlinearity should be avoided for better convergence. Thus, the time-domain modeling algorithm and such tools e.g.

MEEP based on finite-difference time-domain (FDTD) [164], and PicWAVE based on time-domain travelling-wave (TDTW) [165], are more appropriate for the active devices where light interacts quite a lot with the carriers, such as LEDs and diode lasers [98-100, 166].

Based on Maxwell's equations, FDTD is a rigorous full-wave optical solver and perhaps the most widely used approach. It finite-differently discretizes Maxwell's equations in time and space, in principle can model virtually anything. However, the major drawback of FDTD is the expensive computational cost, as illustrated in Fig. 3.5.

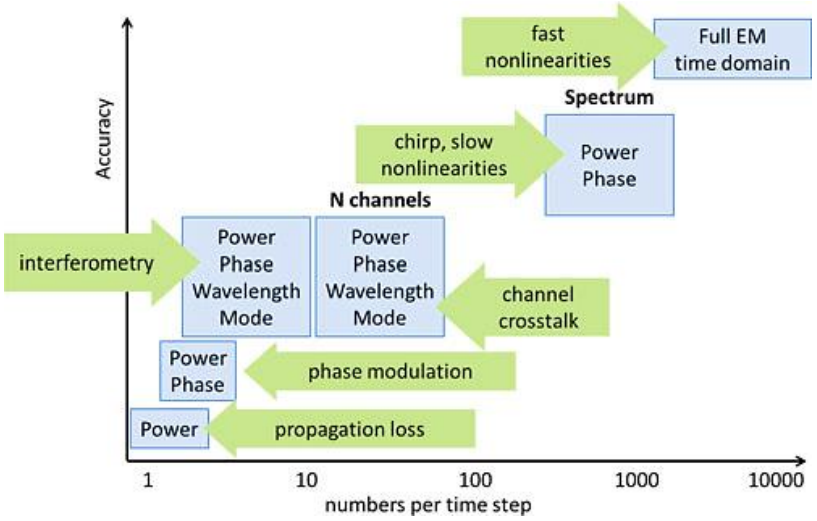

Fig. 3.5 Illustration of the relationship between the complexity of modeling algorithm (e.g. being represented in the floating-point numbers per time step) and the level to which they contain physical details [167].

For better efficiency and at the same time the sufficient accuracy, TDTW approach is typically used. Based on a slowly varying envelope approximation and the previous discussion, the advection equations used in this work for the counter-propagating waves are written as follows [100]

$$\pm\frac{\partial E^{\pm}(z,t)}{\partial z}+\frac{1}{v_g}\frac{\partial E^{\pm}(z,t)}{\partial t}=-\frac{\alpha_i}{2}E^{\pm}(z,t)-jP^{\pm}(z,t)+F^{\pm}(z,t) \tag{3.24}$$

With BC:
$$E^{+}(0,t)=r_0E^{-}(0,t),E^{-}(L,t)=r_LE^{+}(L,t) \tag{3.25}$$

where

$$F^{\pm}(z,t)\Delta z = \sum_{i=1}^{N}\sum_{m}\left[\Gamma\sqrt{\frac{\hbar\omega_{im}}{\pi\Gamma\Delta t}\frac{\beta_{\mathrm{sp}}N_{im}^{e,h}(z,t)}{2\tau_{sp,TE}^{im}}}I_{im}^{\mathrm{sp}\pm}(z,t)\right] \tag{3.26}$$

with

$$I_{im}^{\mathrm{sp}\pm}(z,t) = \int_{-\infty}^{t} e^{j(\omega_{im}-\omega_0)(t-\tau)}e^{-\Gamma(t-\tau)}e^{j\varphi_{im}(z,\tau)}d\tau \tag{3.27}$$

representing the fraction (β_{sp}) of spontaneous emission coupled with the guided mode, as shown in Fig. 3.4, α_i is the intrinsic waveguide loss, r_0 and r_L are the reflectivity of field at $z = 0$ (rear) and $z = L$ (front) FP cavity facet, and $P^{\pm}(z,t)$ is the macroscopic polarization as given in Eq. (3.16). This approach can be solved in time-domain like FDTD but with much larger time and space steps because the fast varying part $e^{j(\beta z-\omega t)}$ has been removed, at the expense of range of propagating direction, i.e. only forward and backward slowly varying fields along *y*-axis of the waveguide are modeled, which is sufficient for this work.

The TDTW models the optical field over a broad spectral range just as the FDTD, with the advantage of an adjustable algorithm for increasing the computation speed [168]. The basic TDTW approach can be further extended, as shown in our previous study, Jiao *et al.* have improved the model by including the nonlinear effects, i.e. group-velocity dispersion (GVD) and self-phase modulation (SPM) [97]. In terms of implementations, TDTW allows the inclusion of both CW and dynamic characteristics of many different active devices such as QD-SOAs [169], QD-FP MLLs [98, 100], and QD-DFB lasers [170]. Notably, Bardella *et al*. have recently rigorously applied TDTW to account for the passive self-mode-locking mechanism in single-section QD-based FP EELs without introducing any empirical parameters, e.g. gain compression factor or saturation intensity [98].

3.6 Numerical Framework for Macroscopic Modeling

Although there are a variety of commercial FDTD tools available, e.g. Lumerical FDTD etc. [171], we want a fully tunability and extendibility of our model for the study. Therefore, we use MATLAB in macroscopic modeling [172]. For the sake of completeness and better clarification, skipping all

the aforementioned details, the numerical framework of macroscopic modeling is conceptionally sketched here as shown in Fig. 3.6. For the detailed descriptions of iteration and numerical realization of e.g. convolution in software, one can refer to our previous work [97]. Note the GVD and SPM effects are excluded in this work for simplicity and efficiency.

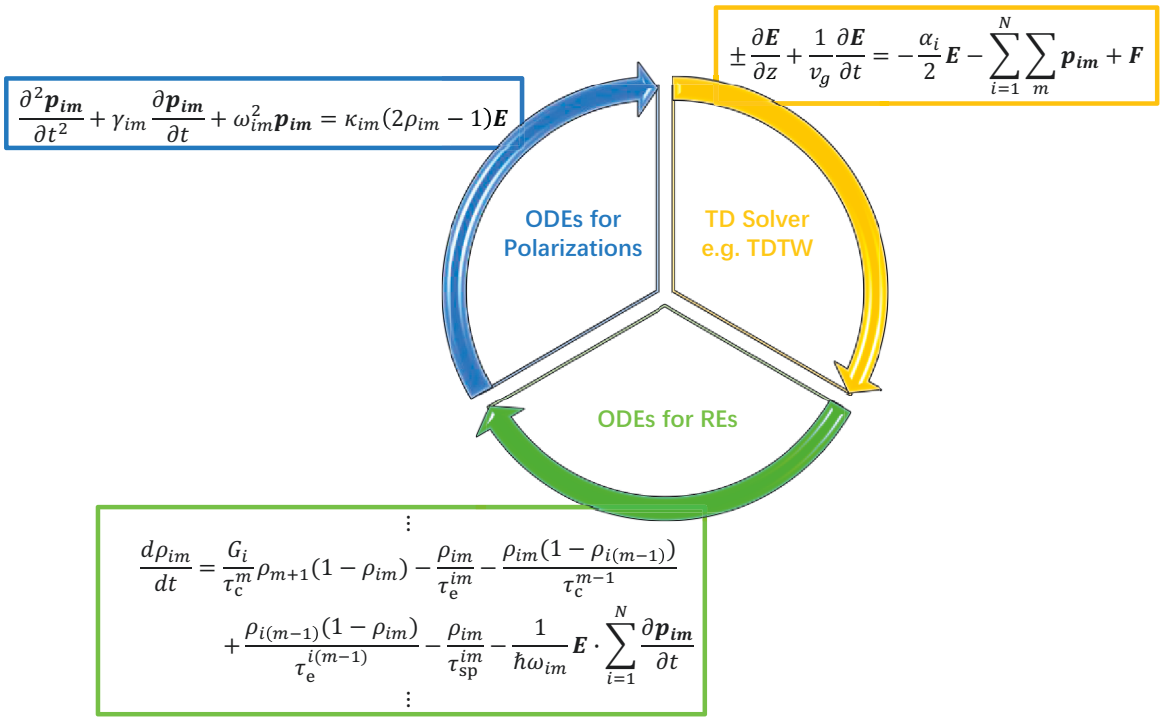

Fig. 3.6 Sketch of workflow that shows the framework for macroscopic modeling of QD laser diodes. Note the ordinary differential equation (ODE) responsible for the injection term in REs is not shown here.

3.7 Conclusions

In this chapter we started with the typical FP EEL structure consisting of a ridge waveguide and QD active region. The corresponding energy band diagram at the scale of device has also been shown. Then, the expression of modal gain and spontaneous emission spectrum which are

associated with the structure have been derived. Based on these expressions as well as the carrier-induced refractive index change, microscopic and macroscopic polarizations have been derived from the complex optical susceptibility then were input as parameters to a full set of rate equations, as the REs account for the carrier kinetics between subbands of the system. Next, the time-domain modeling has been compared with the frequency-domain counterpart and was considered more appropriate for our modeling of QD laser. Therefore, TDTW equations have been shown, which is considered a powerful tool, well balancing the relationship between efficiency and accuracy when modeling the propagating optical fields.

Chapter 4 Simulation of InAs/InP QD Lasers

4.1 Introduction

In this chapter, we show an example of model identical to the one being illustrated in Sec. 2.5.3 and Fig. 2.10. First, in Sec. 4.2, an accurate method of modeling a single self-assembled QD including a novel two-step elastic strain analysis rigorously following the realistic double-capping growth procedure as shown in Fig. 1.5. Based on the rigorous analysis, both microscopic and macroscopic approaches are sequentially applied first to a single 3D QD (Secs. 4.3, 4.4) and then to a QD ensemble (Secs. 4.5, 4.6) thus the structures and resulting spectra are explicitly related (Sec. 4.6.5). In particular, in Sec. 4.6 our two-step model is naturally extended into a multi-step model when applied to a vertical QD stack structure, a more realistic unidirectional strain accumulation is reproduced by applying such multi-step strain analysis, in comparison to the bidirectional accumulation commonly demonstrated by using the conventional one-step model. Note the Coulombic potential arising from exciton is negligible small (i.e. on the order of 0.01 mV) based on our simulation, therefore the few particle interaction is trivial and omitted in this work.

4.2 Strain Distribution

4.2.1 Conventional one-step model

The accurate control over the size distribution of self-assembled (SA) QD is always the most fascinating and significant part in QD engineering work. Since the specific properties of QDs were discovered, such as the ability of tuning the emission wavelength range through modifying the QD height, great effort has been made to the high performance QD lasers for optical fiber communications in C- and L-band (1.53–1.6 μm) [1]–[3]. The often-used self-assembled InAs/InP QD material system has few well-known drawbacks: The smaller lattice mismatch (3.1%) leads to a larger QD size fluctuation, thereby resulting in a broader PL linewidth and smaller modal gain

[4], compared to the lattice misfit in InAs/GaAs system (6.7%). Furthermore, despite being growth conditions dependent, the emission peak wavelength falls into a range longer than desired wavelength easily at RT [5], when no management of QD heights is applied.

Many approaches have been proposed to reduce the height dispersion and the overgrowth of this nanostructure semiconductor. The double-capping procedure method, based on a discontinuous capping management, is the most popular in SAQD design and fabrication during the past decade [6]–[11], as shown in Fig. 1.5. On the other hand, the one-step model has been widely used in modeling self-assembled InAs/InP QD [12]–[16]. However, the conventional elastic strain analysis used in all the previous studies needs to be improved because it does not consider double-capping growth procedure, which may degrade the accuracy of modeling.

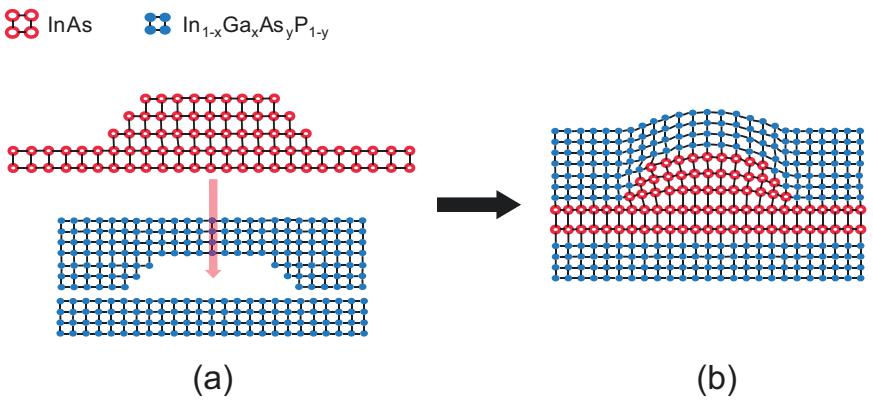

Fig. 4.1 Schematic illustration of one-step model without the consideration of separated growth procedure.

Here we present briefly the one-step model for better comparison, as illustrated in Fig. 4.1. Epitaxial self-assembled QDs arise from the lattice mismatch between the deposited InAs and the barrier InGaAsP, as shown in Fig. 4.1(a). From Eq. (2.22), the in-plane strain is defined as

$$\epsilon_0 = \frac{a_{\mathrm{InAs}} - a_{\mathrm{InGaAsP}}}{a_{\mathrm{InAs}}} \tag{4.1}$$

where a_{InAs} and a_{InGaAsP} are the intrinsic lattice constants of InAs used in QD and the quaternary alloy used in barrier layers, respectively. In conventional one-step model, as illustrated in Fig. 4.1(b), this mismatch is taken simply as initial strain in all three dimensions, i.e.

$$\epsilon_{0xx} = \epsilon_{0yy} = \epsilon_{0zz} = \epsilon_0 \tag{4.2}$$

and

$$\boldsymbol{\epsilon_0} = \begin{pmatrix} \epsilon_{0xx} & 0 & 0 \\ 0 & \epsilon_{0yy} & 0 \\ 0 & 0 & \epsilon_{0zz} \end{pmatrix} \tag{4.3}$$

4.2.2 Novel two-step model

In contrast to the description in the last subsection, the QD growth with double-capping procedure needs strain analysis with separated stages to be precisely described. Therefore, more details need to be discussed based on the evolution of QD deformation in each stage.

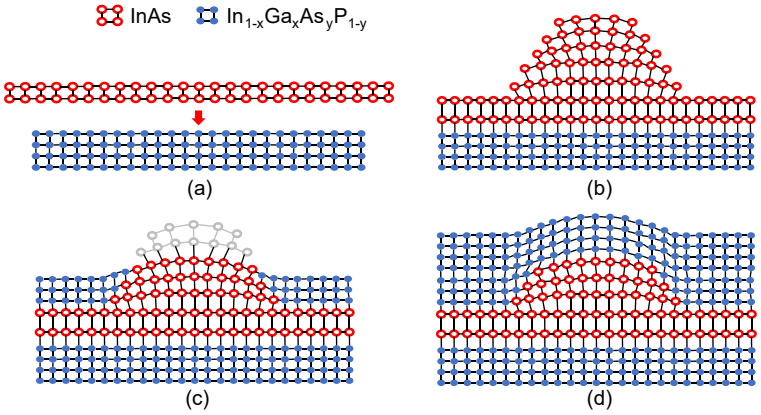

Fig. 4.2 Schematic illustration of the epitaxial growth of self-assembled QDs with the double-capping procedure. (a) Deposition of InAs onto the lower barrier layer of InGaAsP leading to an accumulation of biaxial strain due to the lattice mismatch. (b) QDs formed on top of the wetting layer to minimize the total energy of the system when the critical thickness is reached. (c) QDs partially capped with the FCL followed by growth interruption, resulting in a reduction of QD height. (d) SCL grown to complete the whole capping process.

First, as shown in Fig. 4.2(a), a thin InAs film is built up to a critical thickness under biaxial compression, and then is followed by a random formation of small islands or artificial QDs. During this first stage, only in-plane lattice mismatch is taken into calculations, i.e., no initial strain along the *z*-direction. It can be observed in Fig. 4.2(b) that the lattice constant is not homogeneous in QD: The lattice is compressed laterally and stretched vertically near the bottom, and then is relaxed gradually to intrinsic constant near the top. This stage can be expressed as

$$\epsilon_{0xx} = \epsilon_{0yy} = \epsilon_0 \tag{4.4}$$

and

$$\boldsymbol{\epsilon_0} = \begin{pmatrix} \epsilon_{0xx} & 0 & 0 \\ 0 & \epsilon_{0yy} & 0 \\ 0 & 0 & 0 \end{pmatrix} \tag{4.5}$$

Secondly, a thin InGaAsP FCL is grown to partially cap the QDs, and then a reduction of their height is followed due to mixed and exchanged As/P flux [173]. Different from [115] in which vertical initial strain due to the lattice mismatch is not included between two materials throughout the calculation, the calculated deformation field in the first stage *along with an extra out-of-plane FCL/QD intrinsic lattice misfit* is taken as initial input during this second stage of our model. This can be expressed as

$$\boldsymbol{\epsilon_0'} = \begin{pmatrix} -\epsilon_{0xx}' & -\epsilon_{0xy}' & -\epsilon_{0xz}' \\ -\epsilon_{0xy}' & -\epsilon_{0yy}' & -\epsilon_{0yz}' \\ -\epsilon_{0xz}' & -\epsilon_{0yz}' & -\epsilon_{0zz}' + \epsilon_{0zz} \end{pmatrix} \tag{4.6}$$

where ϵ_0' are the resulting strain tensors obtained from first stage. The total free energy, as suggested in Fig. 4.2(c), is minimized through a further relaxation of the uncapped pop-out part (grey), which is wiped off in a later step as described in double-capping procedure. The wiping does not change the lattice constant anymore when the system is considered stable. Therefore, *no extra in-plane initial strain is introduced* due to the negligible FCL/WL and FCL/QD (near base area) lattice mismatch in *x*- and *y*-direction. The SCL has no contribution to further elastic strain analysis because the lattice constants are matched near the new top of "shortened" QD, as shown in Fig. 4.2(d).

For simplicity, the sub-steps such as partial-removal and second-capping procedure are combined in the simulation, due to the minor significance of the SCL. The rest of the calculations, i.e., linear and quadratic PZT potential and eight-band $\boldsymbol{k \cdot p}$ model are the same as introduced in Sec. 2.5.3. The semiconductor material parameters used are listed in Table 4.1. Most parameters of quaternary alloy are calculated by linear interpolation.

Table 4.1 Material parameters used in the following calculations at RT/LT.

	Unit	Temp.	InAs	GaP	$In_{1-x}Ga_xAs_yP_{1-y}$
a	Å	RT[1]	6.0583	5.4505	$5.6533xy+6.0583(1-x)y+5.4505x(1-y)+5.8687(1-x)(1-y)$
		LT	6.0584	5.4512	$5.6525xy+6.0584(1-x)y+5.4512x(1-y)+5.8688(1-x)(1-y)$
ρ	kg/m^3	RT/LT	5668	4130	$5317.5xy+5668(1-x)y+4130x(1-y)+4790(1-x)(1-y)$
ε_r		RT	14.55	11.1	$13.18xy+14.55(1-x)y+11.1x(1-y)+12.35(1-x)(1-y)$
		LT	14.55	10.86	$12.4xy+14.55(1-x)y+10.86x(1-y)+11.77(1-x)(1-y)$
C_{11}	GPa	RT	83.29	140.5	$119xy+83.29\ (1-x)y+140.5x(1-y)+101.1(1-x)(1-y)$
		LT	83.3	143.9	$122.3xy+83.3\ (1-x)y+143.9x(1-y)+102.2(1-x)(1-y)$
C_{12}	GPa	RT	45.26	62.03	$53.8xy+45.26(1-x)y+62.03x(1-y)+56.1(1-x)(1-y)$
		LT	45.3	65.2	$57.1xy+45.3(1-x)y+65.2x(1-y)+57.6(1-x)(1-y)$
C_{44}	GPa	RT	39.59	70.33	$59.4xy+39.59(1-x)y+70.33x(1-y)+44.2(1-x)(1-y)$
		LT	39.6	70.14	$60xy+39.6(1-x)y+70.14x(1-y)+46(1-x)(1-y)$
e_{14}	C/m^2	RT/LT	0.045	0.1	$-0.18(1-y)^2+0.15(1-y)-0.05$
B_{114}	C/m^2	RT/LT	–0.5	–0.7	$-0.4xy-0.5(1-x)y-0.7x(1-y)-1.1(1-x)(1-y)$
B_{124}	C/m^2	RT/LT	–4.1	–2.2	$-3.8xy-4.1(1-x)y-2.2x(1-y)-3.8(1-x)(1-y)$
B_{156}	C/m^2	RT/LT	0.2	–0.7	$-0.7xy+0.2(1-x)y-0.7x(1-y)-0.5(1-x)(1-y)$
m_e	m_0	RT	0.0213	Barrier	$0.0632xy+0.0213(1-x)y+0.158x(1-y)+0.077(1-x)(1-y)$
		LT	0.023	Barrier	$0.0665xy+0.023(1-x)y+0.17x(1-y)+0.08(1-x)(1-y)$
γ_1^L		RT/LT	20.4	Barrier	$7.1xy+20.4(1-x)y+4.04x(1-y)+5.33(1-x)(1-y)$
γ_2^L		RT/LT	8.3	Barrier	$2.02xy+8.3(1-x)y+0.53x(1-y)+1.57(1-x)(1-y)$
γ_3^L		RT/LT	9.1	Barrier	$2.91xy+9.1(1-x)y+1.26x(1-y)+2.11(1-x)(1-y)$
a_c	eV	RT/LT	–10.2	–7.14	$-7.6+1.6x+[0.85xy-1(1-x)y-1.7x(1-y)+0.6(1-x)(1-y)]$
a_v	eV	RT/LT	1	1.7	$-0.85xy+1(1-x)y+1.7x(1-y)-0.6(1-x)(1-y)$
b	eV	RT/LT	–1.8	–1.7	$-1.85xy-1.8(1-x)y-1.7x(1-y)-1.7(1-x)(1-y)$
d	eV	RT/LT	–3.6	–4.4	$-5.1xy-3.6(1-x)y-4.4x(1-y)-4.3(1-x)(1-y)$
E_c	eV	RT	$0.709-0.37y$	$2.43-0.37y$	$0.14(1-y)^2+0.46(1-y)+0.75$
		LT	$0.768-0.37y$	$2.565-0.37y$	$1.423+0.689x-1.185y+0.758x^2+0.18y^2+0.763xy-1.14x^2y-0.845xy^2+0.875x^2y^2$
E_v	eV	RT/LT	$0.35-0.37y$	$-0.33-0.37y$	0
Δ	eV	RT	0.41	0.08	$0.108(1-y)+0.33y-0.06y^2$
		LT	0.38	0.08	$0.341xy+0.38(1-x)y+0.082x(1-y)+0.108(1-x)(1-y)$
E_p	eV	RT/LT	21.5	Barrier	$28.8xy+21.5(1-x)y+31.4x(1-y)+20.7(1-x)(1-y)$

4.2.3 Impact on confinement potentials

In the following study, a TP QD with h = 2.7 nm and D = 30 nm, surrounded by 1.15Q (i.e. $In_{0.818}Ga_{0.182}As_{0.397}P_{0.603}$) matrix, is selected as an example. The out-of-plane strain distributions

[1] RT = 300 K, LT ≤ 10 K based on [133, 238-240]. However, it is also a good approximation for the LT case when T = 20 K due to the negligible difference.

with deformations in three-dimensional space at the end of first and the second stage, i.e., before and after capping, are given in Fig. 4.3. The deformations are moderately exaggerated to show the evolution of QD more clearly.

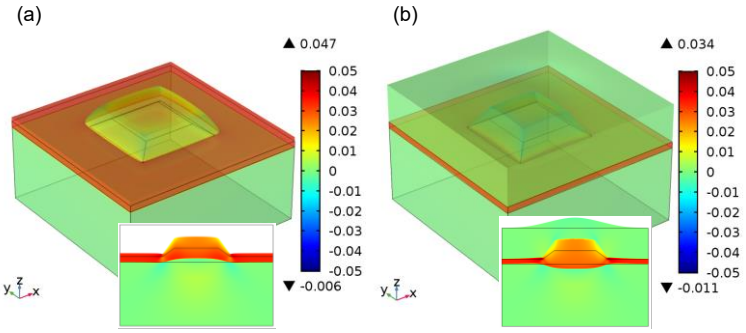

Fig. 4.3 Illustration of the out-of-plane strain distributions with deformations of a TP QD (*h* = 2.7 nm, *D* = 30 nm) buried in 1.15Q in three-dimensional space when (a) the QD is uncapped and (b) the capping layer is finished. The insets show the cross-sectional strain distributions of ϵ_{zz} with deformations. The deformations are moderately exaggerated to show the evolution of QD more clearly.

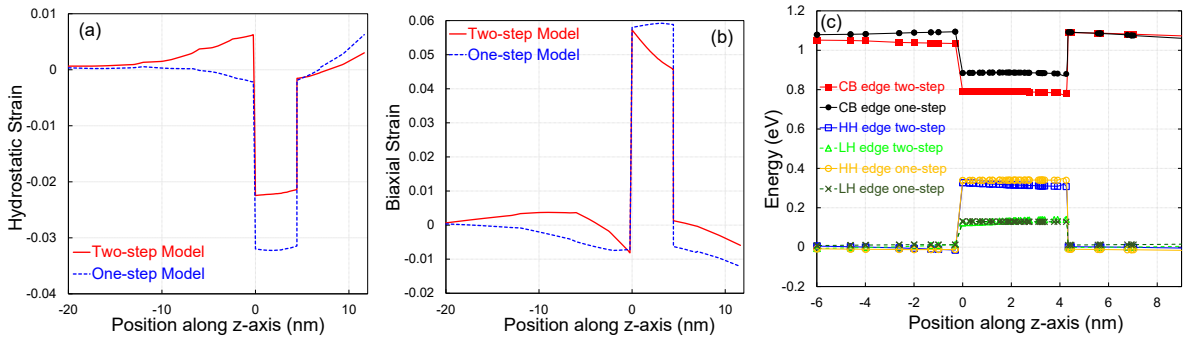

Fig. 4.4 (a) Hydrostatic strain and (b) biaxial strain distribution along the *z*-axis through the center of QD using the two models; and (c) the strained energy band edges for electrons, heavy holes and light holes along the (001) direction.

The confinement potential energy (CPE) is the key to QD investigation. The CPE is characterized by hydrostatic strain and biaxial strain, which are defined in Eq. (2.45). Fig. 4.4(a)−(b) compare the one-step and two-step models in terms of hydrostatic and biaxial strains through the center of the single QD along (001) direction. Notably, the hydrostatic strain increases and peaks in the lower barrier layer near the InAs/InGaAsP interface by using a two-step model,

significantly different from that using the one-step model, with which the strain drops smoothly and consistently as shown in Fig. 4.4(a). This difference arises from a larger tension in *x*- and *y*-directions (in-plane) by using the two-step model. It is understood that, for the two-step model, the lower barrier layer alone experiences all the in-plane tensile strain from the QD, whereas the in-plane strain can be shared by the lower barrier layer together with the capping layer in the one-step model in which all of them are regarded as a single body. Consequently, a smaller absolute value of hydrostatic strain within the dot results in a lower CBE or less modified CPE by using two-step model, as shown in Fig. 4.4(c).

On the other hand, the biaxial strain results in a tilted top using the two-step model, which is closer to the experimental strain profile given by D. Cooper *et al* [174], instead of the fact that a flat top is obtained as shown in Fig. 4.4(b) using the one-step model. The tilted top clearly reflects the fact that the within-dot-vertical-tension induced by initial in-plane compression relaxes quickly along the *z*-axis. However, no relaxation is found in the one-step strain model. A slight difference is observed in HH and LH band edges near the top of QD between the two models, as shown in Fig. 4.4(c). Since having very similar strain and potential profiles in (001) direction, the flat-lens-shaped QD case is skipped here.

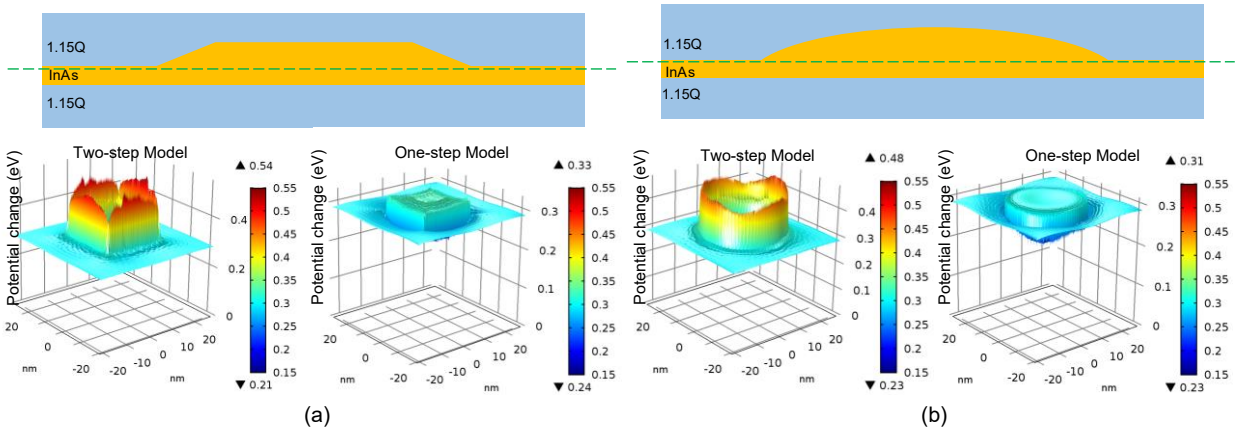

Fig. 4.5 Strain-induced modifications of lateral CPEs along a plane paralleled to *x*- and *y*-axis in (a) TP QD and (b) FL QD. Red (blue) colors correspond to high (low) change of electronic confinement due to the strain. Both two strain-analysis methods are used to show different impacts.

Since the study of CPE along a line axis can only give us a very restricted view, the lateral CPE profile is investigated in the following. A measured plane in WL, just beneath the interface of FCL/WL, is chosen because the hydrostatic strain shows the largest difference between the two models. The impact of different strain treatments is more impressive on the lateral CPE profile, as shown in Fig. 4.5 for a comparison of the two models that are used for modeling two QD shapes. The height refers to the change of two-dimensional (2D) in-plane potential in magnitude due to the strains. Using the two-step model, the potential peaks around the dot edge, and sinks in the center of the dot, thus the potential profile looks like a "tulip", due to the smaller lifting of band edge inside than outside, as shown in the left figures of Fig. 4.5. In contrast to the two-step model, the potential profile looks like an "inverted box (barrel)" when the one-step model is used, as shown in the right figures of Fig. 4.5, which means that the band edge shifts upward more inside than outside. Moreover, despite being very small (of the order of 15 mV by calculations), the PZT potential reduces the lateral symmetry in C_{2v} in the two models. Again, note the "tulip" resembles the experimental 2D-CPD maps extracted from Kelvin probe force microscopy (KPFM) measurements impressively, performed by S. Shusterman *et al.* [175]. This attests that the two-

step model is more accurate than the one-step model.

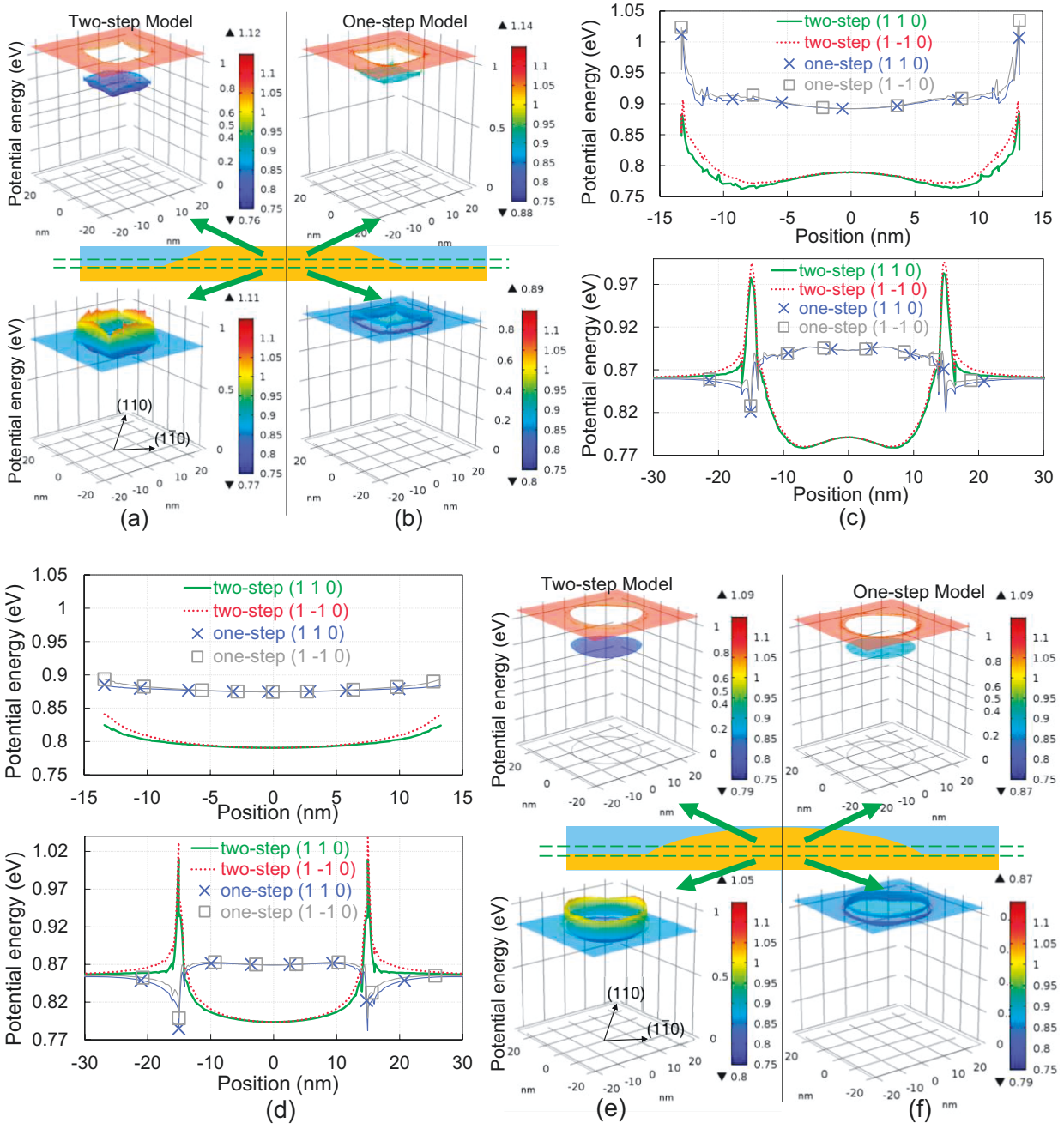

Fig. 4.6 CBE energies along two planes paralleled to *x*-*y* plane, in wetting layer just beneath the interface of heterostructure and halfway up the QD island, respectively, in: (a) TP QD using two-step model and (b) using one-step model; (e) FL QD using two-step model and (f) using one-step model. Comparison between the lateral potentials along (110) and (1$\bar{1}$0) directions in (c) TP QD and (d) FL QD show symmetry reduction due to PZT effects.

Fig. 4.6(a)−(b) present the lateral CBE profile in two positions: in the middle and near the base of a TP QD. Due to the abrupt change of potentials at the InAs/InGaAsP interface, a full picture of the potentials is not easy to be obtained. However, Fig. 4.6 still give us some insights. As expected, the 2D potential well from the two-step model is much deeper than that from the one-step strain model, as shown in Fig. 4.6(a) and (b), attributed to the different behaviors of hydrostatic strain as explained before. Similar results are obtained for the FL QD, shown in Fig. 4.6(e) and (f). The comparisons between the lateral potentials along (110) and $(1\bar{1}0)$ directions in the TP and FL QD using the two models are also illustrated in Fig. 4.6(c) and (d), for quantitatively presenting the symmetry reduction mentioned above. The lateral confinement potential profiles may be diverse from case to case; however, a universal behavior can be observed: The difference in potential between the two directions is getting larger from the middle ahead to the edge within a dot. Furthermore, a larger potential difference or "more C_{2v} symmetry" can be observed in each case using the two-step model. To summarize, the different depths of the potential well will lead to total different eigenstates and wavefunctions for electrons, thereby different optical transition energies and emission spectra. The different degradation in symmetry of potential well will result in different splitting between states for electrons with different spin orientations. The results in details will be shown and discussed in the following section.

4.3 Single Particle States

4.3.1 Bright exciton splitting

Unlike the self-assembled QDs with InAs/GaAs that are often formed in the shape of full pyramid, the self-assembled QDs with InAs/InGaAsP/InP often show a flat top and large base-to-height-aspect-ratio (D/h), especially for those using the double-capping technique. In these TP or FL types, HH and LH band edges show less coupling, which results in negligible mixing of holes states [131]. It is confirmed by the probability amplitude in single QD calculated by strain-dependent eight-band $\boldsymbol{k} \cdot \boldsymbol{p}$ model, defined as

$$P_m = \iiint_{\Omega} \Psi_m^{\dagger}(x,y,z)\Psi_m(x,y,z)\mathrm{d}x\mathrm{d}y\mathrm{d}z. \tag{4.7}$$

Part of the unnormalized results is listed in Table 4.2 as an example, where ↑↓ (⇑⇓) denote the electron (heavy hole) spin orientation. The dominant type in each hole state, which is larger than the others by roughly two or three orders of probability magnitude, is highlighted in bold. These huge differences in probability indicate that these holes states are almost "pure". It can be inferred from Table 4.2 that the highest holes states relevant to optical transitions are predominated by heavy holes in the InAs/InGaAsP self-assembled QDs, which along with the low symmetry gives rise to optical selection rules leading to excitonic fine structure. In terms of ground state, two fundamental transitions between the initial state E1↓ (E1↑) and final state HH1⇑ (HH1⇓) can be optically excited, whereas the other two (↑⇑ and ↓⇓) are optically inactive, which follow the selection rule that the difference of angular momentum must equal to ±1 [139].

Table 4.2 Example of unnormalized probability amplitudes for holes[2]

States (eV)	LH⇓	HH⇓	HH⇑	LH⇑	SO⇓	SO⇑
0.26146	130.95	3.3710	**64485**	71.904	1.4691	75.020
0.26118	68.235	**64585**	8.1268	173.21	86.153	6.4544
0.24825	317.79	13.394	**51308**	293.89	3.4168	173.19
0.24744	253.63	**51958**	10.694	429.10	202.29	14.917
0.24687	298.90	16.598	**50494**	248.08	3.0995	162.34
0.2461	239.24	**51234**	12.520	422.32	198.35	16.733

Fig. 4.7 presents the lowest (and highest) six energy states for electrons (and holes) and the corresponding *s*-like and *p*-like isosurfaces of probability density function (PDF) defined by the term in the triple integral symbol of Eq. (4.7) for the TP and FL QD shapes. As expected, due to the deeper confinement potential well for electrons, the electron states are confined more tightly within the dot from the two-step model, as shown in Fig. 4.7(a) and (c). On the other hand,

[2] All the results are obtained in a TP QD (h = 2.7 nm, D = 30 nm) buried in 1.15Q by using a two-step model. The signs "⇑" and "⇓" denote being spin-up and spin-down of hole states, respectively.

correspondingly, the hole states are confined better from the one-step model, as shown in Fig. 4.7(b) and (d), due to the slightly deeper well for holes [see Fig. 4.4(c)].

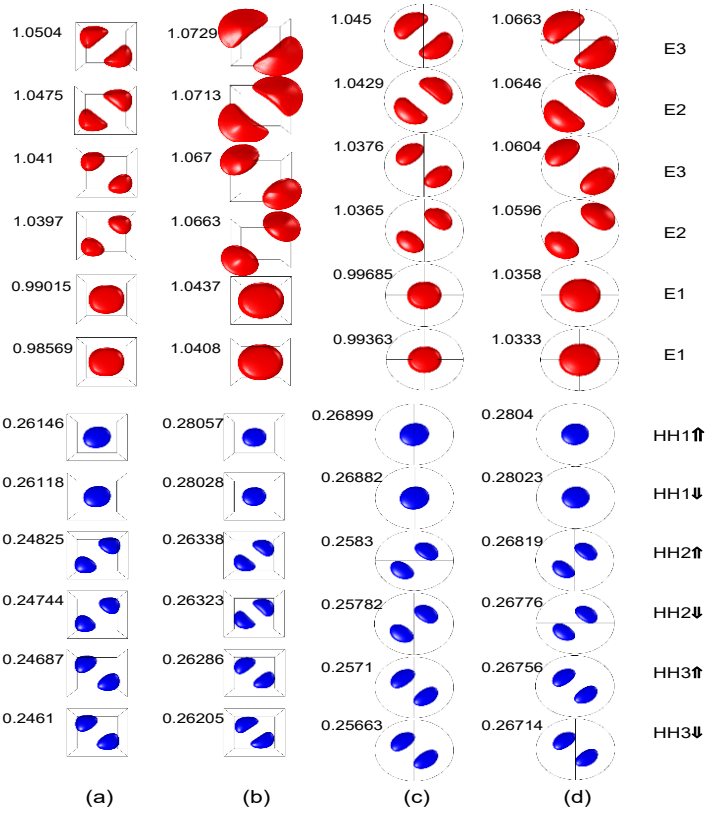

Fig. 4.7 Eigenstates and corresponding probability density isosurfaces for s- and p-like orbitals of the bound electron (red) and hole (blue) in (a) TP QD using two-step model, and (b) using one-step model, and in (c) FL QD using two-step model, and (d) using one-step model. Energy values are given in eV. The isosurfaces enclose 50% of the probability densities.

The energy difference between the two bright excitonic states (↓⇑ and ↑⇓), referred to bright exciton splitting (BES), is related to the confinement potential anisotropy [76, 176-178]. The two fundamental transition energies ↓⇑ of 0.72423 eV and ↑⇓ of 0.72897 eV for TP QD [Fig. 4.7(a)], or ↓⇑ of 0.72464 eV and ↑⇓ of 0.72803 eV for FL QD [Fig. 4.7(c)] is calculated using the two-step model. Correspondingly, the obtained transition energies using the one-step model are 0.76023 and 0.76342 eV [Fig. 4.7(b)], and 0.7529 and 0.75557 eV [Fig. 4.7(d)] for the two QD shapes. Thus, the BES calculated using the two-step model is 4.7 meV and 3.4 meV for the TP and FL QD shape, respectively, considerably larger than that calculated using the one-step model with which the BES

is 3.2 meV and 2.7 meV for the TP and FL QD shape respectively. The larger BES from the two-step model may offer a possible way to explain a partial source of optical spectrum-splitting phenomenon found in semiconductor QD lasers emission, which has excited a lot of interests for a while.

To our best knowledge, the study of fine structure is generally for the single-quantum-dot-based applications such as qubit [179, 180]. For the semiconductor lasers with a huge number of quantum dots, the "gap" in optical spectrum arising from the splitting is supposed to be easily smoothed out by homogeneous broadening effect, since the calculated BES is very small [76], and even zero (degenerated ground state) according to the previous works using the conventional one-step model [36, 78, 131]. Therefore, despite a lot of hypotheses proposed about the ground state spectrum-splitting (GSSS) occurring in self-assembled QD based semiconductor lasers [181-184], none of them has connected this phenomenon with BES. In this work, a BES energy of ~5 meV corresponding to ~10 nm of wavelength in emission spectrum around 1550 nm is found from the two-step model. This result is in a good agreement with the ones given in [181-183], in which the spectral separations between first and second peaks are ~10 nm at low injection experimentally. Thus, the larger BES in two-step model becomes a possible way to explain the GSSS phenomenon.

4.3.2 Dimensional evolution of single QD

The exact dependence of average base diameter and dot height of self-assembled InAs/InP QD was not included in previous sections. Instead, a variation range of base diameter was given for the sake of error estimation, when the dot height was varied. However, some study (e.g. QD stack in Sec. 4.6) requires a more precise description of QD dimensional evolution is crucial for further investigation. It is noteworthy that Schliwa *et al.* have found that the separation between GS and ES is correlated to the dimensional evolution in self-assembled InAs/GaAs QD, and when the base length is increased in 2- or 3-ML steps with increase of dot height in 1-ML step, their calculated GS-ES energy separation agrees well with the experimental results at LT, which demonstrated a

nearly constant GS-ES energy separation as a function of dot height [149].

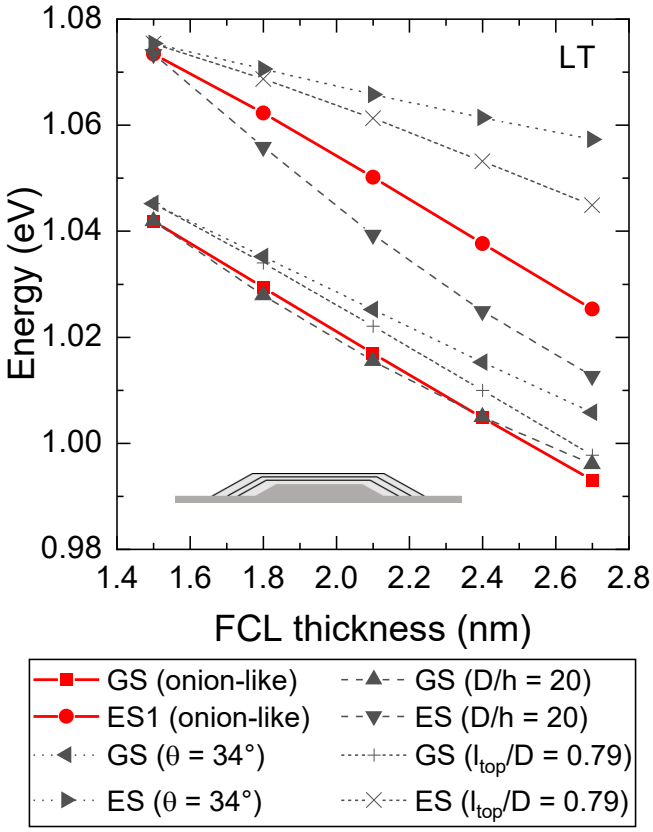

Fig. 4.8 Simulated energies of the GS and the first ES (ES1) in TP InAs/1.15Q QDs as a function of FCL thickness. The red symbols refer to a series of five QDs with an onion-like dimensional dependence of *D* and FCL thickness, i.e. *D* increases in 8-ML steps with the increase of FCL thickness in 1-ML steps. The results are compared to other three cases as shown in the legend, which disagree with our presumption of constant GS-ES energy separation.

Although there is a lack of experimental and theoretical evidence for the InAs/InP counterpart, we might make a bold presumption that, for InP based QD, there is a similar constant GS-ES energy separation at LT as well. Based on the parameters given in Table 4.1 and our trial and error simulations, as shown in Fig. 4.8, a resemble onion-like dimensional dependence of average base diameter and dot height is found, as the former increases in ca. 8-ML steps with increase of height in 1-ML steps. The fitting function is expressed by

$$D = 30 + (h - 1.5)/0.12. \tag{4.8}$$

In addition, the fitting function Eq. (4.8) perfectly agrees with the experimental observations: When the average QD height is varied in the range of 1.5 to 2.7 nm, the variation of dependent base diameter is kept in the range of 30 to 40 nm [35]. This aspect ratio suggests InP based QD has much more flat shape compared to GaAs based counterpart, in agreement with the observations to these two types of self-assembled QD.

4.4 Optical Properties

4.4.1 Impact of FCL thickness

To illustrate the influence of the FCL thickness on the RT PL characteristics, we consider many FCL thicknesses but a constant total CL thickness (10 nm). Note the QD growth is finite, as reported by J. M. Ulloa *et al*, a maximum possible height 3.5 nm could be reached, in other words, the FCL thickness and QD height are no longer relevant for the FCL thickness larger than 3.5 nm since a thicker FCL will bury the most of QD completely and invalidate the double-cap [37]. However, we actually presume that the detuning begins when the FCL thickness increases to around 2.7 nm, after carefully observing S. Luo and coworkers' measurement results: The blue-shift of PL peak wavelength drastically slows down, and the PL full width at half magnitude (FWHM) rises rapidly as the FCL reaches beyond 2.7 nm [40]. It is suggested that the majority of QDs stop growing when their heights reach 2.7 nm. As most of QDs are buried before the accomplishment of FCL, the uniformity of QD heights is lost. This increased fluctuation leads to the detuning between the FCL thickness and the transition energies, as well as the increased PL FWHM. The possible distribution of dot heights is illustrated in Fig. 4.9.

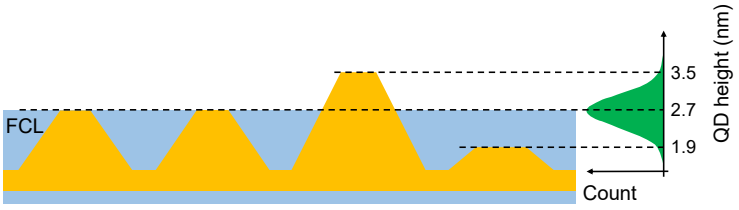

Fig. 4.9 Schematic illustration of a possible distribution of QD heights when continuous capping is applied during fabrication, the same as the case of sample G in [35].

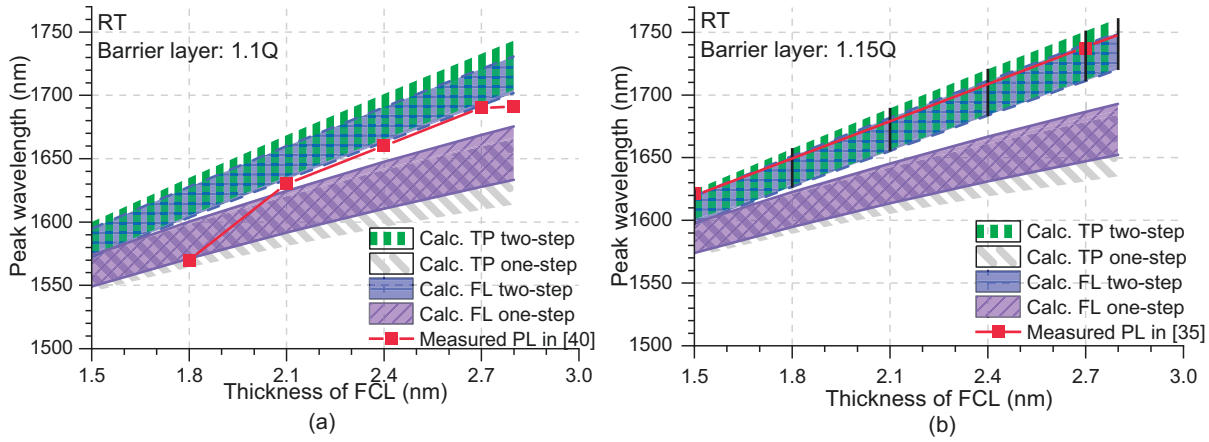

Fig. 4.10 Comparison of transition energies (RT PL peak wavelengths) between calculated values and experimental data in [40] and [35] of (a) QD surrounded by 1.1Q and (b) QD surrounded by 1.15Q. The patterned area denote the tunable ranges of PL peak wavelengths calculated in TP and FL QD by using two-step model and one-step model, respectively. Error bars in (b) denote simulation results of TP QD two-step model with exactly the same quaternary material (x = 0.184, y = 0.392) described in [35] for the sake of accuracy. The tunable ranges calculated by using one-step model show a deviation from the measurements results.

Based on above presumption, a range from 1.5 to 2.8 nm of FCL thickness is selected in the simulation with the two models, and then the results are compared with the RT PL measurement results, which is shown in Fig. 4.10. The shadowed/patterned area denotes the tunable ranges of PL peak wavelengths calculated from the fundamental transition energies ↓⇑ at 300K. The upper and lower margins of these area are determined by the tunable ranges from QDs with the same dot height but with the largest and smallest base size, i.e., a diameter of 40 nm and 30 nm, respectively. As shown in Fig. 4.10(a) and (b) for both 1.1Q and 1.15Q barrier material, respectively used in the two models, the results calculated by the two-step model (patterned in green vertical stripes for TP QD and translucent blue with dotted borderline for FL QD) are in better agreement with the experimental data (red dots) in each comparison. By contrast, no matter which shape of the QD is, the fundamental transition energies calculated by using the one-step model (patterned in grey diagonal stripes for TP QD and translucent purple with solid borderline for FL QD) are much larger than the measured ones. These deviations are getting larger with the increase of average dot height

or FCL thickness. Note that since the 1.15Q used by P. J. Poole and coworkers is slightly different from the above calculated one (x = 0.184, y = 0.392 versus x = 0.182, y = 0.397) [35], error bars are calculated and shown in Fig. 4.10(b), for the sake of accuracy. The result suggests a negligible difference in between.

It is seen that the measurement data are closer to the lower and upper margins of the tunable range in Fig. 4.10(a) and (b), respectively, suggesting that the average diameters of the dot bases in two settings are approximately 30 nm and 40 nm, which coincide with the descriptions about the QD size in [40] and [35], respectively. It is also indicated that the shape is not a key point since almost the entire tunable ranges from FL QD (patterned in translucent blue with dotted borderline) is overlapped by which from TP QD (patterned in green vertical stripes) both in Fig. 4.10(a) and (b).

4.4.2 Impact of SCL thickness

Boundary condition (BC) used for the study of the capping layer is needed to define first. The type of BC defines the constraint at each boundary applied to the wavefunctions of electron and hole. As the top boundary of capping layer (or of uppermost barrier layer) may be very close to targeted QD (e.g. down to 3.5 nm away from the top interface of dot/barrier matrix), the impact of different BCs applied to this top boundary should be taken into account. Here, closed BC stands for the Dirichlet BC being applied to all outermost boundaries, and open BC stands for no treatment of BC being applied to the top boundary (i.e. considered as an internal interface or so-called Neumann BC), and the other boundaries are considered closed BC.

It is significant to clear up at this stage the wholly capping thickness T_c (i.e. FCL plus SCL) dependence in single QD. In this subsection, the influences of T_c on the strain field and single-particle electron (hole) GS are studied, by using both the two-step and one-step method (for reference) when single QD is *deeply* buried. Fig. 4.11(a) and (b) present the evolution of strain tensors ϵ_{zz} and ϵ_{xx} ($\equiv \epsilon_{yy}$) along (001) through the center of QD, with T_c = 5, 10, and 25 nm,

calculated by the two-step and one-step model. Basically, the ϵ_{xx} along (001) does not exhibit obvious change with the varied capping layer thickness for both models. Therefore, it can be deduced from Eqs. (2.24)−(2.28) that the strain effect on electronic structure is mainly determined by ϵ_{zz}, thus we only discuss the evolution of ϵ_{zz} hereinafter.

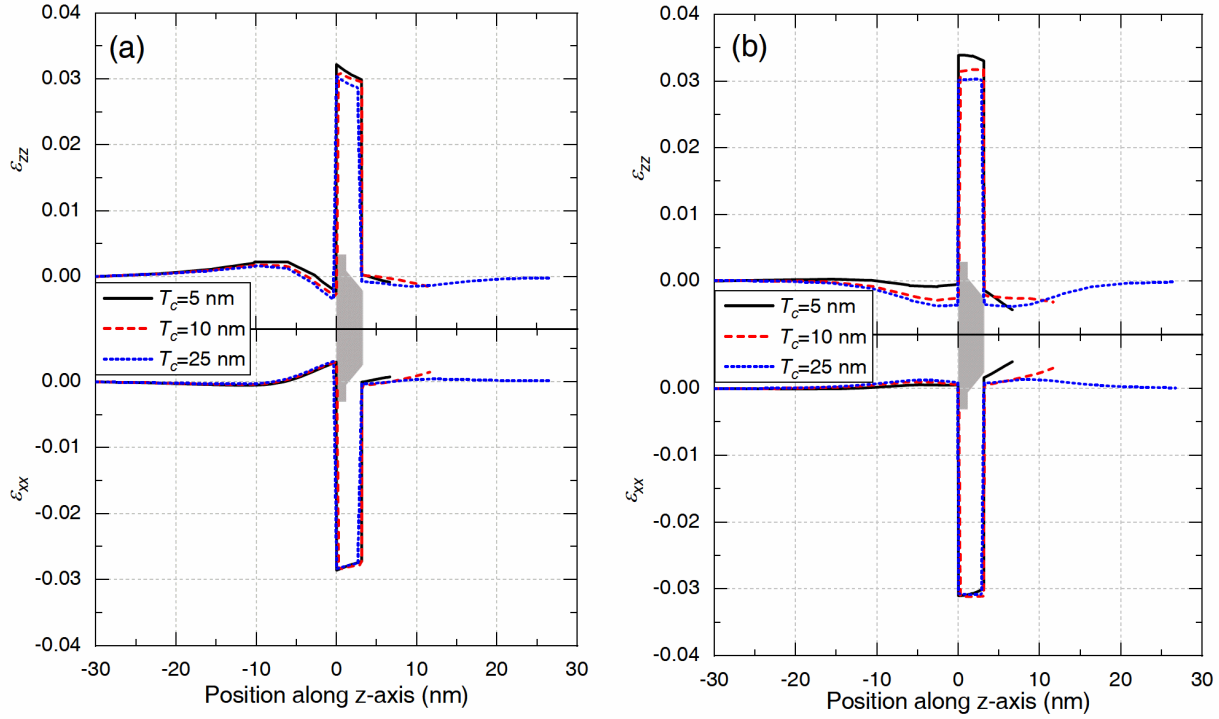

Fig. 4.11 Evolution of strain tensors ϵ_{zz} and ϵ_{xx} along (001) through the center of a single QD, with T_c = 5, 10, and 25 nm, calculated by (a) two-step and (b) one-step model. ϵ_{zz} in upper and ϵ_{xx} in lower figure.

Three distinct features are exhibited from the two-step model in Fig. 4.11(a) compared to the one-step model in Fig. 4.11(b), as the latter two features lead to the different symmetry properties in the strain profile of these two models:

a) Both of the two models show a decreasing tensile strain and increasing compressive strain with the increase of T_c. However, the one-step model results in a much higher sensitivity to T_c than the two-step model, particularly when T_c varies between 5−10 nm (see the black solid and red dashed lines in Fig. 4.11).

b) A much faster relaxation of strain beneath the WL/barrier interface (i.e. below the QD bottom)

is observed in Fig. 4.11(a), i.e. the two-step model, leads to relax rapidly over a distance of ca. 5 nm, and at away from the interface of ca. 5 nm, the compressive strain is transited to tensile strain. Instead, by the one-step model, the compressive strain gradually decreases to zero from the interface till ca. 20 nm away from the interface.

c) A smaller compressive strain (ca. 50%) and a slower relaxation (ca. 20 nm) in the capping layer (i.e. above the QD top) are observed from the two-step model compared to the one-step model, and also the strain profile obtained by the one-step model is almost the same at both the QD bottom and top, i.e. like a mirror image as shown in Fig. 4.11(b). Notably, this strain profile asymmetry, as shown in Fig. 4.11(a), only obtained by the two-step model, agrees better to the experimental results of strain profile along (001) obtained by the high-resolution HAADF STEM [185].

Fig. 4.12(a) and (b) show the calculated single-particle GS energy and PL peak wavelength corresponding to the separation of electron-hole GS energies of series "1+0" using both two-step and one-step model. As shown in Fig. 4.11 that the strain profiles are different from each other, but a very similar behavior of single-particle energy as a function of T_c is found for the two models as shown in Fig. 4.12(a): On the one hand, the lowest electron state energies (E1 in Fig. 4.12(a)) from both models decrease rapidly with the increase of T_c from 5 to 10 nm, and are almost constant when T_c varies between 10−30 nm. The highest hole state energies (H1), on the other hand, slightly decrease consistently with the increase of T_c. Moreover, the electron and hole state energy are smaller using the two-step model compared to the one-step model, in particular for electron state. Correspondingly, Fig. 4.12(b) shows the PL peak wavelength versus T_c, for which closed and open BC both are considered for vision of the boundary impact. It is seen that a redshift is found when T_c varies from 5 to 10 nm, and then a consistent blueshift is obtained when T_c exceeds 10 nm by both models with the closed BC. This red- and blue-shifting behavior agree to the experimental observation [186]. This intriguing phenomenon, to our best knowledge, has not been commonly mentioned and predicted in the published theoretical works. On the contrary, the above PL

wavelength behavior with T_c is not predicted by the two models with the open BC.

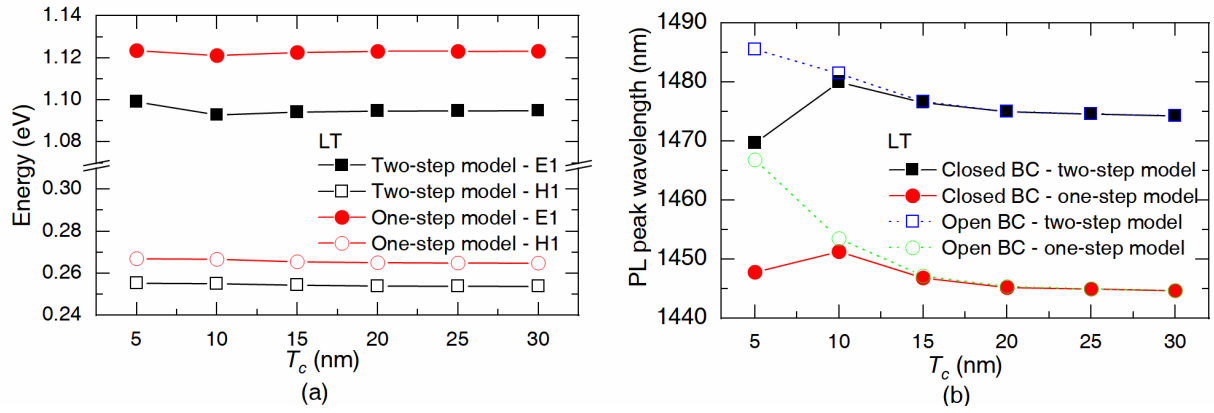

Fig. 4.12 (a) Calculated single-particle GS energy and (b) PL peak wavelength (corresponding to the separation of electron-hole GS energies) of series "1+0" at LT, for which closed and open BC are applied to calculate the wavefunctions of electron and hole. E1 and H1 denote the lowest electron and highest hole state energies involved in the fundamental transition, respectively.

In Fig. 4.12(b), since the closed and open BC, only differ at the top boundary of the capping layer, the PL peak wavelength behavior in Fig. 4.12(b) is caused only by the top boundary difference. Next, the impact of T_c on electron and hole will be discussed, which is used to explain the impact of the BC. The electron behavior is originated by the comparatively small effective mass that results in a much larger barrier penetration and thereby larger spread of wavefunction. When the top boundary with the Dirichlet (i.e. closed) BC is very close to the QD, i.e., the wavefunction of electron is forced to be zero at the top boundary, unlike the case of open BC in which the continuity of wavefunction is retained at both sides of the interface. In other words, the electron is more localized for the smaller T_c, leading to an increased kinetic energy. At away from the top boundary, the localization effect of electron is reduced, and a PL redshift is expected until the boundary is far away enough so that the localization effect is negligible [see the solid lines in Fig. 4.12(b)]. The localization of hole, on the other hand, is less affected by the increase of T_c, or mostly compensated by the increasing strain effect, due to its weaker barrier penetration. In fact, the hole state is more susceptible to the increasing mass of the capping layer, thereby the enhanced

confinement introduced by the strain effect, which is the main reason for spectral blueshift, determines the behavior of PL peak wavelength versus T_c [187]. This explanation is evidenced by applying open BC to the top boundary [see the dotted lines in Fig. 4.12(b)]: The spectral redshift is not predicted when there is no barricade of wavefunction from freely spreading out through the top boundary, i.e., the capping/air interface. However, this open BC at capping/air interface is not the fact in the real world, as the electron needs very high energy to escape from semiconductor. Therefore, *the closed BC will be used in the following study*.

4.4.3 Impact of barrier composition

To investigate the correlation between the composition and the electronic band structure in QDs, the arsenic mole fraction y is swept from zero to one, with the FCL thickness and base diameter fixed to 2.7 nm and 30 nm, respectively.

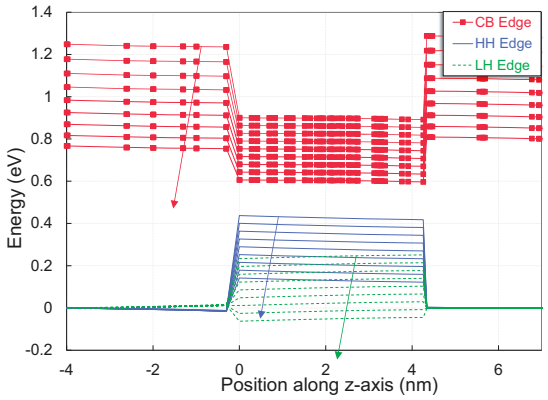

Fig. 4.13 CBE (red lines with square marks), HH (blue solid lines), and LH (green dotted lines) band edges are dropped down gradually with the increase of arsenic mole fraction *y* from 0.1 to 0.9 in the barrier layers.

Fig. 4.13 presents how the barrier composition affects the CBE, HH, and LH band edge. All of CBE, HH, and LH band edges are dropped down gradually with the increase of arsenic mole fraction y in the barrier layers. The explanation is followed. Firstly, with the unstrained VBE fixed to zero in barrier layer, the increase of y converts to the decrease in the VBE in the QD, due to the

nearly linear dependence between *y* and the VBO of InGaAsP/InP, and the constant VBO of InAs/InP at RT. Then, it also results in a CBE drop due to the constant bandgap energy of InAs at RT. However, the amounts of drop are different between the CBEs in two materials of heterostructure, since *y* and the bandgap energy of InGaAsP are not linearly dependent. As shown in Fig. 4.13, the CBO of InAs/InGaAsP also declines.

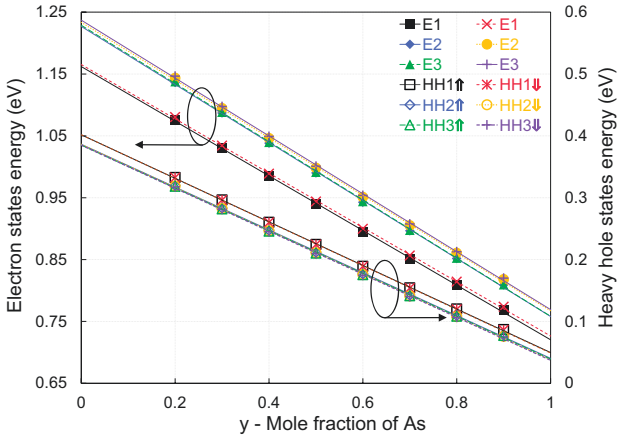

Fig. 4.14 Electronic fine structure as a function of arsenic mole fraction *y* in quaternary alloy of the barrier matrix. The *y*-axis on the left and right denote the energy tuning ranges for CBE and HH band edges, respectively.

The case is more complex as to the energy states of electrons and holes. Obviously, the lower CBE and VBE bring down the state levels of electrons and holes simultaneously. However, the electron states drop faster than hole states, as shown in Fig. 4.14, which is in agreement with the decline in CBO. This leads to a redshift in peak wavelengths of RT PL. A tuning range from 1630 nm to 1840 nm is obtained in this TP QD (h = 2.7 nm, D = 30 nm).

Fig. 4.15 shows that the BES energy is linearly tuned by arsenic content of quaternary InGaAsP used in barrier layer. A tuning range from 3.5 meV to 6.8 meV is observed. Since new applications associated to GSSS have already emerged such as dual-mode-locking [181] and pulse-width-narrowing [188], the BES simulation results can be used in future fabrications of mode-locked QD lasers.

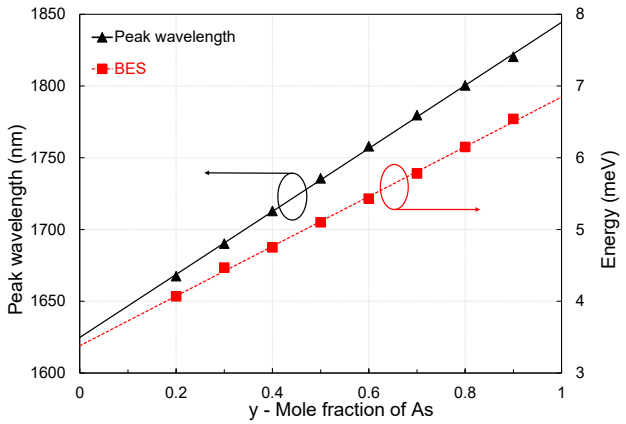

Fig. 4.15 Calculated RT PL peak wavelengths and bright exciton splitting energies as a function of arsenic mole fraction *y* in the quaternary alloy of barrier matrix. The *y*-axis on the left and right denote the RT PL peak wavelengths tuning range and BES energies tuning range, respectively.

4.5 Lateral Coupling among Neighboring QDs

In this section, we present a comprehensive study of the interaction of QDs at RT considering inter-dot distance in paralleled coupling, in tilted coupling, and QD size homogeneity affecting on the coupling. The InAs QDs on a 3.2-ML WL are capped with two 1.25Q InGaAsP (x = 0.253, y = 0.55) capping layers, composed of a thin FCL and a thick SCL controlling the QD height. The QD height h and surface ratio l_{top}/D are fixed to 1.5 nm and 0.65, respectively. The total lengths of the substrate in x- and y-directions are 75 nm and 59 nm in the calculation, which is considered big enough given by the practical size of QDs. A side view of two QDs overlapping with each other is shown in Fig. 4.16. Parameters and interpolation are the same as ones given in Table 4.1.

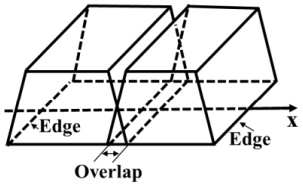

Fig. 4.16 Schematic side view of a big QD (*left*) and a small QD (*right*) overlapped.

4.5.1 Impact of paralleled coupling

Only the GS of electrons and holes of the composite system are our focuses in this section. First, the effects of overlapping of two TP QDs have a square base with a base length of 19 nm (big dot) and 17 nm (small dot) [as shown in Fig. 4.17(a)] are simulated. Fig. 4.17(b) shows the PDF and eigenvalues of the GS of electrons and holes for the two dots overlapped by 10, 8, 5, 4, 3, and 2 nm as well as separated by 2 nm. It can be noticed that the high PDF (i.e. light black area) of electrons is concentrated together, and two dots are like one big dot, but the transition energy is lower than that of the single big dot when the overlap is higher than 5 nm. This suggests that the electronic coupling between the two QDs is high. The electronic coupling then decreases obviously as the overlap reduces, and the location of the high PDF of the GS tends to shift from the middle of the two QDs to the center of the big QD, while the PDF in the small QD gradually decreases to a low level. The high PDF starts showing discontinuity at the 4 nm overlap and becomes extremely tiny in the small QD at the 3 nm overlap. At the 2 nm overlap, the high PDF does not exist in the small QD anymore, which means that the chance of finding electrons in the small QD is very low. When the two dots are separated by 2 nm, only low PDF (i.e. blue area) is left in the small QD, indicating that it is almost impossible to find electrons in the small QD in this case. This is quite different from the single small dot as shown in Fig. 4.17(a).

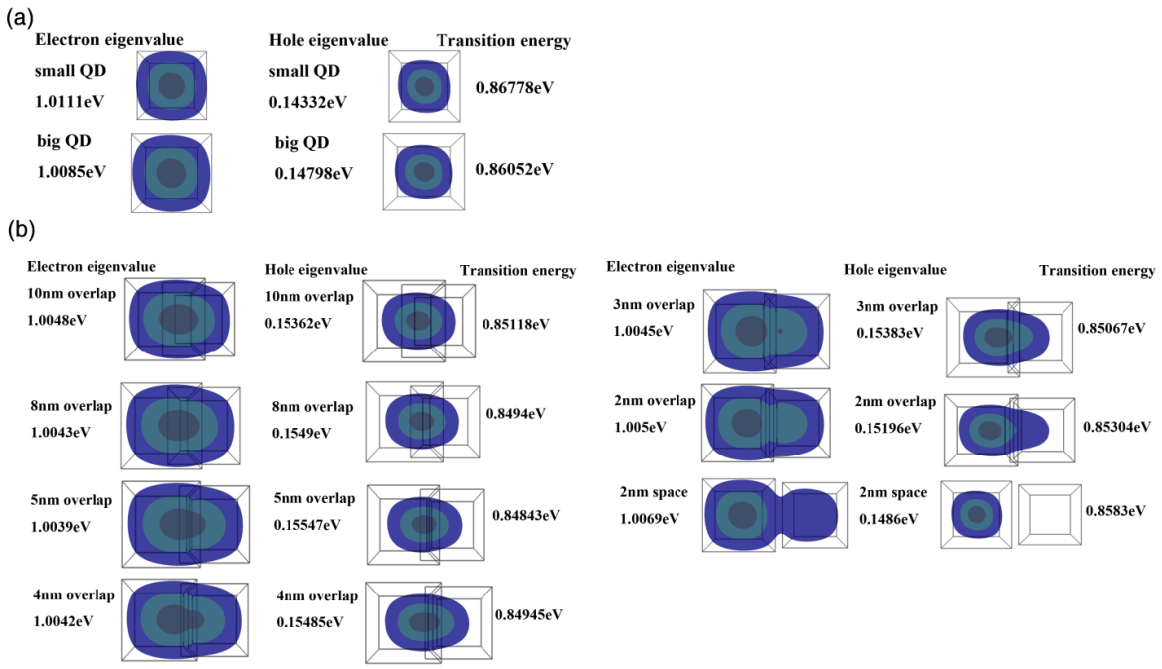

Fig. 4.17 (a) Probability density isosurface in the *x-y* plane and corresponding eigenvalue of the GS for electrons (*left column*) and holes (*right column*) for small and big isolated single QD, and (b) for two dots overlapped by 10, 8, 5, 4, 3, and 2 nm as well as separated by 2 nm. Four colors represent different levels of PDF (light black: 100%, green: 70%, blue: 40%, white: 0%).

4.5.2 Impact of tilted coupling

Next, the effects of relatively tilted QD positions are studied, as two QDs with offsets in *y*-axis direction are considered. The two dots overlap are fixed to be 3 nm. Fig. 4.18 shows the PDF distribution of the GS electrons and holes for the two dots with offsets of −1, 4, 9, and 14 nm (the negative means opposite offset) and corresponding eigenvalues of electrons and holes as well as transition energy are also given. As the offset increases from -1 nm to 9 nm, the medium PDF area (green) of electrons reduces by half in the small QD, and the medium PDF area (green) of holes in the small QD reduces as well. Moreover, the medium PDF almost disappears in the small QD when the offset is 9 nm and above, and in fact only a tiny low PDF (blue) of holes is left in the small QD. When the offset is 14 nm, only the low PDF (blue) of electrons in the small QD is left, and the low PDF (blue) of holes in the small QD completely disappears. The above clearly shows that

the high PDF of either electrons or holes is dominated by the big QD, which means that most photoemissions are created by the big QD rather than the small QD. The transition energy increases towards the energy of the single big QD as the offset increases, which is due to the reduced coupling between the two QDs. The transition energy within the 15 nm offset (from −1 to 14 nm) is increased by around 0.00934 eV, which corresponds to 15.83 nm wavelength blue shift.

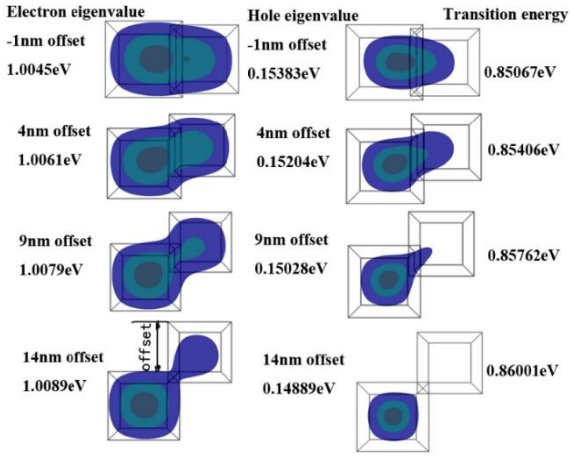

Fig. 4.18 Probability density isosurfaces in the *x-y* plane and corresponding eigenvalue of the ground states for electrons (*left column*) and holes (*right column*) at an offsets of −1, 4, 9 and 14 nm.

4.5.3 Impact of size homogeneity on coupling

Finally, the interaction of two dots with different sizes is investigated. The left dot in Fig. 4.17(a) with a base side length of 19 nm is fixed, while the base side length of the right dot is varied. The overlap and surface ratio are fixed to be 4 nm and 0.65, respectively. Fig. 4.19(a) shows the PDF of electrons and holes for the right dot with side base length of 21, 19, 17, 15, and 13 nm. An obvious trend can be seen that the high PDF of both electrons and holes gradually shifts from the small dot to big dot. When the two dots have the same size, the high PDF area is divided equally, which is different from Ref. [189]. Whenever the two QDs are different enough in size such as 21 nm, 15 nm, 13 nm in Fig. 4.19(a), the high PDF always tends to stay in the bigger QD, which suggests that most of the photoemissions of the GS come from the bigger QD, which was also

shown in [189]. As expected, the transition energy increases as the small QD decreases in size. The transition energy within 8 nm change of the base side length of the small QD is increased by around 0.00781 eV, which corresponds to 13.42 nm wavelength blue shift.

Instead of having two QDs with different sizes close to each other, there could also be multiple QDs surrounding each other. Fig. 4.19(b) presents the PDF of the GS electrons and holes for three QDs with a base length of 19, 16 and 13 nm, which are overlapped with each other as indicated in Fig. 4.19(b). Such a structure of the three-QDs can be equivalent to a large QD with irregular shape. Similar to the two-QDs, the high PDF of the GS always tends to stay in the biggest QD, independent of where the biggest QD is (center, left or right) and how big the overlap is. The high PDF of electrons can cover almost the entire area of the PDF of holes, which means there is very high spatial overlap between each other, leading to strong photoemission.

However, the above observation may not apply to the first ES of those structures. Neglecting the details of energy levels, Fig. 4.19(c)−(f) phenomenologically shows the PDF distribution of the first ES electrons and holes for the three dots and two dots overlapping. The overlaps are indicated in Fig. 4.19(c)−(f). The high PDF tends to locate in the small QD, different from the GS. But obviously, it is seen that the high PDF of electrons always tends to stay towards the edge of the QD structure, while the high PDF of holes tends to stay towards the center of the QD structure. This spatial difference greatly reduces the spatial overlap between each other. Thus the photoemission from the small QDs is suppressed. This finding can offer a further explanation for the previous experimental results reported in [35], where the peak wavelength shifted to the longer wavelength region was discovered when the dot density of QDs grown by double-capping procedure was increased. Apparently, the higher the dot density is, the closer the QDs are to each other, which increases the chance of QDs overlapping with each other and leads to the reduction of the independent photoemissions from small QDs. This also explains why most of the experimental results in [35, 40, 51] showed the tendency of shifting to longer wavelength (red shift) region in the PL spectrum.

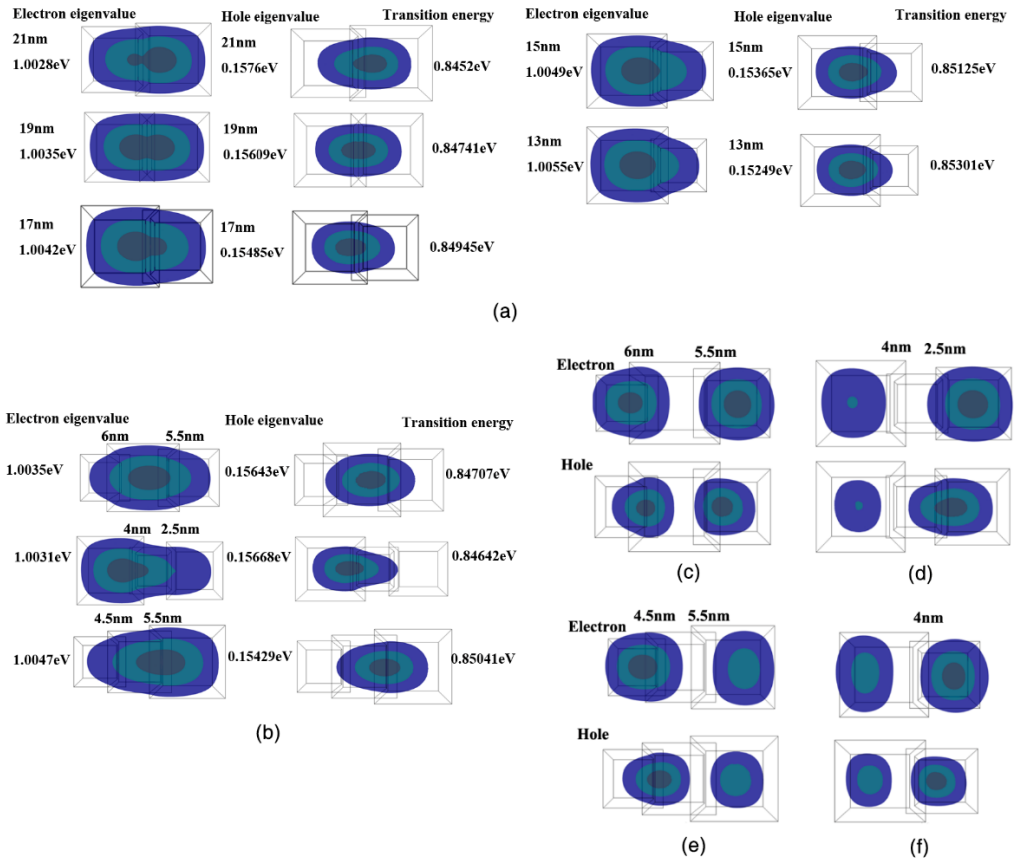

Fig. 4.19 Probability density isosurface in the *x-y* plane and corresponding eigenvalue of the ground states for electrons (*left*) and holes (*right*) for the two dots with base side length of 19 nm (*left dot*) and (a) 21, 19, 17, 15, and 13 nm (*right dot*), and the overlap of 4 nm; and (b) for the three QDs with base side lengths of 19 nm, 16 nm, and 13 nm and overlaps indicated in the figure. (c)−(f) Probability density isosurface of electrons (*top*) and holes (*bottom*) of the first ES for the three dots (base length of 19 nm, 16 nm, & 13 nm) with the big QD at (c) left, (d) center, (e) right of the three QDs; and (f) two QDs (base length of 19 nm, & 15 nm) with the big dot at left.

4.6 Vertical Coupling among Stacked QDs

In this section, the vertically stacked self-assembled dots are investigated in detail, which exhibits much richer tunability of optical characteristics compared with the counterpart of laterally coupled ones, as introduced in last section [190], due to the interplay of its three principal coupling mechanisms, viz. strain coupling, resonant electronic coupling, and nonresonant quantum

tunnelling. The coupling physics and electronic/optical properties of vertically stacked self-assembled dots have been theoretically studied intensively [73, 83, 149, 191-196], where symmetric strain profiles along QD growth direction are generally predicted by using the conventional strain model. The symmetric strain profiles in these works calculated by the so-called one-step model always lead to symmetric vertical confinements and electronic band edges regardless of what the SLNs are considered. Nevertheless, the actual cross-sectional microscopy images of closely stacked QDs show an obvious nonidentical deformation from the lowermost to uppermost of QDs [108, 197, 198], which suggests asymmetric vertical confinement due to the cumulative strain along QD growth direction. The average deformation of the upper dots should depend on the SLN, which is not supported by the conventional one-step model. As the strength of electronic state resonance is closely related to this physical symmetry of quantum confinement along (001) and thus related to the strain, the latter should be studied carefully.

4.6.1 Structures to be investigated

In this subsection, we apply the multistep strain analysis method presented in previous sections to model a 3D self-assembled multilayer InP-based QD stack at LT, as the modeling follows the growth process to reproduce the realistic strain distribution. Based on the novel model, we investigate the influence of inter-dot distance (determined by spacer thickness in this section) on optical properties of a multilayer structure with vertically stacked QDs. Regarding the methodology, existing studies on the influence of spacer (specifically referring to the barrier layer sandwiched by two dot-layers) also include the contributions of capping layer (referring to the uppermost barrier layer), i.e., even for the same stacked QDs sample, different capping thickness can lead to different optical transition energy, and this impact should be excluded in investigation of spacer thickness (T_s). In our study, *the topmost QD is kept uncapped to avoid the influence of capping thickness* (T_c). With respect to the baseline setting, instead of modeling the single-particle electron and hole energies with a constant T_c for reference, we firstly calculate and obtain the

dependence of single-QD states with respect to T_c as a baseline, for the sake of isolating the coupling effect of neighboring QDs from the contribution of capping layer. Fig. 4.20 gives an overview of the investigated structure series featured by the SLNs/alignment conditions at LT.

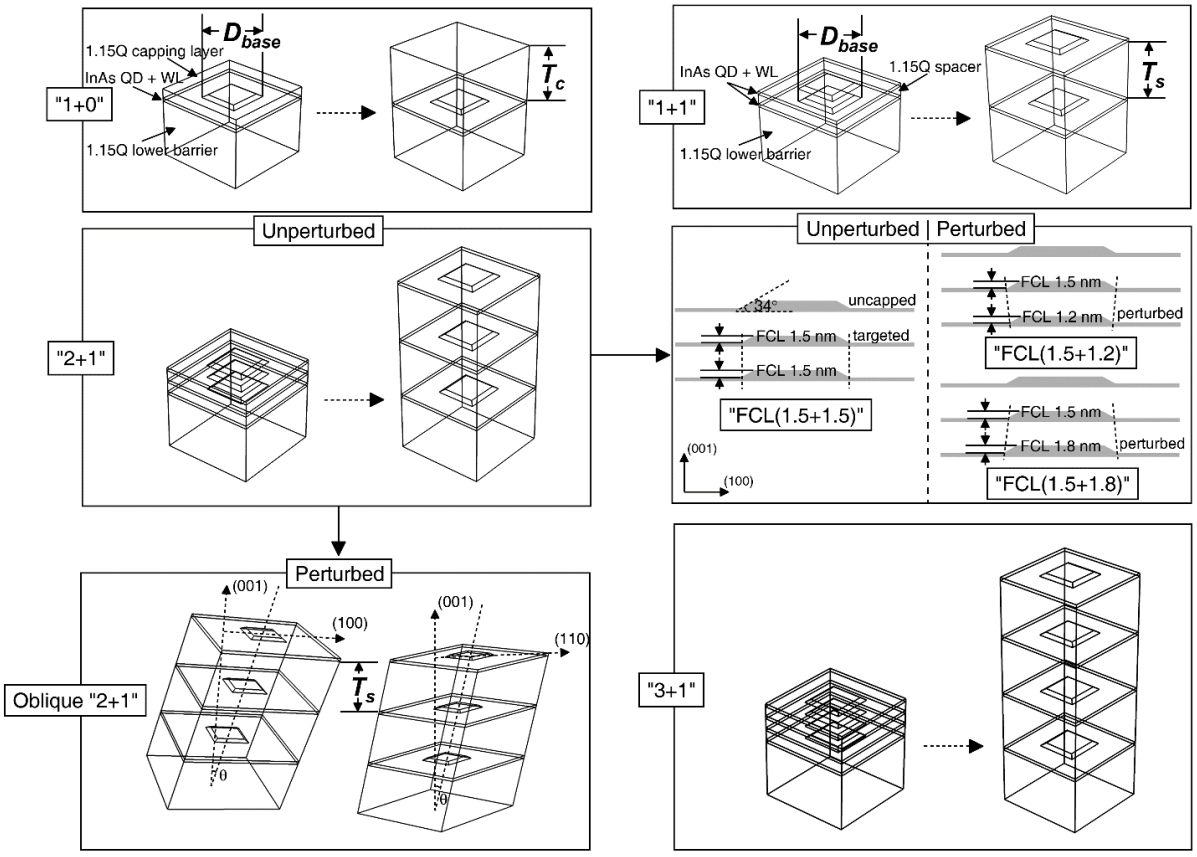

Fig. 4.20 Unperturbed and perturbed structure considered in this section.

a) *Series "1+0" (fundamental baseline).* A flat truncated-pyramidal InAs QD embedded in InP-lattice-matched quaternary $In_{0.816}Ga_{0.184}As_{0.392}P_{0.608}$ (1.15Q) capping layer with a varying T_c between 5−30 nm. If not specified, the default dimensions of QD in this study are as follows: first capping layer (FCL) thickness 1.5 nm, WL thickness 5.4 monolayers (MLs), base diameter (D_{base}, diagonal length of the square base) 30 nm, and base angle 34˚.

b) *Series "1+1".* Two-layer QD stack, in which the lower InAs QD is embedded in the 1.15Q barrier layer with a varying T_s between 5−30 nm, then the upper InAs QD is kept uncapped.

c) *Series "2+1".* Three-layer QD stack, in which the lower two InAs QDs with the default ["FCL(1.5+1.5)"] or perturbed height ["FCL(1.5+1.2)" and "FCL(1.5+1.8)"] (as shown in Fig. 4.20), are embedded in 1.15Q barrier layer with a varying T_s between 5−30 nm, then the upper InAs QD is kept uncapped. Note D_{base} in the perturbed structures is a variable as a function of the FCL thickness, which will be discussed at the end of this part.

d) *Series "Oblique 2+1".* By applying a small deviation from (001) direction on the structure "FCL(1.5+1.5)", with a deviation angle θ varying between 5−30˚, inclining along either (100) or (110) direction.

e) *Series "3+1".* Four-layer QD stack, in which the lower three InAs QDs with the default size is embedded in 1.15Q barrier layer with a varying T_s between 5−30 nm, then the upper InAs QD is kept uncapped.

Table 4.3 Material parameters used in the calculations at LT.

	Unit	InAs	$In_{0.816}Ga_{0.184}As_{0.392}P_{0.608}$ (1.15Q)
a	Å	6.0584	5.8671
ρ	kg/m^3	5668	5035.1
ε_r		14.55	12.6029
C_{11}	GPa	83.3	102.2693
C_{12}	GPa	45.3	54.4797
C_{44}	GPa	39.6	47.6632
e_{14}	C/m^2	0.045	–0.0253
B_{114}	C/m^2	–0.5	–0.8128
B_{124}	C/m^2	–4.1	–3.717
B_{156}	C/m^2	0.2	–0.3129
m_e	m_0	0.023	0.0709
γ_1^L		20.4	10.1338
γ_2^L		8.3	3.6388
γ_3^L		9.1	4.3085
a_c	eV	–10.2	–7.4567
a_v	eV	1	0.1511
b	eV	–1.8	–1.7428
d	eV	–3.6	–4.1450
E_c	eV	0.6230	1.1591
E_v	eV	0.205	0
Δ	eV	0.38	0.2089
E_p	eV	21.5	22.7372

The dimensional evolution of InAs/InP QDs is needed in this study, as introduced in Sec. 4.3.2. The material parameters used in calculations at LT are listed in Table 4.3 extracted from Table 4.1 for the convenience of reading.

4.6.2 Impact of vertical strain coupling

Fig. 4.11 in Sec. 4.4.2 shows that single-particle energy for a single QD structure is hardly affected strikingly by T_c, but the distinct asymmetric strain profile along (001) plays a vital role in the strain coupling for a multilayer QD stack. It is known that the interior strain of a central QD in a multilayer QD stack is superposed by the exterior strain of its upper and lower neighboring QDs.

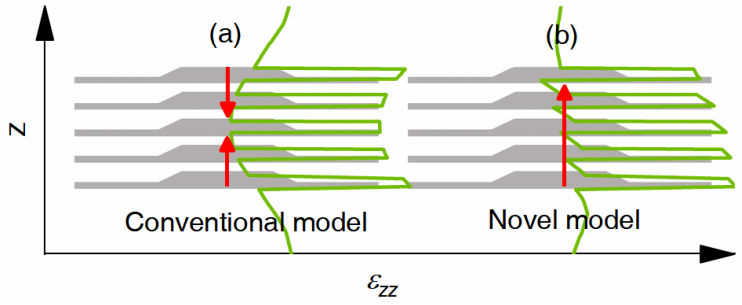

Fig. 4.21 Schematic illustration of (a) bidirectional and (b) unidirectional compressive strain accumulations for the conventional and our multistep (novel) model applied to a deeply buried stack of five dot layers, respectively. The red arrowhead lines visualize the cumulative direction, and the green lines indicate the total ϵ_{zz} along the growth direction.

The impact of strain distribution on the neighboring QD for the multi-layer stacking QD with multistep strain analysis differs from the one-step conventional model: For the conventional model, a symmetric superposed strain profile (e.g., see Refs. [195] and [196]), formed by the symmetric strain distribution along (001) of individual QD, results in a *bidirectional* accumulation of compressive strain with the increase of SLN, from the outermost (i.e., uppermost and lowermost) to the innermost (i.e., central). Therefore, the innermost QD is always the most significantly strained in all dot layers, as shown in Fig. 4.21(a). By contrast, intuitively, for the multistep model, a *unidirectional* accumulation of compressive strain with the increase of SLN from the lowermost

to the uppermost QD, e.g. see Fig. 1.9(i) as an example of uneven size distribution resulting from such unidirectional strain accumulation. This uneven growth results from the asymmetric strain distribution, i.e. the lower QD has a larger impact on the upper QD by compressive strain. The cumulative strain remarkably affects the uppermost QD, as shown in Fig. 4.21(b). This upwardly cumulative strain may not be completely relaxed in very thin barrier layers, and thus a very rough surface is formed, resulting in a stop of QD formation after 4 or 5 stacked layers for InAs/GaAs system [199].

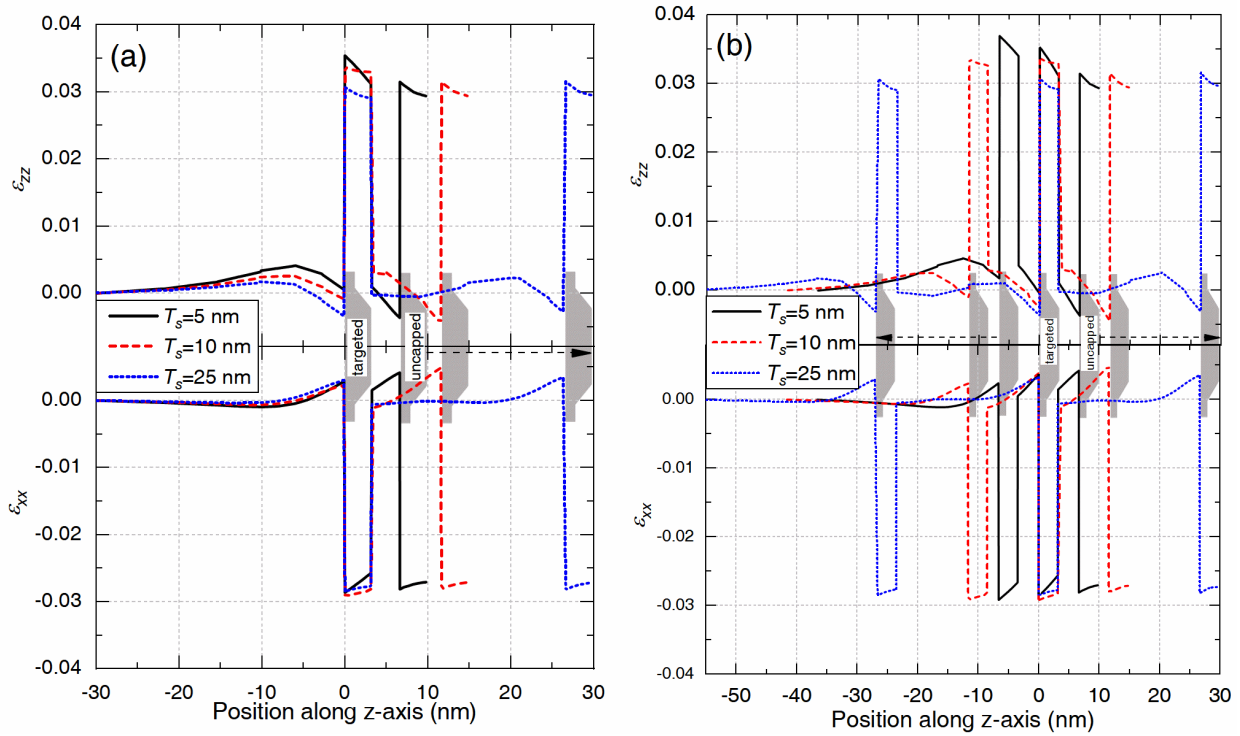

Fig. 4.22 Evolution of strain tensors ϵ_{zz} and ϵ_{xx} along (001) through the center of stacked QDs, at T_s = 5, 10, and 25 nm for (a) series "1+1" and (b) series "2+1" at LT. For the latter, strain profiles are aligned with respect to targeted QD to show the impact clearly.

To understand the impact of the inter-dot distance, the evolution of vertical strain coupling for the series "1+1" and "2+1" are studied carefully, as shown in Fig. 4.22(a) and (b), respectively. Similar to the single dot, the ϵ_{xx} in stacked dots exhibits a negligible effect on the electronic band edges, as shown in Fig. 5, and thus the evolution of ϵ_{zz} versus T_s will be only discussed hereinafter. The series "1+1" in Fig. 4.22(a) illustrates how the upper uncapped QD affects the lower targeted

QD as a function of T_s: For closely stacked scenario (T_s = 5 nm), at the top, the targeted QD is affected by the compressive strain introduced by the upper QD; while at the bottom, on the other hand, the targeted QD is affected by the tensile strain, resulting in a strain profile with a tilted top in the dot [see the black solid line in Fig. 4.22(a)]. When T_s is getting larger (e.g., 10 nm), the targeted QD is only affected by the tensile strain at both of the top and bottom, leading to a more homogeneous strain distribution in the dot [see the red dashed line in Fig. 4.22(a)]. As the upper QD keeps being further away, the tensile strain is gradually out of reach, reducing the magnitude of strain in the targeted QD [see the blue dotted line in Fig. 4.22(a)]. This decrease of tensile strain in the dot corresponds to an increase of the conduction band edge and electron energy as well. Similarly, the series "2+1" in Fig. 4.22(b) presents how the outermost neighboring QD concurrently affects the innermost targeted QD as a function of T_s: The compressive strain provided by the lowermost QD partially compensates the tensile strain. Apparently, this compensating effect is comparatively more constant for T_s in 5−10 nm and disappears for T_s = 25 nm.

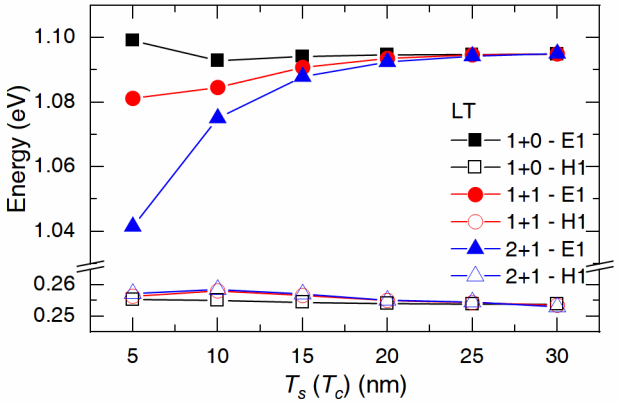

Fig. 4.23 Evolution of electron and hole GS energies as a function of T_s (or T_c) in targeted QD for series "1+1" and "2+1" at LT, with series "1+0" serving as a baseline for the sake of comparison.

Fig. 4.23 shows the evolution of electron and hole GS energies as a function of T_s (or T_c) in the targeted QD for series "1+1" and "2+1", with the series "1+0" serving as the baseline (see the black lines with square marks in Fig. 4.23, which is calculated in Sec. 4.4.1). Note since no electron

or hole is trapped in the topmost uncapped QD; there is no recombination or emission occurring in this layer. The calculations of piezoelectric potential and electronic band structure are only taken into account for the lower (two) QD(s). As analyzed in the last paragraph, an expected lowering of the electron GS energy (by 15 meV for T_s = 5 nm) with respect to the baseline can be seen in the series "1+1", and this lowering gradually vanishes with the increase of T_s (see the red lines with circular marks). However, surprisingly, the expected lifting of electron GS energy for the series "1+1", introduced by the compensating effect of tensile strain as analyzed in the last paragraph, is *not* seen in the series "2+1". On the contrary, a drastic decrease by 40 meV for T_s = 5 nm is shown, probably attributed to the electron coupling between the lower two QDs. Thus, it is necessary to investigate the resonant electronic coupling effect, which will be discussed in the next section.

4.6.3 Impact of unperturbed/perturbed electronic coupling

Let us first recapitulate the most three significant factors for the strength of electronic coupling: (1) The similar energies of single-QD states for resonance (i.e., resonance condition), (2) the spatial overlap of wavefunctions, and (3) the same-sign (in-phase) wavefunction overlap (i.e., symmetry condition). In general, the electronic coupling of QDs results in a formation of bonding and antibonding electron states, and the total number of formed electron s-orbital state equals to the SLN (e.g., one bonding and one antibonding s-orbital states for two coupled QDs). Besides, the bonding GS has smaller single-particle energy than the uncoupled single-QD GS, which is the reason for unexpected lower GS energy observed in the series "2+1", neutralizing the strain compensating effect. On the other hand, the antibonding state has larger energy compared to the uncoupled counterpart. The energy separation between bonding and antibonding states is proportional to the coupling strength.

We can clearly see from Fig. 4.23 in the last subsection that the difference between the evolutions of electron and hole GS energies as a function of T_s due to the different coupling strength: Compared to the baseline (here is the series "1+1"), starting from T_s = 25 nm, stronger

couplings in the series "2+1" (see the blue lines with triangle marks) are observed in the electron GS for thinner spacer, due to the stronger wavefunction spatial overlap; in contrast, basically no coupling can be seen in the hole GS even for very small T_s, due to the weaker barrier penetration and negligible wavefunction spatial overlap. Moreover, based on the strain distribution shown in Fig. 4.21, the unidirectional strain accumulation breaks the symmetry and resonance conditions, contributing to the coupling suppression, and thus pushes further the hole GS out of resonance.

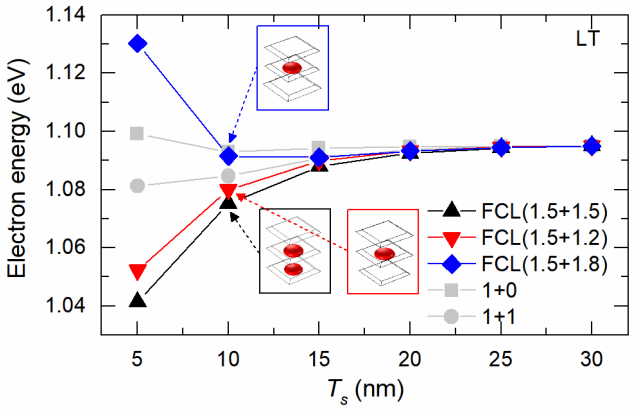

Fig. 4.24 Evolution of electron GS energy as a function of T_s in targeted QD for series "FCL(1.5+1.2)" and "FCL(1.5+1.8)" at LT, with series "FCL(1.5+1.5)" (i.e. series "2+1" of Fig. 4.23) serving as the baseline for the sake of comparison. Insets show the probability density (isosurface at 70%) for the electron of each series when T_s = 10 nm.

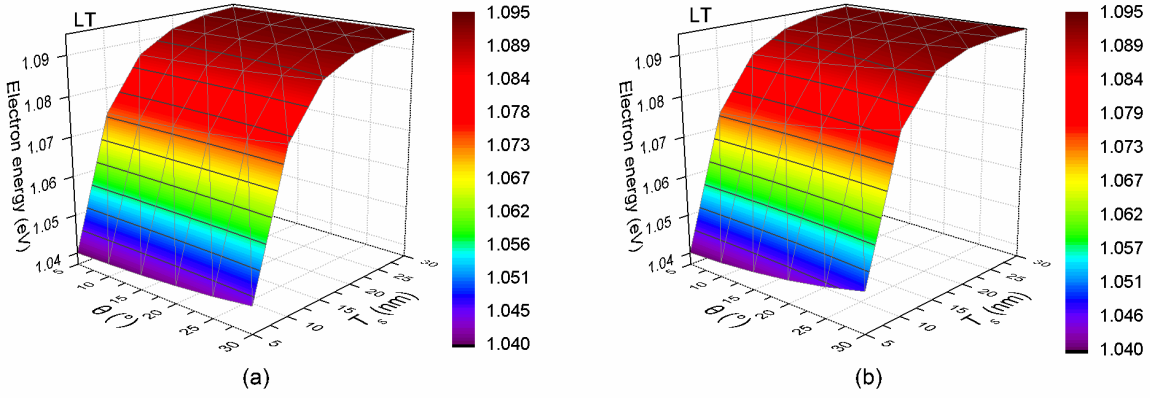

Fig. 4.25 Evolution of electron GS energy as a function of T_s and θ in targeted QD for series "2+1" at LT, perturbed by small deviations from (001) direction along (a) (100) and (b) (110) direction.

Definitely, any perturbation in the electronic coupling conditions, such as the QD size inhomogeneity and the misalignment of QD stack, leads to a suppression of electronic coupling, even though the mechanisms may be different. Fig. 4.24 shows the coupling suppression effect on the electron energies in the targeted QD when the adjacent QD size is perturbed. For the series "FCL(1.5+1.2)", the decrease of electron GS energy (i.e., bonding state) introduced by electronic coupling is obviously suppressed by 10 meV for T_s = 5 nm (see the red line with inversed triangle marks), compared to the unperturbed "FCL(1.5+1.5)" case. This coupling suppression is related to the hampered resonance condition. It is also notable that the wavefunction of the bonding state is mostly localized in the targeted QD, due to its larger size than the perturbed QD. In contrast, the GS wavefunction is mostly localized in the larger perturbed QD for the series "FCL(1.5+1.8)", resulting in higher optical transition energy in the targeted QD, governed by the antibonding state (see the blue line with diamond marks). Compared to the fundamental baseline, the antibonding energy is much higher (50 meV) than single-QD "1+1" for T_s = 5 nm, then quickly drops with the increase of T_s, getting even lower than single-QD for T_s =15 nm. This finding is probably related to the balancing effect between strain coupling and electron coupling. Eventually, a convergence to 1.09 eV of perturbed and unperturbed electron energies can be observed for T_s larger than 25 nm, equivalent to the single-QD electron energy, denoting the vanishing of both coupling effects. Fig. 4.25(a) and (b) show the coupled electron GS energies in the targeted QD, perturbed by small deviations of adjacent QDs from (001) direction, along (100) and (110) direction, respectively. Instead of the hampered resonance condition, this coupling suppression is related to the reduced wavefunction spatial overlap. As expected, the evolution of coupling suppression as a function of θ for "oblique 2+1" along (110) is more drastic than along (100) (e.g., 6.8 versus 3.5 meV for T_s = 5 nm when θ varies between 5−30˚), due to the faster decrease of electron wavefunction overlap between the lower two QDs. On the other hand, similar trends of dwindling suppression with the increase of T_s are observed for both two cases.

4.6.4 Impact of vertical coupling on electronic states

In this subsection, the electronic states for the series "3+1" influenced by various coupling effects at low temperature (LT) are investigated, accounting for the situation of a multilayer QD stack. There is no "targeted QD" in this subsection; instead, except for the uncapped QD, the lower three coupled dots are studied as a whole.

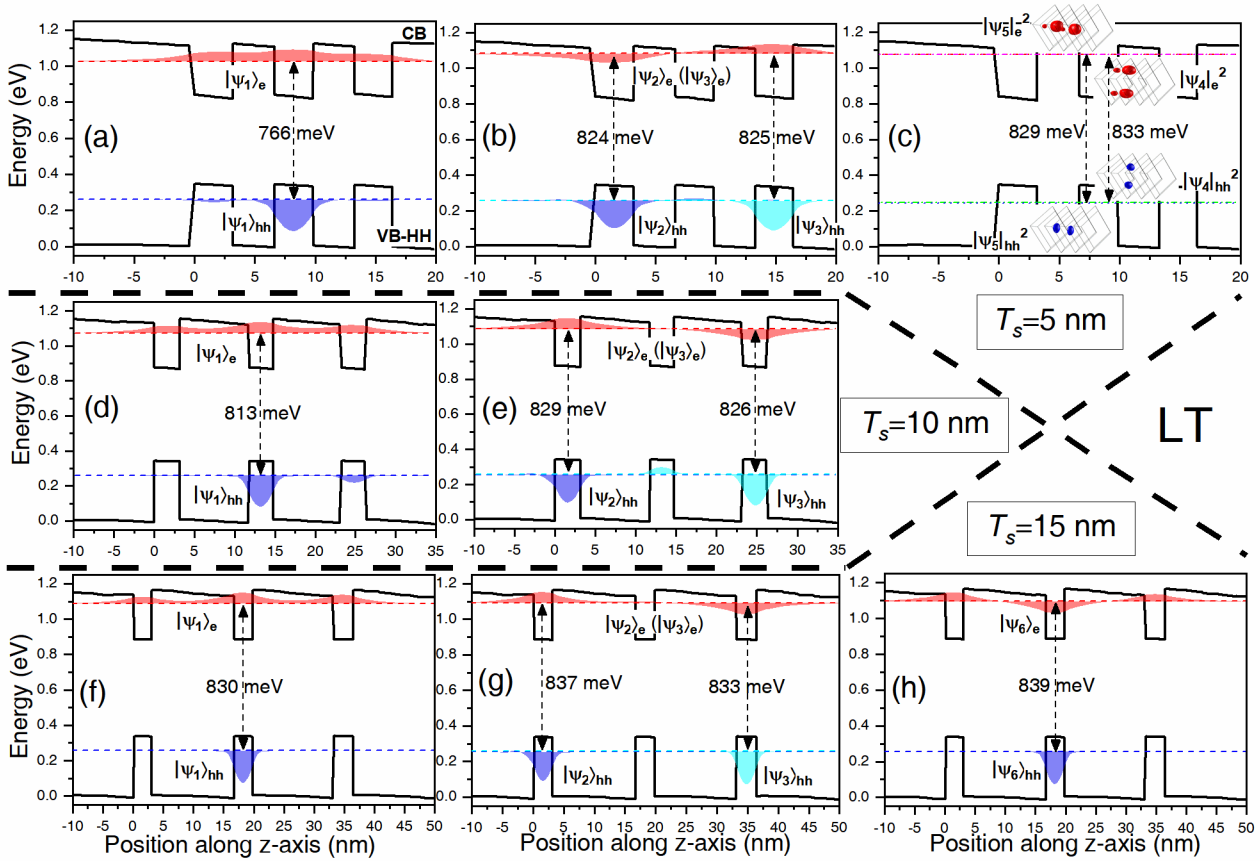

Fig. 4.26 Part of typical eigen-states $|\Psi_i\rangle$ (i = 1–6) and corresponding energy levels for series "3+1" at LT as (a)−(c) T_s = 5 nm, (d)−(e) T_s = 10 nm, and (f)−(h) T_s = 15 nm, respectively. CB and VB-HH denote conduction and heavy-hole band edges, respectively. Double arrowhead dashed lines visualize the most significant optical transitions between respective states. Insets show the p-orbital probability density $|\Psi_i|^2$ (isosurface at 70%) in 3-D for electron and hole.

Here we list part of typical eigen-states $|\Psi_i\rangle$ (i = 1–6) and the corresponding energy levels, obtained by solving a 3-D Schrödinger equation $H\Psi_i = E_i\Psi_i$ for T_s = 5, 10, and 15 nm, as shown

in the first, second, and third rows of Fig. 4.26, respectively. On the other hand, the first and second columns of Fig. 4.26 present the bonding and antibonding s-orbital states for various T_s. In the first column, the single electron has the largest probability of attending in the central QD, since the wavefunctions originating from adjacent QDs partially overlap with the middle one. This bonding s-orbital state is referred to as $|\Psi_1\rangle$ group hereinafter. In the second column, a single electron has identical probability of attending in the upper and the lower coupled QD. Thus there are two hole-states related to the most significant optical transitions, localized in the corresponding QDs. Therefore, this antibonding state is regarded as two electron-states in the study of optical properties, referred to as $|\Psi_2\rangle$ and $|\Psi_3\rangle$ groups hereinafter. Note for the bonding p-orbital, the probability of attending at the center axis of QD stack is zero, i.e., no wavefunction can be observed as shown in Fig. 4.26(c), referred to as $|\Psi_4\rangle$ and $|\Psi_5\rangle$ groups hereinafter. For T_s = 15 nm, another antibonding state with a different wavefunction phase is shown in Fig. 4.26(h), referred to as $|\Psi_6\rangle$ group.

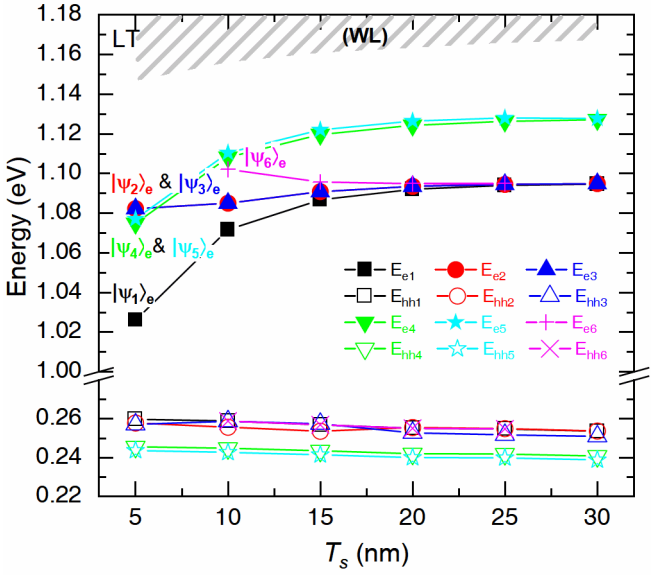

Fig. 4.27 Evolution of energy levels close to CB and VB-HH as a function of T_s for series "3+1" at LT. A "quasi-continuum band" comprised of antibonding s-orbital $|\Psi_2\rangle/|\Psi_3\rangle$ and bonding p-orbital $|\Psi_4\rangle/|\Psi_5\rangle$ for T_s = 5 nm. The area patterned in grey diagonal stripes denotes the continuum band in WL.

Fig. 4.27 shows the evolution of energy levels close to CB and VB-HH as a function of T_s for

each state group. Most strikingly, the energy levels of $|\Psi_2\rangle$~$|\Psi_5\rangle$ are very close to each other, forming a "quasi-continuum band" for T_s = 5 nm, as a double spin degeneracy is also taken for each state. Theoretically, the "quasi continuum band" concurrently holds advantages of (1) the high absorption due to the quantum feature of wavefunction localization, as well as (2) the high relative occupation probability resembling a real continuum band, due to a large number of accessible states and relaxation channels. Such quasi continuum band does not arise from the coupling of single QD and WL states [200] nor QD elongation [201]. On the other hand, the GS transition may be severely hampered by two types of phonon-bottleneck effect (1) due to the low-energy phonons at LT (i.e., random population effect [151]), and (2) the much less accessibility of carrier-relaxation paths from ES to GS [202, 203], which also gives rise to stronger ES emission than GS, even when not under high injection. In addition, for better clarification, the lowest energies in WL as a function of T_s have also been calculated and visualized as patterned areas in Fig. 4.27.

4.6.5 Impact of vertical coupling on gain and PL spectra

Although various attempts have been made, to interpret and even predict the emission behaviour of a specified structure by given SLN and spacer thickness is still a very challenging work [204]. For instance, a decrease of spacer thickness in a largely spaced stack results in a reduced fundamental transition energy or a red-shifting of PL peak wavelength, which can be interpreted resulting from a stronger resonant electronic coupling (e.g., see Ref. [83] and Sec. 4.6.3), or can be attributed to a reduced critical thickness for QD formation [205]; however, when reduced further to some extent, a further decrease of spacer thickness results in a distinct blue-shifting of PL peak wavelength, which has often been observed and reported [55-60, 206]. With respect to this intriguing phenomenon, the current interpretations are even more divergent and difficult to validate: Although the previous studies attempted to attribute the blue-shifting to the shallowed confinement depth and/or reduced lattice mismatch at QD/barrier interface introduced by the material

intermixing [58, 59, 207], or to the structural defect [60], or to the growth interruption [205], all of them did not quantitatively explain why these effects could overcome the known influence of increasing resonant electronic coupling and quantum tunnelling to upper larger-sized QDs. Therefore, there is no satisfactory model of QD stack provided for engineering the potential new applications to date, which requires a more comprehensive understanding of coupling physics. Based on the investigation in the last section, the finding of a group of closely-spaced electronic states (i.e., "quasi-continuum band") or highly degenerate ES above the GS may account for this unknown blue-shifting of PL peak wavelength with the decrease in T_s in this subsection.

To simulate the LT PL spectra and verify the variation of PL peak wavelength induced by the enhanced ES emission in the experiments, the occupation probabilities of electron and hole on each energy state have to be determined, which requires a rate equation (RE) model. Here, to simplify the model, we assume:

a) A four-level model consists of two confined states for carriers in the InAs QDs (i.e., ES and GS), and two states at higher energies represent the lowest edges of continuum band in the InAs WL and 1.15Q separate confinement heterostructure (SCH). To fit in the previously calculated electronic states with this model for each T_s, the "quasi-continuum band" for the 5-nm case is considered consisting of an *eight-fold* degenerate ES (1.08 eV) and a *two-fold* GS (1.026 eV), $|\Psi_1\rangle$~$|\Psi_3\rangle$ and $|\Psi_4\rangle$~$|\Psi_6\rangle$ in the 10-nm case are approximated by *six-fold* ES (1.11 eV) and GS (1.072 eV), respectively.
b) A 532-nm laser beam serves as PL excitation for the electron-hole pair generation, the same as that of Refs [55] and [56]. The excitation power density (unit: W/cm^2) is converted into the form of equivalent current density (unit: A/cm^2) via photon flux to fit in with the rate equation model, as it is assumed that each incident photon will excite an electron-hole pair.
c) The electron and hole dynamics are correlated (excitonic approximation), thus in this work, the electron and hole occupation probabilities are not independent for any dot.
d) Only cascade relaxation paths are considered in this simulation.

e) TE-polarized spontaneous emission dominates the PL spectrum in multilayered QDs with flat truncated-pyramidal dots, due to the fact that the highest hole states involved in PL emission are occupied by the heavy hole [208].

Table 4.4 Main parameters used in the RE & TDTW models.

Quantity	Values
Material parameters	
Temperature T	20 K
SCH-WL separation $\Delta E^{e}_{\mathrm{SCH-WL}}$	14 meV (5-nm case) 5 meV (10-nm case)
WL-ES separation $\Delta E^{e}_{\mathrm{WL-ES}}$	67 meV (5-nm case) 46 meV (10-nm case)
Number of QD groups N	15
Interband transition $\hbar\omega_{i\mathrm{ES}}$ for $i = (N + 1)/2$	0.835 eV (5-nm case) 0.865 eV (10-nm case)
Interband transition $\hbar\omega_{i\mathrm{GS}}$ for $i = (N + 1)/2$	0.766 eV (5-nm case) 0.813 eV (10-nm case)
FCL thickness H_{QD}	1.5 nm
Effective refractive index η	3.5755
Number of QD layers N_{l}	3
QD surface density N_{D}	3×1010 cm-2
State degeneracy D_m for m = ES, GS	8, 2 (5-nm case) 6, 6 (10-nm case)
Homogeneous linewidth $\hbar\Gamma$	10 meV
Inhomogeneous broadening FWHM ΔE	45 meV
Dipole matrix element d_m for m = ES, GS	0.34, 0.36 e·nm
Relaxation time τ_{c}^{m} for m = WL, ES, GS	3, 3, 1 ps
Spontaneous emission coupling factor β_{sp}	1 × 10-4
Intrinsic waveguide loss α_i	17 cm-1
Sample parameters	
Lateral size of the device (QD layer width) W	2.5 μm
Length of sample L	456 μm
Field confinement factor Γ_{xy}	0.06
Power reflectivity r_0^2, r_L^2	0, 0

Based on those assumptions, a model with a full set of REs [Eqs. (3.17)−(3.20)] coupled with a forward/backward propagation of optical wave can be built up based on the TDTW model [Eqs. (3.24), (3.25)]; PL measurement is generally conducted before the formation of any laser cavity so that the real electronic structure can be obtained. Thus, by setting r_0, r_L = 0 and by solving the REs

iteratively, the occupation probabilities $\rho_{im}^{e,h}$ in steady-state can be obtained, so that the optical gain spectrum $g(\omega)$ and PL emission spectrum $I_{PL}(\omega)$ can be calculated [Eqs. (3.5)−(3.7)]. The main parameters used in this simulation are given in Table 4.4. Note the time constant τ_c^m are not specifically chosen. Therefore, the random population effect is omitted in this work.

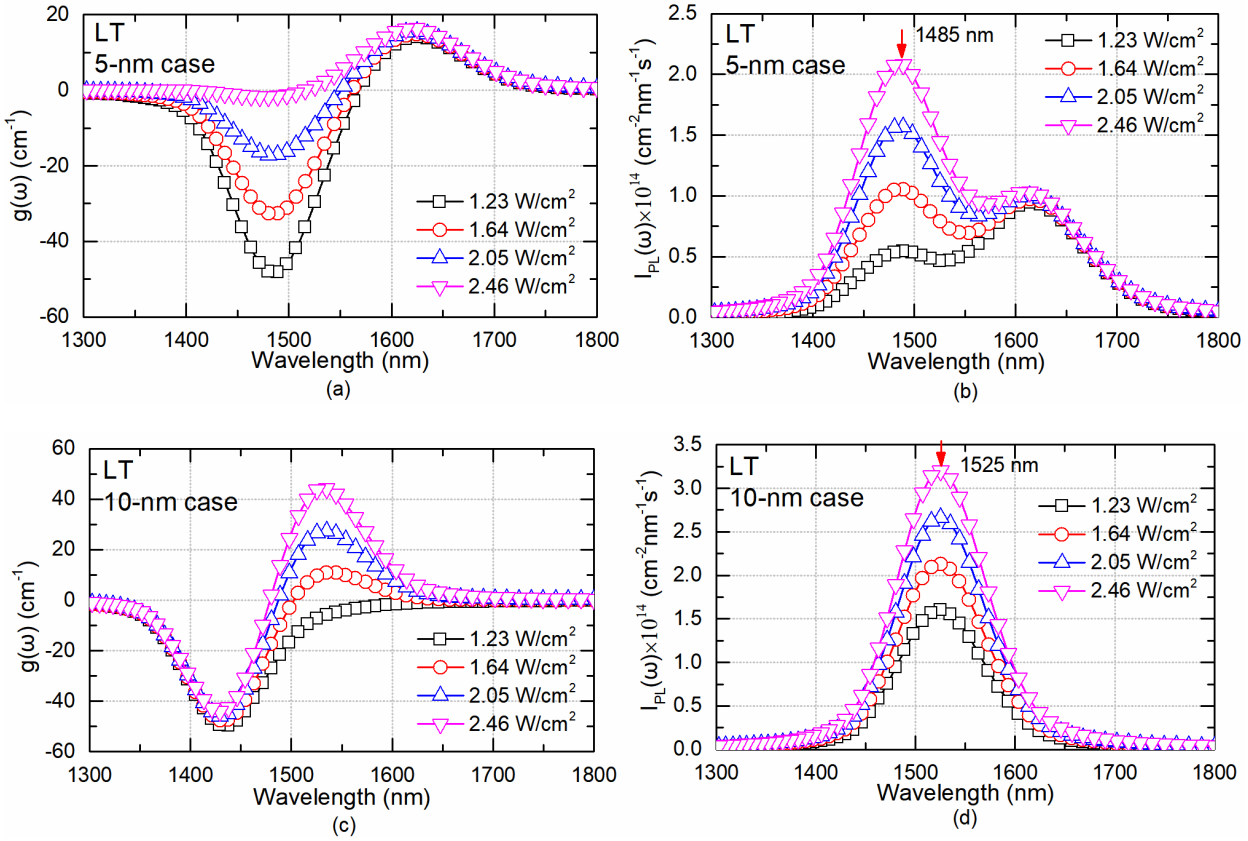

Fig. 4.28 Evolution of calculated optical gain and PL spectra for: (a) and (b) T_s = 5, and (c) and (d) T_s = 10 nm at LT, when the excitation power density varies between 1.23 and 2.46 W/cm^2.

The evolution of calculated LT spectra $g(\omega)$ and $I_{PL}(\omega)$ for the 5-nm and 10-nm cases are shown in Fig. 4.28, when the excitation power density increases from 1.23 to 2.46 W/cm^2. With respect to the optical gain spectra $g(\omega)$ for the 5-nm and 10-nm cases, as shown in Fig. 4.28(a) and (c), at first (e.g., 1.64 W/cm^2) optical gains only occur for GS transitions, while ES transitions at higher energies are absorbing in both cases; nevertheless, distinct behaviors are observed with the increasing injection levels: Since the ES for the 5-nm case is quadruply degenerate, it is populated

much faster than GS, and the transparency energy (i.e., the energy where the gain is zero, equals to the internal quasi-Fermi level separation [11]) moves toward the ES transition energy very rapidly. By contrast, the majority of injected energy goes to populate the GS for 10-nm case instead of ES due to their equal degeneracies, and the relaxation time from ES to GS is much shorter compared with the radiative recombination time for spontaneous emission.

This distinction of the spontaneous emission spectra $I_{PL}(\omega)$ between the 5-nm and 10-nm cases can also be seen in Fig. 4.28(b) and (d): As the injection increases, an increasing fraction of the emission comes from the ES; eventually, ES emission accounts for the majority of the emission. By contrast, the ES is not populated, and only GS emission continues to grow for the 10-nm case throughout the process. Thus, we can conclude that the ES for the 5-nm case is easier to populate at low injection level, compared to a case with larger T_s.

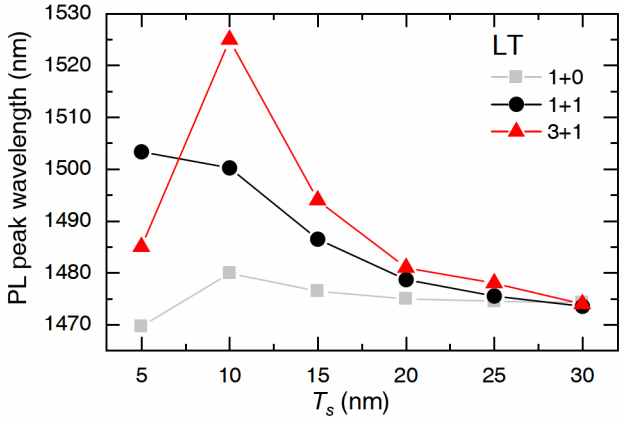

Fig. 4.29 LT PL peak wavelength as a function of T_s for the series "1+0", "1+1", and "3+1".

Moreover, it can be expected that the majority of the emissions for all the T_s larger than 10 nm are only provided by the GS transition. Therefore, the LT PL peak wavelength as a function of T_s for the series "3+1" can be drawn, as shown in Fig. 4.29. Phenomenologically, a blueshift of 40 nm can be observed as T_s decreases from 10 to 5 nm. In contrast, the blueshift for series "1+0" due to the electron localization effect is 10 nm, and there is no blueshift for series "1+1".

This finding (i.e. potential sole lasing at "quasi-continuum" ES in FP EELs with closely-stacked QD active region) is of significance, not only because it paves the way for high-

performance semiconductor laser devices with closely stacked QDs, avoiding the degradation of dot density and dot size homogeneity induced by fairly-spaced dot layers (e.g., see Refs. [198] and [35]), and without suffering from the unwanted decrease of fundamental transition energy induced by resonant electronic coupling; but also, more importantly, it may help the design of laser diodes emitting solely on ES, which have currently attracted a lot of attention due to its smaller linewidth enhancement factor (LEF) and better modulation response [209]. A detailed analysis will be given in Sec. 5.4.

4.7 Conclusions

In this chapter, we have developed a SAQD modeling method, including a detailed description of the two-step elastic strain analysis in Secs. 4.2−4.4. The model can be applied to the calculations of electronic band structure for this semiconductor nanostructure with various shapes, sizes, and barrier layer compositions. The simulation results from this accurate model quantitatively agree better with previously reported experimental RT PL results, owing to the ability to reproduce a practical self-assembly epitaxy growth process with double-capping procedure better than the conventional one-step model. Based on the accurate model, we have also studied the effect of different capping thickness on single QD, and an electron energy decrease is found, introduced by reduced electron localization when the capping thickness is increased from 5 to 10 nm. The effect of different barrier composition has been systematically studied for the first time.

After investigating the lateral coupling in terms of inter-dot distance in a QD ensemble in Sec. 4.5, this two-step model has been extended into a multi-step model in Sec. 4.6. In this section, we have systematically investigated the vertical coupling in a QD ensemble in terms of the dependence between the main structural parameters such as spacer thickness and dot layers' number, and the optical properties affected by the coupling among dots, by applying our accurate modeling method to various unperturbed and perturbed stacked InP-based QD structures. We have carefully investigated the superposition of exterior strain in the targeted QD, contributed by neighboring

upper and lower QDs. By comparing the asymmetric strain ϵ_{zz} obtained by our model with the symmetric one obtained by the conventional model, a more realistic unidirectional strain accumulation in QD stack is found, from lowermost to uppermost. For the three-layer stack, an unexpected 40 meV decrease of electron energy is found, introduced by enhanced resonant electronic coupling when QDs are closely stacked. Various small perturbations are introduced into the three-layer stack to study the coupling suppression. Eventually, the four-layer stack has been elaborately investigated, and a "quasi-continuum band" comprised of bonding and antibonding states is observed for the closely stacked QDs. A set of REs coupled with a TDTW equation are used to simulate this specific case, and a 40-nm blueshift of LT PL peak is found as T_s decreases from 10 to 5 nm, which resembles the intriguing phenomenon reported in the experiments. Furthermore, our calculations predict that the majority of the emission is provided by the ES transition for closely stacked QDs, and this finding may pave the way for designing the high-performance laser devices operating on ES.

Chapter 5 Optimization and Innovation in QD Laser Applications

5.1 Introductions

In this chapter, we propose three optimized (and novel) structures used for different purposes:

First, in Sec. 5.2, based on aforementioned separated-step strain analysis, the QD active region structure with an additional ultra-thin GaP interlayer/sublayer is investigated, which is reported experimentally allowing a blueshift in the wavelength of the emission peak. In our investigated structure, the ultra-thin GaP interlayer is inserted beneath the WL, therefore only the term *sublayer* is used hereinafter. In Sec. 5.3, a *novel* chirped multi-layer structure based on the predicted transition-energy-shifting when GaP sublayers are employed, which has been obtained in Sec. 5.2. With the joint action of well-designed variation in the QD height (controlled using double-capping) and sublayer thickness, the wavelength blue-shifting and gain spectral bandwidth in such stacked QD structure is greatly improved. Note the vertical coupling effects are not included since a sufficiently large spacer thickness is assumed at this stage.

In Sec. 5.4, a QD-based FP EEL with closely stacked multi-layer based on the investigation in Sec. 4.6 is simulated, which allows a possible promotion of two-state lasing at RT under CW electrical pumping. To our best knowledge, the achievement of simultaneous dual-state lasing from GS and ES has not been reported except with optical pumping or pulsed current injection.

5.2 Blue-Shifting Emission Peak

5.2.1 Impact on confinement potentials

The model of single InAs/InGaAsP QD with an ultrathin GaP sublayer is presented, and the impact of confinement potential energy induced by a GaP sublayer in a QD is analyzed, as shown in Fig. 5.1. Settings of QD structure: h = 2.7 nm, D = 30 nm, d_{WL} = 1.64 nm, and d_{sub} = 0.28 nm; 1.15Q

for capping/barrier; RT parameters are selected as listed in Table 4.1.

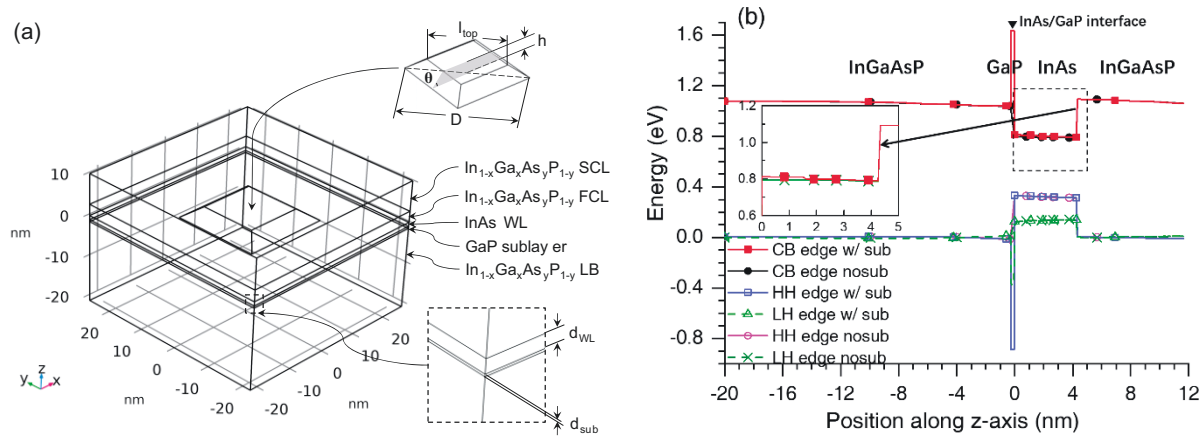

Fig. 5.1 (a) Schematic and geometry of single InAs/InGaAsP QD model with an ultrathin GaP sublayer; *h*, *D*, d_{WL} and d_{sub} in the inset denote the dot height, the diameter of dot base, the thickness of wetting layer and sublayer, respectively. (b) Strained energy band edges for electrons, heavy holes (HHs) and light holes (LHs) along the (001) direction for a QD with a GaP sublayer in comparison to a QD without sublayer. Zoom-in conduction band edges (CBEs) in the inset suggest the impact of confinement potential in QD induced by the sublayer.

Fig. 5.1 depicts the impact of potential energy along the direction of growth, when a GaP sublayer is inserted to a QD. For the CBE in the QD, there is a small lifting of energy near the InAs/GaP interface, which disappears gradually with the position being away from the interface. This lifting of the CBE energy, i.e. enhanced quantum confinement, can lead to larger energy of electronic eigenstates in the QD, resulting in a PL wavelength blue-shifting. For the HH and LH band edges, on the other hand, there is no obvious difference between the QDs with and without the sublayer.

Fig. 5.2 shows the impact of the CBE profile laterally. Two positions, at the middle and near the base of an InAs QD, are selected for a better view of the sublayer impact. The CBE profiles are basically identical along the plane halfway up the island between the model with and without sublayer, as shown in the upper figures of Fig. 5.2. However, the CBE profile shows a higher valley energy inside the dot, and a smaller peak energy surrounding the dot, as shown in the lower figures

of Fig. 5.2(b). Note the sublayer increases the minimum and reduces the maximum potential as indicated in two lower figure legends of Fig. 5.2.

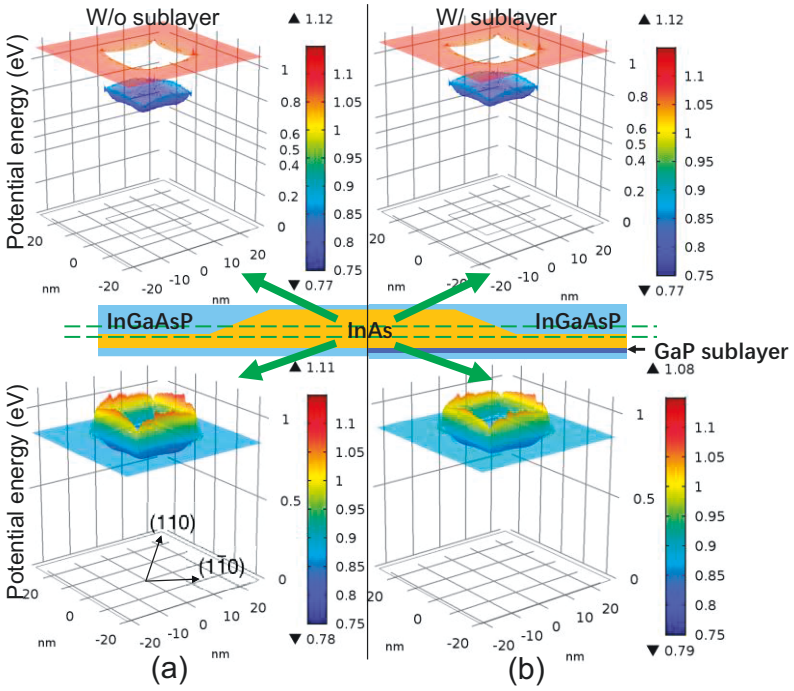

Fig. 5.2 CBE energy along two planes paralleled to the *x-y*-plane, in wetting layer just beneath the interface of heterostructure (*lower figures*) and halfway up the island (*upper figures*) in models (a) without (*left figures*) and (b) with (*right figures*) GaP sublayer.

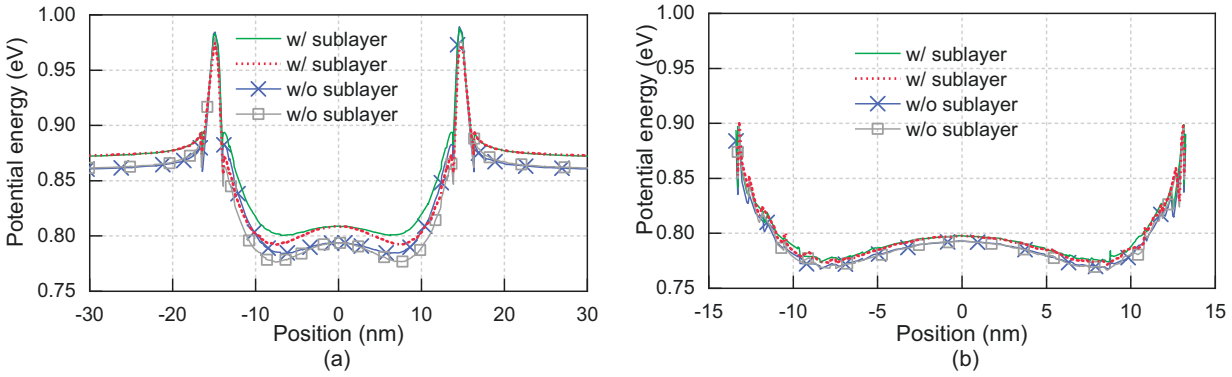

Fig. 5.3 Comparison between the lateral potentials for QDs with/without sublayer, along two planes paralleled to *x-y* plane: (a) a plane in wetting layer just beneath the interface of heterostructure (*corresponding to lower figures in Fig. 5.2*), and (b) a plane halfway up the island (*corresponding to upper figures in Fig. 5.2*).

Corresponding to Fig. 5.2, Fig. 5.3 shows the impact of the CBE profiles in (110) and $(1\bar{1}0)$ directions at the two positions indicated in Fig. 5.2. It is clearly shown that there is a larger lifting of energy at the bottom of the potential well at the position closer to the InAs/GaP interface, as shown in Fig. 5.3(a), while much smaller difference is observed in Fig. 5.3(b) at the position further away from the interface. It is believed that the shallowed depth of potential well probably leads to a PL wavelength blue-shifting. Moreover, this impact is brought by the strain field induced by the GaP sublayer.

5.2.2 Simulated tunable range

The influence of the GaP sublayer on the RT PL characteristics of the QDs is shown in Fig. 5.4. The calculated tunable ranges with the GaP sublayer (lower patterned area) also agree well with the measured PL peak wavelengths in [35]. Moreover, according to the simulations, a blue-shift of around 70 nm is observed by simply inserting 0.28 nm GaP sublayer, which shows a high efficiency of wavelength blue-shifting. The simulation results show that the PL peak wavelength blue-shifting still occurs without including this As/P exchange into the calculation, i.e. the identical geometries and settings are applied to both models. Indeed, the change brought by the sublayer only occurs in strain field or confinement potential profile. Definitely, this finding will benefit to the QD society since the effect of strain can be quantitatively estimated.

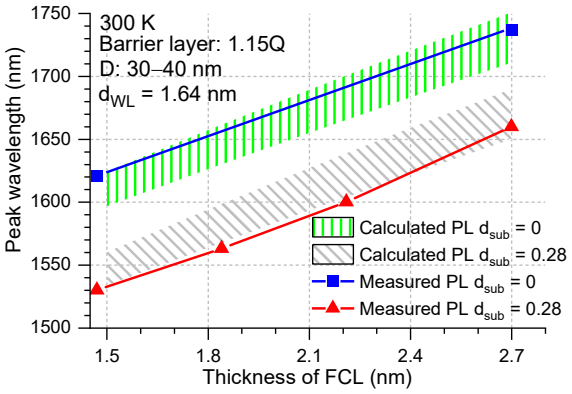

Fig. 5.4 Calculated tunable ranges without (*upper*) and with (*lower*) GaP sublayer, comparing with measurements to the samples without (*upper*) and with (*lower*) a 0.28 nm GaP sublayer beneath in [35], respectively.

It is also found in Fig. 5.4 that the QD base diameter is varied in 35−40 nm without the GaP sublayer, and in 30–35 nm with the GaP sublayer. This is consistent with the finding of the statistical distribution of lateral sizes of QDs in [35]. The GaP sublayer seems to reduce the dispersion of dot base sizes and prevent the lateral overgrowth.

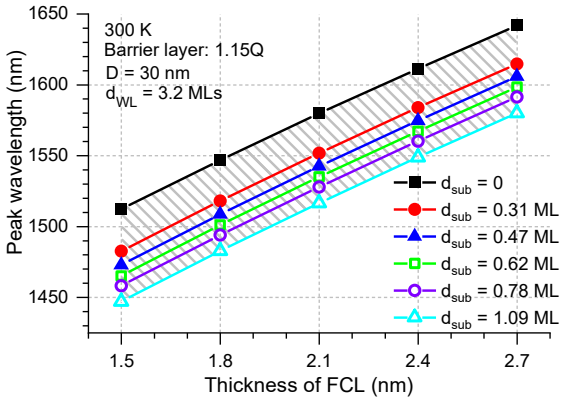

Fig. 5.5 Calculated tunable range of RT PL peak wavelengths emitted from the dots with varying dot heights and GaP sublayer thicknesses.

Fig. 5.5 gives the calculated ultra-broadband tunable range of gain at RT. It can be clearly observed that for the case without the sublayer, the maximum shifting range to shorter peak wavelengths is ~130 nm, with the peak wavelengths varied from 1512 to 1642 nm as the dot height is modified from 1.5 to 2.7 nm. Now, based on the above findings, the GaP sublayer thickness is

varied as shown in Fig. 5.5. It is seen that more shifting range for a shorter peak wavelengths is obtained. For the GaP sublayer thickness with 1.09 ML, the shifting range to the shorter peak wavelengths has additional ~65 nm, i.e. totally 195 nm shifting range of peak wavelengths, with the peak wavelength down to 1447 nm at *h* of 1.5 nm, which corresponds to a 50% enhancement.

5.3 Promoting Ultra-Broad Gain

It is possible to obtain a broadband optical gain by multiple QD active layers with unequal thickness, referred to as chirped structure [42, 44, 45], which was based on varied dot height only to date. In fact, by our findings in this work, the wavelength tunability/blue-shifting can be further enhanced if the advantage brought by varied sublayers can also be taken into consideration. Indeed, by using additional GaP sublayers in the structure, the emission peak is shifted to shorter wavelength range, which is preferable in InAs/InP self-assembled QD case.

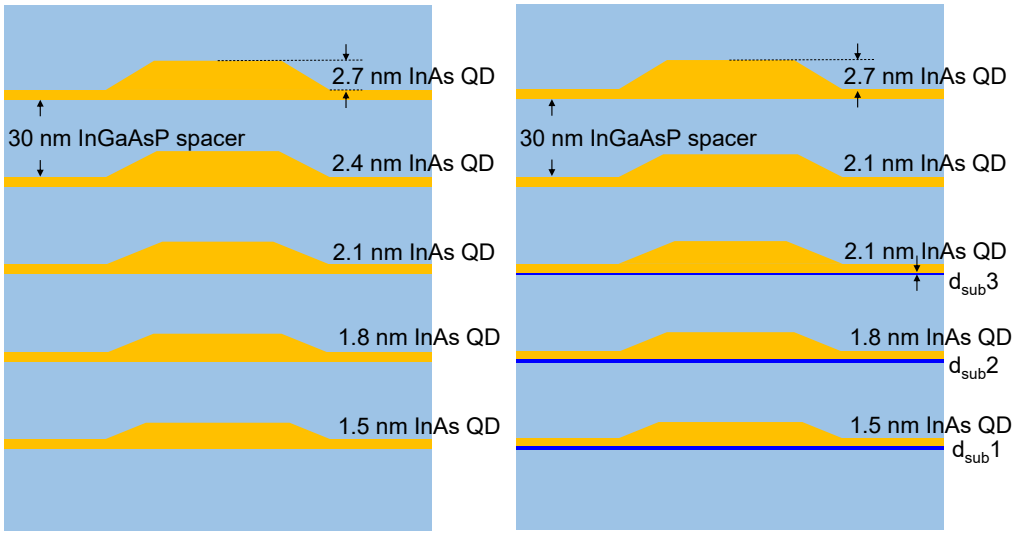

Fig. 5.6 Schematic cross-sectional diagrams of chirped active structures with chirped dot heights only (*left*) and with both chirped dot heights and chirped sublayer thicknesses (*right*). In the second chirped structure, the thicknesses of GaP sublayers d_{sub} 1, 2, and 3 are 1.09, 1.09, and 0.62 ML, respectively.

Based on the simulation results of RT PL peak wavelength for both cases (without and with a GaP sublayer) in Fig. 5.5, an improved structure revealing the advantage of combined techniques

(chirped dot heights and chirped sublayer thicknesses) is presented in Fig. 5.6. The conventional chirped structure on the left only consists of five non-identical InAs QD active layers with the FCL thicknesses of 1.5, 1.8, 2.1, 2.4, and 2.7 nm. On the other hand, the improved chirped structure on the right consists of five non-identical dot layers with the FCL thicknesses of 1.5, 1.8, 2.1, 2.1, and 2.7 nm, as well as three non-identical GaP sublayers underneath the lower three dot-layers with sublayer thicknesses of 1.09, 1.09, and 0.62 ML, with the other two dot-layers without sublayer underneath. The thickness of spacer is fixed to 30 nm between WLs for both structures.

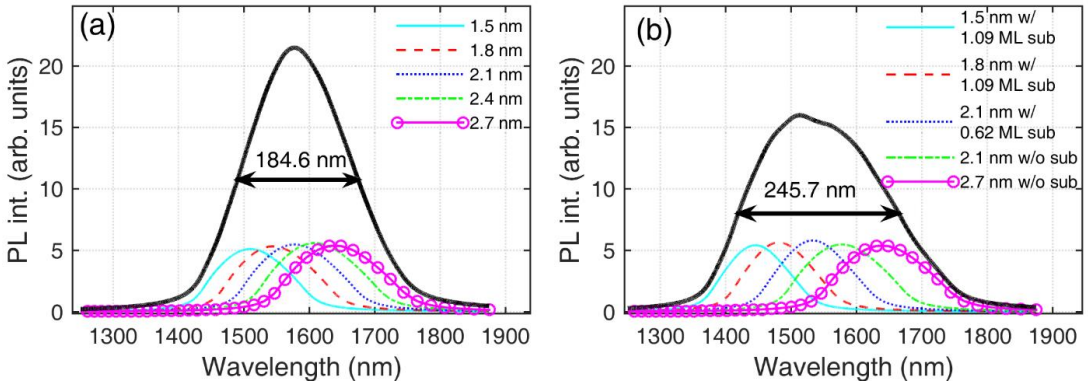

Fig. 5.7 Comparison of simulated gain spectra in conventional and improved structure, respectively. Base diameter of QDs in simulation is 30 nm.

Table 5.1 Parameters of QD layers used in calculation

Quantity	Values
Transverse optical confinement factors Γ_{xy} (1.5, 1.8, 2.1, 2.4, 2.7 nm FCL)	0.02, 0.025, 0.03, 0.035, 0.038
State degeneracy D_{GS}	2
QD surface density N_d	3×10^{14} m^{-2}
Refractive index η	3.5755
Number of QD groups N	15
Homogeneous linewidth $\hbar\Gamma$	10 meV
Inhomogeneous broadening ΔE	70, 60 meV
Dipole matrix element d_{GS}	0.285e·nm

Assuming the conduction band for confined GS is full, i.e. $\rho_{iGS}^{e,h} = 1$, the gain spectrum of a single QD layer with a specific FCL thickness can be calculated by Eq. (3.5). All parameters used in this simulation are given in Table 5.1. The calculated PT gain spectra are then given with the

help of the peak wavelengths found in Fig. 5.5. Fig. 5.7(a) presents five colored/patterned curves peaking at the wavelengths of 1512, 1547, 1580, 1611, and 1642 nm, denoting the corresponding gain spectrum of each dot layers of the conventional structure. The FWHM of total gain (bold black solid line) is 184.6 nm, centered at the wavelength of 1580 nm. On the other hand, Fig. 5.7(b) shows the corresponding gain spectra of the improved structure with peak wavelengths of 1447, 1483, 1535, 1580, and 1642 nm, respectively. The FWHM of gain spectral bandwidth reaches 245.7 nm in total, corresponding to a 30% enhancement. Furthermore, the peak wavelength is blue-shifted to around 1510 nm, which is preferable for the application of C-band. On top of the MLLs, this design methodology can also be implemented in fabricating tunable lasers and SOAs, etc.

5.4 Promoting Two-State Lasing

Two-state lasing, i.e., coherent lights simultaneously emit at two distinct wavelengths corresponding to QD GS and first ES, was achieved only using QDs [155]. Therefore, two-state lasing is a unique feature of QD-based semiconductor lasers and has been intensively studied over the past decade. For instance, in comparison to GS emission, QD lasers operating on ES exhibit lower RIN and phase noise accompanied by near-zero LEF [209-211], as well as broader modulation bandwidth [212, 213]. Even, GS emission itself can also benefit from the two-state lasing in terms of dynamic stability and modulation capability [214, 215]. Moreover, mode-locking could be achieved via the two-state lasing [216, 217].

Nevertheless, two-state lasing is generally observed in InAs/GaAs QD lasers with a single [155, 212, 218-221], or two-section structure [216, 217, 222-224]. In contrast, it is still a challenging work to obtain a stable two-state lasing experimentally for InAs/InP lasers. Platz *et al*. demonstrated that, for InP-based QDs at RT, two-state lasing was only achieved under optical injection, and sole GS lasing was observed under CW electrical bias [225]. It was implied that it is due to the non-uniform carrier injection and poor hole mobility in barrier layers. However, ES

emission was not observed by Moreau *et al*. [226], even with the help of p-doping in barrier layers. To understand two-state lasing, there have been some reported works to theoretically study the two-state lasing [94, 153], and those works have mainly focused on the two-state lasing under optical injection. Thus, the physics that leads to the absence of ES lasing for InAs/InP QDs has not been understood yet.

Two-state lasing behavior is generally related to the phonon-bottleneck effect [155], which refers to a phenomenon that the intraband (e.g. ES to GS) carrier-relaxation process is hampered. In InAs/InP QDs, the GS transitions may be severely hampered by two types of phonon-bottleneck effect due to (1) the low-energy phonons at LT (i.e. random population effect [151]), and (2) much reduced carrier-relaxation probabilities from ES to GS due to Pauli blocking, determined by the ES to GS degeneracy ratio. Moreover, it was also found that a thin spacer layer results in high ES to GS degeneracy ratio in LT QDs (Sec. 4.6). It would be expected that high degeneracy ratio resulting from a reduction of spacer thickness between QD layers at RT (i.e. random population effect is omitted) may occur too, and thus the ES lasing is enabled due to the bottleneck effect. Enabling ES lasing at RT is important for long-haul communications, because not only (1) GS lasers based on self-assembled InAs/InP QDs inherently emit at 1.60~1.65 μm at RT, while the ES emission consequently provides an alternative solution back to C-band wavelength [227], but also (2) the reduction of the spacer thickness is beneficial to dot uniformity, dot density, dot alignment [198], and modulation performance [213, 228].

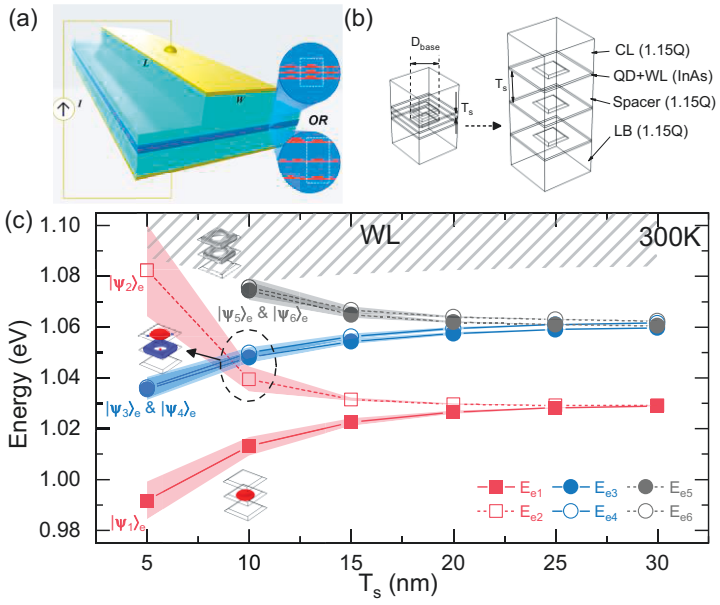

Fig. 5.8 (a) Schematic drawing of the simulated single-section QD laser. (b) Geometry of the QD stacks formed by three identical flat-truncated-pyramidal QDs as considered in our microscopic model. (c) Evolution of six lowest calculated electron energy levels as a function of spacer thickness T_s at RT. An approximate six-fold degenerate ES is formed by anti-binding *s*-orbital $|\Psi_2\rangle$ mixed with two binding *p*-orbitals $|\Psi_3\rangle$ and $|\Psi_4\rangle$ for $T_s \approx 10$ nm. The insets visualize the corresponding 3D electron probability densities $|\sum \Psi_i|^2$ (isosurface at 70%) of the degenerate states. The colorfully patterned areas denote the error margins of eigenstate energies, corresponding to the spacer thickness variations of ±1.25 nm.

5.4.1 Microscopic modeling

We sketch in Fig. 5.8, the typical single-section self-assembled InAs/InP QD laser (a) and the extracted QD stacks (b) formed by three identical flat-truncated-pyramidal InAs QDs grown on InP-lattice-matched quaternary $In_{0.816}Ga_{0.184}As_{0.392}P_{0.608}$ (1.15Q), similar to the series "2+1" in Sec. 4.6, except for an additional capping layer (CL) included here. The structure consists of a varied (5−30 nm) spacer thickness (T_s) of 1.15Q spacer layers and a fixed (30 nm) 1.15Q lower barrier (LB), plus a fixed (30 nm) 1.15Q CL. Details of calculation method with dimensions of QD can be found in Sec. 4.6.4. The RT material parameters used are directly given or can be calculated (linear interpolation), as listed in Table 4.1.

By solving a 3D Schrödinger equation $H\Psi_i = E_i\Psi_i$, six lowest electron energy levels $E_{1\text{–}6}$ as a function of the spacer thickness T_s between QD layers are calculated and shown in Fig. 5.8(c). The most striking observation is a large energy splitting between binding states (solid lines) and anti-binding states (dotted lines) for small T_s, resulting from the resonant electronic coupling. The splitting becomes smaller with the increase of T_s, originated from the lifted energy levels of the binding *s*- (squares) and *p*-like (circles) states and the dropped counterparts of the anti-binding. The splitting is undistinguishable for $T_s \approx 20$ nm and eventually vanishes for $T_s = 30$ nm. Moreover, the anti-binding *s*-orbital $|\Psi_2\rangle$ (red dotted line with empty squares) crosses with the two binding *p*-orbitals $|\Psi_3\rangle$ and $|\Psi_4\rangle$ (blue solid lines with circles) for $T_s \approx 10$ nm, resulting in a mixture of many states or "quasi continuum band" at an energy level of ~1.049 eV (a double spin degeneracy taken for each state). Therefore, Fig. 5.8(c) clearly illustrates that the ES degeneracy (six-fold) can be increased significantly by using a thin spacer layer, and thus the phonon bottleneck effect and sequential ES lasing can be enhanced.

5.4.2 Macroscopic modeling

To predict and compare the lasing behaviors in a single-section FP QD laser for the two specific cases of T_s = 10 and 30 nm (referred to as *10-nm/30-nm case* hereinafter), a simplified four-level RE model is used, which consists of two QD-confined states (i.e. ES and GS), and two states on the lowest edges of continuum band located in WL and 1.15Q SCH, coupled with a pair of forward/backward propagating electric fields, same as given in Sec. 4.6.5. The optical spectra are obtained by the numerical Fourier transform of output electric field $E_{\text{out}}(t) = \sqrt{1 - r_L^2}E^+(L,t)$ at the front cavity facet in the last 120 ns of simulations. Note since there was no GS quenching observed in measurement [225], in contrast to InAs/GaAs system [158, 229], we assume here that the electron/hole dynamics in InAs/InP QDs are totally symmetric. Part of the main parameters used in this simulation is given in Table 5.2. Other parameters that are not shown are listed in Table 4.4.

Table 5.2 Main parameters used in the macroscopic model at RT.

Quantity	Values
Temperature T	300 K
WL-ES separation $\Delta E^{e}_{\mathrm{WL-ES}}$	28 meV (10-nm case) 23 meV (30-nm case)
Interband transition $\hbar\omega_{i\mathrm{ES}}$ for $i = (N+1)/2$	0.805 eV (10-nm case) 0.821 eV (30-nm case)
Interband transition $\hbar\omega_{i\mathrm{GS}}$ for $i = (N+1)/2$	0.755 eV (10-nm case) 0.776 eV (30-nm case)
State degeneracy D_m for m = ES, GS	6, 2 (10-nm case) 8, 4 (30-nm case)
Inhomogeneous broadening FWHM ΔE	35, 40 meV
Ridge width W	2.5 μm
Cavity length L	456 μm
Power reflectivity r_0^2, r_L^2	99%, 33%

5.4.3 Dual lasing condition and characterization

In this subsection, we report simulation results for a 456 μm long FP laser with a cold cavity free spectral range (FSR) of 92 GHz. The simulated optical spectra at various levels of CW bias currents ranging from 1 to 6 times of threshold currents (I_{th}) for the 10-/30-nm case and IHB levels of FWHM ΔE = 35 and 40 meV are depicted in Fig. 5.9(a)−(d), which illustrate four cases: (a) high bottleneck effect plus low IHB, (b) high bottleneck effect plus high IHB, (c) low bottleneck effect plus low IHB, and (d) low bottleneck effect plus high IHB. The calculated I_{th} are shown in the insets of Fig. 5.9. There are three obvious distinctions exhibited from the normalized optical spectra evolutions:

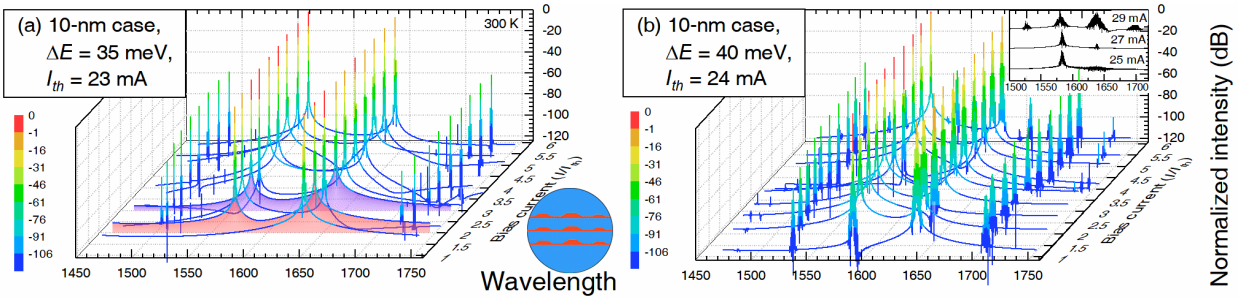

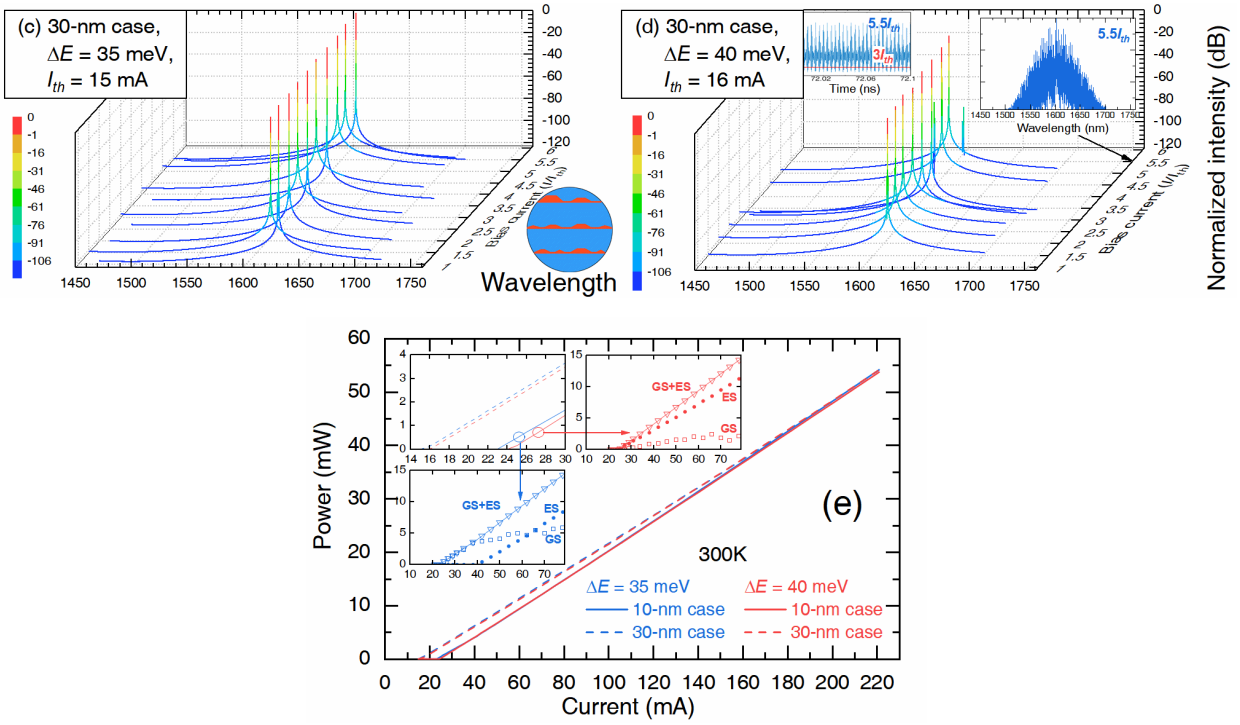

Fig. 5.9 Evolution of simulated optical spectra as a function of bias current at RT for T_s=10 (a)−(b) and 30 nm (c)−(d) with IHB of FWHM ΔE = 35 and 40 meV, and (e) the total L-I characteristics for 10- (solid) and 30-nm (dashed) with IHB FWHM ΔE = 35 (blue) and 40 meV (red). The red patterned spectrum in (a) indicates the onset of two-state lasing at $\lambda \approx$ 1560 nm (ES) and $\lambda \approx$ 1640 nm (GS) at $2I_{th}$; the inset in (b) shows the zoom-in evolution at bias ranging from 25 to 29 mA; the insets in (d) illustrate the distinctive output power in time- (*left*) and frequency-domain (*right*) at $5.5I_{th}$; and the insets in (e) depict the zoom-in total (*upper left*) and corresponding state-resolved L-I characteristics.

1) By comparing Fig. 5.9(a) and (b) with (c) and (d), the two-state lasing at $\lambda \approx$ 1560 nm (ES) and $\lambda \approx$ 1640 nm (GS) only exists in the 10-nm case [Fig. 5.9(a)−(b)], which shows the impact of the bottleneck effect and thus incomplete gain clamping of GS [155, 230], due to an increase of the ES to GS degeneracy ratio (i.e. 3:1). In contrast, for the 30-nm case [Fig. 5.9(c)−(d)], sole GS lasing around 1600 nm is observed only, which reproduces the electroluminescence (EL) result in Ref. [225]. This is due to a relatively smaller ES to GS degeneracy ratio (i.e. 2:1) at a larger T_s. Therefore, a thin spacer layer enhances ES lasing.
2) By comparing Fig. 5.9(a) and (b) for both with a high bottleneck effect, shown in Fig. 5.9(a) (high bottleneck effect plus low IHB) exhibits a standard optical emission behavior resembling

the observations of most experiments [155, 212, 216, 218-224], and the photoluminescence (PL) results in Ref. [225], i.e. first GS at I_{th} and then simultaneous GS plus ES lasing at ~2I_{th} (patterned in red) are achieved. When $I \approx 3I_{th}$ (patterned in purple) the peak power of ES emission starts to exceed GS. In contrast, high bottleneck effect plus high IHB in Fig. 5.9(b) leads to a reversal of the emission-state-transition similar to Ref. [217], i.e. the onset of stable ES lasing instead. The ES emission is always higher than GS in peak power for this case. To further clarify the emission contribution of each state, it is necessary to isolate ES and GS emission and calculate each state-resolved output power. This process is done by filtering the output electric field $E_{\mathrm{out}}(t)$ of stable ES and GS emission at uncoated facet for each bias level, with Hanning windows of suitable width (e.g. 8 × FSR) centered at the ES and GS lasing frequency, then time-averaging the state-resolved temporal power $P_m(t) = (1 - r_L^2)|E_m^+(L,t)|^2$ where m = ES, and GS. The state-resolved L-I characteristics are depicted in the other two insets of Fig. 5.9(e). Compared to the high bottleneck effect plus low IHB (blue line with marks in lower inset), the high IHB (red line with marks in upper right inset) leads to much smaller ES threshold $I_{th\text{-}ES}$ (25 versus 42 mA) and suppressed GS power P_{GS} (almost a half at ~ 3I_{th}). Therefore QDs with larger ΔE is favorable for ES lasing. This reversal may be interpreted as follows: The differential gain is inversely proportional to the IHB level, and the ES leads to much higher differential gain than GS. In other words, GS suffers significantly more than ES from larger dot-size-dispersion for providing sufficient gain to overcome the intra-cavity loss, leading to a decrease in GS lasing probability; on the other hand, the intermediate subbands located in GS and ES emission overlapping, which is made up of the emissions from GS of small-size QDs and ES of large-size QDs, are enhanced by expansion of the GS and ES emission overlapping, which arises from enlarged IHB. These intermediate subbands serve bridges, which result in a higher carrier escape rate from GS to ES, and thereby an increased probability of ES lasing.

3) By comparing Fig. 5.9(c) and (d) for both with a low bottleneck effect, the influence of

intermediate subbands for the 30-nm case is discovered. The consistent absence of ES lasing (no beam at $\lambda \approx 1510$ nm) is observed in Fig. 5.9(c) and (d) due to the low ES to GS degeneracy ratio and sequential insufficient bottleneck effect. Fig. 5.9(c) shows that a low IHB always leads to single wavelength operation. However, for a high IHB shown in Fig. 5.9(d), for bias below $5I_{th}$, single wavelength emission occurs only, and for a bias at $5.5I_{th}$, a very broad optical spectrum in frequency domain [see right inset of Fig. 5.9(d)] and a pulse train in time domain are obtained, i.e. multi-wavelength operation [see left inset of Fig. 5.9(d), for comparison, optical power vs. time for a bias of $3I_{th}$ also shown by red line]. The self-generation of new side longitudinal modes originated from amplified spontaneous emissions in Fig. 5.9(d) may be attributed to the carrier redistribution that arises from enhanced gain of intermediate subbands and the nonlinear interaction (e.g. spatial hole burning, cascading four-wave mixing, etc.) between electric field and gain medium [98]. This simulated *self-pulsing* behavior resembles the experimental observations [231], which may account for triggering of self-generated mode-locking in single-section QD FP lasers under CW bias.

Fig. 5.10 shows calculated minimum 3-dB spectral linewidth for T_s of 10- (GS plus ES) and 30-nm (GS mainly) and ΔE of 35 (i.e. low IHB) and 40 (i.e. high IHB) meV. By comparison of Fig. 5.10(a) and (b), the phase noise induced by the amplified spontaneous emissions at side longitudinal modes or other "dark" states without lasing (off-resonant) [232] is obtained by directly tracking the minimum linewidth [233], provided by the fundamental lasing line at maximum gain peak. A small minimum linewidth is achievable for $T_s = 10$ nm (high bottleneck effect) in Fig. 5.10 both (a) and (b) (see blue lines with squares) thanks to the existence of ES lasing [209].

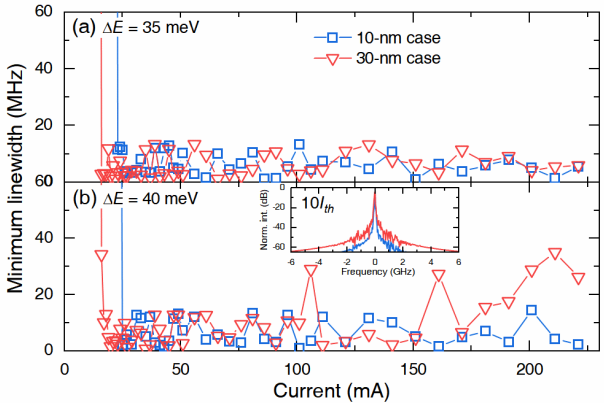

Fig. 5.10 Calculated spectral linewidth as a function of bias current at RT for 10- (blue) and 30-nm (red) case with IHB of FWHM (a) ΔE = 35 and (b) 40 meV. The inset in (b) compares the minimum linewidth of the two cases at $10I_{th}$, which confirms the linewidth rebroadening under high injection for the sole GS lasing with larger dot-size-dispersion.

However, for T_s = 30 nm (i.e. low bottleneck effect) in Fig. 5.10(a) (red line with triangles), i.e. low bottleneck effect plus low IHB, GS lasing linewidth is not affected significantly by ES spontaneous emission. The stably small linewidth is probably due to the relatively large energy separation between GS and off-resonant ES [232]. In contrast, Fig. 5.10(b) (red line with triangles) shows that high IHB leads to significant fluctuations and some drastic rises of minimum linewidth with increasing bias current, which suggests that the phase noise is considerably induced by the self-generated side longitudinal modes since the intermediate subbands are much closer to GS. The increasing tendency of minimum linewidth can be interpreted: Higher bias induces higher nonlinearities and thus more off-resonant subbands are involved in amplified emissions. The simulated linewidth *rebroadening* is in agreement with measurements [234-236], indicating the fact that the minimum achievable linewidth is indeed limited by the joint action of IHB and nonlinear effects. Note additional nonlinearities, such as gain compression are intentionally excluded from the simulation. If included, then self-pulsing and linewidth rebroadening could occur under even lower (just above threshold) bias [99].

In the following, we report simulation results of RIN at CW bias of up to 288 mA for a better comparison of 10-nm/30-nm case with ΔE of 40 (i.e. high IHB) meV. The calculations of RIN

spectrum [$RIN(f)$] and integrated RIN ($iRIN$) are given by [98, 233]:

$$RIN(f) = \frac{|\mathcal{F}\{|E^+(L,t)|^2 - \langle|E^+(L,t)|^2\rangle\}|^2}{\langle|E^+(L,t)|^2\rangle^2}, \qquad iRIN = \frac{\int_B RIN(f)df}{B},$$

where $\mathcal{F}\{\cdot\}$ denotes the Fourier transform operator, $\langle\cdot\rangle$ indicates the time-average operator and B represents the electrical bandwidth ranging from 10 MHz to 10 GHz.

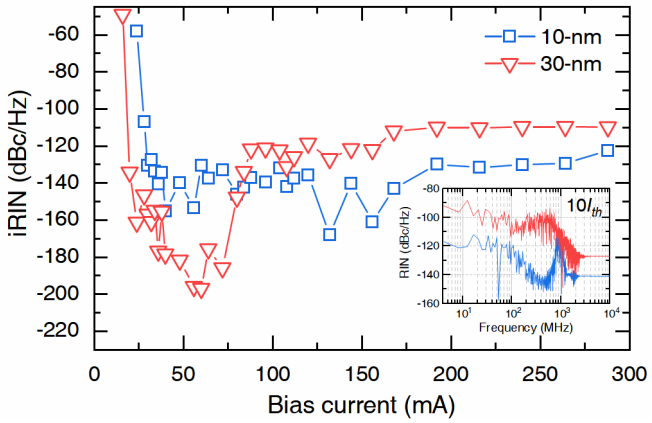

Fig. 5.11 Calculated integrated RIN as a function of bias current at RT for 10- (blue) and 30-nm (red) case with IHB of FWHM 40 meV. The inset compares RIN spectra of the two cases at 10I_{th}.

We first compare the integrated RIN, as shown in Fig. 5.11, for low and high bottleneck effect when both operating in the few-wavelength regime, i.e. below 5I_{th} (80 mA) for 30-nm case and below 6.5I_{th} (156 mA) for 10-nm case: Both of two cases exhibit a rapid decrease of integrated RIN with increasing bias current, due to an increasing average optical power in the beginning; then the integrated RIN from 10-nm case stays steadily after reaching to −140 dBc/Hz at bias of 36 mA, while 30-nm case exhibits a consistently reduced integrated RIN down to −197 dBc/Hz at bias of 60 mA. This ultra-low RIN from the latter case thanks to its CW output power. However, with stronger nonlinearities induced by increasing bias, different behaviors are shown in the multi-wavelength regime: A drastically increased integrated RIN up to around −110 dBc/Hz is shown in the 30-nm case, while the integrated RIN from 10-nm case keeps below −130 dBc/Hz and at least 20 dB lower than that with low bottleneck effect (e.g. see inset of Fig. 5.11 for RIN spectra comparison). The distinct behaviors are consistent with the above observations of spectral

linewidth, revealing that RIN and phase noise are linked to each other [237].

5.5 Conclusions

In this chapter, the impact of the sublayer on gain spectrum blue-shifting is first analyzed. It is found that the sublayer provides enhanced quantum confinement rather than stronger Ga–P bond or thereby smaller QD size. Thus, additional freedom is introduced for engineering the emission peak wavelength as well as the total gain spectral bandwidth by precisely managing sublayer. The physic model has been applied to generate an ultra-broadband gain spectrum of up to 245.7 nm, as an example, by managing GaP sublayer with a chirped QD structures, corresponding to a 30% enhancement compared to no sublayer. Moreover, the combination of sublayer thickness optimization and double-capping technique can offer more freedom in the fabrications of QD-based devices.

Then, by simulating the three-stack InAs/InP QDs with different spacer thickness of 10 and 30 nm, and with different in-plane inhomogeneity of the dot, we show that increasing the inhomogeneity with narrow spacer, it is possible to achieve simultaneous dual-state lasing from GS and ES of QDs under CW current injection. Moreover, we also analyzed the linewidth and RIN of the lasing spectrums at GS and ES.

Chapter 6 Concluding Remarks

6.1 Summary

An accurate modeling method for both self-assembled InAs/InP single QD and ensemble is proposed and validated in this thesis. Based on the simulation results, the following conclusions are drawn:

1) The improved two-step elastic strain analysis taking into account of double-capping procedure is found in better agreement with the previously reported RT PL measurements, compared with the conventional one-step model. The proposed model is numerically implemented by using the COMSOL Multiphysics FEM tool, first to investigate the relationship between optical properties and barrier layer composition. A tuning range from 1630 nm to 1840 nm is obtained in terms of RT PL peak wavelength, and a tuning range from 3.5 meV to 6.8 meV is observed in terms of BES energy, with the arsenic content changed from zero to one. Moreover, a spectrum-splitting phenomenon in the ground state is found to be enhanced approximately 50% compared with the counterpart using conventional model. This enhancement makes the BES nonnegligible in terms of lasing spectra, which may account for the source of GSSS.
2) Although without the aid of proof, based on the presumption that for InAs/InP QD there is a constant GS-ES energy separation at LT, an onion-like dimensional dependence of average base diameter and dot height is found i.e. the diameter proportionally varies in 8-ML steps when the height varies in 1-ML steps. It suggests a much more flat TP InAs/InP QD compared with InAs/GaAs counterpart in terms of morphology.
3) Apart from the composition, the impact of thickness of barrier, in particular the capping layer is investigated, which is related to the setting of BC. Dirichlet BC provides additional localization effect of electron when top boundary is very close (i.e. smaller than 10 nm) to QD and the emission is spectrally blue-shifted i.e. 15 nm shorter in peak wavelength compared with the counterpart applied Neumann BC at top boundary.

4) The impact of the ultra-thin GaP sublayer is then investigated by developing a novel three-step modeling method. Omitting the As/P exchange effect, the blue-shifting of PL peak is still predicted in agreement with the measurements. This suggests that the sublayer provides enhanced quantum confinement rather than stronger Ga–P bond or thereby smaller QD size.
5) An improved chirped multi-layer structure is proposed based on the simulation results of the sublayer, through joint action of well-designed variation in both QD height and sublayer thickness. An ultra-broadband gain spectrum of up to 245.7 nm is obtained in the simulation, corresponding to a 30% enhancement compared to no sublayer. With better manageable and broader gain coverage, this improved chirped structure is expected, preferably in various applications such as MLL and SOA, etc.
6) In terms of lateral coupling in the QD ensemble, the impacts of inter-dot distance in paralleled and tilted coupling are studied, as well as the size homogeneity. An obvious tendency from all results is shown that the PDF of lowest electron state (i.e. the first bonding state) is more likely to be localized in bigger dots, therefore the most of photoemission of GS is considered from bigger dots of a layer; while the opposite conclusion can be drawn when comes to the first antibonding state, that the PDF of which tends to stay in smaller QDs within one layer.
7) In terms of vertical coupling in QD ensemble, the impacts of inter-dot distance controlled by spacer thickness are studied by extending the two-step model into the multi-step model, thus the realistic unidirectional strain accumulation is reproduced in better agreement with measurements, arising from the uneven strain distribution at upper and lower regions in barrier of QD layer. Apart from strain coupling, the resonant electronic coupling is considered another important factor. Thus a variety of perturbed and unperturbed structures are simulated. Particularly, the results of three-layer stack shows an eight-fold degenerate ES (mixing of bonding and antibonding states) at 1.08 eV regarded as a “quasi-continuum band” which may account for the unknown blue-shifting of PL peak with reduced spacer thickness in measurements, as the photoemission of GS (pure lowest bonding state) is suppressed.

8) The macroscopic modeling approaches are applied to this QD stack, and our assumption about the dependence between spacer thickness and emission peak shifting is confirmed: A blueshift of 40 nm is observed as T_s decreases from 10 to 5 nm, which is not found in isolated QD model.
9) Based on this finding, a deeply-buried three-layer QD stack is modeled, in which the highly degenerate ES (or high bottleneck effect) is found at the spacer thickness of 10 nm. In this device simulation (i.e. a 456 μm long FP EEL with cold cavity FSR of 92 GHz), the effect of IHB is also considered. The results show that, in order to obtain two-state lasing under CW electrical pumping, the sufficiently high bottleneck effect is a prerequisite. In addition, this dual lasing benefits from fairly high IHB level, as the onset of sole ES lasing is at comparatively lower bias. We also compare GS and ES in terms of spectral linewidth and RIN, and the results show that ES lasing has better performance (i.e. at least 20 dB lower in RIN) at higher bias ($I \geq 100$ mA).

6.2 Recommendations for Future Work

Although thorough analysis and sufficient results have been presented to provide guidelines to realize new features in QD-based lasers, there is still some future work based on the analysis enclosed in this thesis, which is recommended as follows to enrich the work further:

1) Taking into account the variation in the inhomogeneity across the stacks (i.e. different ΔE for each stack) as with the thin barrier layer the overgrown QDs would be significantly influenced by the below grown QD layer during the actual growth.
2) Taking into account the joining of sublayer into the stacks, including a variety of cases with fixed or varied thickness, evenly or unevenly, to see the modified localization of envelope function across the stacked QD layers and its effect on the QD system. For instance, although not being displayed in this thesis, the deeply-buried three-layer stack (Sec. 5.4.1) shows that the envelope function (or PDF) of GS is mostly localized in the upper two QD layers. Therefore, the photoemission from the lowermost QD is totally suppressed. Interestingly, based on our

preliminary simulation results, the joining of sublayer results in a downwards shifting of localization in the PDF of GS across the stacks, which theoretically enhances the efficiency.

3) Taking into account the resonant electronic coupling in the chirped structure when these chirped QD layers are closely stacked, since the variation of QD height across the stack is regarded as a perturbation for electronic coupling, and the interplay in between will make the problem more complex. In addition, at this stage, the growth order of chirped layers may play an important role, which is closely related to the localization of PDF across the stack. Indeed, although being neglected in this work (Sec. 5.3), the actual chirped structures utilized as active region in diode lasers face the same efficiency problem even the dot layers being fairly separated (e.g. 30 nm), since the layers with smaller dots might not have any photoemission at all even at very high current injection.
4) Taking into account the intraband transitions (e.g. ES-GS and WL-ES) as the transition matrix element is related to the capture and escape rates in REs [Eqs. (3.17)−(3.20)] between these band. The expressions of these rates can replace the time constants of the RE model to see their effect on the final lasing spectrum. In this thesis only interband transitions are studied.

References

[1] N. Basov, O. Krokhin, and Y. Popov, "Production of negative-temperature states in p-n junctions of degenerate semiconductors," *Sov. Phys. JETP*, vol. 13, no. 6, pp. 1320–1321, 1961.

[2] H. Kroemer, "A proposed class of hetero-junction injection lasers," in *Proceedings of the IEEE*, 1963.

[3] Z. I. Alferov and R. F. Kazarinov, "Semiconductor laser with electric pumping," *U.S.S.R Inventor's Certificate No. 181737 (in Russian)*, 1963.

[4] P. YU and M. Cardona, *Fundamentals of Semiconductors: Physics and Materials Properties*. Graduate Texts in Physics, Berlin, Germany: Springer Berlin Heidelberg, 2010.

[5] R. Dingle and C. H. Henry, "Quantum effects in heterostructure lasers," *US Patent #3,982,207*, 1976.

[6] Y. Arakawa and H. Sakaki, "Multidimensional quantum well laser and temperature dependence of its threshold current," *Appl. Phys. Lett.*, vol. 40, no. 11, pp. 939–941, 1982.

[7] N. Kirstaedter, N. N. Ledentsov, and M. Grundmann, "Low threshold, large To injection laser emission from (InGa)As quantum dots," *Electron. Lett.*, vol. 30, no. 17, pp. 1416–1417, 1994.

[8] D. Huffaker, G. Park, Z. Zou, O. Shchekin, and D. Deppe, "Continuous-wave low-threshold performance of 1.3-μm InGaAs-GaAs quantum-dot lasers," *IEEE J. Sel. Top. Quantum Electron.*, vol. 6, no. 3, pp. 452–461, 2000.

[9] M. Asada, Y. Miyamoto, and Y. Suematsu, "Gain and the threshold of three-dimensional quantum-box lasers," *IEEE J. Quantum Electron.*, vol. 22, no. 9, pp. 1915–1921, 1986.

[10] V. Ustinov, A. Zhokov, A. Zhukov, O. U. Press, A. Egorov, and N. Maleev, *Quantum Dot Lasers*. Oxford science publications, New York, USA: Oxford University Press, 2003.

[11] P. Blood, *Quantum Confined Laser Devices: Optical Gain and Recombination in*

Semiconductors. New York, USA: Oxford University Press, 2015.

[12] A. Zhukov, M. Maksimov, and A. Kovsh, "Device characteristics of long-wavelength lasers based on self-organized quantum dots," *Semiconductors*, vol. 46, no. 10, pp. 1225–1250, 2012.

[13] S. Anantathanasarna, R. Nötzel, and P. J. van Veldhoven, "Lasing of wavelength-tunable (1.55 μm region) InAs/InGaAsP/InP (100) quantum dots grown by metal organic vapor-phase epitaxy," *Appl. Phys. Lett.*, vol. 89, no. 7, p. 073115, 2006.

[14] S. Anantathanasarn and R. Nötzel, "Wavelength-tunable (1.55-μm region) InAs quantum dots in InGaAsP/InP (100) grown by metal-organic vapor-phase epitaxy," *J. Appl. Phys.*, vol. 98, no. 1, p. 013503, 2005.

[15] S. Fréchengues, N. Bertru, V. Drouot, B. Lambert, S. Robinet, S. Loualiche, D. Lacombe, and A. Ponchet, "Wavelength tuning of InAs quantum dots grown on (311)B InP," *Appl. Phys. Lett.*, vol. 74, no. 22, pp. 3356–3358, 1999.

[16] H. Saito, K. Nishi, and S. Sugou, "Ground-state lasing at room temperature in long-wavelength InAs quantum-dot lasers on inp(311)B substrates," *Appl. Phys. Lett.*, vol. 78, no. 3, pp. 267–269, 2001.

[17] J. Kotani, P. J. v. Veldhoven, T. d. Vries, B. Smalbrugge, E. A. J. M. Bente, M. K. Smit, and R. Nötzel, "First demonstration of single-layer InAs/InP (100) quantum-dot laser: continuous wave, room temperature, ground state," *Electron. Lett.*, vol. 45, no. 25, pp. 1317–1318, 2009.

[18] D. Zhou, R. Piron, F. Grillot, and O. Dehaese, "Study of the characteristics of 1.55 μm quantum dash/dot semiconductor lasers on InP substrate," *Appl. Phys. Lett.*, 2008.

[19] N. Bertru, C. Paranthoen, O. Dehaese, A. Folliot, H.and Le Corre, R. Piron, F. Grillot, W. Lu, J. Even, G. Elias, C. Levallois, S. Loualiche, M. Bozkurt, J. Ulloa, P. Koenraad, and A. Ponchet, "QD laser on InP substrate for 1.55 μm emission and beyond," in *Proceedings of SPIE, Quantum Sensing and Nanophotonic Devices VII*, vol. 7608, p. 76081B, 2010.

[20] S. White and M. Cataluna, “Unlocking spectral versatility from broadly-tunable quantum-dot lasers,” *Photonics*, vol. 2, no. 2, pp. 719–744, 2015.

[21] T. Müller, S. J, A. Krysa, J. Huwer, M. Felle, M. Anderson, R. Stevenson, J. Heffernan, D. Ritchie, and A. Shields, “A quantum light-emitting diode for the standard telecom window around 1,550 nm,” *Nat. Commun.*, vol. 9, no. 1, p. 862, 2018.

[22] L. Tripathi, Y. He, u. Dusanowski, P. Wroński, C. Lu, C. Schneider, and S. Höfling, “Resonance fluorescence from an atomic-quantum-memory compatible single photon source based on GaAs droplet quantum dots,” *Appl. Phys. Lett.*, vol. 113, no. 2, p. 021102, 2018.

[23] C. Ye, *Tunable External Cavity Diode Lasers*. Singapore: World Scientific, 2004.

[24] W. Kaiser, S. Deubert, J. P. Reithmaier, and A. Forchel, “Singlemode tapered quantum dot laser diodes with monolithically integrated feedback gratings,” *Electron. Lett.*, vol. 43, no. 17, pp. 926–927, 2007.

[25] M. Nakazawa, S. Okamoto, T. Omiya, K. Kasai, and M. Yoshida, “256-QAM (64 Gb/s) coherent optical transmission over 160 km with an optical bandwidth of 5.4 GHz,” *IEEE Photon. Technol. Lett.*, vol. 22, no. 3, pp. 185–187, 2010.

[26] M. Grundmann, “Feasibility of 5 Gbit/s wavelength division multiplexing using quantum dot lasers,” *Appl. Phys. Lett.*, vol. 77, no. 26, pp. 4265–4267, 2000.

[27] H. A. Haus, “Mode-locking of lasers,” *IEEE J. Sel. Top. Quantum Electron.*, vol. 6, no. 6, pp. 1173–1185, 2000.

[28] L. Li, M. Rossetti, A. Fiore, L. Occhi, and C. Velez, “Wide emission spectrum from superluminescent diodes with chirped quantum dot multilayers,” *Electron. Lett.*, vol. 41, no. 1, pp. 41–43, 2005.

[29] E. Rafailov, M. Cataluna, and W. Sibbett, “Mode-locked quantum-dot lasers,” *Nat. Photonics*, vol. 1, no. 7, pp. 395–401, 2007.

[30] M. Z. M. Khan, T. K. Ng, and B. S. Ooi, “Self-assembled InAs/InP quantum dots and

quantum dashes: Material structures and devices," *Prog. Quantum Electron.*, vol. 38, no. 6, pp. 237–313, 2014.

[31] C. Gosset, K. Merghem, A. Martinez, G. Moreau, G. Patriarche, G. Aubin, A. Ramdane, J. Landreau, and F. Lelarge, "Subpicosecond pulse generation at 134GHz using a quantum-dash-based Fabry-Perot laser emitting at 1.56μm," *Appl. Phys. Lett.*, vol. 88, no. 24, p. 241105, 2006.

[32] J. Renaudier, R. Brenot, B. Dagens, F. Lelarge, B. Rousseau, F. Poingt, O. Legouezigou, F. Pommereau, A. Accard, P. Gallion, and G. H. Duan, "45 GHz self-pulsation with narrow linewidth in quantum dot Fabry-Perot semiconductor lasers at 1.5 μm," *Electron. Lett.*, vol. 41, no. 18, pp. 1007–1008, 2005.

[33] A. E. Zhukov, A. R. Kovsh, and V. M. Ustinov, "Temperature dependence of the gain of lasers based on quantum-dot arrays with an inhomogeneously broadened density of states," *Semiconductors*, vol. 33, no. 11, pp. 1260–1264, 1999.

[34] O. Qasaimeh, "Effect of inhomogeneous line broadening on gain and differential gain of quantum dot lasers," *IEEE Trans. Electron. Devices*, vol. 50, pp. 1575–1581, 2003.

[35] P. Poole, K. Kaminska, P. Barrios, Z. Lu, and J. Liu, "Growth of InAs/InP-based quantum dots for 1.55μm laser applications," *J. Cryst. Growth*, vol. 311, no. 6, pp. 1482–1486, 2009.

[36] C. Cornet, A. Schliwa, J. Even, F. Doré, C. Celebi, A. Létoublon, E. Macé, C. Paranthoën, A. Simon, P. M. Koenraad, N. Bertru, D. Bimberg, and S. Loualiche, "Electronic and optical properties of InAs/InP quantum dots on InP (100) and InP (311)B substrates: Theory and experiment," *Phys. Rev. B*, vol. 74, p. 035312, Jul 2006.

[37] J. Ulloa, P. Koenraad, E. Gapihan, and A. Letoublon, "Double capping of molecular beam epitaxy grown InAs/InP quantum dots studied by cross-sectional scanning tunneling microscopy," *Appl. Phys. Lett.*, vol. 91, no. 7, p. 073106, 2007.

[38] G. Elias, A. Létoublon, R. Piron, and I. Alghoraibi, "Achievement of high density InAs/GaInAsP quantum dots on misoriented InP (001) substrates emitting at 1.55 μm," *Jpn.*

J. Appl. Phys., vol. 48, no. 7R, p. 070204, 2009.

[39] Z. Jiao, Z. Lu, J. Liu, P. J. Poole, P. J. Barrios, D. Poitras, G. Pakulski, J. Caballero, and X. Zhang, "Linewidth enhancement factor of InAs/InP quantum dot lasers around 1.5 μm," *Opt. Commun.*, vol. 285, no. 21–22, pp. 4372–4375, 2012.

[40] S. Luo, H. Ji, X. Yang, and T. Yang, "Impact of double-cap procedure on the characteristics of InAs/InGaAsP/InP quantum dots grown by metal-organic chemical vapor deposition," *J. Cryst. Growth*, vol. 375, pp. 100–103, 2013.

[41] C. Paranthoen, N. Bertru, O. Dehaese, A. Corre, S. Loualiche, B. Lambert, and G. Patriarche, "Height dispersion control of InAs/InP quantum dots emitting at 1.55 μm," *Appl. Phys. Lett.*, vol. 78, no. 12, p. 1751, 2001.

[42] C. Chia, S. Chua, J. Dong, and S. Teo, "Ultrawide band quantum dot light emitting device by postfabrication laser annealing," *Appl. Phys. Lett.*, vol. 90, no. 6, p. 061101, 2007.

[43] S. Haffouz, S. Raymond, Z. Lu, P. Barrios, D. Roy-Guay, X. Wu, J. Liu, D. Poitras, and Z. Wasilewski, "Growth and fabrication of quantum dots superluminescent diodes using the indium-flush technique: A new approach in controlling the bandwidth," *J. Cryst. Growth*, vol. 311, no. 7, pp. 1803–1806, 2009.

[44] M. Z. M. Khan, T. K. Ng, C.-S. Lee, D. H. Anjum, D. Cha, P. Bhattacharya, and B. S. Ooi, "Distinct lasing operation from chirped InAs/InP quantum-dash laser," *IEEE Photonics Journal*, vol. 5, no. 4, p. 1501308, 2013.

[45] F. Gao, S. Luo, H. M. Ji, S. T. Liu, F. Xu, Z. R. Lv, D. Lu, C. Ji, and T. Yang, "Ultrashort pulse and high power mode-locked laser with chirped InAs/InP quantum dot active layers," *IEEE Photon. Technol. Lett.*, vol. 28, no. 13, pp. 1481–1484, 2016.

[46] S. K. Ray, K. M. Groom, M. D. Beattie, H. Y. Liu, M. Hopkinson, and R. A. Hogg, "Broad-band superluminescent light-emitting diodes incorporating quantum dots in compositionally modulated quantum wells," *IEEE Photon. Technol. Lett.*, vol. 18, no. 1, pp. 58–60, 2006.

[47] M. Rossetti, L. Li, A. Markus, A. Fiore, L. Occhi, C. Velez, S. Mikhrin, I. Krestnikov, and

A. Kovsh, “Characterization and modeling of broad spectrum InAs–GaAs quantum-dot superluminescent diodes emitting at 1.2–1.3 μm,” *IEEE J. Quantum Electron.*, vol. 43, no. 8, pp. 676–686, 2007.

[48] J. X. Chen, A. Markus, A. Fiore, U. Oesterle, R. P. Stanley, J. F. Carlin, R. Houdré, M. Ilegems, L. Lazzarini, L. Nasi, M. T. Todaro, E. Piscopiello, R. Cingolani, M. Catalano, J. Katcki, and J. Ratajczak, “Tuning InAs/GaAs quantum dot properties under Stranski-Krastanov growth mode for 1.3 μm applications,” *J. Appl. Phys.*, vol. 91, no. 10, pp. 6710–6716, 2002.

[49] D. C. Heo, J. D. Song, W. J. Choi, J. I. Lee, J. C. Jung, and I. K. Han, “High power broadband InGaAs/GaAs quantum dot superluminescent diodes,” *Electron. Lett.*, vol. 39, no. 11, pp. 863–865, 2003.

[50] Z. Y. Zhang, Z. G. Wang, B. Xu, P. Jin, Z. Z. Sun, and F. Q. Liu, “High-performance quantum-dot superluminescent diodes,” *IEEE Photon. Technol. Lett.*, vol. 16, no. 1, pp. 27–29, 2004.

[51] R. Nötzel, S. Anantathanasarn, and R. P. J. van Veldhoven, “Self assembled InAs/InP quantum dots for telecom applications in the 1.55 μm wavelength range: Wavelength tuning, stacking, polarization control, and lasing,” *Jpn. J. Appl. Phys.*, vol. 45, no. 8S, pp. 6544–6549, 2006.

[52] Q. Gong, R. Nötzel, V. P. Veldhoven, and J. Wolter, “InAs/InP quantum dots emitting in the wavelength region by inserting ultrathin GaAs and GaP interlayers,” *J. Cryst. Growth*, vol. 85, no. 8, pp. 1404–1406, 2005.

[53] E. S. Semenova and I. Kulkova, “Metal organic vapor-phase epitaxy of InAs/InGaAsP quantum dots for laser applications at 1.5 μm,” *Appl. Phys. Lett.*, vol. 99, no. 10, p. 101106, 2011.

[54] S. Yoon, Y. Moon, T.-W. Lee, E. Yoon, and Y. Kim, “Effects of As/P exchange reaction on the formation of InAs/InP quantum dots,” *Appl. Phys. Lett.*, vol. 74, no. 14, pp. 2029–2031,

1999.

[55] S. Shetty, S. Adhikary, B. Tongbram, A. Ahmad, H. Ghadi, and S. Chakrabarti, “The optical properties of strain-coupled InAs/GaAs quantum-dot heterostructures with varying thicknesses of GaAs and InGaAs spacer layers,” *J. Lumin.*, vol. 158, pp. 231–235, 2015.

[56] B. Tongbram, N. Sehara, J. Singhal, P. D. Panda, and S. Chakrabarti, “A detailed investigation of strain patterning effect on bilayer InAs/GaAs quantum dot with varying GaAs barrier thickness,” in *SPIE Proc. 9758*, p. 975802, 2016.

[57] H. Heidemeyer, S. Kiravittaya, C. Müller, J. NY, and O. Schmidt, “Closely stacked InAs/GaAs quantum dots grown at low growth rate,” *Appl. Phys. Lett.*, vol. 80, no. 9, pp. 1544–1546, 2002.

[58] M. O. Lipinski, H. Schuler, O. G. Schmidt, K. Eberl, and N. Y. Jin-Phillipp, “Strain-induced material intermixing of InAs quantum dots in GaAs,” *Appl. Phys. Lett.*, vol. 77, no. 12, pp. 1789–1791, 2000.

[59] W. Chang, W. Chen, A. Chou, T. Hsu, P. Chen, Z. Pei, and L. Lai, “Effects of spacer thickness on optical properties of stacked Ge/Si quantum dots grown by chemical vapor deposition,” *J. Appl. Phys.*, vol. 93, no. 9, pp. 4999–5002, 2003.

[60] E. Petitprez and E. Marega, “On the origin of the optical emission peak shifts in QD superlattices,” *Phys. Status Solidi B*, vol. 232, no. 1, pp. 164–168, 2002.

[61] B. Ilahi, L. Sfaxi, F. Hassen, B. Salem, and B. G. C, “Optimizing the spacer layer thickness of vertically stacked InAs/GaAs quantum dots,” *Mater. Sci. Eng. C.*, vol. 26, no. 2–3, pp. 374–377, 2006.

[62] J. Tatebayashi, N. Nuntawong, P. Wong, Y. Xin, L. Lester, and D. Huffaker, “Strain compensation technique in self-assembled InAs/GaAs quantum dots for applications to photonic devices,” *J. Phys. D: Appl. Phys.*, vol. 42, no. 7, p. 073002, 2009.

[63] D. Panda, A. Ahmad, H. Ghadi, S. Adhikary, B. Tongbram, and S. Chakrabarti, “Evidence of quantum dot size uniformity in strain-coupled multilayered In(Ga)As/GaAs QDs grown

with constant overgrowth percentage," *J. Lumin.*, vol. 192, pp. 562–566, 2017.

[64] Z. Wasilewski, S. Fafard, and M. JP, "Size and shape engineering of vertically stacked self-assembled quantum dots," *J. Cryst. Growth*, vol. 201–202, pp. 1131–1135, 1999.

[65] J. Tatebayashi, N. Nuntawong, Y. Xin, P. Wong, S. Huang, C. Hains, L. Lester, and D. Huffaker, "Ground-state lasing of stacked InAs/GaAs quantum dots with GaP strain-compensation layers grown by metal organic chemical vapor deposition," *Appl. Phys. Lett.*, vol. 88, no. 22, p. 221107, 2006.

[66] P. J. Simmonds, M. Sun, R. B. Laghumavarapu, B. Liang, A. G. Norman, J.-W. Luo, and D. L. Huffaker, "Improved quantum dot stacking for intermediate band solar cells using strain compensation," *Nanotechnology*, vol. 25, no. 44, p. 445402, 2014.

[67] G. S. Solomon, J. A. Trezza, A. F. Marshall, and J. S. Harris, Jr., "Vertically aligned and electronically coupled growth induced InAs islands in GaAs," *Phys. Rev. Lett.*, vol. 76, pp. 952–955, 1996.

[68] R. Heitz, A. Kalburge, Q. Xie, M. Grundmann, P. Chen, A. Hoffmann, A. Madhukar, and D. Bimberg, "Excited states and energy relaxation in stacked InAs/GaAs quantum dots," *Phys. Rev. B*, vol. 57, pp. 9050–9060, 1998.

[69] N. Ledentsov, V. Shchukin, M. Grundmann, N. Kirstaedter, J. Böhrer, O. Schmidt, D. Bimberg, V. Ustinov, Y. A. Egorov, A. Zhukov, P. Kop'ev, S. Zaitsev, Y. N. Gordeev, Z. I. Alferov, A. Borovkov, A. Kosogov, S. Ruvimov, P. Werner, U. Gösele, and J. Heydenreich, "Direct formation of vertically coupled quantum dots in Stranski-Krastanow growth," *Phys. Rev. B*, vol. 54, no. 12, pp. 8743–8750, 1996.

[70] G. Bester, J. Shumway, and A. Zunger, "Theory of excitonic spectra and entanglement engineering in dot molecules," *Phys. Rev. Lett.*, vol. 93, no. 4, p. 047401, 2004.

[71] E. Biolatti, R. C. Iotti, P. Zanardi, and F. Rossi, "Quantum information processing with semiconductor macroatoms," *Phys. Rev. Lett.*, vol. 85, no. 26, p. 5647, 2000.

[72] S. Anantathanasarn, R. Nötzel, P. van Veldhoven, F. van Otten, T. Eijkemans, Y. Barbarin,

T. de Vries, E. Smalbrugge, E. Geluk, E. Bente, Y. Oei, M. Smit, and J. Wolter, “Stacking, polarization control, and lasing of wavelength tunable (1.55μm region) InAs/InGaAsP/InP (100) quantum dots,” *J. Cryst. Growth*, vol. 298, pp. 553–557, 2007.

[73] V. Tasco, M. Usman, M. D. Giorgi, and A. Passaseo, “Tuning of polarization sensitivity in closely stacked trilayer InAs/GaAs quantum dots induced by overgrowth dynamics,” *Nanotechnology*, vol. 25, no. 5, p. 055207, 2014.

[74] M. Gong, K. Duan, C. Li, R. Magri, G. Narvaez, and L. He, “Electronic structure of self-assembled InAs/InP quantum dots: Comparison with self-assembled InAs/GaAs quantum dots,” *Phys. Rev. B*, vol. 77, no. 4, p. 045326, 2008.

[75] M. Gong, W. Zhang, C. G. Guo, and L. He, “Atomistic pseudopotential theory of optical properties of exciton complexes in InAs/InP quantum dots,” *Appl. Phys. Lett.*, vol. 99, no. 23, p. 231106, 2011.

[76] M. Zieliński, “Valence band offset, strain and shape effects on confined states in self-assembled InAs/InP and InAs/GaAs quantum dots,” *J. Phys.: Condens. Matter*, vol. 25, no. 46, p. 465301, 2013.

[77] M. Holm, M.-E. Pistol, and C. Pryor, “Calculations of the electronic structure of strained InAs quantum dots in InP,” *J. Appl. Phys.*, vol. 92, no. 2, pp. 932–936, 2002.

[78] O. Stier, M. Grundmann, and D. Bimberg, “Electronic and optical properties of strained quantum dots modeled by 8-band $k \cdot p$ theory,” *Phys. Rev. B*, vol. 59, no. 8, pp. 5688–5701, 1999.

[79] J. Even, F. Doré, C. Cornet, and L. Pedesseau, “Semianalytical model for simulation of electronic properties of narrow-gap strained semiconductor quantum nanostructures,” *Phys. Rev. B*, vol. 77, no. 8, p. 085305, 2008.

[80] H. Ilatikhameneh, T. Ameen, and G. Klimeck, “Universal behavior of atomistic strain in self-assembled quantum dots,” *IEEE J. Quantum Electron.*, vol. 52, no. 7, p. 7000308, 2016.

[81] J. Saha, D. Panda, D. Das, V. Chavan, and S. Chakrabarti, “Enhanced luminescence and

optical performance through strain minimization in self-assembled InAs QDs using dual quaternary-ternary/ternary-quaternary capping," *J. Lumin.*, vol. 197, pp. 297–303, 2018.

[82] C. Pryor, "Eight-band calculations of strained InAs/GaAs quantum dots compared with one-, four-, and six-band approximations," *Phys. Rev. B*, vol. 57, pp. 7190–7195, 1998.

[83] M. Tadić, F. Peeters, K. Janssens, M. Korkusiński, and P. Hawrylak, "Strain and band edges in single and coupled cylindrical InAs/GaAs and InP/InGaP self-assembled quantum dots," *J. Appl. Phys.*, vol. 92, no. 10, p. 5819, 2002.

[84] M. Grundmann, O. Stier, and D. Bimberg, "InAs/GaAs pyramidal quantum dots: Strain distribution, optical phonons, and electronic structure," *Phys. Rev. B*, vol. 52, pp. 11969–11981, 1995.

[85] C. Pryor, M.-E. Pistol, and L. Samuelson, "Electronic structure of strained InP/$Ga_{0.51}In_{0.49}P$ quantum dots," *Phys. Rev. B*, vol. 56, pp. 10404–10411, 1997.

[86] C. E. Pryor and M.-E. Pistol, "Band-edge diagrams for strained III-V semiconductor quantum wells, wires, and dots," *Phys. Rev. B*, vol. 72, p. 205311, 2005.

[87] M. Zieliński, K. M., and P. Hawrylak, "Atomistic tight-binding theory of multiexciton complexes in a self-assembled InAs quantum dot," *Phys. Rev. B*, vol. 81, no. 8, p. 085301, 2010.

[88] A. Lanacer, N. Shtinkov, P. Desjardins, R. Masut, and R. Leonelli, "Optical emission from InAs/InP self-assembled quantum dots: evidence for As/P intermixing," *Semicond. Sci. Tech.*, vol. 22, no. 12, p. 1282, 2007.

[89] S. Lee, O. Lazarenkova, P. Allmen, F. Oyafuso, and G. Klimeck, "Effect of wetting layers on the strain and electronic structure of InAs self-assembled quantum dots," *Phys. Rev. B*, vol. 70, no. 12, p. 125307, 2004.

[90] E. Goldmann, *From Structure to Spectra: Tight-Binding Theory of InGaAs Quantum Dots*. PhD thesis, Dept. Phys. Electron., Universität Bremen, Bremen, Germany, 2014.

[91] J. C. Phillips, "Energy-band interpolation scheme based on a pseudopotential," *Phys. Rev.*,

vol. 112, pp. 685–695, 1958.

[92] G. Bester, “Electronic excitations in nanostructures: an empirical pseudopotential based approach,” *J. Phys. Condens. Matter*, vol. 21, no. 2, p. 023202, 2009.

[93] M. Sanaee, A. Zarifkar, and M. Sheikhi, “Frequency noise analysis of 1.55 μm indium arsenide/indium phosphide quantum dot lasers: impact of non-linear gain and direct carrier transition,” *IET Optoelectronics*, vol. 10, no. 4, pp. 134–141, 2016.

[94] F. Grillot, K. Veselinov, M. Gioannini, I. Montrosset, J. Even, R. Piron, E. Homeyer, and S. Loualiche, “Spectral analysis of 1.55-μm InAs–InP (113) B Quantum-Dot lasers based on a multipopulation rate equations model,” *IEEE J. Quantum Electron.*, vol. 45, no. 7, pp. 872–878, 2009.

[95] M. Gioannini and I. Montrosset, “Numerical analysis of the frequency chirp in quantum-dot semiconductor lasers,” *IEEE J. Quantum Electron.*, vol. 43, no. 10, pp. 941–949, 2007.

[96] M. Sugawara, K. Mukai, Y. Nakata, and H. Ishikawa, “Effect of homogeneous broadening of optical gain on lasing spectra in self-assembled $In_xGa_{1-x}As$/GaAs quantum dot lasers,” *Phys. Rev. B*, vol. 61, no. 11, pp. 7595–7603, 2000.

[97] Z. Jiao, R. Zhang, X. Zhang, and J. Liu, “Modeling of single-section quantum dot mode-locked lasers: Impact of group velocity dispersion and self phase modulation,” *IEEE J. Quantum Electron.*, vol. 49, no. 12, pp. 1008–1015, 2013.

[98] P. Bardella, L. L. Columbo, and M. Gioannini, “Self-generation of optical frequency comb in single section quantum dot Fabry-Perot lasers: a theoretical study,” *Opt. Express*, vol. 25, no. 21, pp. 26234–26252, 2017.

[99] M. Gioannini, P. Bardella, and I. Montrosset, “Time-Domain Traveling-Wave analysis of the multimode dynamics of quantum dot Fabry-Perot lasers,” *IEEE J. Sel. Top. Quantum Electron.*, vol. 21, no. 6, pp. 698–708, 2015.

[100] M. Rossetti, P. Bardella, and I. Montrosset, “Time-Domain Travelling-Wave model for quantum dot passively Mode-Locked lasers,” *IEEE J. Quantum Electron.*, vol. 47, no. 2,

pp. 139–150, 2011.

[101] M. Rossetti, P. Bardella, and I. Montrosset, “Modeling passive Mode-Locking in quantum dot lasers: A comparison between a Finite-Difference Traveling-Wave model and a delayed differential equation approach,” *IEEE J. Quantum Electron.*, vol. 47, no. 5, pp. 569–576, 2011.

[102] C. Wang, F. Grillot, and J. Even, “Modelling the gain compression effects on semiconductor quantum-dot laser through a new modulation transfer function,” in *IEEE Photonics Conference 2012*, pp. 46–47, Sept 2012.

[103] K. Kayhani and E. Rajaei, “Investigation of dynamical characteristics and modulation response function of InAs/InP (311)B quantum dot lasers with different QD size,” *Photonics Nanostructures*, vol. 25, pp. 1–8, 2017.

[104] J. S. Kim, M. Kawabe, and N. Koguchi, “Ordering of high-quality InAs quantum dots on defect-free nanoholes,” *Appl. Phys. Lett.*, vol. 88, no. 7, p. 072107, 2006.

[105] N. Kleemans, J. van Bree, M. Bozkurt, P. J. van Veldhoven, P. A. Nouwens, R. Nötzel, A. Y. Silov, P. M. Koenraad, and M. E. Flatté, “Size-dependent exciton *g* factor in self-assembled InAs/InP quantum dots,” *Phys. Rev. B*, vol. 79, p. 045311, 2009.

[106] Y. Akanuma, I. Yamakawa, Y. Sakuma, T. Usuki, and A. Nakamura, “Scanning tunneling microscopy study of interfacial structure of InAs quantum dots on InP(001) grown by a double-cap method,” *Appl. Phys. Lett.*, vol. 90, no. 9, p. 093112, 2007.

[107] H. Eisele, A. Lenz, R. Heitz, R. Timm, M. Dähne, Y. Temko, T. Suzuki, and K. Jacobi, “Change of InAs/GaAs quantum dot shape and composition during capping,” *J. Appl. Phys.*, vol. 104, no. 12, p. 124301, 2008.

[108] L. Ouattara, A. Mikkelsen, E. Lundgren, M. Borgström, L. Samuelson, and W. Seifert, “Stacked InAs quantum dots in InP studied by cross-sectional scanning tunnelling microscopy,” *Nanotechnology*, vol. 15, no. 12, pp. 1701–1707, 2004.

[109] B. Grandidier, Y. M. Niquet, B. Legrand, J. P. Nys, C. Priester, D. Stiévenard, J. M. Gérard,

and V. Thierry-Mieg, “Imaging the wave-function amplitudes in cleaved semiconductor quantum boxes,” *Phys. Rev. Lett.*, vol. 85, pp. 1068–1071, Jul 2000.

[110] T. Maltezopoulos, A. Bolz, C. Meyer, C. Heyn, W. Hansen, M. Morgenstern, and R. Wiesendanger, “Wave-function mapping of InAs quantum dots by scanning tunneling spectroscopy,” *Phys. Rev. Lett.*, vol. 91, no. 19, p. 196804, 2003.

[111] S. Kadkhodazadeh, E. Semenova, K. Yvind, and D. R.E., “Investigating the chemical and morphological evolution of GaAs capped InAs/InP quantum dots emitting at 1.5μm using aberration-corrected scanning transmission electron microscopy,” *J. Cryst. Growth*, vol. 329, no. 1, pp. 57–61, 2011.

[112] T. Inoue, T. Kita, O. Wada, M. Konno, T. Yaguchi, and T. Kamino, “Electron tomography of embedded semiconductor quantum dot,” *Appl. Phys. Lett.*, vol. 92, no. 3, p. 031902, 2008.

[113] V. A. Shchukin and D. Bimberg, “Spontaneous ordering of nanostructures on crystal surfaces,” *Rev. Mod. Phys.*, vol. 71, pp. 1125–1171, 1999.

[114] A. Romanov, G. Beltz, W. Fischer, P. Petroff, and J. Speck, “Elastic fields of quantum dots in subsurface layers,” *J. Appl. Phys.*, vol. 89, no. 8, pp. 4523–4531, 2001.

[115] M. Kuo, T. Lin, K. Hong, B. Liao, H. Lee, and C. Yu, “Two-step strain analysis of self-assembled InAs/GaAs quantum dots,” *Semicond. Sci. Technol.*, vol. 21, no. 5, pp. 626–632, 2006.

[116] J. Sólyom, *Fundamentals of the Physics of Solids*. New York, USA: springer, 2007.

[117] E. O’Reilly, *Quantum Theory of Solids*. London, UK: CRC Press, 2002.

[118] J. C. Slater and G. F. Koster, “Simplified LCAO method for the periodic potential problem,” *Phys. Rev.*, vol. 94, pp. 1498–1524, Jun 1954.

[119] D. J. Chadi and M. L. Cohen, “Analytic expression for the electronic charge density distribution in diamond-structure crystals,” *Phys. Status Solidi B*, vol. 62, no. 1, pp. 235–248.

[120] F. R. Waugh, M. J. Berry, D. J. Mar, R. M. Westervelt, K. L. Campman, and A. C. Gossard,

"Single-electron charging in double and triple quantum dots with tunable coupling," *Phys. Rev. Lett.*, vol. 75, pp. 705–708, 1995.

[121] R. Nötzel and K. H. Ploog, "Direct synthesis of semiconductor quantum-wire and quantum-dot structures," *Adv. Mater.*, vol. 5, no. 1, pp. 22–29.

[122] L. Spanhel, M. Haase, H. Weller, and A. Henglein, "Photochemistry of colloidal semiconductors. 20. surface modification and stability of strong luminescing CdS particles," *J. Am. Chem. Soc.*, vol. 109, pp. 5649–5655, 1987.

[123] V. Colvin, A. Goldstein, and A. Alivisatos, "Semiconductor nanocrystals covalently bound to metal surfaces with self-assembled monolayers," *J. Am. Chem. Soc.*, vol. 114, no. 13, 1992.

[124] H. Lee, P. H. Holloway, and H. Yang, "Synthesis and characterization of colloidal ternary ZnCdSe semiconductor nanorods," *J. Chem. Phys.*, vol. 125, no. 16, p. 164711, 2006.

[125] S. Kadkhodazadeh, "High resolution STEM of quantum dots and quantum wires," *Micron*, 2013.

[126] J. C. Norman, D. Jung, Z. Zhang, Y. Wan, S. Liu, C. Shang, R. W. Herrick, W. W. Chow, A. C. Gossard, and J. E. Bowers, "A review of high-performance quantum dot lasers on silicon," *IEEE J. Quantum Electron.*, vol. 55, no. 2, pp. 1–11, 2019.

[127] Y. Shirasaki, G. Supran, M. Bawendi, and V. Bulović, "Emergence of colloidal quantum-dot light-emitting technologies," *Nat. Photonics*, vol. 7, no. 1, pp. 13–23, 2013.

[128] C. Pryor, J. Kim, L. Wang, A. Williamson, and A. Zunger, "Comparison of two methods for describing the strain profiles in quantum dots," *J. Appl. Phys.*, vol. 83, no. 5, pp. 2548–2554, 1998.

[129] M. Tadić, F. M. Peeters, and K. L. Janssens, "Effect of isotropic versus anisotropic elasticity on the electronic structure of cylindrical InP/$Ga_{0.51}In_{0.49}P$ self-assembled quantum dots," *Phys. Rev. B*, vol. 65, p. 165333, 2002.

[130] J. L. Birman, "Theory of the piezoelectric effect in the zincblende structure," *Phys. Rev.*,

vol. 111, pp. 1510–1514, Sep 1958.

[131] A. Schliwa, M. Winkelnkemper, and D. Bimberg, “Impact of size, shape, and composition on piezoelectric effects and electronic properties of In(Ga)As/GaAs quantum dots,” *Phys. Rev. B*, vol. 76, no. 20, p. 205324, 2007.

[132] G. Bir and G. Pikus, *Symmetry and Strain-Induced Effects in Semiconductors*. New York, USA: Wiley, 1974.

[133] I. Vurgaftman, J. Meyer, and L. Ram-Mohan, “Band parameters for III–V compound semiconductors and their alloys,” *J. Appl. Phys.*, vol. 89, no. 11, pp. 5815–5875, 2001.

[134] S. Chuang, *Physics of Photonic Devices*. Wiley Series in Pure and Applied Optics, New Jersey, USA: Wiley, 2012.

[135] D. L. Smith and C. Mailhiot, “Theory of semiconductor superlattice electronic structure,” *Rev. Mod. Phys.*, vol. 62, pp. 173–234, 1990.

[136] G. Bester and A. Zunger, “Cylindrically shaped zinc-blende semiconductor quantum dots do not have cylindrical symmetry: Atomistic symmetry, atomic relaxation, and piezoelectric effects,” *Phys. Rev. B*, vol. 71, p. 045318, 2005.

[137] G. Bester, X. Wu, D. Vanderbilt, and A. Zunger, “Importance of second-order piezoelectric effects in zinc-blende semiconductors,” *Phys. Rev. Lett.*, vol. 96, no. 18, p. 187602, 2006.

[138] M. A. Migliorato, D. Powell, A. G. Cullis, T. Hammerschmidt, and G. P. Srivastava, “Composition and strain dependence of the piezoelectric coefficients in $In_xGa_{1-x}As$ alloys,” *Phys. Rev. B*, vol. 74, p. 245332, 2006.

[139] F. Klotz, *Spin Effects in Self-Assembled Semiconductor Quantum Dots*. PhD thesis, Dept. Phys., Technische Universität München, München, Germany, 2012.

[140]J. M. Luttinger, “Quantum theory of cyclotron resonance in semiconductors: General theory,” *Phys. Rev.*, vol. 102, pp. 1030–1041, May 1956.

[141] B. A. Foreman, “Valence-band mixing in first-principles envelope-function theory,” *Phys. Rev. B*, vol. 76, p. 045327, 2007.

[142] O. Stier, *Electronic and Optical Properties of Quantum Dots and Wires*. PhD thesis, Technische Universität Berlin, Berlin, Germany, 2001.

[143] P. Löwdin, "A note on the quantum-mechanical perturbation theory," *J. Chem. Phys.*, vol. 19, no. 11, pp. 1396–1401, 1951.

[144] E. Kane, "Band structure of indium antimonide," *J. Phys. Chem. Solids*, vol. 1, pp. 249–261, 1957.

[145] S. Steiger, *NEMO5 User Manual*. Purdue University, West Lafayette, IN, USA, 2012.

[146] M. Gayer, *NanoFEM Platform - Documentation Draft*, 2009.

[147] COMSOL, Inc., *Introduction to COMSOL Multiphysics, version 5.4*. Burlington, MA, USA, 2018.

[148] L. Vegard, "Die Konstitution der Mischkristalle und die Raumfüllung der Atome," *Zeitschrift fur Physik*, vol. 5, pp. 17–26, 1921.

[149] A. Schliwa, *Electronic Properties of Self-Organized Quantum Dots*. PhD thesis, Dept. Math. Nat. Sci., Technische Universität Berlin, Berlin, Germany, 2007.

[150] L. Coldren, S. Corzine, and M. Mashanovitch, *Diode Lasers and Photonic Integrated Circuits*. Wiley Series in Microwave and Optical Engineering, New Jersey, USA: Wiley, 2012.

[151] I. O'Driscoll, P. Blood, and P. M. Smowton, "Random population of quantum dots in InAs–GaAs laser structures," *IEEE J. Quantum Electron.*, vol. 46, no. 4, pp. 525–532, 2010.

[152] C. H. Henry, R. A. Logan, and F. R. Merritt, "Measurement of gain and absorption spectra in AlGaAs buried heterostructure lasers," *J. Appl. Phys.*, vol. 51, no. 6, pp. 3042–3050, 1980.

[153] K. Veselinov, F. Grillot, C. Cornet, J. Even, A. Bekiarski, M. Gioannini, and S. Loualiche, "Analysis of the double laser emission occurring in 1.55-μm InAs-InP (113)B Quantum-Dot lasers," *IEEE J. Quantum Electron.*, vol. 43, no. 9, pp. 810–816, 2007.

[154] C. Wang, F. Grillot, and J. Even, "Impacts of wetting layer and excited state on the modulation response of quantum-dot lasers," *IEEE J. Quantum Electron.*, vol. 48, no. 9,

pp. 1144–1150, 2012.

[155] A. Markus, J. Chen, C. Paranthoën, A. Fiore, C. Platz, and G. O, "Simultaneous two-state lasing in quantum-dot lasers," *Appl. Phys. Lett.*, vol. 82, no. 12, pp. 1818–1820, 2003.

[156] E. Viktorov, P. Mandel, Y. Tanguy, J. Houlihan, and G. Huyet, "Electron-hole asymmetry and two-state lasing in quantum dot lasers," *Appl. Phys. Lett.*, vol. 87, no. 5, p. 053113, 2005.

[157] C. Meuer, J. Kim, M. Laemmlin, S. Liebich, G. Eisenstein, R. Bonk, T. Vallaitis, J. Leuthold, A. Kovsh, I. Krestnikov, and D. Bimberg, "High-speed small-signal cross-gain modulation in quantum-dot semiconductor optical amplifiers at 1.3 μm," *IEEE J. Sel. Top. Quantum Electron.*, vol. 15, no. 3, pp. 749–756, 2009.

[158] M. Gioannini, "Ground-state power quenching in two-state lasing quantum dot lasers," *J. Appl. Phys.*, vol. 111, no. 4, p. 043108, 2012.

[159] V. Korenev, A. Savelyev, A. Zhukov, A. Omelchenko, and M. Maximov, "Effect of carrier dynamics and temperature on two-state lasing in semiconductor quantum dot lasers," *Semiconductors*, vol. 47, no. 10, pp. 1397–1404, 2013.

[160] A. Röhm, *Modes of Operation of QD Lasers*, pp. 28–36. Wiesbaden: Springer Fachmedien Wiesbaden, 2015.

[161] W. Pauli, "Über den zusammenhang des abschlusses der elektronengruppen im atom mit der komplexstruktur der spektren," *Zeitschrift für Physik*, vol. 31, no. 1, pp. 765–783, 1925.

[162] Optiwave System, Inc., *Introduction to OptiBPM*. Ottawa, ON, Canada.

[163] Photon Design Ltd, *Introduction to FIMMPROP: A bi-directional optical propagation tool*. Oxford, UK.

[164] A. F. Oskooi, D. Roundy, M. Ibanescu, P. Bermel, J. D. Joannopoulos, and S. G. Johnson, "MEEP: A flexible free-software package for electromagnetic simulations by the FDTD method," *Comput. Phys. Commun.*, vol. 181, pp. 687–702, 2010.

[165] L. M. Zhang, S. F. Yu, M. C. Nowell, D. D. Marcenac, J. E. Carroll, and R. G. S. Plumb, "Dynamic analysis of radiation and side-mode suppression in a second-order DFB laser

using time-domain large-signal traveling wave model," *IEEE J. Quantum Electron.*, vol. 30, no. 6, pp. 1389–1395, 1994.

[166] J. Mulet and J. Mork, "Analysis of timing jitter in external-cavity mode-locked semiconductor lasers," *IEEE J. Quantum Electron.*, vol. 42, no. 3, pp. 249–256, 2006.

[167] W. Bogaerts, M. Fiers, and P. Dumon, "Design challenges in silicon photonics," *IEEE J. Sel. Top. Quantum Electron.*, vol. 20, no. 4, pp. 1–8, 2014.

[168] J. Javaloyes and S. Balle, "Multimode dynamics in bidirectional laser cavities by folding space into time delay," *Opt. Express*, vol. 20, no. 8, p. 8496, 2012.

[169] D. Puris, S. C, K. Lüdge, N. Majer, E. Schöll, and K. Petermann, "Time-domain model of quantum-dot semiconductor optical amplifiers for wideband optical signals," *Opt. Express*, vol. 20, no. 24, p. 27265, 2012.

[170] M. Gioannini and M. Rossetti, "Time-domain traveling wave model of quantum dot DFB lasers," *IEEE J. Sel. Top. Quantum Electron.*, vol. 17, no. 5, pp. 1318–1326, 2011.

[171] Lumerical Solutions, Inc, *FDTD solution: Refernce guide, release 7.5*. Vancouver, BC, Canada, 2011.

[172] MathWorks, Inc., *PDF Documentation for MATLAB*. Natick, Massachusetts, USA.

[173] P. Poole, R. Williams, J. Lefebvre, and S. Moisa, "Using As/P exchange processes to modify InAs/InP quantum dots," *J. Cryst. Growth*, vol. 257, no. 1–2, pp. 89–96, 2003.

[174] D. Cooper, J.-L. Rouviere, A. Béché, S. Kadkhodazadeh, E. Semenova, K. Yvind, and R. Dunin-Borkowski, "Quantitative strain mapping of InAs/InP quantum dots with 1 nm spatial resolution using dark field electron holography," *Appl. Phys. Lett.*, vol. 99, no. 26, p. 261911, 2011.

[175] S. Shusterman, A. Raizman, A. Sher, A. Schwarzman, O. Azriel, A. Boag, Y. Rosenwaks, P. Galindo, and Y. Paltiel, "Two-dimensional imaging of III-V quantum dots confinement potential," *Europhys. Lett.*, vol. 88, no. 6, p. 66003, 2010.

[176] M. Bayer, G. Ortner, and O. Stern, "Fine structure of neutral and charged excitons in self-

assembled In(Ga)As/(Al)GaAs quantum dots," *Phys. Rev. B*, vol. 65, no. 19, p. 195315, 2002.

[177] R. Singh and G. Bester, "Effects of atomic ordering on the electronic and optical properties of self-assembled $In_xGa_{1-x}As$/GaAs semiconductor quantum dots," *Phys. Rev. B*, vol. 84, no. 24, p. 241402, 2011.

[178] R. Seguin, A. Schliwa, S. Rodt, K. Pötschke, U. Pohl, and D. Bimberg, "Size-Dependent Fine-Structure splitting in Self-Organized InAs/GaAs quantum dots," *Phys. Rev. Lett.*, vol. 95, no. 25, p. 257402, 2005.

[179] D. Press, T. Ladd, B. Zhang, and Y. Yamamoto, "Complete quantum control of a single quantum dot spin using ultrafast optical pulses," *Nature*, vol. 456, no. 7219, pp. 218–221, 2008.

[180] Warburton and J. Richard, "Single spins in self-assembled quantum dots," *Nat. Mater.*, vol. 12, no. 6, pp. 483–493, 2013.

[181] J. Liu, Z. Lu, S. Raymond, P. J. Poole, and P. J. Barrios, "Dual-wavelength 92.5 GHz self-mode-locked InP-based quantum dot laser," *Opt. Lett.*, vol. 33, no. 15, pp. 1702–1704, 2008.

[182] S. Li, Q. Gong, and C. Cao, "Multicolor InAs/InP (100) quantum dot laser," *Chin. Phys. Lett.*, vol. 28, no. 11, p. 114212, 2011.

[183] S. Li, Q. Gong, X. Wang, C. Cao, Z. Zhou, and H. Wang, "Cavity length and stripe width dependent lasing characteristics of InAs/InP (100) quantum dot lasers," *Infrared Phys. Technol.*, vol. 75, pp. 51–55, 2016.

[184] Z. Lin, G. Yuan, and Z. Wang, "Analysis of ground state spectral splitting of quantum dot lasers aimed for tunable terahertz generation," *J. Opt. Soc. Am. B: Opt. Phys.*, vol. 33, no. 10, pp. 2114–2119, 2016.

[185] P. Vullum, M. Nord, M. Vatanparast, S. Thomassen, C. Boothroyd, R. Holmestad, B. Fimland, and T. Reenaas, "Quantitative strain analysis of InAs/GaAs quantum dot materials," *Sci. Reports*, vol. 7, p. 45376, 2017.

[186] S. Lee, J. Kim, S. Noh, J. Choe, and K. Lee, "Evolution of structural and optical characteristics in InAs quantum dots capped by GaAs layers comparable to dot height," *J. Cryst. Growth*, vol. 284, no. 1-2, pp. 39–46, 2005.

[187] J. Persson, U. Hakanson, J. M. Johansson, L. Samuelson, and E. M. Pistol, "Strain effects on individual quantum dots: Dependence of cap layer thickness," *Phys. Rev. B*, vol. 72, no. 8, p. 085302, 2005.

[188] C. Mesaritakis, C. Simos, H. Simos, and S. Mikroulis, "Pulse width narrowing due to dual ground state emission in quantum dot passively mode locked lasers," *Appl. Phys. Lett.*, vol. 96, no. 21, p. 211110, 2010.

[189] D. Barettin, M. Auf der Maur, R. De Angelis, P. Prosposito, M. Casalboni, and A. Pecchia, "Inter-dot strain field effect on the optoelectronic properties of realistic InP lateral quantum-dot molecules," *J. Appl. Phys.*, vol. 117, no. 9, p. 094306, 2015.

[190] X. Chen, Y. Xiong, and X. Zhang, "Interaction of self-assembled InAs/InGaAsP/InP (001) quantum dots," *Opt. Commun.*, vol. 429, pp. 18 – 28, 2018.

[191] M. Korkusiński and P. Hawrylak, "Electronic structure of vertically stacked self-assembled quantum disks," *Phys. Rev. B*, vol. 63, p. 195311, Apr 2001.

[192] H. Shin, W. Lee, and Y.-H. Yoo, "Comparison of strain fields in truncated and un-truncated quantum dots in stacked InAs/GaAs nanostructures with varying stacking periods," *J. Phys.: Condens. Matter*, vol. 15, pp. 3689–3699, may 2003.

[193] M. Tadić and F. M. Peeters, "Binding of electrons, holes, and excitons in symmetric strained InP/$In_{0.49}Ga_{0.51}P$ triple quantum-dot molecules," *Phys. Rev. B*, vol. 70, p. 195302, Nov 2004.

[194] W. Jaskólski, M. Zieliński, G. W. Bryant, and J. Aizpurua, "Strain effects on the electronic structure of strongly coupled self-assembled InAs/GaAs quantum dots: Tight-binding approach," *Phys. Rev. B*, vol. 74, p. 195339, 2006.

[195] T. Saito, H. Ebe, Y. Arakawa, T. Kakitsuka, and M. Sugawara, "Optical polarization in columnar InAs/GaAs quantum dots: 8-band $k \cdot p$ calculations," *Phys. Rev. B*, vol. 77,

p. 195318, May 2008.

[196] M. Usman, T. Inoue, Y. Harda, G. Klimeck, and T. Kita, "Experimental and atomistic theoretical study of degree of polarization from multilayer InAs/GaAs quantum dot stacks," *Phys. Rev. B*, vol. 84, p. 115321, Sep 2011.

[197] H. Eisele, O. Flebbe, T. Kalka, C. Preinesberger, F. Heinrichsdorff, A. Krost, D. Bimberg, and M. Dähne, "Cross-sectional scanning-tunneling microscopy of stacked InAs quantum dots," *Appl. Phys. Lett.*, vol. 75, no. 1, pp. 106–108, 1999.

[198] Q. Xie, A. Madhukar, P. Chen, and N. P. Kobayashi, "Vertically Self-Organized InAs quantum box islands on GaAs(100)," *Phys. Rev. Lett.*, vol. 75, no. 13, pp. 2542–2545, 1995.

[199] S. Adhikary, N. Halder, S. Chakrabarti, S. Majumdar, S. Ray, M. Herrera, M. Bonds, and N. Browning, "Investigation of strain in self-assembled multilayer InAs/GaAs quantum dot heterostructures," *J. Cryst. Growth.*, vol. 312, no. 5, pp. 724–729, 2010.

[200] M. Sabaeian and M. Shahzadeh, "Self-assembled strained pyramid-shaped InAs/GaAs quantum dots: The effects of wetting layer thickness on discrete and quasi-continuum levels," *Physica E: Low.-Dimens. Syst. Nanostruct.*, vol. 61, pp. 62–68, 2014.

[201] S.-S. Li, K. Chang, and J.-B. Xia, "Effective-mass theory for hierarchical self-assembly of GaAs/$Al_xGa_{1-x}As$ quantum dots," *Phys. Rev. B*, vol. 71, p. 155301, Apr 2005.

[202] S. Raymond, S. Fafard, P. J. Poole, A. Wojs, P. Hawrylak, S. Charbonneau, D. Leonard, R. Leon, P. M. Petroff, and J. L. Merz, "State filling and time-resolved photoluminescence of excited states in $In_xGa_{1-x}As$/GaAs self-assembled quantum dots," *Phys. Rev. B*, vol. 54, pp. 11548–11554, 1996.

[203] M. Syperek, J. Andrzejewski, E. Rogowicz, J. Misiewicz, S. Bauer, V. Sichkovskyi, J. Reithmaier, and G. Sek, "Carrier relaxation bottleneck in type-II InAs/InGaAlAs/InP(001) coupled quantum dots-quantum well structure emitting at 1.55 μm," *Appl. Phys. Lett.*, vol. 112, no. 22, p. 221901, 2018.

[204] H. Shin, E. Yoon, K.-S. Hong, W. Lee, and Y.-H. Yoo, "Blueshifts of emission energy from

InAs quantum dots in GaAs matrix due to narrowed interdot spacing: A token of the integrity of a nanostructure," *Appl. Phys. A: Mater. Sci. Process*, vol. 81, pp. 715–719, Sep 2005.

[205] P. Howe, E. C. Le Ru, E. Clarke, R. Murray, and T. S. Jones, "Quantification of segregation and strain effects in InAs/GaAs quantum dot growth," *J. Appl. Phys.*, vol. 98, no. 11, p. 113511, 2005.

[206] J. He, Y. C. Zhang, B. Xu, and Z. G. Wang, "Effects of seed dot layer and thin GaAs spacer layer on the structure and optical properties of upper In(Ga)As quantum dots," *J. Appl. Phys.*, vol. 93, no. 11, pp. 8898–8902, 2003.

[207] O. G. Schmidt and K. Eberl, "Multiple layers of self-asssembled Ge/Si islands: Photoluminescence, strain fields, material interdiffusion, and island formation," *Phys. Rev. B*, vol. 61, pp. 13721–13729, May 2000.

[208] Y. Xiong and X. Zhang, "An accurate method of modeling self-assembled InAs/InGaAsP/InP (001) quantum dot with double-capping procedure," *IEEE J. Quantum Electron.*, vol. 53, no. 6, pp. 1–11, 2017.

[209] C. Wang, B. Lingnau, K. Lüdge, J. Even, and F. Grillot, "Enhanced dynamic performance of quantum dot semiconductor lasers operating on the excited state," *IEEE J. Quantum Electron.*, vol. 50, no. 9, pp. 1–9, 2014.

[210] F. Zubov, M. Maximov, E. Moiseev, A. Savelyev, Y. Shernyakov, D. Livshits, N. Kryzhanovskaya, and A. Zhukov, "Observation of zero linewidth enhancement factor at excited state band in quantum dot laser," *Electron. Lett.*, vol. 51, no. 21, pp. 1686–1688, 2015.

[211] H. Huang, D. Arsenijević, K. Schires, T. Sadeev, D. Bimberg, and F. Grillot, "Multimode optical feedback dynamics of InAs/GaAs quantum-dot lasers emitting on different lasing states," *Aip Adv.*, vol. 6, no. 12, p. 125114, 2016.

[212] D. Arsenijević, A. Schliwa, H. Schmeckebier, M. Stubenrauch, M. Spiegelberg, D. Bimberg, V. Mikhelashvili, and G. Eisenstein, "Comparison of dynamic properties of

ground- and excited-state emission in p-doped InAs/GaAs quantum-dot lasers," *Appl. Phys. Lett.*, vol. 104, no. 18, p. 181101, 2014.

[213] D. Arsenijević and D. Bimberg, "Quantum-dot lasers for 35 Gbit/s pulse-amplitude modulation and 160 Gbit/s differential quadrature phase-shift keying," in *SPIE Proc. 9892*, p. 98920S, 2016.

[214] A. Röhm, B. Lingnau, and K. Lüdge, "Ground-state modulation-enhancement by two-state lasing in quantum-dot laser devices," *Appl. Phys. Lett.*, vol. 106, no. 19, p. 191102, 2015.

[215] S. Meinecke, B. Lingnau, A. Röhm, and K. Lüdge, "Stability of optically injected two-state quantum-dot lasers," *Ann. Phys. (Berlin)*, vol. 529, no. 12, p. 1600279, 2017.

[216] M. Cataluna, D. I. Nikitichev, S. Mikroulis, H. Simos, C. Simos, C. Mesaritakis, D. Syvridis, I. Krestnikov, D. Livshits, and E. U. Rafailov, "Dual-wavelength mode-locked quantum-dot laser, via ground and excited state transitions: Experimental and theoretical investigation," *Opt. Express*, vol. 18, no. 12, pp. 12832–12838, 2010.

[217] S. Breuer, M. Rossetti, W. Elsässer, L. Drzewietzki, P. Bardella, I. Montrosset, M. Krakowski, and M. Hopkinson, "Reverse-emission-state-transition mode locking of a two-section InAs/InGaAs quantum dot laser," *Appl. Phys. Lett.*, vol. 97, no. 7, p. 071118, 2010.

[218] B. Tykalewicz, D. Goulding, S. P. Hegarty, G. Huyet, D. Byrne, R. Phelan, and B. Kelleher, "All-optical switching with a dual-state, single-section quantum dot laser via optical injection," *Opt. Lett.*, vol. 39, no. 15, pp. 4607–4610, 2014.

[219] M. Sugawara, N. Hatori, H. Ebe, M. Ishida, Y. Arakawa, T. Akiyama, K. Otsubo, and Y. Nakata, "Modeling room-temperature lasing spectra of 1.3-μm self-assembled InAs/GaAs quantum-dot lasers: Homogeneous broadening of optical gain under current injection," *J. Appl. Phys.*, vol. 97, no. 4, p. 043523, 2005.

[220] Z. Zhang, Q. Jiang, and R. Hogg, "Simultaneous three-state lasing in quantum dot laser at room temperature," *Electron. Lett.*, vol. 46, no. 16, pp. 1155–1157, 2010.

[221] A. Zhukov, M. Maximov, Y. M. Shernyakov, D. Livshits, A. Savelyev, F. Zubov, and V. Klimenko, "Features of simultaneous ground- and excited-state lasing in quantum dot lasers," *Semiconductors*, vol. 46, no. 2, pp. 231–235, 2012.

[222] A. Markus, M. Rossetti, V. Calligari, C. D, J. Chen, A. Fiore, and R. Scollo, "Two-state switching and dynamics in quantum dot two-section lasers," *J. Appl. Phys.*, vol. 100, no. 11, p. 113104, 2006.

[223] H. Wang, H. Cheng, S. Lin, and C. Lee, "Wavelength switching transition in quantum dot lasers," *Appl. Phys. Lett.*, vol. 90, no. 8, p. 081112, 2007.

[224] R. Pawlus, L. Columbo, P. Bardella, S. Breuer, and M. Gioannini, "Intensity noise behavior of an InAs/InGaAs quantum dot laser emitting on ground states and excited states," *Opt. Lett.*, vol. 43, no. 4, pp. 867–870, 2018.

[225] C. Platz, C. Paranthoën, P. Caroff, N. Bertru, C. Labbé, J. Even, O. Dehaese, H. Folliot, L. A. Corre, S. Loualiche, G. Moreau, J. Simon, and A. Ramdane, "Comparison of InAs quantum dot lasers emitting at 1.55 μm under optical and electrical injection," *Semicond. Sci. Tech.*, vol. 20, no. 5, pp. 459–463, 2005.

[226] G. Moreau, S. Azouigui, D. Cong, K. Merghem, A. Martinez, G. Patriarche, A. Ramdane, F. Lelarge, B. Rousseau, B. Dagens, F. Poingt, A. Accard, and F. Pommereau, "Effect of layer stacking and p-type doping on the performance of InAs/InP quantum-dash-in-a-well lasers emitting at 1.55μm," *Appl. Phys. Lett.*, vol. 89, no. 24, p. 241123, 2006.

[227] Y. Xiong and X. Zhang, "Wavelength Blue-Shifting and gain spectral bandwidth of InAs/InP quantum dots for laser applications around 1.55 μm," *IEEE J. Quantum Electron.*, vol. 54, no. 1, pp. 1–9, 2017.

[228] D. Gready and G. Eisenstein, "Carrier dynamics and modulation capabilities of 1.55-μm Quantum-Dot lasers," *IEEE J. Sel. Top. Quantum Electron.*, vol. 19, no. 4, p. 1900307, 2013.

[229] A. Röhm, B. Lingnau, and K. Lüdge, "Understanding Ground-State quenching in Quantum-Dot lasers," *IEEE J. Quantum Electron.*, vol. 51, no. 1, pp. 1–11, 2015.

[230] Y. Xiong and X. Zhang, "InAs/InP quantum dots stacking: Impact of spacer layer on optical properties," *J. Appl. Phys.*, vol. 125, no. 9, p. 093103, 2019.

[231] Z. Lu, J. Liu, P. Poole, S. Raymond, P. Barrios, D. Poitras, G. Pakulski, P. Grant, and R. D, "An L-band monolithic InAs/InP quantum dot mode-locked laser with femtosecond pulses," *Opt. Express*, vol. 17, no. 16, pp. 13609–13614, 2009.

[232] C. Wang, J. Zhuang, F. Grillot, and S. Chan, "Contribution of off-resonant states to the phase noise of quantum dot lasers," *Opt. Express*, vol. 24, no. 26, pp. 29872–29880, 2016.

[233] R. Hui and M. O'Sullivan, "Chapter 3 - characterization of optical devices," in *Fiber Optic Measurement Techniques* (R. Hui and M. O'Sullivan, eds.), pp. 259–363, Boston: Academic Press, 2009.

[234] C. Redlich, B. Lingnau, H. Huang, R. Raghunathan, K. Schires, P. Poole, F. Grillot, and K. Ludge, "Linewidth rebroadening in quantum dot semiconductor lasers," *IEEE J. Sel. Top. Quantum Electron.*, vol. 23, no. 6, pp. 1–10, 2017.

[235] J. Duan, H. Huang, Z. Lu, P. Poole, C. Wang, and F. Grillot, "Narrow spectral linewidth in InAs/InP quantum dot distributed feedback lasers," *Appl. Phys. Lett.*, vol. 112, no. 12, p. 121102, 2018.

[236] C. Weber, P. Bardella, L. Columbo, M. Gioannini, and S. Breuer, "Radio-frequency analysis of self-mode-locked quantum dot laser," *Mater. Today Proc.*, vol. 7, pp. 908–911, 2019.

[237] C. Henry, "Theory of the linewidth of semiconductor lasers," *IEEE J. Quantum Electron.*, vol. 18, no. 2, pp. 259–264, 1982.

[238] E. Li, "Material parameters of InGaAsP and InAlGaAs systems for use in quantum well structures at low and room temperatures," *Physica E: Low Dimens. Syst. Nanostruct.*, vol. 5, no. 4, pp. 215–273, 2000.

[239] S. Adachi, *Properties of Semiconductor Alloys: Group-IV, III-V and II-VI Semiconductors*. Chichester, U.K.: Wiley, 2009.

[240] B. Annie, P. Prodhomme, and G. Bester, "First- and second-order piezoelectricity in III-V

semiconductors," *Phys. Rev. B*, vol. 84, no. 19, p. 195207, 2011.

Publications

[1] **Yiling Xiong** and Xiupu Zhang, "Two-state lasing at room temperature in InAs/InP quantum dots," *J. Appl. Phys.*, vol. 126, no. 13, p. 133102, Oct. 2019. DOI: 10.1063/1.5110316.

[2] **Yiling Xiong** and Xiupu Zhang, "InAs/InP quantum dots stacking: Impact of spacer layer on optical properties," *J. Appl. Phys.*, vol. 125, no. 9, p. 093103, Mar. 2019. DOI: 10.1063/1.5082722.

[3] **Yiling Xiong** and Xiupu Zhang, "Wavelength blue-shifting and gain spectral bandwidth of InAs/InP quantum dots for laser applications around 1.55 μm," *IEEE J. Quantum Electron.*, vol. 54, no. 1, pp. 1–9, Feb. 2018. DOI: 10.1109/JQE.2017.2779880.

[4] **Yiling Xiong** and Xiupu Zhang, "An accurate method of modeling self-assembled InAs/InGaAsP/InP (001) quantum dot with double-capping procedure," *IEEE J. Quantum Electron.*, vol. 53, no. 6, pp. 1–11, Dec. 2017. DOI: 10.1109/JQE.2017.2762400.

[5] X. Chen, **Y. Xiong**, and X. Zhang, "Interaction of self-assembled InAs/InGaAsP/InP (001) quantum dots," *Opt. Commun.*, vol. 429, pp. 18 – 28, Aug. 2018. DOI: 10.1016/j.optcom.2018.07.083